the Ceramic Society of Japan, International Edition
ISSN 0912-9200

ɔurnal of the CERAMIC SOCIETY of ɟpan, *ternational Edition*

ol.100 September1992

18 Papers from Journal of the Ceramic Society of Japan(Japanese version), Vol. 100 No.9 1992

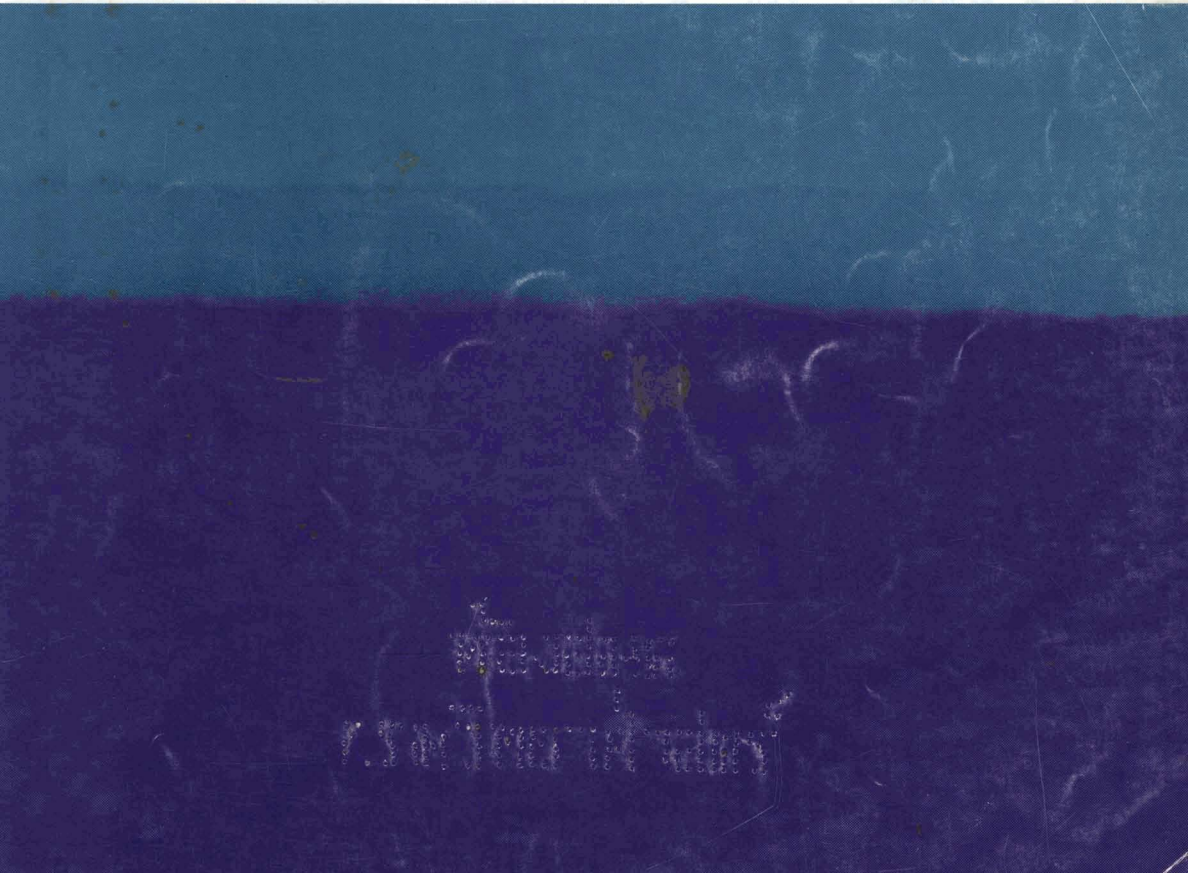

Journal of the Ceramic Society of Japan, *International Edition*

Vol.100 No.9
Sept. 1992

Editorial Board
Dr. Nobuyasu Mizutani
Prof., Tokyo Institute of Technology
Dr. Yusuke Moriyoshi
Director, Nat. Inst. for Res. in Inorganic Materials
Dr. Teruo Sakaino
Prof. Emeritus, Tokyo Institute of Technology
Prof. Kitao Takahara
Yukio Endo
Chairman, Koyo-Sha Co., Ltd.
Dr. Yoshiro Suzuki
Executive Director,
The Ceramic Society of Japan
Dr. Takashi Hanazawa
Director, The Ceramic Society of Japan
Keiji Hayashi
Managing Editor

Editorial Staff
Managing Editor Keiji Hayashi
Associate Editor Kohsuke Odani
Assistant Artists Toshimitsu Irie
Misao Tomita
Assistant Kiyoe Kojima
Ji-Ye Zhang
Circulation Youko Matsumoto
Publisher Keiji Hayashi

Published Monthly by
FUJI TECHNOLOGY PRESS LTD.
7F Daini Bunsei Bldg.
11-7, Toranomon 1-chome
Minato-ku, Tokyo 105, Japan
Tel:81-3-3508-0051
Fax:81-3-3592-0648

One year subscription
Air Mail ¥200,000
Copyright - © 1992 by
The Ceramic Society of Japan and Fuji Technology Press Ltd. All rights reserved.

No part of this publication may be reproduced, stored in a retrieval system, or transmitted, in any form or by any means, electronic, mechanical, photo copying, recording, or otherwise, without the prior written permission of the publishers. The papers, excluding those on information and communications, reviews, etc., were originally received by Journal of the Ceramic Society of Japan, and translated for this journal. The responsibility for the translation lies with the Editional Board.

CONTENTS

Papers:

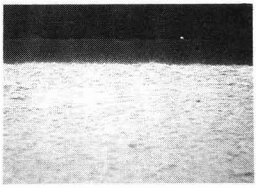

Cover

A epitaxal PLZT thin film fabricated on MgO single crystal substrate.

Prof. Nobuyasu Mizutani, Tokyo Institute of Technology, fabricated an epitaxial growth 1.5μm thick PLZT film perfectly arranged on C axis direction with MOCVD process.

Papers, Letters and Notes

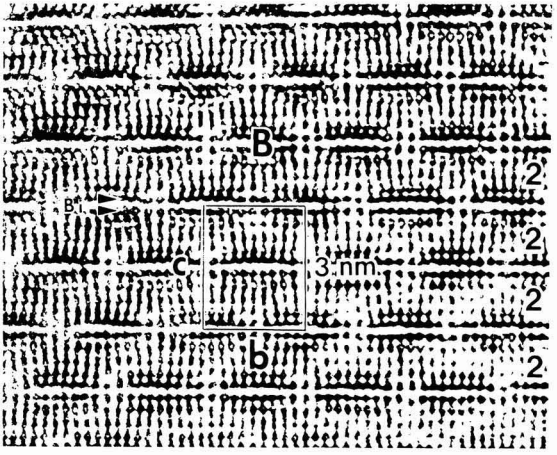

High resolution electron microscope photograph of the modulation doped structure of $Bi_2Sr_2CaCu_2O_y$ (T_c=80K) in the [100] direction. Figures at right side indicate number of copper layers, symbol B indicates bismuth rich region.

Changes in the Crystal Structure of RF-Magnetron Sputtered $BaTiO_3$ Thin Films

Kenji Uchino, Nam-Yang Lee, Tamaki Toba, Narikazu Usuki, Hideaki Aburatani, and Yukio Ito

Department of Physics, Sophia University
7-1, Kioi-cho, Chiyoda-ku, Tokyo, 102 Japan

The crystal structure of $BaTiO_3$ thin films fabricated by RF-magnetron sputtering has been investigated. As-sputtered films exhibited a cubic structure with a small grain size of about 6-8nm. After annealing at a temperature above 1100°C, the crystal structure changed from cubic to tetragonal, because the annealing process caused grain growth. The critical grain size of the thin films which provided the cubic structure existed in the range of 0.1-0.2μm. This value agreed well with the critical grain size of $BaTiO_3$ fine particles, 0.12μm.
[Received December 11, 1991; Accepted May 21, 1992]

Key-words: RF-magnetron sputtering, $BaTiO_3$ thin film, Annealing process, Critical grain size, Phase transition

1. Introduction

With increasing the demand for ferroelectric thin films for the applications to optical wave guides, non-volatile memories and so on, many studies have been attempted using RF sputtering and other thin film fabrication techniques.[1-4] However, ferroelectric films fabricated by these methods frequently have not shown so good ferroelectricity as seen in bulk sintered ceramics or single crystals. Although many researchers have attempted to give explanations to this phenomenon, they have been insufficient so far.

Nagatomo et al. have reported that the ferroelectric $BaTiO_3$ thin film could be prepared at a relatively low substrate temperature of 700°C by using RF planar-magnetron sputtering, however, the ferroelectricity of those films was weak or absent for the fine-grained film, and it was necessary to anneal at 1000°C in order to obtain ferroelectric $BaTiO_3$ films with high quality.[1,4] They have explained these phenomena by the 90° domain model suggested by Arlt et al.[5] However, the reason why the fine-grained film exhibits cubic symmetry and non-ferroelectric properties has not been discussed.

The purpose of this study is to clarify why the as-grown $BaTiO_3$ thin films do not show ferroelectricity. Our discussion is based upon the "critical grain size" model.

We have reported the particle/grain size dependence of ferroelectricity for powder and polycrystalline samples of $BaTiO_3$, and clarified that both the tetragonality, c/a,and the Curie temperature, T_c, are decreased drastically at a particle size of 0.12μm.[6] Fine particles less than this critical grain size will not exhibit ferroelectricity because the crystal lattice becomes a cubic structure.

In order to explain this phenomenon, we have proposed an "effective surface tension" model.[6,7] A fine particle with R in radius experiences a hydrostatic pressure of $2\gamma/R$ (γ: surface tension), and this hydrostatic pressure decreases the Curie temperature of the particle down below room temperature and changes the structure into cubic. It is interesting that the surface tension γ revealed in perovskite ferroelectrics ((Pb, Ba)TiO_3, (Ba, Sr)TiO_3) shows an almost constant value of 50N/m. This extraordinarily large value has not been explained yet, however, it may be attributed to the surface layer generated by the permanent dipoles.

2. Experiments

2.1. Sample Preparation

The $BaTiO_3$ film was deposited by using an RF-magnetron sputtering system (Anelva, SPE-430HS). Corning 7059 and fused quartz substrates with 15mm×15mm×1mm in size were used. All the substrates were cleaned by using trichloromethane (TCE) and acetone, and then placed in a stainless steel holder by clips prior to film deposition. The target had a stoichiometric composition of $BaTiO_3$ with purity of 99.9%. The size was 100mm in diameter and 5mm in thickness. The sputtering conditions are summarized in **Table 1**. The thickness of the sputtered films was more than 2μm, much thicker than the grain size.

In order to control the grain size the as-sputtered thin films were annealed at the temperature range of 600°-1200°C for 12h. Chemical analysis of the composition was made by the ICPS(Inductively Coupled Plasma Spectroscopy) method and the Ba/Ti ratio was proved to be nearly 1.0.

2.2. Measurement

An X-ray diffractometer (JEOL, JDX-11PA) was employed to examine as-grown and annealed thin films. The crystal symmetry and the consequent lattice constants of samples were calculated by averaging the {100} and {200} reflections of the $BaTiO_3$ perovskite cell. Average grain size in the range of sub-micron was determined from SEM (HITACHI, S-900) micrographs using a line intercept method. In the range of grain size of nano-meter Scherrer's

Table 1. Summary of sputtering conditions.

Substrate temperature	room temperature - 800°C
RF power	200W
Target-substrate distance	43 - 70mm
Gas pressure	0.5 - 2.0Pa
Sputtering time	3hrs

equation[8] was used for {100} peaks. The grain sizes determined by SEM and X-ray diffraction were almost the same (≃0.1μm) for the sample annealed at 1000°C; this suggests that the crystallite size almost corresponds to the grain size.

3. Results and Discussions

Figure 1 shows the X-ray diffraction patterns of as-grown films sputtered at the gas pressure of 1.0Pa for various substrate temperatures. The film sputtered at room temperature showed an amorphous phase, but he film fabricated above 500°C showed a crystalline phase. The lattice constant decreased with the substrate temperature from 4.15Å at 500°C down to 4.07Å at 800°C, but it was still larger than that of sintered $BaTiO_3$ (a; 3.989Å, c; 4.029Å).

Only two peaks due to the preferential orientation along {100} appeared and the preference did not change significantly with the substrate temperature. This result is different from previous researches. It has been reported that if the mobility of atoms during deposition is high (i.e., at a high substrate temperature), the films grow with the orientation of {110} due to its highest occupation density compared to the other planes with low indices.[3,4] The decrease in the X-ray intensity and the peak broadening for the substrate temperature of 800°C seems to be caused by the slight mis-orientation due to higher substrate temperature.

The samples were annealed at various temperatures to increase the grain size so that they were compared to the fine grain ceramic $BaTiO_3$. **Figure 2** shows the XRD patterns of {200} reflection of films annealed at 1000°, 1100°, and 1200°C. The diffraction pattern of the film annealed at 1000°C shows a symmetrical pattern. On the other hand, the peak of the film annealed at 1100°C or 1200°C skews to the right side from the center, revealing an additional peak at a lower angle. This seems to be attributed to the appearance of the (002) peak, although the peak was not entirely separated from the (200) peak. In conclusion, the phase

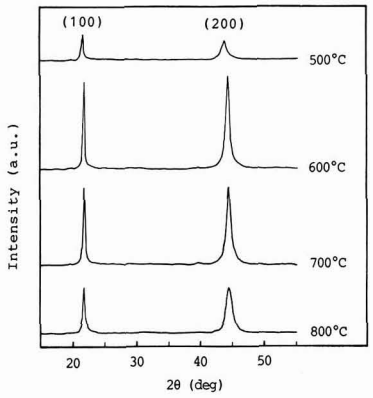

Fig. 1. XRD patterns of films sputtered on the substrate at various temperatures.

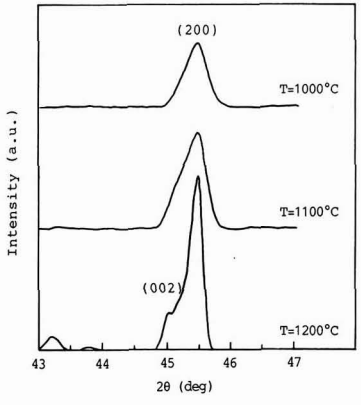

Fig. 2. XRD peaks of the {200} reflections of $BaTiO_3$ annealed at various temperatures.

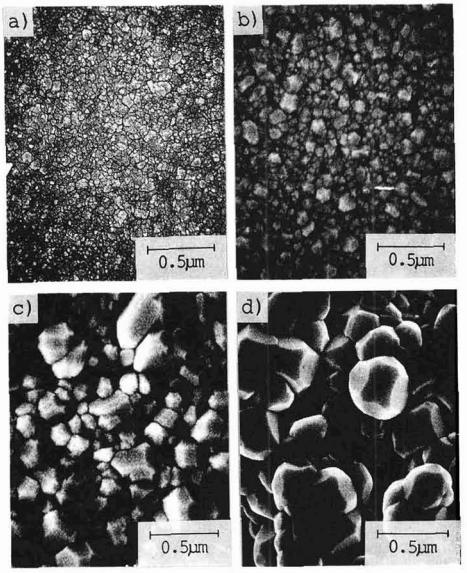

Fig. 3. SEM photographs of $BaTiO_3$ thin films annealed at various temperatures. (a) 600°C, (b) 1000°C, (c) 1100°C, (d) 1200°C.

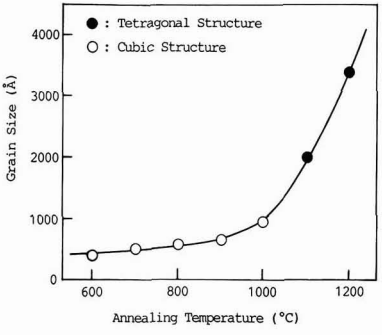

Fig. 4. Relationship between grain size and annealing temperature. The crystal symmetry is also indicated.

transition from cubic to tetragonal was caused by thermal annealing at the temperature above 1100°C. The microstructure of annealed samples was observed by using SEM and the results are shown in **Fig.3**. By the annealing process, the grains grew from about 40nm to 350nm.

Figure 4 plots the relationship between the grain size and the annealing temperature, where the crystal structure is also indicated. The crystal structure was cubic below 0.1μm in grain size, and tetragonal above 0.2μm. Therefore, it is shown that the critical grain size might exist between 0.1 and 0.2μm. This result agrees exactly with that obtained by the study on the particle size dependence of the crystal structure of fine powder $BaTiO_3$,[6] where the critical grain size was indicated to be 0.12μm. The grain size of as-sputtered thin films ranged over 6-8nm in this study. Iijima has reported that the grain size of evaporated $BaTiO_3$ thin films ranges over 35-70nm and the film without heat-treatment did not show any ferroelectric properties.[9] Although there are some differences among these values due to fabrication methods, both of them are below the critical grain size, 0.12μm. Accordingly, it can be thought that the cubic structure and non-ferroelectric properties of as-sputtered films are attributed to the small grain size.

4. Conclusion

The results of this study are summarized:

1) As-sputtered films prepared on the substrate of 500°-800°C exhibited a cubic crystal structure.

2) The crystal structure of sputtered films changed from cubic to tetragonal after annealed at a temperature above 1100°C.

3) The critical grain size separating cubic and tetragonal phases existed in the range of 0.1-0.2μm, and was in good agreement with the critical grain size of 0.12μm determined from the fine powder of $BaTiO_3$.

References:

1) T. Nagatomo and O. Omoto, Jpn. J. Appl. Phys., 26 Suppl. 26-2, 11-14 (1987).
2) K. Sreenivas, M. Sayer and P. Gattett, Thin Solid Films, 172, 251-267 (1989).
3) C.H. Lee and S.J. Park, J. Mat. Sci.: Mat. in Elect., 1, 219-224 (1990).
4) T. Nagatomo, T. Kosaka, S. Omori and O. Omoto, Ferroelectrics, 37, 681-684 (1981).
5) G. Arlt, D. Hennings and G. de With, J. Appl. Phys., 58, 1619-1625 (1985).
6) K. Uchino, E. Sadanaga and T. Hirose, J. Am. Ceram. Soc., 72, 1555-1448 (1989).
7) T. Yamakawa and K. Uchino, Proc. 7th Int. Sympo. Appl. Ferroelectrics, Illionis (1990) in press.
8) B.D. Cullity, Elements of X-ray Diffraction, 2nd Ed., ed. by Addison-Weley Publishing (1978) 99-106.
9) Y. Iijima, Jpn J. Appl. Phys., 24, Suppl. 24-2, 401-3 (1985).

This article appearing in English in Journal of the Ceramic Society of Japan (Japanese version), Vol.100, No.9, pp.1091-1093, 1992.

Alkali Passivation Mechanism of Sol-Gel Derived TiO_2-SiO_2 Films Coated on Soda-Lime-Silica Glass Substrates

Atsunori Matsuda, Yoshihiro Matsuno, Shinya Katayama, Toshio Tsuno, Noboru Tohge* and Tsutomu Minami*

Tsukuba Research Laboratory, Nippon Sheet Glass Co., Ltd.
5-4, Tokodai, Tsukuba-shi, 300-26 Japan
*Department of Applied Chemistry, University of Osaka Prefecture
1, Gakuencho, Sakai-shi, 591 Japan

Alkali passivation mechanism of sol-gel derived TiO_2-SiO_2 glass films with different TiO_2 contents coated on a soda-lime-silica glass substrate has been studied by SIMS and XPS analyses, and compared with the results of a sol-gel derived pure SiO_2 film. An increase in TiO_2 content in the TiO_2-SiO_2 film increased the sodium concentration in the film, which was induced by sodium migration from the glass substrate during the heat-treatment. It was also found that the chemical state of solidum ions in the TiO_2-SiO_2 films was different from the state of those either in the glass substrate or in the sol-gel derived pure SiO_2 film. It is thus concluded that the TiO_2-SiO_2 films serve not as a barrier but as an effective getter of alkali ions and thereby effectively improve the weathering resistance of the glass substrate.
[Received December 21, 1991; Accepted June 16, 1992]

Key-words: Sol-gel method, Alkali passivation, Titania-silica, Coating film, Gettering effect

1. Introduction

Binary oxides in the TiO_2-SiO_2 system exhibit very interesting physical and chemical properties such as very low or negative thermal expansion,[1,2] a high refractive index,[2,3] photocatalytic properties[4] and solid acidic properties.[5,6] Recently we have experimentally found that the TiO_2-SiO_2 glass film prepared by the sol-gel method serves as an effective alkali passivation layer on a soda-lime-silica glass substrate and that the film is superior to a sol-gel derived pure SiO_2 film from the view point of weathering resistance improvement.[7,8] It is therefore of special interest to investigate analytically the alkali passivation mechanism of the TiO_2-SiO_2 film.

In the present work, the depth profiles of sodium ions in the TiO_2-SiO_2 films coated on soda-lime-silica glass substrates and their changes in an environment of high temperature and high humidity have been measured using secondly ion mass spectroscopy (SIMS). The chemical state of the sodium ions in the films has also been investigated using X-ray photoelectron spectroscopy (XPS). The alkali passivation mechanism of the TiO_2-SiO_2 coating films has been discussed on the basis of the above data, in comparison with that of the sol-gel derived pure SiO_2 films.

2. Experimental

TiO_2-SiO_2 coating films containing different TiO_2 molar percentages up to 20 were prepared from the corresponding metal alkoxides. The preparation procedure of the TiO_2-SiO_2 coating films was essentially the same as that described in previous papers.[7,8] Silicon tetraethoxide, $Si(OEt)_4$, in ethanol, EtOH, was firstly hydrolyzed with water containing 1wt% HCl at room temperature for 30min; the molar ratios of EtOH and H_2O to $Si(OEt)_4$ were 5 and 4, respectively. The hydrolyzed $Si(OEt)_4$ solution was then mixed with titanium tetra-n-butoxide, $Ti(O\text{-}n\text{Bu})_4$, diluted with EtOH, the molar ratio of EtOH/$Ti(O\text{-}n\text{Bu})_4$ being 20, and stirred continuously for 30min. The solution was further diluted with EtOH and finally served as a coating solution.

A glass substrate used in this study was a commercially available soda-lime-silica glass plate (50×40×1.1mm). The composition of the glass was $72.5SiO_2 \cdot 7.2CaO \cdot 4.0MgO \cdot 13.5Na_2O \cdot 0.9K_2O \cdot 1.8Al_2O_3$ in wt%. A film was formed on the glass substrate from the coating solution prepared above by dipping-withdrawing in an ambient atmosphere. The glass substrate coated with the film was heat-treated at 350°C for 30min in air using a Class-100 clean oven. After the heat-treatment at this temperature, all the films were not densified completely and thus porous. The heat-treated TiO_2-SiO_2 coating film was found to be amorphous. The thickness of the film was controlled to be about 200nm after the heat-treatment.

Weathering tests of the glass substrate coated with the film were carried out at 70°C and 90% relative humidity (R.H.) for 100h using a temperature- and humidity-controlled equipment. Depth profiles of sodium and hydrogen in the film coated on the glass substrate before and after the weathering tests were obtained using SIMS (Atomika, A-DIDA 3000–30). The SIMS analysis was performed using 2.0keV oxygen ions for sodium, whereas 12.0keV caesium ions for hydrogen, since caesium ions have much higher sensitivity for hydrogen than oxygen ions.[9] Charge compensation was achieved with 1.0keV electron beams. To understand the alkali migration mechanism from the glass substrate into the coating film, the heat-treatment of glass substrate coated with the film was carried out in vacuum. X-ray photoelectron spectra (XPS) of the sodium ions in the film, as well as in the glass substrate, were obtained using a photoelectron spectrometer (Shimadzu, ESCA-750). In XPS measurements, samples were sputtered with 2.0keV argon ions at the rates of 3-4nm/min. Binding energies of

sodium ions were corrected with respect to the binding energy of C(1s) and the accuracy of ±0.2eV was achievable.

3. Results and Discussion

3.1. Depth Profiles of Sodium and Hydrogen

Figure 1 shows the depth profiles of sodium in the soda-lime-silica glass substrate; (a) is for the substrate coated with a pure SiO_2 film and (b) for the substrate coated with a $9TiO_2{\cdot}91SiO_2$ (in mol%) film. The broken and solid lines in each figure indicate the profiles before and after the weathering test (70°C and 90% R.H. for 100h), respectively. In the case of the glass substrate coated with a pure SiO_2 film, the steep increase in the intensity of sodium near surface is observed. Sodium ions can migrate in the SiO_2 coating film and reach the surface of the coating film. In the case of the glass substrate coated with the TiO_2-SiO_2 film, the concentration of sodium in the film gradually decreases with an increase of distance from the interface between the film and the glass substrate. The difference in the depth profile of sodium ions between the TiO_2-SiO_2 coating film and the pure SiO_2 coating film indicates that the alkali passivation mechanism of the TiO_2-SiO_2 film differs from that of the pure SiO_2 film, although the concentration of sodium ions increases after the weathering tests in both coating films. Details will be discussed later.

Figure 2 shows the depth profiles of hydrogen in the glass substrate; (a) is for the glass substrate coated with the pure SiO_2 film and (b) for the substrate coated with the $9TiO_2{\cdot}91SiO_2$ (in mol%) film. The broken and solid lines in each figure have the same meanings as in Fig.1. There is almost no appreciable change in the concentration of hydrogen, i.e. SiOH groups, in both coating films after the weathering tests. Though water molecules should permeate into the coating films during the weathering tests, adsorbed water would be lost from the coating films when the samples were put into the vacuum chamber for the measurements. Therefore adsorbed water may not be involved in the hydrogen profile measured. On the other hand, the concentration of hydrogen in the glass substrate increases after the tests, especially in the vicinity of the interface of the substrate with the coating film.

To make clear the source of the hydrogen which migrated into the glass substrate, the heat-treatment of the substrate coated with the TiO_2-SiO_2 film was carried out in an ambient atmosphere and in vacuum; the depth profiles of sodium were compared between both substrates. **Figure 3** shows the depth profiles of sodium in the soda-lime-silica glass substrates coated with $16.5TiO_2{\cdot}83.5SiO_2$ (in mol%) films, which were heat-treated at 350°C for 30min in 3×10^{-5} Torr (solid line) and in an ambient atmosphere (broken line). The concentration of sodium in the coating film heat-treated in vacuum is lower by about 2 orders of magnitude than that in the coating film heat-treated in an ambient atmosphere. It is evident that the heat-treatment in vacuum depresses the migration of alkali ions from glass substrates. This finding indicates that water vapor in the atmosphere plays an important role in the diffusion of sodium ions from glass substrates into the films during the heat-treatment and, that is, the main source of the hydrogen in the glass substrate with a coating film is water vapor in the atmosphere.

The concentration of hydronium ions (or protons) at the interface between the substrate and the film is considered to

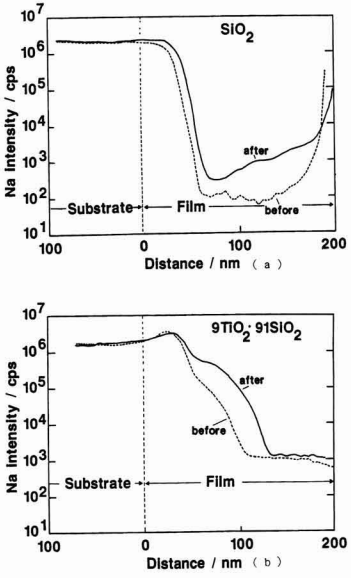

Fig. 1. Depth profiles of sodium in the soda-lime-silica glass substrate; (a) is for the substrate coated with a pure SiO_2 film and (b) for the substrate coated with a $9TiO_2{\cdot}91SiO_2$. The broken and solid lines show the profiles before and after the weathering tests (70°C and 90% R.H. for 100h), respectively.

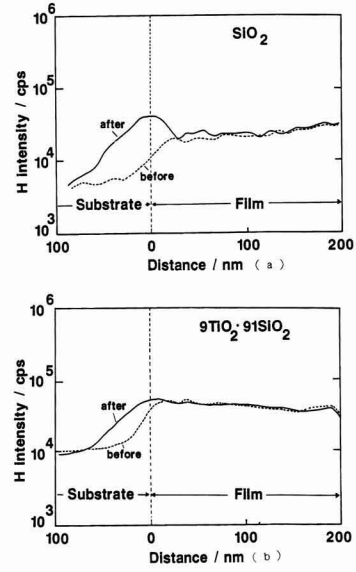

Fig. 2. Depth profiles of hydrogen in the soda-lime-silica glass substrate; (a) is for the substrate coated with a pure SiO_2 film and (b) for the substrate coated with a $9TiO_2{\cdot}91SiO_2$. The broken and solid lines have the same meanings as in Fig.1.

have a great influence on the sodium migration from the substrate into the film. It is supposedly easy for water molecules to permeate through the films to the interface, because the present films are porous as mentioned above. Under the condition where sufficient water molecules are supplied, the concentration of hydronium ions (or protons) at the interface is defined by water molecules and the counter-diffusion of sodium ions and hydronium ions (or protons) can proceed with little change in the concentration of silanol groups in the films. This situation is applicable to the heat-treatment at relatively high temperatures in an ambient atmosphere and the weathering test in high humidity.

3.2. Effect of TiO_2 Content on Alkali Diffusion

Figure 4 shows the depth profiles of sodium in TiO_2-SiO_2 films of different TiO_2 contents coated on glass substrates. All the coating films were heat-treated at 350°C for 30min and not subjected to weathering tests. It is worth noting that the concentration of sodium in the coating films increases with an increase in TiO_2 content and that the concentration of sodium in the $20TiO_2 \cdot 80SiO_2$ (in mol%) coating film is as much as that in the soda-lime-silica glass substrate.

In **Fig.5**, the mean distance of sodium diffusion is plotted against the TiO_2 content in the coating films; the mean distance of sodium diffusion was defined as the distance from the interface between the glass substrate and the coating film to the point at which the intensity of sodium ions drops to 10^3 cps. The point was obtained by extrapolating the slop of sodium diffusion curve. It can be seen that the mean distance of the sodium diffusion in the coating film increases monotonously with an increase in TiO_2 content of the film.

3.3. XPS of Na(1s) in the Coating Films

Figure 6 shows the depth profile of XPS spectra for

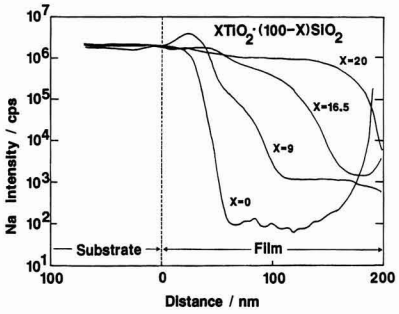

Fig. 4. Depth profiles of sodium in TiO_2-SiO_2 films of different TiO_2 contents. All the coating films were heat-treated at 350°C for 30min and not subjected to weathering tests.

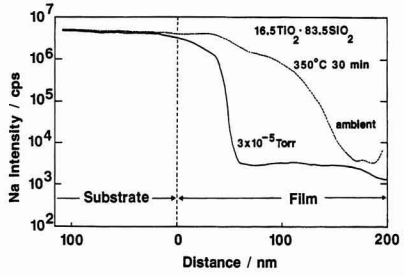

Fig. 3. Depth profiles of sodium in the soda-lime-silica glass substrates coated with $16.5TiO_2 \cdot 83.5SiO_2$ films heat-treated at 350°C for 30min in 3×10^{-5} Torr (solid line) and in an ambient atmosphere (broken line).

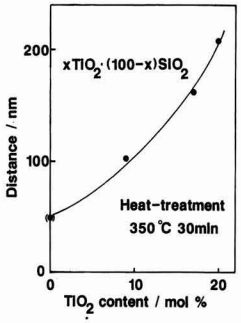

Fig. 5. TiO_2 content dependence of the mean distance of sodium diffusion, which was defined as the distance from the interface between the glass substrate and the coating film to the point at which the intensity of sodium ions dropped to 10^3cps.

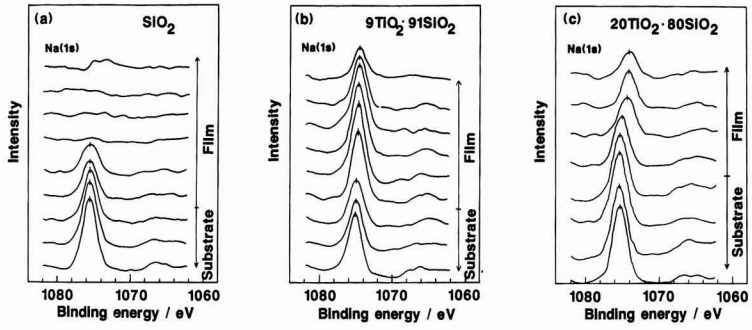

Fig. 6. Depth profiles of XPS spectra for Na(1s) in a soda-lime-silica glass substrate coated with a pure SiO_2 film (a), with a $9TiO_2 \cdot 91SiO_2$ film (b) and with a $20TiO_2 \cdot 80SiO_2$ film (c).

Na(1s) in a soda-lime-silica glass substrate coated with a pure SiO_2 film (a), with a $9TiO_2 \cdot 91SiO_2$ film (b) and with a $20TiO_2 \cdot 80SiO_2$ film (c), respectively. The binding energy of the Na(1s) band in the pure SiO_2 almost equals that (1075.4eV) in the soda-lime-silica glass substrate, whereas the binding energy in the TiO_2-SiO_2 coating film shifts to lower values by 1.1eV in $9TiO_2 \cdot 91SiO_2$ and by 1.4eV in $20TiO_2 \cdot 80SiO_2$ than that of the glass substrate. It is known that the difference in binding energy or the chemical shift corresponds to the difference in chemical states such as oxidation number of the atom.[10] These findings indicate that the chemical state of sodium ions in the TiO_2-SiO_2 coating films differs from that of those either in the pure SiO_2 film or in the glass substrate.

The concentration of sodium ions which migrated from soda-lime-silica glass substrate is higher in the TiO_2-SiO_2 coating films than in the pure SiO_2 coating film as shown in Figs.4 and 5. However, the TiO_2-SiO_2 coating films provide the glass substrates with much better weathering resistance than the pure SiO_2 coating films.[7,8] Furthermore the sodium ions in the TiO_2-SiO_2 are in the different chemical states from either in the pure SiO_2 coating film or in the glass substrate. From these results obtained, the sol-gel derived TiO_2-SiO_2 coating film is concluded to act not as a barrier but as a getter of alkali ions and improve the weathering resistance of the glass substrate by suppressing the formation of alkali reaction products such as sodium carbonate and sodium hydrogencarbonate[7,8] on the surface of the coating film.

4. Conclusion

Alkali passivation mechanism of sol-gel derived TiO_2-SiO_2 films with different TiO_2 contents coated on a soda-lime-silica glass substrate has been studied by SIMS and XPS analyses, and compared with the results of a sol-gel derived pure SiO_2 film.

The concentration of sodium in the coating film heat-treated in vacuum was lower by about 2 orders of magnitude than that in the coating film heat-treated in an ambient atmosphere. Water molecules adsorbed on the coating film should permeate into the film and hydronium ions (or protons) produced from the water molecules act as counter diffusion cations for sodium ions, which migrate from the glass substrate into the film. An increase of TiO_2 content in the TiO_2-SiO_2 film increased the sodium concentration in the film. XPS spectra showed that the chemical state of the sodium ions in the TiO_2-SiO_2 film was different from that of the ions in the glass substrate and in the sol-gel derived pure SiO_2 film. It is thus concluded that the TiO_2-SiO_2 films serve not as a barrier but as an effective getter of alkali ions and improve the weathering resistance of the substrate.

Acknowledgement

The authors thank Ms. A. Nakama for SIMS analyses, Mr. K. Shimoda for XPS analyses and Dr. Y. Mitsuhashi for critical reading of the manuscript.

References:

1) K. Kamiya and S. Sakka, J. Non-Cryst. Solids, 52, 357-363 (1982).
2) T. Hanada, T. Aikawa and N. Soga, J. Am. Ceram. Soc., 67, 52-57, (1984).
3) H. Dislich and E. Hussmann, Thin Solid Films, 77, 129-139 (1981).
4) M. Anpo, H. Nakaya, S. Kodama, Y. Kubokawa, K. Domen and T. Onishi, J. Phys. Chem., 90, 1633-1636 (1986).
5) K. Tanabe, T. Sumiyoshi, K. Shibata, T. Kiyoura and J. Kitagawa, Bull. Chem. Soc. Jpn. 47, 1064-1066 (1974).
6) M. Itoh, H. Hattori and K. Tanabe, J. Catalysis. 35, 225-231 (1974).
7) A. Matsuda, Y. Matsuno, S. Katayama and T. Tsuno, J. Mater. Sci. Lett., 8, 902-904 (1989).
8) A. Matsuda, Y. Matsuno, s. Katayama, T. Tsuno, N. Tohge and T. Minami, J. Ceram. Soc. Jpn., 99, 545-549 (1991).
9) H.A. Storms, K.F. Brown and J.D. Stein, Analy. Chem., 49, 2023-2030 (1977).
10) M. Takahashi and Y. Kaneko, Review Journal on Surface & Technology, Avant-Garde, 27, 667-677 (1989).

This article appearing in English in Journal of the Ceramic Society of Japan (Japanese version), Vol.100, No.9, pp.1094-1097, 1992.

^{29}Si MAS NMR Study on Structural Change of Silicate Anions with Carbonation of Synthetic 11Å Tobermorite

Yasuhisa Ikeda, Yoshiyuki Yasuike, Mikio Kumagai, Yoon-Yul Park*, Masayuki Harada,* Hiroshi Tomiyasu* and Yoichi Takashima

Kashiwa Laboratory, Institute of Research and Innovation
1201, Takada, Kashiwa-shi, 277 Japan
*Research Laboratory for Nuclear Reactors, Tokyo Institute of Technology
2-12-1, Ookayama, Meguro-ku, Tokyo, 152 Japan

Structural change of synthetic 11Å tobermorite with the carbonation was examined by IR spectroscopy and XRD method. The synthetic 11Å tobermorite decomposed into $CaCO_3$ (calcite) and silica gel with the carbonation. In such a decomposition process, $CaCO_3$ existed in three crystal forms (calcite, vaterite and aragonite) in the low carbonated tobermorites, all of which were transformed into calcite with the progress of carbonation. In addition, the structural change of silicate anions with the carbonation of synthetic 11Å tobermorite was studied by ^{29}Si MAS NMR method. Three ^{29}Si NMR peaks assigned to Q^1, Q^2 and Q^3 were observed at –79.7, –85.9 and –95.9 ppm in the low carbonated tobermorites and further carbonation (>40%) led to the disappearance of Q^1 peak and appearance of peaks due to Q^4. In the carbonation more than 80%, only Q^4 peaks were observed at –101 and –111ppm, which were assigned to the silicon atoms of (HO)Si*(OSi≤)$_3$ and Si*(OSi≤)$_4$ in silica gel. ^{29}Si NMR data revealed that the silicate anions in synthetic 11Å tobermorite change from a double chain structure with some Si-O-Si bridges to the three dimensional cross-linked framework structure with the progress of carbonation.

[Received March 19, 1992; Accepted June 16, 1992]

Key-words: ^{29}Si NMR, Tobermorite, Carbonation, Silicate anions, Calcite, Vaterite, Aragonite, Silica gel

1. Introduction

Tobermorite is one of the hydrous calcium silicate minerals, which was first discovered by Heddle at Tobermory in Scotland.[1] Tobermorite is classified into three groups based on the basal spacing, i.e. 14Å, 11Å and 9Å tobermorites. Among them, 11Å tobermorite is most easily synthesized by hydrothermal reaction using SiO_2 and CaO as starting materials and also known to be a main crystal phase of autoclaved lightweight concrete(ALC).

In 1964, it was found that the main crystal phase of ALC, i.e. 11Å tobermorite, is decomposed through the action of CO_2 under moisture conditions into calcium carbonate (aragonite(A), vaterite(V) or calcite (C)) and silica gel. This phenomenon has been referred as the carbonation of ALC and studied by several authors.[2-5] They have clarified that the density of ALC increases with the progress of carbonation and that the drying shrinkage of carbonated ALC becomes bigger than that of the normal ALC. These suggest that the carbonation of ALC is one of the important factors relating to the durability of ALC.

The bigger drying shrinkage of the carbonated ALC has been considered to be due to the polymerization of silica gel formed with the carbonation of 11Å tobermorite.[6] However, little information is available with respect to the structural change of silicate anions with the carbonation of 11Å tobermorite. This is attributed to the lack of effective methods for analyzing the forms of silicate anions in solid state.[7]

Lippmaa et al. have indicated that the solid-state high resolution ^{29}Si NMR is an efficient method for the structural analyses of solid silicates and aluminosilicates.[8] They have found that ^{29}Si NMR chemical shifts in silicates are dependent on the degree of condensation of SiO_4 tetrahedra, i.e. monosilicates Q^0 (–66 to –74ppm from TMS), disilictes and chain end groups Q^1 (–77 to –82ppm), middle groups in chain Q^2 (–85 to –89ppm), chain branching sites Q^3 (–95 to –100ppm) and three-dimensional cross-linked framework Q^4 (–103 to –115ppm).

On the basis of the reports of Lippmaa et al., the structural studies on silicate anions in various synthetic 11Å tobermorites have been carried out by using ^{29}Si MAS NMR.[9-13] However, the structural change of silicate anions with the carbonation of 11Å tobermorite have little been studied in detail. Recently, the present authors studied the structural change of silicate anions in 11Å tobermorite contained in ALC with the progress of carbonation of ALC by ^{29}Si MAS NMR method and reported that the silicate anions change from double chain structure with Si-O-Si bridges to three-dimensional cross-linked framework.[14]

In the present study as an extension of the previous work, purely synthesized 11Å tobermorite was used to clarify in more detail the structural change of silicate anions with the progress of carbonation.

2. Experimental

11Å tobermorite was synthesized from finely ground quartz and CaO (Ca/Si=0.84) at 180°C under hydrothermal conditions in an autoclave. Carbonation of synthetic 11Å tobermorite (abbreviation: Syn-Tob for the singular, Syn-Tobs for the plural) was carried out by bubbling 17% CO_2 gas into the mixture of Syn-Tob and distilled water at 60°C. The degree of carbonation, which is defined as the percentage of (mole of carbonated CaO in Syn-Tob)/(mole of CaO in Syn-Tob), was determined by measuring the concentration of CO_2 gas generated by the reaction of the carbonated Syn-Tob with H_2SO_4 using Shimadzu IRA107 CO_2 analyzer.

IR spectra of samples were measured with a BIO-RAD FTS-40 FT-IR spectrophotometer using diffuse refluctance method. Crystal phases of samples were assigned by XRD patterns using a Rigaku Denki Geiger-Flex X-ray diffractometer with CuKα radiation. ^{29}Si NMR spectra were recorded on a JEOL JNM-EX270 NM-ESH27MU solid-state high resolution NMR spectrometer at 53.54MHz using magic angle spinning (MAS) method. Cross-polarization (CP) method was also used to enhance sensitivity. NMR measurement conditions are as follows; data point=8k, spectral width=20kHz, and number of scans=600 or 10000. ^{29}Si NMR chemical shifts were recorded with respect to TMS (tetramethylsilane).

3. Results and Discussion

3.1. XRD Measurement

Figure 1 shows the XRD patterns of Syn-Tobs at various degrees of carbonation. With the progress of carbonation the intensities of peaks corresponding to Syn-Tob decrease and the peaks assigned to calcite (max. peak: 2θ=29.2°), vaterite (max. peak: 2θ=27.0°) and aragonite (max. peak: 2θ=26.2°) appear. At low degree of carbonation, the formed $CaCO_3$ exists mainly as vaterite (Fig.1 (2)). As the carbonation proceeds, the fraction of calcite becomes relatively high, i.e. the order of existence ratio; calcite > vaterite > aragonite (Fig.1 (3)). In the highly carbonated Syn-Tobs, the fraction of calcite further increases (Fig.1 (4)). In the complete carbonation, only calcite is detected (Fig.1 (5)). These results indicate that CaO phase of Syn-Tob changes to $CaCO_3$ (vaterite, aragonite and calcite) with the progress of carbonation and that vaterite and aragonite are finally transformed into calcite.

3.2. IR Spectral Measurements

Figure 2 shows the change of IR spectra of Syn-Tob with the carbonation. The bands at 712, 800, 877, 1790 and around 1460cm^{-1} increase and that at 673cm^{-1} decrease with the carbonation of Syn-Tob. Furthermore, the bands in the range 900–1220cm^{-1} are found to change drastically with the carbonation. These phenomena were examined by comparing with the IR spectra of $CaCO_3$ (calcite, vaterite and aragonite) and silica gel.[14,15]

The bands at 712, 877 and around 1460cm^{-1} become very intense with the carbonation and are assigned to ν_2, ν_3 and ν_4 due to CO_3^{2-} of calcite.[16] According to the XRD data, vaterite and aragonite are also formed with the carbonation of Syn-Tob. However, their IR bands are unobserved because of the overlapping with those of calcite.[15] Only ν_2 band due to CO_3^{2-} of aragonite is observed at 856cm^{-1}. The intensity of this band increases with the progress of carbonation and then decrease in the carbonation more than 75%, followed by disappearance at 100% carbonation. This is consistent with the result of XRD measurements.

With the progress of carbonation, the band at 980cm^{-1} decreases and the absorbance at 1090cm^{-1} becomes intense. The band at 1090cm^{-1} is consistent with ν_3 due to SiO_4 of silica gel. This result suggests that the band at 980cm^{-1} is assigned to ν_3 due to SiO_4 in Syn-Tob. In the IR spectra of the highly carbonated Syn-Tobs, the band and shoulder are observed at 800 and around 1200cm^{-1}. This is attributed to the formation of silica gel, because the IR spectrum in 900–1220cm^{-1} region of the completely carbonated Syn-Tob is in fair agreement with that of silica gel.[14] Furthermore, the

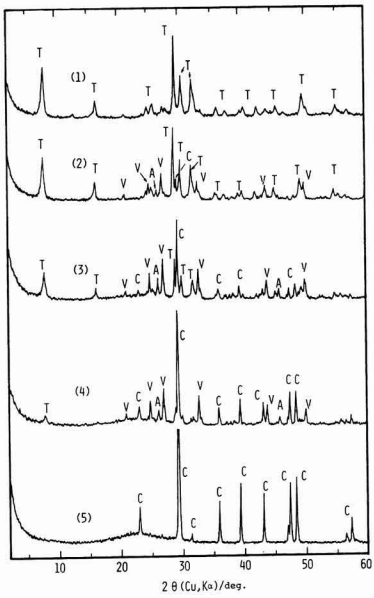

Fig. 1. XRD patterns of synthetic 11Å tobermorites at various degrees of carbonation. (1): 4%, (2): 27%, (3): 61%, (4): 82%, (5): 100%. T: 11Å tobermorite, C: Calcite, V: Vaterite, A: Aragonite.

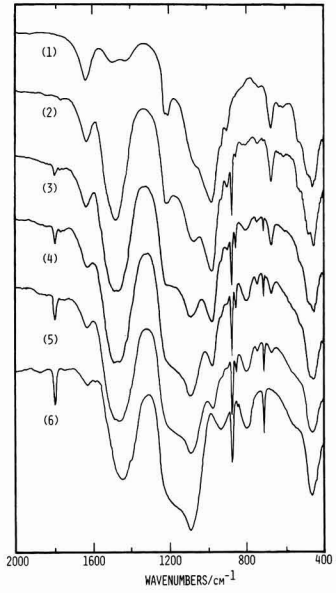

Fig. 2. IR spectra of synthetic 11Å tobermorites at various degrees of carbonation. (1): 4%, (2): 27%, (3): 53%, (4): 74%, (5): 82%, (6): 100%.

Table 1. ^{29}Si NMR chemical shifts of synthetic 11Å tobermorites at various degrees of carbonation.

Tobermorites	Degree of carbonation (%)	^{29}Si chemical shifts (ppm from TMS) Q^1	Q^2	Q^3	Q^4		Ref.
Syn-Tob(Ca/Si=0.07)	~0	-79.7	-86.0	-96.4			9)
Syn-Tob(Ca/Si=0.8)	~0		-85.8	-95.9			9)
Syn-Tob(A)*	~0		-85.7	-95.7			10)
Syn-Tob(Ca/Si=0.84)	4	-79.7	-85.9	-95.9			This work
Syn-Tob(Ca/Si=0.84)	23	-79.4	-85.6	-95.8			This work
Syn-Tob(Ca/Si=0.84)	44	-79.8	-85.7	-95.8	-103	-111	This work
Syn-Tob(Ca/Si=0.84)	64		-85.7	-95.9	-101	-113	This work
Syn-Tob(Ca/Si=0.84)	87				-101	-112	This work
Syn-Tob(Ca/Si=0.84)	100				-102	-111	This work

*: Syn-Tob(A) = Synthetic anomalous 11Å tobermorite.

absorbance peak of SiO_4 (v_4) observed at around 470cm^{-1} is split in the low carbonated Syn-Tobs and becomes single with the progress of carbonation. This phenomenon is also reasonably explained by the formation of silica gel, since SiO_4 (v_4) band in silica gel is well known to be singlet.[17]

These results indicate that Syn-Tob decomposes into silica gel and $CaCO_3$ with the carbonation, where in the low carbonated Syn-Tobs $CaCO_3$ exists in three crystal forms, i.e. vaterite, calcite and aragonite (existence ratio: vaterite > calcite > aragonite) and with the progress of carbonation vaterite and aragonite are transformed into calcite.

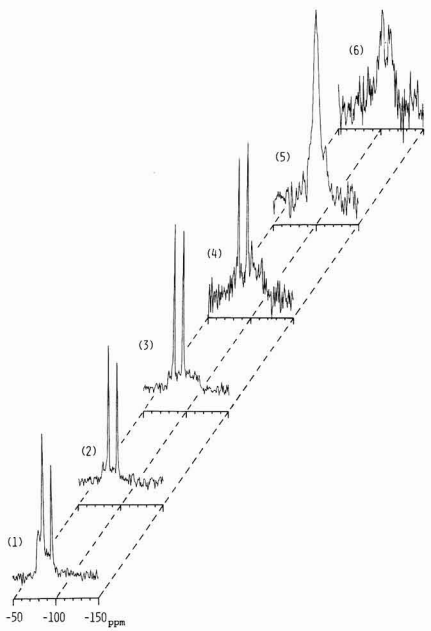

Fig. 3. ^{29}Si CP/MAS NMR spectra of synthetic 11Å tobermorites at various degrees of carbonation. (1): 4%, (2): 23%, (3): 44%, (4): 64%, (5): 87%, (6): 100%.

3.3. ^{29}Si NMR Measurement

From the results of XRD and IR measurements, it was found that Syn-Tob decomposes into calcite and silica gel with the carbonation. However, these results do not make clear the structural change of silicate anions with the carbonation of Syn-Tob. Therefore, ^{29}Si NMR spectra of Syn-Tobs at various degrees of carbonation were measured by using CP/MAS method. The results are shown in **Fig.3**. The ^{29}Si NMR Chemical shifts of the carbonated Syn-Tobs are summarized in **Table 1** with the data reported by Wieker et al. and Komarneni et al..[9,10]

In fresh Syn-Tob (4% carbonation), three peaks are observed at –79.7, –85.9 and –95.9ppm. These peaks are assigned to chain end groups or disilicates (Q^1), chain middle groups (Q^2) and chain branching sites (Q^3) respectively on the basis of the report of Lippmaa et al.. This is consistent with the results of Wieker et al. and supports that Syn-Tob has a double chain structure with some Si-O-Si bridges between the chains, as proposed by several authors.[9-12,18] It is found from Fig.3 that the peak for Q^1 decreases with the progress of carbonation. This result demonstrates an increase in the degree of condensation of tobermorite chains, because the decrease in Q^1 peak corresponds to the decrease of the chain end groups. In the carbonation more than 40%, new peaks seem to appear in the high field more than –96ppm. This becomes further apparent in Syn-Tob at the degree of carbonation of 64%, where tow new peaks are observed at around –101 and –111ppm. These signals are assigned to silicon atoms in Q^4 type. This indicates that the silicate anions with the three-dimensional cross-linked framework structure are formed with the carbonation of Syn-Tob, i.e. the formation of silica gel. In addition, it was found that in further carbonation (>80%) the peaks assigned to Q^2 and Q^3 types disappear and only peaks due to Q^4 type appear at –102 and –111ppm. These results indicate that in the carbonation process between 60 and 80%, the double chain structure of Syn-tob is almost destroyed and silica gel

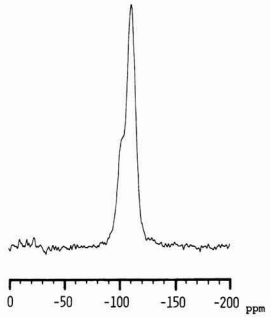

Fig. 4. ^{29}SiMAS NMR spectrum of syntectic 11Å tobermorite at the degree of carbonation of 87%.

is formed with the condensation of the silicate anions. In the complete carbonation, all silicate anions form the structure of silica gel.

Maciel and co-worker have measured ^{29}Si NMR spectra of silica gel by using CP/MAS method[19] and reported that three peaks are observed at –109.3, –99.8 and –90.6ppm and assigned to the silicon atoms in $Si^{*}(OSi\leftarrow)_4$, (HO)$Si^{*}(OSi\leftarrow)_3$ and $(HO)_2Si^{*}(OSi\leftarrow)_2$, respectively. Hence, the peaks observed at around –111 and –102ppm in the highly carbonated Syn-Tobs are considered to be due to the silicon atoms of $Si^{*}(OSi\leftarrow)_4$ and $(HO)Si^{*}(OSi\leftarrow)_3$ structures in silica gel, respectively. In order to confirm this assignment, ^{29}Si MAS NMR spectrum of 87% carbonated Syn-Tob was measured without using CP method. The result is shown in **Fig.4**. The peak intensity at around –102ppm becomes relatively small compared with that at around –111ppm. This means that the signal at –102ppm is due to the silicon atoms having the hydrogen atom in the neighborhood, i.e. $(HO)Si^{*}(OSi\leftarrow)_3$.

These NMR data indicate that the silicate anions in Syn-Tob change from the double chain structure with some Si-O-Si bridges to the three-dimensional cross-linked framework structure with the progress of carbonation. Furthermore, the double chain structure is found to be kept even at a considerably high degree of carbonation. This may cause pseudomorphism phenomenon observed in the carbonation of 11Å tobermorite, where the apparent structure does not change even at a considerably high degree of carbonation.[3]

4. Summary

The results obtained are summarized as follows:

1) Syn-Tob is decomposed by reacting with CO_2 into $CaCO_3$ and silica gel.

2) In the decomposition process, $CaCO_3$ is present as three crystal forms (vaterite, aragonite and calcite) in the low carbonated Syn-Tobs. With the progress of carbonation, the fraction of calcite increases and in the complete carbonation all $CaCO_3$ is transformed into calcite.

3) Silicate phase in Syn-Tob is composed of the double chain structure with some Si-O-Si bridges between the chains. This double chain structure is destroyed with the carbonation and finally silica gel with the three-dimensional cross-linked framework structure is formed.

4) The double chain structure is kept even at a considerably high degree of carbonation (around 70%). This may cause the pseudomorphism phenomenon.

5) In the completely carbonated Syn-Tob, two ^{29}Si NMR peaks are observed at around –111 and –102ppm, which are assigned to the silicon atoms of $Si^{*}(OSi\leftarrow)_4$ and (HO)$Si^{*}(OSi\leftarrow)_3$ structures in silica gel.

Acknowledgement

The authors express their thanks to Mr. M. Yamamoto of Nichiasu Corp. for helpful suggestions.

References:

1) M.F. Heddle, Mineral. Mag., 4, 119-123 (1880).
2) S. Asano, Y. Kamatani and Y. Inoue, Yogyo Kyokaishi, 79, 303-311 (1971).
3) Z. Sauman, Cem. Concr. Res., 2, 541-549 (1972).
4) T. Baird, A.G. C-Smith and D.S. Snell, J. Colloid Interface Sci., 50, 387-391 (1975).
5) Z. Yuping, L. Dedong and S. Guokuang, 8th Int. cong. chemistry of Cement (1986) 93-98.
6) E.S. Silaenkov, Izv. Vyssh, Uchebn. Stoit. Arkhit., 18, 67-70 (1975).
7) T. Yasue and Y. Arai, Gypsum and Lime, 211, 35-45 (1987).
8) E. Lippmaa, M. Magi, A. Samoson, G. Engelhardt and A.-R. Grimmer, J. Am. Chem. Soc., 102, 4889-4893 (1980).
9) W. Wieker, A. -R. Grimmer, A. Winkler, M. Magi, M. Tarmak and E. Lippmaa, Cem. Concr. Res., 12, 333-339 (1982).
10) S. Komarneni, R. Roy, D.M. Roy, C.A. Eyfe, G.J. Kennedy, A.A. Bothner-By, J. Dadok and A.S. Chesnick, J. Mater. Sci., 20, 4209-4214 (1985).
11) S. Komarneni and M. Tsuji, J. Am. Ceram. Soc., 72, 1668-1674 (1989).
12) M. Ogai, Y. Ohno and T. Mitsuda, Proc. Ann. Mtg. Ceram. Soc. Jpn. (1990) 395.
13) T. Mitsuda, Gypsum and Lime, 229, 80-86 (1990).
14) Y. Ikeda, Y. Yasuike and Y. Takashima, Seramikkusu Ronbunshi, 99, 423-428 (1991).
15) L. Brecevic and A.E. Nielsen, J. Crystal Growth, 98, 504-510 (1989).
16) K. Nakamoto, Infrared and Raman Spectra of Inorganic and Coordination Compounds, John Wiley and Sons, (1978).
17) K. Suzuki, N. Nishikawa and T. Hatashi, Semento Gijutsu Nenpo, 42, 36-39 (1988).
18) T. Mitsuda and H.F. W. Taylor, Mineral. Mag., 42, 229-235 (1978).
19) G.E. Maciel and D.W. Sindorf, J. Am. Chem. Soc., 102, 7607-7608 (1980).

This article appearing in English in Journal of the Ceramic Society of Japan (Japanese version), Vol.100, No.9, pp.1098-1102, 1992.

Pyrolytic Behavior of CVD Coated SiC Fibers

Hideya Inagaki, Toshio Shimoo*, Kiyohito Okamura* and Kuniaki Honjo**

Graduate Student, University of Osaka Prefecture
1, Gakuen-cho, Sakai-shi, 593 Japan
*Department of Metallurgical Engineering, College of Engineering, University of Osaka Prefecture
1, Gakuen-cho, Sakai-shi, 593 Japan
**Government Industrial Research Institute, Osaka
1-8-31, Midorigaoka, Ikeda-shi, 563 Japan

The effect of SiC coating on the pyrolysis of SiC fiber (Nicalon) has been investigated. SiC coating was carried out by chemical vapor deposition at 1473K using a mixture of CH_3SiCl_3 and H_2 as source gases. The composition and crystallinity of the coating changed with the flow rates of CH_3SiCl_3 and H_2. The composition of the coating with an increase in H_2 gas flow rate was close to that of stoichiometric SiC as determined by the scanning Auger electron spectroscopy. X-ray diffraction patterns showed that the coating was β-SiC crystallites. The rate of pyrolysis of Nicalon with and without SiC coating was measured with a thermobalance in an argon atmosphere at temperatures from 1673 to 1973K. The rate of pyrolysis of SiC coated Nicalon was mixed-controlled by both diffusion of SiO and CO gases through the coating and crystal growth of SiC in the fiber. These results showed that high-temperature pyrolytic reaction of Nicalon was suppressed by coating SiC on the fiber.
[Received August 16, 1991; Accepted June 16, 1992]

Key-words: SiC fiber (Nicalon), SiC coating, Chemical vapor deposition, Monomethyltrichlorosilane, Pyrolysis, Mixed-control

1. Introduction

Recently extensive studies have been made on silicon carbide fibers as reinforcements for composite materials such as fiber reinforced ceramics (FRC) for high-temperature structural materials.[1] Among the fibers currently on the market are Si-C-O fiber (Nicalon made by Nippon Carbon), Si-Ti-C-O fiber (Tyranno made by Ube Industries, Ltd.) and CVD-SiC fiber (SCS made by Textron Specialty Materials). The Si-C-O fiber is manufactured by spinning a soluion of polycarbosilane as an organic silicon polymer, thermal-oxidizing the strands at about 423K to make them infusible, and firing the product in a nonoxidizing atmosphere at around 1273 to 1573K.[2] Containing more carbon and oxygen than the stoichiometric composition of SiC, this fiber is amorphous, represented by SiC_xO_y. When held at a high temperature, it is crystallized by pyrolysis into thermodynamically stable β-SiC, while emitting SiO and CO gases and losing some mass. As the reactions here proceed, pits are formed in the surface and inside the fiber, causing the tensile strength of the fiber to greatly decrease.[3,4] The pyrolytic reactions here are particularly prominent in high temperature ranges above 1600K. In order to use silicon carbide fibers as FRC reinforcements, it is important to improve the high-temperature strength, and studies using the radiation infusibility method without oxygen are currently underway.[5]

Some recent studies involve the ceramic coating of the fiber surface as a means for improving the thermal stability of silicon carbide fibers. The morphology, compositions, and crystal structures of the products made by coating Si-C-O fibers with C or SiC under a chemical vapor deposition method (reaction gases: $SiCl_4$, CH_4 and H_2) in order to improve the heat resistance and surface quality of the fibers[6] have been investigated. Some studies have also examined the mechanical properties and thermal stability of Nicalon coated under a CVD method, reporting that the coatings C and C+SiC served as effective barriers against diffusion at high temperatures, prevented the pyrolysis of the fiber, and thus improved the thermal stability of Nicalon.[7]

Considering that it is necessary to investigate pyrolysis in high temperature ranges in order to improve the high-temperature strength of fibers, we have been pursuing studies with Si-C-O and Si-Ti-C-O fibers.[4,8,11] As a result, through kinetic analysis, we estimated that the pyrolysis of these fibers was governed by nucleus formation and grain growth processes and controlled by diffusion rates. We continued our studies proceeding to the pyrolytic behavior of coated fibers. The present study is a kinetic study on the pyrolytic behavior of the Si-C-O fibers coated in various thicknesses of crystal SiC under a CVD method (reaction gases: CH_3SiCl_3 and H_2).

2. Test Method

2.1. SiC Coating of Nicalon

For the samples of silicon carbide fibers, we used Nicalon NL200 made by Nippon Carbon Co., Ltd. Chemical analysis was conducted to determine its mol composition as $SiC_{1.20}O_{0.41}$. Fiber diameters were measured as 14.4μm on the average. Tensile tests showed a tensile strength of 3.02GPa and an elastic modulus of 179GPa. The fiber was coated with SiC under a CVD method. **Figure 1** shows the sketched CVD reactor. The reaction temperature was 1473K. For material gases, CH_3SiCl_3 and H_2 diluted with Ar were used. CH_3SiCl_3, which is liquid at room temperature, was fed in at a rate of $42\times10^{-6}m^3s^{-1}$ together with Ar as a carrier gas. The vapor pressure was held constant by keeping the temperature of CH_3SiCl_3 at 293K with the help of a thermostat oven. This also made the CH_3SiCl_3 feed constant: $6.7\times10^{-8}m^3s^{-1}$. The composition and crystallinity of the coatings were varied by adjusting the hydrogen feed to 0, 0.83×10^{-7}, 1.7×10^{-7}, 3.3×10^{-7}, 5.0×10^{-7}, 6.7×10^{-7}, and

$8.3\times10^{-7}m^3s^{-1}$. The SiC coated fibers were submitted to Auger Electron Spectroscopic Analysis (AES JAMP-30 made by Nipppon Denshi).

2.2. Measureement of Pyrolytic Behavior

Each sample of SiC coated Nicalon was placed in a graphite crucible and hung in the soaking zone of a Tammann furnace conditioned to the specified temperature. Using an automatic balance (capacity: 100g; sensitivity: 0.1mg), the decreases in mass due to pyrolysis were continuously measured, while Ar was fed in from the furnace bottom at a rate of $2.5\times10^{-5}m^3/s$. About 100mg of each sample was used per test. Using an empty crucible before each measurement, the same process was carried out, finding that mass decreases as a blank value. Corrections were made accordingly. Before and after reactions, the samples were observed under an SEM (JSM-T20 made by Nippon Denshi) and submitted to X-ray diffraction analysis (XRD, RINT1500 made by Rigaku Denki, CuKα, rotating target).

3. Test Results and Discussion

3.1. SiC Coating of Nicalon

3.1.1. Auger Electron Spectroscopic Analysis (AES)

Nicalon samples were coated with SiC at hydrogen flow rates of $0.83\times10^{-7}m^3s^{-1}$ and SiC-coated samples were submitted to AES. The results are shown in **Figs.2** and **3**. The horizontal axis represents the depth of the fiber from surface to center. Judging from the Si, C, and O distributions, in Fig.2, a line can be drawn at a depth of about 1.0μm between the coating and fiber. As shown here, the coating is mainly composed of carbon. In Fig.3, the demarcation between the coating and fiber can be drawn at a depth of about 2.3μm. In this coating, Si and C are produced approximately at a 1 to 1 ratio, allowing an SiC phase to be formed. This phase was also identified β-SiC by XRD, as described later.

3.1.2. Relationship between Coating Thickness and CVD Reaction Time

Figure 4 shows the relationship between coating thickness and CVD reaction time with a hydrogen flow rate of $5.0\times10^{-7}m^3/s$ for CVD processing. The coating thickness was calculated from SEM photographs. The coating thickness increased as time elapsed, but the relationship between them was not proportional in short time ranges. This trend was common in all cases of hydrogen feed.

3.1.3. Results of SEM Observation

Figure 5 shows the SEM photographs of (A) the surface of a Nicalon sample, (B) the surface of a Nicalon sample SiC coated under a CVD method, and (C) the cross-section of the sample in (B). The hydrogen feed was $5.0\times10^{-7}m^3/s$ for 0.9ks coating, and the coating thicknesses were approximately 2.3μm.

While the Nicalon surfaces were smooth, the SiC coated Nicalon surfaces showed a pebble (rugged) structure of

Table 1. The flow rate of source gases.

flow rate / m^3s^{-1}(STD)	
CH_3SiCl_3 (Ar carrier)	6.7×10^{-8}
H_2	$0\sim8.3\times10^{-7}$
Ar	4.2×10^{-6}

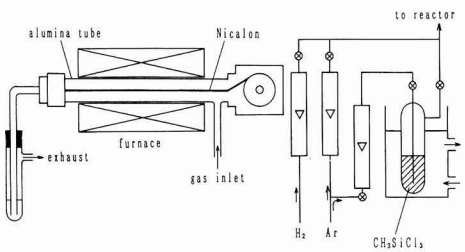

Fig. 1. Apparatus for silicon carbide CVD coating.

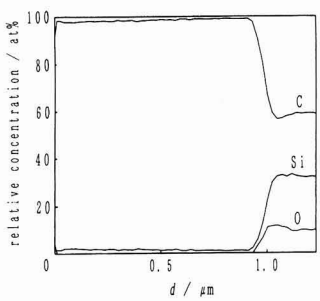

Fig. 2

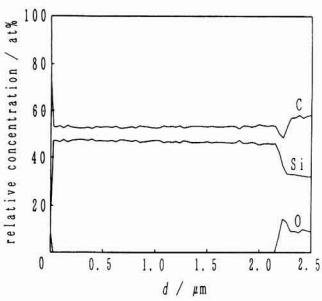

Fig. 3

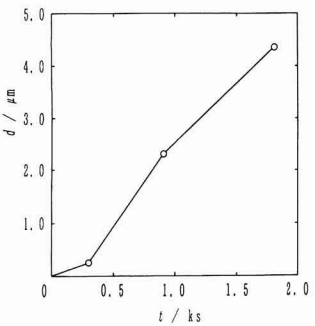

Fig. 4

Fig. 2. Depth profile of CVD coated Nicalon at the hydrogen flow rate of $0.83\times10^{-7}m^3s^{-1}$ measured by scanning Auger electron spectroscopy.
Fig. 3. Depth profile of CVD coated Nicalon at the hydrogen flow rate of $5.0\times10^{-7}m^3s^{-1}$ measured by scanning Auger electron spectroscopy.
Fig. 4. Relation between CVD coating time and coating thickness at the hydrogen flow rate of $5.0\times10^{-7}m^3s^{-1}$.

about 0.1μm thick, although the coating covered the surface evenly. It is reported that on the Nicalon surface under CVD-SiC coating, a carbon-rich layer is first formed, which is followed by the formation of an SiC layer.[6] However, the results of AES, SEM photographs in the present study showed no such intermediate layers were produced, and no gaps were observed between the coating and fiber.

3.1.4. X-ray Diffraction (XRD)

Under XRD analysis, variations in the composition and crystallinity of coatings due to variations in hydrogen feed were observed. Measurements were carried out with fibers pasted in a strip pattern on the X-ray sample holder. This method allows the diffraction patterns for coatings on the fiber surfaces to be intensified. The results are shown in **Fig.6**. With no hydrogen feed, amorphous carbon is produced. In other cases, crystalline β-SiC is produced and the diffraction peaks turn maximum of $3.3\times10^{-7}m^3s^{-1}$. This trend is also reported in studies of coating under a similar method using a carbon fiber (TORAYCA M40).[12] When β-SiC is produced by CVD reactions, the overall reaction is given by

$$CH_3SiCl_3 \xrightarrow{H_2} SiC + 3HCl \quad \cdots\cdots\cdots (1)$$

H_2 does not directly react but is engaged in the production of β-SiC resulting from the dissolution of CH_3SiCl_3 in the CVD reaction. The crystallinity of β-SiC is determined by the H_2 to CH_3SiCl_3 (pressure ratio feed ratio).[12] SiC coating fibers used to measure pyrolytic behavior were CVD coated under the hydrogen feed of consistent $5.0\times10^{-7}m^3s^{-1}$.

3.2. Measurement of Pyrolytic Behavior

3.2.1. Pyrolysis of SiC Coated Fiber

When highly heated, amorphous Nicalon turns into crystalline β-SiC which is thermodynamically more stable. The Nicalon having a composition $SiC_{1.20}O_{0.41}$ contains carbon in excess of the equivalent ratio of SiC and oxygen, and it produces SiO and CO[4] when highly heated.

$$SiC_{1.20}O_{0.41}\ (s) \rightarrow a\cdot\beta\text{-}SiC\ (s) + b\cdot SiO\ (g) + c\cdot CO\ (g) \quad \ldots\ (2)$$

where a, b, and c vary with the type of fiber, reaction temperature and other condition. As gases are produced due to this pyrolytic reaction, Nicalon shows a loss in mass. Using a thermobalance and with bare Nicalon and Nicalon samples coated in differing thicknesses with SiC, at 1973K, the decreases in mass due to pyrolysis over a certain period were measured. The results are shown in **Fig.7**. Here, the mass decrease ratio $100\times\Delta W/W_0$ denotes the percentage of mass decrease ΔW to the initial mass W_0 of Nicalon in each sample. Also, in the figure, *a* represents bare Nicalon and *b*, *c* and *d* represent Nicalon samples coated with SiC in thick-

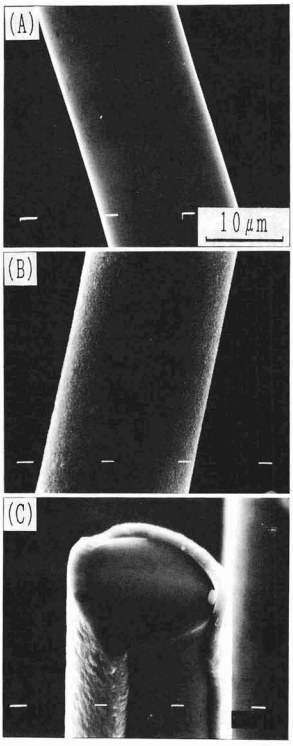

Fig. 5. SEM photographs of fibers: (A) surface of original Nicalon, (B) surface of SiC coated Nicalon and (C) cross section of SiC coated Nicalon.

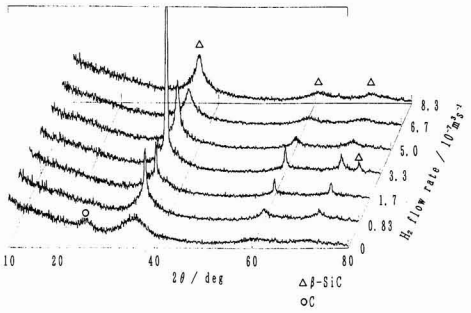

Fig. 6. XRD patterns of SiC coated Nicalon at various hydrogen flow rate.

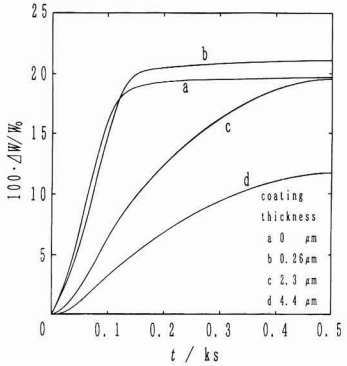

Fig. 7. Mass loss with pyrolysis of Nicalon and SiC coated Nicalon at 1973K.

nesses 0.26, 2.3 and 4.4μm respectively. In variation patterns, *b* was similar to *a*. With *c* and *d*, the loss in mass decreased as the CVD-SiC coating thickness increased,. If the Nicalon completely decomposes according to Eq.(2), then the mass decrease ratio will be 26.9%. However, it is approximately 20% even for *a* in Fig.7. This is because the samples do not always completely react and because the ratio of products varies with temperature and other conditions. Again, as described later, the coated surfaces after heat treatments in high temperature ranges showed coarse SiC crystal grains. However, such grains are a little compared to the coating and seem to have little effect on mass variations. The pyrolytic reaction shown in Eq.(2) naturally results in a decrease in mass because it produces a gas emission. Mass decreases in Fig.7 were smaller than expected, which can be ascribed to the suppression of the pyrolytic reaction. All of the pyrolytic curves are sigmoid, peculiar to the pyrolytic reactions of solids, or show a pattern composed of induction, acceleration, and termination periods. This trend was also observed with other temperatures (1673, 1773 and 1873K).

3.2.2. Results of SEM Observation

Figure 8 shows the SEM photographs of the surfaces of (A) bare Nicalon and (B) SiC-coated Nicalon and (C) the cross-section of SiC-coated Nicalon, after heat treating at 1873K. The bare Nicalon shows large grown crystal grains on the surface and in the cross-section, indicating considerable progress of pyrolysis. On the other hand, in the SiC coated Nicalon, the fiber inside remains in its original state both on the surface and in the cross section. Coarse crystals, which seem to be SiC crystals, are also observed on the coated surface. Such SiC crystal grains are not observed at temperatures below 1773K or on the carbon fiber (TORAYCA M40) coated with SiC and heat-treated at 1973K. From these results, the production of coarse SiC crystal grains can be ascribed not to the recrystallization of the coatings but to the pyrolytic reaction of Nicalon. The SiC-producing reaction here may be the reaction between the SiO gas generated by the pyrolysis of Nicalon in Eq.(3) and the C on the coating surface.

$$SiO\,(g) + 2C\,(s) \rightarrow SiC\,(s) + CO\,(g) \quad \ldots\ldots (3)$$

However, this is not accurate because C on the CVD-SiC coated surface is only a trace and the reaction shown above is also observed in the reaction at 1673K between be graphite crucible and the SiO gas produced by the pyrolysis of Nicalon in Eq.(2). Thus, the production of SiC crystals was ascribed to the vapor-phase reaction given by

$$SiO\,(g) + 3CO\,(g) \rightarrow SiC\,(s) + 2CO\,(g) \quad \ldots (4)$$

If P_{CO_2} at the reaction interface is set low, then the reaction in Eq.(4) can thermodynamically progress. The reasons for setting P_{CO_2} at a low level under the present test conditions are ① consumption of CO_2 due to the progress of the solution loss reaction in Eq.(5) and ② dilution of CO_2 due to SiO and CO fed excessively to the reaction interface by the pyrolytic reaction in Eq.(2).

$$2CO_2\,(g) + 2C\,(s,\ \text{crucible}) \rightarrow 4CO\,(g) \quad \ldots (5)$$

3.2.3. X-ray Diffraction (XRD)

It is known that Nicalon is changed from amorphous to crystal β-SiC by a pyrolytic reaction.[4] This crystallization is different from that by SiC coating. In order to investigate this difference, solid samples were pulverized, and the XRD patterns were measured.

Figure 9 shows the XRD patterns of the bare and SiC coated Nicalon samples before heating; a in the figure represents the bare Nicalon. It shows a broad pattern peculiar to amorphous substances having peaks at 2θ≈36°, 60° and 72°. All of these peaks correspond to β-SiC. b, c, and d in the figure represent the SiC-coated Nicalon samples mentioned from thin to thick coatings. The diffraction peaks for β-SiC appear at the same diffraction angle, irrespective of the difference between crystalline and amorphous, however, diffraction patterns are sharp for crystalline phases and broad for amorphous phases. For a mixture of crystalline and amorphous phases, the diffraction pattern can be assumed as the combination of sharp and broad patterns, varying with the ratio of crystalline β-SiC. In Fig.9, the SiC coated Nicalon samples are mixtures of Nicalon (amorphous) and coatings (crystalline). Thus, for samples having thicker coatings, the diffraction patterns are sharper.

Figure 10 shows the XRD patterns for bare and SiC-coated Nicalon samples 2ks heated at 1873K. The symbols a through d are the same as in Fig.9. In contrast to Fig.9, the thicker the coating, the smaller the height of the corresponding diffraction pattern. In order to investigate variations in diffraction patterns due to heating of CVD-SiC coatings, the carbon fiber (TORAYCA M40) samples were

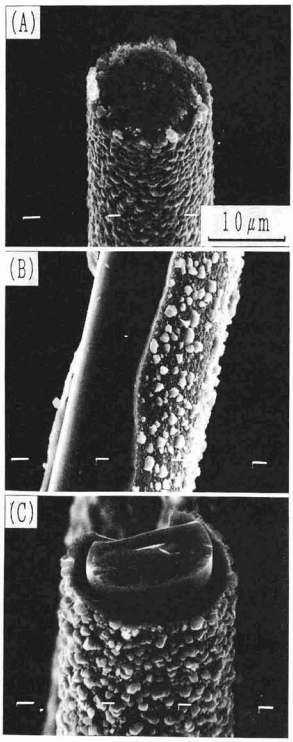

Fig. 8. SEM photographs of fibers after heated at 1873K: (A) surface of original Nicalon, (B) surface of SiC coated Nicalon and (C) cross section of SiC coated Nicalon.

coated with SiC, the diffraction patterns before heating were compared to those after heating. No differences were found. Again SiC grains formed by heating on the coating surface are so scare as compared to the coating that they seem to have little effect on diffraction patterns. In other words, diffraction patterns for coatings do not change, proving that pattern variations by heating are due to the crystallization of the Nicalon cores. As described above, the thicker the CVD-SiC coating, the smaller the peak size change. This suggests that crystallization due to the pyrolysis of Nicalon is controlled by SiC coatings.

3.3. Mechanisms of Pyrolytic Reactions

In this section, the decomposing processes of SiC-coated Nicalon and the rate-determining phases of pyrolytic reactions are discussed. There are five possible decomposing processes:

(1) Nucleation and growth of β-SiC crystals in Nicalon.
(2) Generation of SiO and CO gases due to SiC growth.
(3) Diffusion of SiO and CO gases to Nicalon-coating interface.
(4) Diffusion of SiO and CO gases through micropores in coatings.
(5) Diffusion of SiO and CO gases through the gas film over the coating surface.

Our studies have proved that bare Nicalon allows SiO and CO to be directly emitted from the fiber surface. Pyrolysis is governed by process (1), and can be expressed by the Avrami-Erofeev equation[4]:

$$-\ln(1-X) = k \cdot t^{m} \quad \ldots\ldots\ldots\ldots\ldots\ldots (6)$$

where X is the reflection factor, equivalent to the decomposition ratio ($\Delta W/W$) in Fig.7, and k and m are constants determined by reaction mechanisms and the number and shape of nuclei.

We investigated the applicability of the Avrami equation to pyrolysis of samples. Bare Nicalon samples satisfied the relational expression for diffusion-rate determining 3-dimensional grain growth with m≈1.5, while coated Nicalon samples did not. This suggests that rate-determining processes are affected by coatings. Processes (1) through (5) can also be listed for the rate-determining processes of pyrolytic reactions of coated Nicalon. Among them, only (4) is essentially increased by coating. As described earlier with Fig.7, the thicker the coating, the more pyrolytic reactions are controlled. This suggests that process (4) makes some contribution to the rates of pyrolysis. If only process (4) is rate-determining, then the rate of pyrolysis r is given by

$$r \propto (D_{\mathrm{eff}}/dRT)\cdot(p^{*} - p) \quad \ldots\ldots\ldots\ldots (7)$$

where

D_{eff} : effective diffusion factor
d : coating thickness
p : SiO and CO pressure on Nicalon surface
p^{*} : SiO and CO pressure on coating surface

which can be derived from Fick's first law of diffusion. This equation shows that the rate of pyrolysis r is inversely proportional to coating thickness d. Rates of pyrolysis were obtained by approximately applying the straight-line law in the zone equivalent to the acceleration period of the pyro-

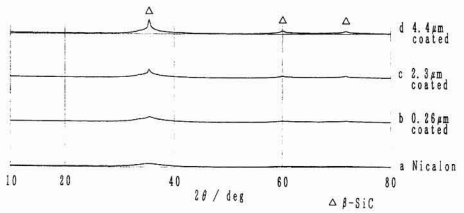

Fig. 9. XRD patterns of original Nicalon and various thickness SiC coated Nicalon.

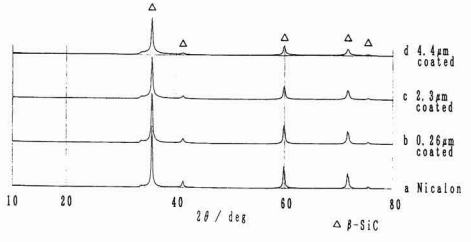

Fig. 10. XRD patterns of Nicalon and various thickness SiC coated Nicalon after heated at 1873K.

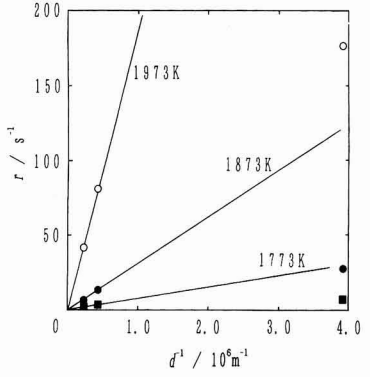

Fig. 11. Relation between inverse of coating thickness and the rate of pyrolysis.

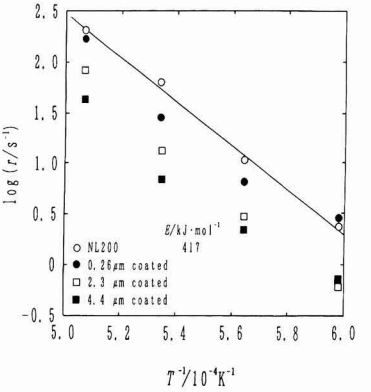

Fig. 12. Arrhenius plots for pyrolytic rate, r.

lytic curves in Fig.7 and at other temperatures. **Figure 11** shows the relationsship between the rate of pyrolysis and the reciprocal of coating thickness $1/d$. In high ranges of coating thickness (small $1/d$), linear relations passing the origin hold, satisfying Eq.(7). As the coating thickness decreases, the relations deviate from the linear relations by growing degrees as the temperature rises. This leads to the assumption that pyrolysis rates of SiC coated Nicalon are mixed-controlled by both processes (1) and (4).

Figure 12 shows the Arrehenius plot for rates of pyrolysis (r). The plots for Nicalon (NL200) satisfies a linear relationship very well. From the gradient of this line, the activation energy was obtained as E=417kJ/mol. This value is relatively close to the activation energy E=484kJ/mol[4] of Nicalon, obtained from rate constant k in the Avrami equation. In addition, from the results of the present test, it is assumed that the rates of Nicalon reactions are controlled only by process (1). On the other band, the SiC coated Nicalon samples, with any coating thickness, do not satisfy linear relationship, and the temperature dependency of rates of pyrolysis is small in low temperature ranges and large in high temperature rages. This may be because the reaction rates for these samples are controlled by processes (1) and (4), the resistances of which vary with temperature. Furthermore, this may be because at high temperatures, grains grow, while the diameter and the number of micropores increase, in the CVD-SiC coatings, causing the diffusion rates of SiO and CO to increase.

4. Conclusion

We investigated the pyrolytic behavior of Si-C-O fibers coated with crystalline SiC under a CVD method in an Ar atmosphere in the temperature range of 1673 to 1973K and examined the reaction mechanisms. The following points were observed:

1) An SiC coating was formed smoothly over the fiber surface under a CVD method.

2) The coatings were mainly composed of carbon in the hydrogen feed range 0 to $0.83\times10^{-7}m^3s^{-1}$ or SiC in the hydrogen feed range above $1.7\times10^{-7}m^3s^{-1}$.

3) Pyrolysis at high temperatures could be controlled by coating the Si-C-O fiber with crystalline SiC.

4) Pyrolytic reaction rates of SiC coated Si-C-O fiber were assumed to be mixed-controlled by the nucleation and growth of β-SiC crystals in the fiber and diffusion of SiO and CO through the coatings.

References:

1) L.M. Sheppard, Am. Ceram. Soc. Bull., 69, 666-673 (1990).
2) S. Yajima ibid., 62, 893-903 (1983).
3) K. Okamura, M. Sato, T. Matsuzawa and Y. Hasegawa, Polym. Prepr., 25 (2984) 6-7.
4) T. Shimoo, M. Sugimoto and K. Okamura, J. Jpn. Soc. metals, 54, 802-808 (1990).
5) K. Okamura, M. Sato, T. Seguchi and S. Kawanishi, Proc. 3rd Int. Conf. Composite Interfaces (ICCI-III), Cleveland, May 21-24 (1990), 209-218.
6) J.X. Li, Y. Matsuo and S. Kimura, Seramikkusu Ronbunshi, 99, 1129-2234 (1991).
7) J.X. Li, Y. Matsuo and S. Kimura, ibid., 99, 1207-1211 (1991).
8) T. Shimoo, M. Sugimoto and K. Okamura, ibid., 98, 1324-1329 (1990).
9) T. Shimoo, M. Sugimoto, Y. Kakehi and K. Okamura, J. Jpn. Soc. Metals, 55, 294-303 (1991).
10) T. Shimoo, M. Sugimoto, Y. Kakehi and K. Okamura, Seramikkusu Ronbunshi 99, 401-406 (1991).
11) T. Shimoo, H. Chen and K. Okamura, J. Ceram. Soc. Jpn., 100, 48-53 (1991).
12) K. Honjo and A. Shindo, Yogyo Kyokaishi 94, 173-178 (1986).

This article is a full translation of the article appearing in the Journal of the Ceramic Society of Japan (Japanese version), Vol.100, No.9, pp.1103-1108, 1992.

Mechanical and Thermal Properties of Pressureless-Sintered MgO-$Mg_4Ta_2O_9$ Composites

Shinsuke Hayashi, Shinji Saito* and Hajime Saito

Toyota Technological Institute
2-12-1, Hisakata, Tenpaku-ku, Nagoya-shi, 468 Japan
*NHK Spring R & D Center Inc.
3-10, Fukuura, Kanazawa-ku, Yokohama-shi, 236 Japan

MgO-based composites containing 10 to 30vol% $Mg_4Ta_2O_9$ were fabricated by pressureless sintering of MgO and Ta_2O_5 powders at 1400° to 1600°C. Mechanical properties and the thermal expansion coefficient of the composites were studied. Under all sintering conditions, Ta_2O_5 reacted with MgO completely to form $Mg_4Ta_2O_9$ and dense (>95% of theoretical density) composites were obtained. Dispersion of $Mg_4Ta_2O_9$ particles inhibited the grain growth of MgO and improved mechanical properties. The maximum bending strength and fracture toughness of composites were 260MPa and 3.2MPa·m$^{1/2}$, respectively, in contrast with 150MPa and 1.6MPa·m$^{1/2}$ for a MgO monolith. The composites may be toughened by the crack deflection due to $Mg_4Ta_2O_9$ particles. The thermal expansion coefficient of the composites decreased slightly with increasing $Mg_4Ta_2O_9$ content and was 12.9×10^{-6}°C^{-1} for the composite with 30vol% $Mg_4Ta_2O_9$.

[Received November 29, 1991; Accepted June 16, 1992]

Key-words: MgO, $Mg_4Ta_2O_9$, Composite, Fracture toughness, Bending strength, Hardness, Thermal expansion coefficient

1. Introduction

Structural materials widely used today are metallic ones centered around iron. The use of composite structures made up of metals and ceramics involves the problems of thermal stresses due to the difference in thermal expansion coefficients between these two types of materials. Thus, there have been studies about high-thermal expansion ZrO_2-CaF_2 composites for the development of high-strength ceramic materials which are comparable with metals in terms of thermal expansion coefficients.[1] Picking up MgO, which has a particularly large thermal expansion coefficient among ceramic materials, Yuan et al. pointed out that it should be regarded as a component material for metal-ceramics composite structures.[2] Although MgO is excellent in electrical insulation and resistance to heat and alkaline corrosion, it is not so good in terms of strength, fracture toughness, and resistance to thermal shock. Active attempts to develop composite ceramic materials as an effective means for improving the mechanical properties of ceramics have yielded reports on MgO-ZrO_2 and MgO-SiC systems in the category of MgO-based composite ceramics.[2-9]

In order to improve the mechanical properties of MgO, the authors tried to manufacture composites having $Mg_4Ta_2O_9$ particles dispersed in the MgO matrix. This was done by reaction sintering MgO and Ta_2O_5 powder under atmospheric pressure. This paper describes the sintering behavior, microstructures, fracture toughness, bending strength, hardness, and thermal expansion coefficients of the composites thus obtained.

2. Experimental Precedure

The MgO powder was prepared by calcining basic magnesium carbonate (made by Nakalai Tesque Co.,Ltd.) in air for 1h at 800°C. This MgO powder was mixed with commercial Ta_2O_5 powder (made by Nakalai Tesque Co.,Ltd.) using ethanol in a ball mill and then dried. From the dry powder, rod-shaped compacts were produced by uniaxially pressing the powder under 30MPa and then cold isostatic pressing it under 200MPa. The compacts were sintered in air for 1h at 1400°, 1500°, and 1600°C. Four compositions of powder mixes were prepared to obtain composites having $Mg_4Ta_2O_9$ contents of 0, 10, 20 and 30vol%. In order to identify the constituent phases in the sintered body, X-ray diffraction was used. Bulk densities were measured by an Archimedean method and converted into relative densities. Here, theoretical densities were calculated on the assumption that all Ta_2O_5 reacts with MgO to produce $Mg_4Ta_2O_9$.

From the sintered body, samples with a cross section a 3mm×4mm were cut out, polished, and bevelled. For finish polishing, 6μm diamond paste was used. 4-point bending strength was measured at room temperature with 10mm inner, span, 30mm outer span, and 0.5mm/min crosshead speed. Under each manufacturing condition 8 samples were prepared. The samples after the bending test were further polished with 0.25μm diamond paste to evaluate Vickers hardness and fracture toughness K_{IC} by an indentation microfracture method at room temperature.[10] Thermal expansion was measured for samples 15mm long over a temperature range from room temperature to 1000°C. In order to observe fractured and polished surfaces, a SEM was used. The polished surfaces were thermally etched in air for 1h at 1300°C.

3. Results and Discussion

3.1. Component Phases

It is known that the MgO-Ta_2O_5 system has 3 compounds: $Mg_4Ta_2O_9$, $MgTa_2O_6$, and $Mg_3Ta_2O_8$ which is stable only at high temperatures.[11] Among these three, $Mg_4Ta_2O_9$

contains the most MgO. The results of X-ray diffraction only showed diffraction peaks for MgO and $Mg_4Ta_2O_9$ in all sintered products obtained from mixed powder of MgO and Ta_2O_5. This proves that all the additive Ta_2O_5 reacted with MgO to produce $Mg_4Ta_2O_9$.

3.2. Relative Densities

Figure 1 shows the relationship between the relative density and $Mg_4Ta_2O_9$ content of the composites. As the $Mg_4Ta_2O_9$ content increased, the relative density increased for the samples sintered at 1400°C, but it decreased for the samples sintered at 1600°C. At a sintering temperature of 1500°C, the sample having a composition of 10vol% $Mg_4Ta_2O_9$ showed a maximum relative density. It has been reported that in hot pressing of MgO-SiC composites, the densification of MgO is obstructed by SiC dispersion.[9] With the composites in the present study, the densification of MgO is not heavily prevented by the dispersion of $Mg_4Ta_2O_9$ particles because they have relative densities above 95%. On the contrary, at sintering temperatures of 1400°C and 1500°C, the relative densities slightly increased due to $Mg_4Ta_2O_9$ dispersion. Yuan et al. and Mikami et al. reported that the addition of ZrO_2 in the MgO-ZrO_2 system causes MgO to be densified. This is because cation vacancies (V''_{Mg}) are produced by Zr^{4+} ions, replacing some of the Mg^{2+} ions, and diffusion of Mg^{2+} ions is promoted.[2,5] Because of a large difference in valence between Mg^{2+} and Ta^{5+} ions, despite a little difference in ionic radius, Ta_2O_5 seems to dissolve in MgO only a little, but it is also assumed that, as shown in the reports above, a contribution is made to densification by the vacancies, as expressed Eq.(1).

$$Ta_2O_5 \rightarrow 2Ta^{\cdot\cdot}_{Mg} + 5O_O^{\times} + 3V''_{Mg} \quad \ldots\ldots\ldots (1)$$

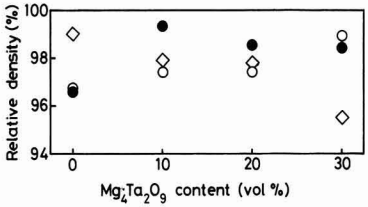

Fig. 1. Relative density of MgO-$Mg_4Ta_2O_9$ composites sintered at 1400°C (○), 1500°C (●) and 1600°C (◇), as a function of $Mg_4Ta_2O_9$ content.

3.3. Microstructures

Figure 2 shows fracture surfaces of a MgO monolith and a sintered sample with 30vol%$Mg_4Ta_2O_9$ sintered at 1500°C. In the MgO monolith, particles larger than 20μm existed and large pores were also found. There were a lot of particles which suggested that fracture took place mainly inside particles and that cracks propagated selectively along cleavage planes of crystals. As shown in Fig.2(b), particle diameters were smaller than 5μm in the composite. The fracture mode was a mixed mode of transgranular and intergranular fracture; the latter was found at a much higher ratio. The higher the sintering temperature, the more prominent the grain growth of MgO. However, the controlling effect of $Mg_4Ta_2O_9$ dispersion on grain growth was found in composites sintered at 1400°C and 1600°C.

Figure 3 shows the polished surfaces of a 30vol%$Mg_4Ta_2O_9$ composite sintered at 1400°C and of a 20vol%$Mg_4Ta_2O_9$ composite sintered at 1500°C. In Fig.3(a), a crack propagation is also seen, which was caused by indent a Vickers indentor. In Fig.3, the dark portions represent MgO, and the bright portions represent $Mg_4Ta_2O_9$. In the sample sintered at 1400°C, all $Mg_4Ta_2O_9$ particles existed at grain boundaries. In the samples sintered at 1500° and 1600°C, some of the $Mg_4Ta_2O_9$ particles were taken into

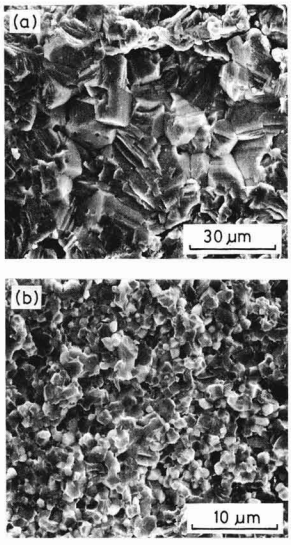

Fig. 2. Fractured surfaces of (a) the MgO monolith and (b) the composite with 30vol%$Mg_4Ta_2O_9$ sintered at 1500°C.

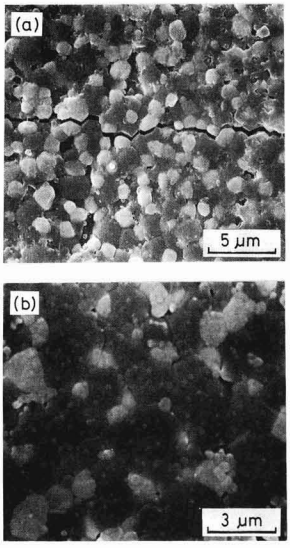

Fig. 3. Polished surfaces of (a) the composite with 30vol% $Mg_4Ta_2O_9$ sintered at 1400°C and (b) that with 20vol%$Mg_4Ta_2O_9$ sintered at 1500°C.

MgO particles. A number of pores were observed at zones where intergranular $Mg_4Ta_2O_9$ particles aggregated. $Mg_4Ta_2O_9$ is a hexagonal crystal.[12] However, the shape of its particles showed no anisotropy in particular.

3.4. Mechanical Properties

Figure 4(a) shows the relationship between fracture toughness and $Mg_4Ta_2O_9$ content of composites. The fracture toughness of the MgO monolith was about 1.6MPa·m$^{1/2}$. The MgO monolith sintered at 1600°C had such large pores that it was difficult to measure the fracture toughness, and it was excluded from the recorded data. Fracture toughness was improved by the dispersion of $Mg_4Ta_2O_9$ particles, and in some cases measured as above 3MPa·m$^{1/2}$. It is well known that as porosity increases, the fracture toughness of ceramics decreases.[13] Measuring the fracture toughness of sintered MgO samples having differing grain sizes, Yasuda et al. reported that fracture toughness is approximately 1.8MPa·m$^{1/2}$, irrespective of grain size.[14] Although decreases in grain size due to dispersion of $Mg_4Ta_2O_9$ particles were detected in the present study, there was no prominent difference in porosity. Thus, the improved fracture toughness observed in the present study can definitely be ascribed to the dispersion of $Mg_4Ta_2O_9$ particles. As shown in Fig.2, transgranular fractures were predominant in the MgO monolith, and intergranular fractures were predominant in composite samples. Fig.3(a) also clearly shows a crack deflection or selective crack propagation along grain boundaries. Improved fracture toughness can be ascribed to crack deflection due to the shift of fracture mode from transgranular to intergranular resulting from MgO-$Mg_4Ta_2O_9$ composite structuring. Conner et al. pointed out that a shift from transgranular to intergranular fractures can cause toughness to improve or decline.[15] The domination of either trend depends on the balance between the decrease in the driving force for crack propagation by crack deflection along grain boundaries and the ratio between transgranular and intergranular fracture toughness. If grain boundaries are very weak, then crack deflection will not allow fracture toughness to improve. In the present study, it is assumed that MgO-$Mg_4Ta_2O_9$ grain boundaries are not very weak and he decrease in the driving force for crack propagation by crack deflection effectively helped to improve fracture toughness. $Mg_4Ta_2O_9$ has a crystal structure similar to that of α-Al_2O_3.[12] In both crystal structures of MgO and $Mg_4Ta_2O_9$, O^{2-} ions are in closest packing, (though one cubic closest and the other hexagonal closest), and cations occupy the 6-fold coordination site. Thus, MgO and $Mg_4Ta_2O_9$ are crystallographically so coherent with each other that fracture toughness at their grain boundaries can be estimated as adequately high. In SiC-TiB_2 composites, the bonding between particles of the two phases is so weak that TiB_2 particles are pulled out during polishing, as often observed.[16] As shown in Fig.3, no such particle pullout was found with the MgO-$Mg_4Ta_2O_9$ composites.

Recently, much attention has been drawn to nano-composite materials and to transgranular nano composite materials having dispersed phases in matrix particles in particular.[5] The present study also discovered that $Mg_4Ta_2O_9$ was taken into MgO particles, as shown in Fig.3(b). However, the amount of $Mg_4Ta_2O_9$ taken up in this way was so small compared to the amount at grain boundaries that we could not detect any contribution of transgranular $Mg_4Ta_2O_9$ to the fracture toughness of composites.

Figure 4(b) shows the relationship between bending strength and $Mg_4Ta_2O_9$ content of the composites. The bending strengths of the MgO monolith are about 150MPa, although they varied slightly depending on sintering temperature. At any sintering temperature, the bending strength was raised by the dispersion of $Mg_4Ta_2O_9$ particles. In particular, the bending strengths of the composite containing 10 and 20vol%$Mg_4Ta_2O_9$ sintered at 1500°C and the composite containing 30vol%$Mg_4Ta_2O_9$ sintered at 1400°C were 250MPa or higher, which are about 1.7 times the 150MPa for MgO monolith. As reported on MgO sintered bodies by Yasuda et al. and Nishida et al., decreases in critical flow size due to decreases in grain size and increases in fracture toughness, as mentioned above, probably help improve bending strength.[14,17]

Figure 4(c) illustrates the relationship between Vickers hardness and $Mg_4Ta_2O_9$ content of the composites. The hardnesses of MgO monolith were approximately 4GPa. As the $Mg_4Ta_2O_9$ content increased up to 30vol%, the hardness monotonously rose up to around 7.5GPa. Although hardnesses were not measured because no dense $Mg_4Ta_2O_9$ sintered body was obtained, the hardness of $Mg_4Ta_2O_9$ is probably higher than that of MgO.

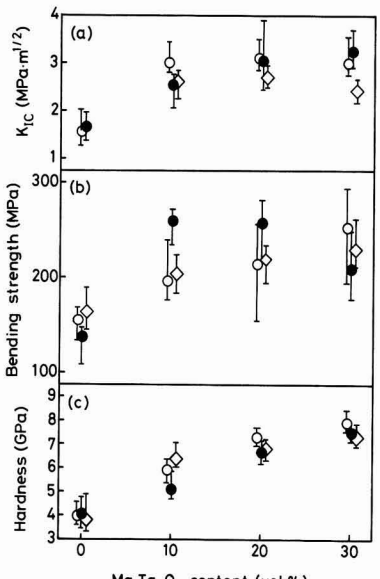

Fig. 4. (a) Fracture toughness, (b) bending strength and (c) Vickers hardness of MgO-$Mg_4Ta_2O_9$ composites sintered at 1400°C (○), 1500°C (●) and 1600°C (◇), as a function of $Mg_4Ta_2O_9$ content.

3.5. Thermal Expansion Coefficients

Figure 5 shows the relationship between thermal expansion coefficients and $Mg_4Ta_2O_9$ contents of the composites sintered at 1400°C. The thermal expansion coefficient of the MgO monolith was 13.8×10^{-6}°C^{-1}, which agreed well with the reported values.[18] As the $Mg_4Ta_2O_9$ content increased, the thermal expansion coefficient decreased. The thermal expansion coefficient of the $Mg_4Ta_2O_9$ sintered body was measured to be 10.7×10^{-6}°C^{-1}, which is lower than

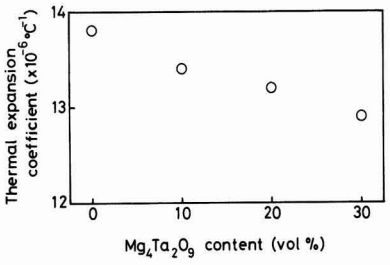

Fig. 5. Thermal expansion coefficient of MgO-$Mg_4Ta_2O_9$ composites sintered at 1400°C, as a function of $Mg_4Ta_2O_9$ content.

that of the MgO monolith. That of the 30vol%$Mg_4Ta_2O_9$ composite, the lowest of all, was $12.9\times10^{-6}°C^{-1}$, which is still high among ceramics.

It is reported that in particle-dispersed composite ceramics, residual stresses due to differences in thermal expansion coefficients and elastic moduli between dispersed phases and matrix result in crack delection, causing fracture toughness to rise.[19,20] Also, in the MgO-$Mg_4Ta_2O_9$ system, probably the same mechanisms acted, causing the fracture toughness to rise.

4. Conclusion

MgO-based ceramic composites were manufactured by reaction sintering MgO and Ta_2O_5 powders at 1400° to 1600°C under atmospheric pressure. Investigating the sinterability, microstructures, mechanical properties, and thermal expansion coefficients of the composites, the following results were obtained:

1) The added Ta_2O_5 reacted with MgO, producing composites having $Mg_4Ta_2O_9$ in the MgO matrix.

2) The relative densities of the composites were above 95%. The grain growth of MgO was inhibited by the dispersion of $Mg_4Ta_2O_9$ particles.

3) The combination of MgO and $Mg_4Ta_2O_9$ caused the fracture toughness, bending strength, and hardness to increase. Increases in fracture toughness could be ascribed to crack deflection.

4) As the $Mg_4Ta_2O_9$ content increased, the thermal expansion coefficient decreased; however, the lowered values were still high among ceramics.

References:

1) A. Tanaka and T. Miyoshi, Seramikkusu Ronbunshi, 96, 1175-1180 (1988).
2) T.C. Yuan, G.V. Srinivasan, J.F. Jue and A.V. Virkar, J. Mater. Sci., 24, 3855-3864 (1989).
3) T. Okamoto, Y. Ikuma, M. Shimaoka, T. Shirotori and W. Komatsu, Seramikkusu Ronbunshi, 97, 812-817 (1989).
4) Y. Ikuma, W. Komatsu and S. Yaegashi, J. Mater. Sci. Lett., 4, 63-66 (1985).
5) R. Mikami, Y. Ikuma and W. Komatsu, Sekko to Sekkai, No.209, 27-32 (1987).
6) K. Niihara, Seramikkusu Ronbunshi, 99, 974-982 (1991).
7) K. Niihara and A. Nakahira, Ceramic Materials and Components for Engines, ed. by V.J. Tennery, Am. Ceram. Soc. (1989) 919-926.
8) T. Nishida, T. Shiono, H. Yamauchi and T. Nishikawa, Zairyo, 36, 17-21 (1987).
9) N. Tamari, I. Kondo, H. Matsuura and M. Kinoshita, Seramikkusu Ronbunshi, 97, 79-84 (1989).
10) K. Niihara, A. Nakahira and T. Hirai, J. Am. Ceram. Soc., 67, C-13-14 (1984).
11) Fig.2318 in Phase Diagrams for Ceramists, 1969 Supplement, ed by E.M. Levin, C.R. Robbins and H.F. McMurdie, Am. Ceram. Soc. (1969) 89.
12) F. Bertaut, L. Corliss and F. Forrat, C.R. Acad. Sci., 251, 1733-1735 (1960).
13) R.W. Rice, K.R. McKinney, C. CM. Wu, S.W. Freiman and W.J.M. Donough, J. Mater. Sci., 20, 1392-1406 (1985).
14) K. Yasuda, S.D. Kim, Y. Kanemichi, Y. Matsuo and S. Kimura, Seramikkusu Ronbunshi, 98, 1103-1108 (1990).
15) C.L. Conner and K.T. Faber, J. Mater. Sci., 25, 2737-2742 (1990).
16) C.H. McMurtry, W.D.G. Boecker, S.G. Seshadri, J.S. Zanghi and J.E. Garnier, Am. Ceram. Soc. Bull., 66, 325-329 (1987).
17) A. Nishida, T. Shimamura and Y. Kohtoku, Seramikkusu Ronbunshi, 98, 412-415 (1990).
18) K. Itatani, S. Sato, F.S. Howell, A. Kishioka and M. Kinoshita, ibid., 97, 593-595 (1989).
19) K.T. Faber, A.G. Evans and M.D. Droy, Fracture Mechanics of Ceramics, Vol.6, ed. by R.C. Bradt, A.G. Evans, D.P.H. Hasselman and F.F. Lange, Plenum Press (1983) 77-90.
20) M. Taya, S. Hayashi, A.S. Kobayashi and H.S. Yoon, J. Am. Ceram. Soc., 73, 1382-1391 (1990).

This article is a full translation of the article appearing in Journal of the Ceramic Society of Japan (Japanese version), Vol.100, No.9, pp.1109-1112, 1992.

Effects of Annealing on Properties of MgO-ZrO_2 Composite Ceramics

Akio Nishida and Kenji Terai

Corporate Research and Development, UBE Industries, Ltd.
1978-5, Kogushi, Ube-shi, 755 Japan

MgO-ZrO_2 composites prepared by the pressureless sintering at 1350°C for 24h were annealed at 1600°C, and the effects of annealing on the properties such as grain size, phase transformation, bending strength and fracture toughness were investigated. The grain size of ZrO_2 in sintered MgO-ZrO_2 containing more than 20wt% ZrO_2 was too large for t-ZrO_2 to be stable at room temperature, so that the t-ZrO_2 to m-ZrO_2 phase transformation occurred during cooling from the sintering temperature. Microcrakcs formed during cooling decreased the bending strength and increased the fracture toughness. When m-ZrO_2 was transformed into c- or t-ZrO_2 by annealing, microcracks in MgO-ZrO_2 composites recombined. Consequently, flaw size in MgO-ZrO_2 composite decreased, resulting in an increase of bending strength. However, fracture toughness decreased due to reduced effect of microcrack toughning mechanism.
[Received December 12, 1991; Accepted May 21, 1992]

Key-words: MgO-ZrO_2 composites, Anneal, Grain size, Phase transformation, Bending strength, Fracture toughness

1. Introduction

Since the discovery by Garvie et el.[1] that partially stabilized zirconia has a very high toughness, efforts have been made to develop high-strength, high-toughness materials by dispersing zirconia in various type of ceramic.[2-4]

Mechanisms used thus far to increase strength and toughness by using zirconia can be classified into the following two categories:

(1) Stress induction phase transition

(2) Microcracking

Mechanism (1) aims to increase strength and toughness by utilizing the phase transformation of tetragonal zirconia (t-ZrO_2) into monoclinic zirconia (m-Z_1O_2) at crack heads.

Mechanism (2) utilizes the generation of microcracks due to volume expansion in a phase transformation from t-ZrO_2 to m-ZrO_2 during cooling after sintering. But this method has the drawback of causing strength to decrease, although it allows toughness to increase.

A phase diagram for a MgO-ZrO_2 system shows that at 1400°C MgO solid-dissolved by 4.7wt% in c-ZrO_2 and by 0.3wt% in t-ZrO_2. It does not solid-dissolve in m-ZrO_2 in all temperature ranges. Thus, when there is a phase transformation to c-ZrO_2 from any other crystal system, there is a solid-dissolution of MgO into ZrO_2. It is interesting to see what effect this phenomenon has on the mechanical properties of sintered ceramics.

t-ZrO_2 and c-ZrO_2 are stable at 1350°C and 1600°C, respectively. Preparing MgO-ZrO_2 sample sintered at 1350°C and heat treated at 1600°C, we investigated their mechanical properties and the effect of the crystal phases and microstructures of ZrO_2 on them. This paper is a report on the results of the study.

2. Test Method

For the raw materials, we used a high-purity superfine single-crystal magnesia (2000A, specific surface area: 8.0m^2/g, purity: 99.9%) made by UBE Industries, Ltd. and a zirconia powder (TZ-O, specific surface area: 8.6m^2/g, purity: 9.99% made by Tosoh Co.). From these powders, we made 4 batches having a ZrO_2 content of 5,10,20 or 30wt% and using ethanol as solvent, mixed each batch in a wet ball mill for 24h. Then, we prepared a granulated powder by crushing in an agate motor the massive product obtained with ethanol puffed out. We then molded the granulated powder under a uniaxial pressure of 150kg/cm^2 and compressed the product under a hydrostatic pressure of 1500kg/cm^2 to manufacture a green compact. The green compact was then heated in an electric furnace (atmosphere: air) at a rate of 100°C/h up to 1350°C, held there for 24h and cooled at a rate of –300°C/h to room temperature. The sintered body obtained was heated again in an electric furnace (atmosphere: air) at a rate of 100°C/h, heat treated as specified at 1600°C and cooled at a rate of –300°C/h to room temperature. The product was cut into 3mm×4mm×40mm test samples with a diamond grinder. X-ray diffraction was used to identify the crystal phases of the sintered body and relative volume percentages were calculated on the assumption that the diffraction intensities of the (111)+(11$\bar{1}$) plane of m-ZrO_2, the (111) plane of t-ZrO_2 and the (111) plane of c-ZrO_2 were proportional to the respective ZrO_2 crystal contents.[7] The density of the sintered body was obtained under an Archimedean method using ethanol as solvent. Fractures of the sintered body were observed under an SEM and films of the sintered body under a transmission electron microscope (TEM). Grain sizes of the sintered body were obtained under an intercept method (or diameter method) using SEM photographs of thermal-etched samples.

Bending strengths were measured in a 3-point bending test with a span of 30mm and a cross head speed of 0.5mm/min in accordance with the testing method for flexural strength (JIS R 1601). Fracture toughness were measured using test specimen II with span/width (S/W)=7.5 under the SEPB method in the testing method for fracture toughness of high performance ceramics (JIS R 1607).

3. Test Result and Discussion

3.1. Properties of the Sintered body before Heat Treatment

The properties of the samples sintered at 1350°C for 24h and not heat treat were as follows. The densities of the samples prepared with ZrO_2 contents of 5, 10, 20 and 30wt% were 99.7, 99.8, 98.7 and 98.4% respectively, proving that all samples were highly densified.

Figure 1 shows the relation between ZrO_2 content and grain size in the sintered body. In addition, TEM observation found out that m-ZrO_2 grains showed a microstructure containing twin crystals. Grain sizes were obtained by determining each zone whose grain boundary was detected under the SEM as one grain. As ZrO_2 content increase, the MgO grain size decreased, while the ZrO_2 grain size increased. This agreed with the result of our previous study.[8)]

Figure 2 shows the relation between ZrO_2 content and ZrO_2 crystal phases. Samples with ZrO_2 contents 5 and 10wt% were composed of t-ZrO_2, about 80%, and m-ZrO_2 and showed slight phase transformation during cooling of the sintered body. The samples with ZrO_2 contents 20 and 30wt% were primarily composed of m-ZrO_2, having a trace of t-ZrO_2 left.

For t-ZrO_2 grains to exist stably at room temperature, they must be smaller than critical grain diameters. Reportedly, critical grain diameters are variable within 0.1 to 1.0μm depending on stabilizers and matrices.[9)] Since the remaining t-ZrO_2 in the present test showed a large difference between ZrO_2 contents 10 and 20wt%, the critical particle diameters of the samples are estimated as around 0.5 to 0.6mm.

Figure 3 shows the results of measurement of bending strength and fracture toughness. The bending strengths prominently depended on ZrO_2 content. They were as thigh as about 450MPa for samples with ZrO_2 contents 5 and 10wt% and much lower with higher ZrO_2 contents. On the other hand, the fracture toughness, increased as ZrO_2 content increased.

These trends can be ascribed to microcracks caused by volume expansion due to a phase transformation from t-ZrO_2 to m-ZrO_2 of the sintered body during cooling. As the ZrO_2 content increases, larger quantities of t-ZrO_2 particles are transformed, causing more microcracks. Thus it is assumed that as the ZrO_2 content increases, fracture toughness increases and strength decreases due to microcracking mechanisms. The samples with ZrO_2 content of 30wt% in particular showed a very low strength of 44Mpa due to macrocracks developed from interlocked microcracks. Again, fracture toughness could not be measured because it was impossible due to such macrocracks to cause precracks in the samples.

3.2. Properties of Sintered body after Heat Treatment

The properties of the samples sintered at 1350°C for 24h and then heat treated at 1600°C for 10h were as follows: The densities of the samples prepared with ZrO_2 contents of 5, 10, 20 and 30wt% were all nearly 100%, showing a little increases due to heat treatment.

Figure 4 shows the relation between ZrO_2 content and grain size in sintered body. As the ZrO_2 content increased, MgO grain sizes decreased and ZrO_2 grain sizes increased. This trend was the same as that before heat treatment. Grain growth was observed in all samples and that of MgO in the samples with ZrO_2 content of 5wt% was most prominent.

Figure 5 shows the relation between ZrO_2 content and ZrO_2 crystal phase. With 5wt%ZrO_2 content, a 100% phase transformation was made to c-ZrO_2. With higher ZrO_2 contents, phase transformation to c-ZrO_2 was by smaller percentages.

Figure 6 shows measured values of bending strength and fracture toughness. Except with 5wt%ZrO_2 content, strength was raised by heat treatment and to the highest with 20wt%ZrO_2 content. Also with this ZrO_2 content, the strength of the sample were particularly widely increased from 200MPa to 578MPa by heat treatment. Except with 5wt%ZrO_2 content, the fracture toughness, in contrast to bending strength was lowered by the heat treatment. Decreases in toughness were largest for the samples with 20wt%ZrO_2. For the samples with 30wt%ZrO_2, like those before heat treatment, no fracture toughness could be measured.

3.3. Effect of Heat Treatment Time

Since the samples with 20wt% ZrO_2 had their properties

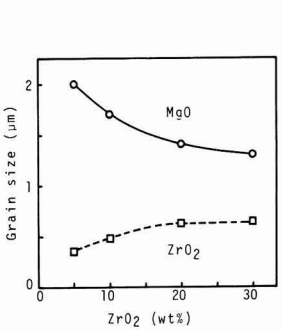

Fig. 1

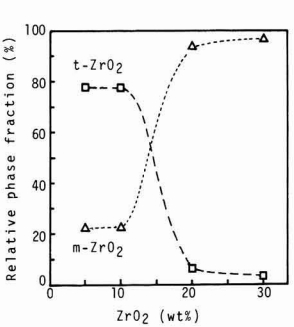

Fig. 2

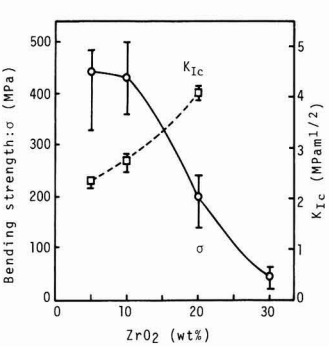

Fig. 3

Fig. 1. Relation between content of ZrO_2 and grain size of MgO-ZrO_2 composite sintered at 1350°C for 24h.

Fig. 2. Relation between content of ZrO_2 and relative phase fraction of MgO-ZrO_2 composite sintered at 1350°C for 24h.

Fig. 3. Bending strength and fracture toughness of MgO-ZrO_2 composite sintered at 1350°C for 24h.

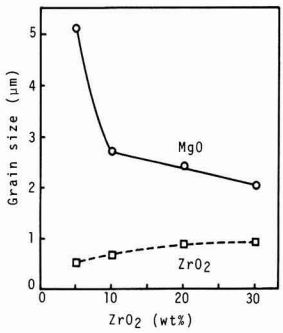

Fig. 4

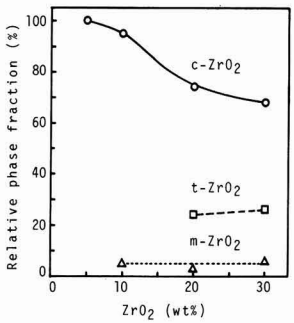

Fig. 5

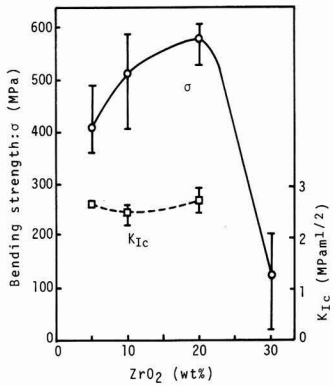

Fig. 6

Fig. 4. Relation between content of ZrO_2 and grain size of MgO-ZrO_2 composite after annealing at 1600°C for 10h.

Fig. 5. Relation between content of ZrO_2 and relative phase fraction of MgO-ZrO_2 composite after annealing at 1600°C for 10h.

Fig. 6. Bending strength and fracture toughnes of MgO-ZrO_2 composite after annealng at 1600°C for 10h.

most heavily affected by heat treatment, we investigated the effect of heat treatment time on them. **Figure 7** shows the relation between heat treatment time and grain size. As the heat treatment time increased, MgO grains also grew larger, while ZrO_2 grains first diminished and then grew larger. This diminution is because although twin crystal were observed among m-ZrO_2 particles before heat treatment, each zone of which the grain boundary was detected under the SEM was counted as one grain, in other words, because the phase transformation after heat treatment enabled the interfaces of twin crystals to be recognized clearly as grain boundaries.

Figure 8 shows the effect of heat treatment time on the percentages of ZrO_2 crystal phases. Before heat treatment, m-ZrO_2 existed by 94% and t-ZrO_2 by the rest. In 30min of heat treatment, c-ZrO_2 and t-ZrO_2 were predominant and m-ZrO_2 existed by less than 5%.

As the heat treatment time increased, the percentage of c-ZrO_2 increased, while that of t-ZrO_2 decreased. With the MgO content of the samples in the present test, no equilibrium has not been reached with this heat treatment time although MgO and c-ZrO_2 are stable phases in a 1600°C heat treatment.

Figure 9 shows the relation between heat treatment time and mechanical properties. Bending strength soared up within the first 1h of heat treatment and reached a maximum 594MPa in 3h. As the heat treatment continued, the strength decreased a little due to grain growth. The fracture toughness, in contrast to strength, plummeted down within the first 1h. This rapid change in mechanical properties may be related to the phase transformation of ZrO_2 due to heat treatment. Before the heat treatment, the strength was low and the fracture toughness was high because m-ZrO_2 was predominant and microcracks existed. It is assumed that the strength is greatly increased, while the fracture toughness is reduced by a heat treatment because a heat treatment causes

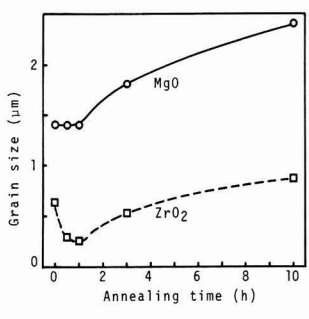

Fig. 7

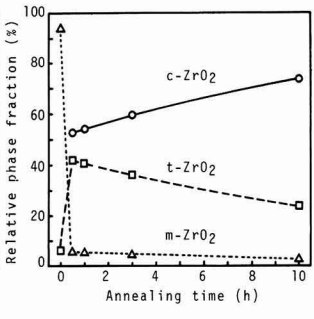

Fig. 8

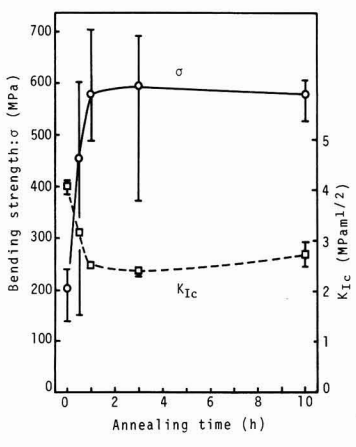

Fig. 9

Fig. 7. Effect of annealing time on grain size of MgO-ZrO_2 composite annealed at 1600°C.

Fig. 8. Effect of annealing time on relative phase fraction of MgO-ZrO_2 composite annealied at 1600°C.

Fig. 9. Effect of annealing time on bending strength and fracture toughness of MgO-ZrO_2 composite annealed at 1600°C.

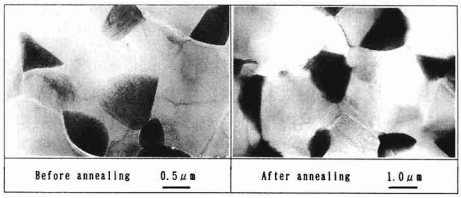

Fig. 10. Transmission electron micrograph of MgO-ZrO_2 composite containing 20wt% ZrO_2 before and after annealing.

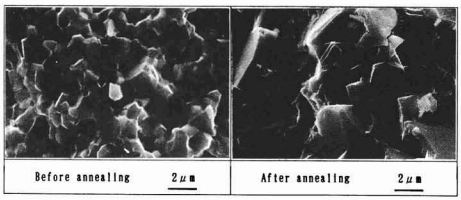

Fig. 11. Scanning electron micrograph of fracture surface of MgO-ZrO_2 composite containing 20wt% ZrO_2 before and after annealing.

m-ZrO_2 to be transformed into c-ZrO_2 or t-ZrO_2, allowing microscracks to be rejoined.

3.4. Changes in Microstructure due to Heat Treatment

The mechanical properties of MgO-ZrO_2(20wt%) composites are greatly affected by heat treatments. This we have already ascribed to the reunion of microcracks due to phase transformation. Let's further look into this supplementarily from the aspects of microstructure.

Figures 10 and **11** show the TEM and fracture surface SEM photographs respectively of sintered body (20wt%ZrO_2) before and after heat treatment. The TEM photographs of sintered body before heat treatment showed some zones with grain boundary layers 0.1μm thick or with intergranular separations. Energy dispersive X-ray spectroscopy and electron diffraction analysis showed that grain boundary layers were composed of microcrystals containing MgO by 60 to 79wt%. The fracture surface SEM photographs proved that intergranular breakdowns were predominant. Thus, the strength of the sintered body before heat treatment was low probably because grain boundaries were weakened by second components and microcracks contained in grain boundary layers.

The sintered body after heat treatment showed no second components and microcracks at grain boundaries. Observation of fractures found out that transgranular breakdown were predominant, which suggests that the grain boundaries of the sintered body after heat treatment are bonded firmly. Probably this led to a smaller size of defects as origin of breakdowns, allowing the strength to increase.

The difference in grain boundary layers between the sintered body before heat treatment and the sintered body after heat treatment seems to be due to the phase transformation of ZrO_2. It is assumed that in the sintered body before heat treatment, a transformation from t-ZrO_2 to m-ZrO_2 took place during cooling. MgO solid dissolves by 0.3wt% in t-ZrO_2 but does nothing in m-ZrO_2. Thus, probably, in a transition from t-ZrO_2 to m-ZrO_2, MgO precipitated at grain boundaries, causing thick parts of grain boundary layers to be formed. In the sintered body after heat treatment, on the other hand, a phase transformation progressed from m-ZrO_2 or t-ZrO_2. MgO solid dissolves in c-ZrO_2 and t-ZrO_2 by 4.7 and 0.3wt%, respectively. This probably caused atoms to more at grain boundaries between MgO and ZrO_2 during heat treatment, allowing grain boundaries to be recombined.

4. Conclusion

Investigating the properties of the MgO-ZrO_2 composites sintered at 1350°C at which t-ZrO_2 is stable and then heat treated at 1600°C at which c-ZrO_2 is stable, we acquired the following findings:

1) As the ZrO_2 content increases in the sintered body before heat treatment, the grain size of t-ZrO_2 exceeds the critical grain size, causing a phase transformation to progress from t-ZrO_2 to m-ZrO_2. Here microcracks are caused by volume expansion, resulting in the low strength and high toughness of the sintered body.

2) When m-ZrO_2 is transformed into c-ZrO_2 or t-ZrO_2 by a heat treatment, microcracks are rejoined. This allows the size of defects in the sintered body to be smaller, causing the strength to increase, while causing the fracture toughness to decrease because toughening functions due to microcracks come to cease.

References:

1) R.C. Garvie, R.H. Hannink and R.T.Pascoe, Nature, 258, 703-704 (1975).
2) N. Claussen, J.Am. Ceram. Soc., 59, 49-51 (1976).
3) N. Claussen, J. Steeb and R.F. Pabst, Am. Ceram. Soc. Bull., 56, 559-62 (1977).
4) R. Shikata, Y. Urata, T. Shioji and T. Nishikawa, Power and Powder Metallur. 37, 357-361 (1990).
5) K. Kobayashi, T. Masaki, Seramikkusu, 17, 427-433 (1982).
6) C.F. Grain, J. Am. Ceram. Soc., 50, 288-290 (1967).
7) R. C. Garvie and P.S.Nicholson, J. Am. Ceram. Soc., 55, 303-305 (1972).
8) A. Nishida, S. Fukuda, Y. Kohtoku and K. Terai, J. Ceram. Soc. Jpn., 100, 191-195 (1992).
9) Y. Sugano, Hyomen Kagaku, 10, 171-174 (1989).

This article is a full translation of the article appearing in Journal of the Ceramic Society of Japan (Japanese version), Vol.100, No.9, pp.1113-1116, 1992.

Fabrication of A Functionally Gradient Material of TiC-SiC System by Chemical Vapor Deposition

Chihiro Kawai, Jun-ichi Teraki*, Tohru Hirano* and Toshio Nomura

Itami Research Laboratories, Sumitomo Electric Industries, Ltd.
1-1-1, Koya-kita, Itami-shi, 664 Japan
*CAE Center, Daikin Industries, Ltd.
1304, Kanaoka-cho, Sakai-shi, 592 Japan

Oxidation-resistant coating using chemical vapor deposition on continuous fiber reinforced ceramics having lower thermal expansion coefficient (a) than the coated layer (SiC) was studied. A SiC-fiber reinforced TiC matrix composite (SiC/TiC composite, a=5.6×10^{-1}K^{-1}) was used as a substrate and the TiC-SiC system was chosen as a coating. The CVD was carried out in $TiCl_4$-$SiCl_4$-CH_4-H_2 system at deposition temperature of 1350°C and total gas pressure of 60Torr. Compositionally gradient TiC-SiC layers were formed by stepwise change of the Ti/(Ti+Si) ratio in the feed gas. Peeling occurred along the edges of the coating in the case of SiC coating, but it did not occur at all in a TiC-SiC coating with an optimum gradient composition. These results agreed with the thermal stress analysis using F.E.M.

[Received January 8, 1992; Accepted May 21, 1992]

Key-words: CVD, TiC, SiC, Composite, FGM, Fiber reinforced ceramics, Thermal stress

1. Introduction

A number of researchers have been investigating the so-called ceramic-base composite materials, in which the second phase such as spherical particles, whiskers, short fibers of continuous fibers, is dispersed in ceramic matrix phase in order to improve mechanical properties.

These composites generally have uniform compositions. However, more recently, the Functionally Gradient Materials (FGM) have been attracting much attention.[1] These are characterized by changing compositions, resulting in continuously changing mechanical properties, such as the thermal expansion coefficient and Young's modulus. This reduces residual stress generated during the cooling process or thermal stress generated while they are operated.

Oxidation-resistant SiC coating of high-temperature structural materials by chemical vapor depostion (CVD) may produce sufficiently high residual thermal stress during the cooling process from the coating to room temperature causing delamination or destruction of the coating layer, when there is a large difference in thermal expansion coefficient between the substrate and coating. The authors have been studying the functionally gradient TiC-SiC coating to prevent the above problems.

It is necessary, when the functionally gradient TiC-SiC composites are produced, to design the optimal compositional distribution to exhibit the gradient functions and to control the structures to realize the designed composition distribution. For these objectives, a CVD process must be developed in order to synthesize the TiC-SiC composites. At the same time, properties, such as thermal expansion coefficient and Young's modulus, of the synthesized composites of different compositions must be known. These properties were discussed previously.[2]

In this study, a continuous fiber reinforced ceramic matrix composite is coated with layers of gradient compositions by the CVD method. The results are compared to those obtained by the thermal stress analysis using the Finite Element Method.

2. Experimental Procedure

2.1. Substrate Materials

A SiC fiber reinforced TiC matrix composite was used as substrates. 2-D SiC fabrics (Nippon Carbon, Nl-2-1-2S) were coated with TiC powder, 1wt%Al_2O_3 as the aid and resin, by electro-deposition to produce the prepreg sheets, which are sintered by Hpt-pressing after having been dried and laminated. The SiC/TiC composite thus prepared is cut in the thickness direction into 30mm×15mm×5mm shapes, in order to prepare the specimens.

Table 1 shows the properties of the SiC/TiC composite.

2.2. Coating of TiC-SiC Gradient Composition

Figure 1 shows the concept of the functionally gradient, TiC-SiC composite material. The thermal expansion coefficent of the coating layer is continuously changed from the substrate surface to the coating surface of SiC, reducing the thermal stress generated in the coating layer when it is cooled from coating temperature to room temperature.

The compositional distribution function for the gradient composition changing from TiC to SiC is given by the following equation:

$$f(x) = 1 - (x/t)^n \quad \ldots\ldots\ldots\ldots\ldots (1)$$

where $f(x)$ is the volume fraction of SiC in the coating layer, x is the distance from the coating layer surface, t is the

Table 1. Properties of SiC-fiber reinforced TiC composite.

	in plane	through the thickness
Density (kg/m^3)	3880	
Young's Modulus (GPa)	325	
Thermal Expansion coefficient (10^{6}K^{-1})	5.6	5.5
Thermal conductivity (W/mK)		30.0
Flexural strength (MPa)	150	
Compressive strength (MPa)	979	

coating layer thickness, and n is the compositional distribution parameter.

In consideration of oxidation-resistance of the composite, the gradient composition of the CVD-coated layer designed in this study is approximately 100μm in total thickness, 20μm for the surface SiC layer and 80μm for the intermediate layer. **Table 2** shows the CVD conditions and thermal expansion coefficient[2] of the prepared TiC-SiC composites. The composition of 40vol% TiC was set at the interface between the substrate and the coating layer to make thermal expansion of the coating layer almost coincide with that of the substrate at the interface.

Figure 2 shows the relationship between the n value and compositional distribution. The compositional distribution approaches the single SiC phase, as the n value increases.

The n values of 0.2 and 1.0 were used in this study for the distributions of the gradient coating compositions. **Figure 3** shows the stepwise gradient composition targeted, realizing the composition having a distribution close to that designed (patterns 1 and 2, corresponding to n=0.2 and 1.0, respectively). The feed gas composition and coating time were changed stepwise to coat the SiC-TiC composite substrate with the gradient composition layer of TiC/SiC of the above structure. The CVD conditions for each pattern are shown in **Table 3**.

The thickness of each layer is controlled by changing coating time, knowing that the deposition rate of the TiC-SiC coating is essentially constant at around 90μm/hr.[2] The specimen coated with the single SiC phase (thickness: approximately 100μm) was also prepared for comparison.

The coated specimen was observed by a scanning electron microscope (SEM) after having been visually observed for their damages and exfoliation. Then, the specimen was cut and ground with diamond paste for analysis using an optical microscope to investigate the compositional distribution of the coating layer.

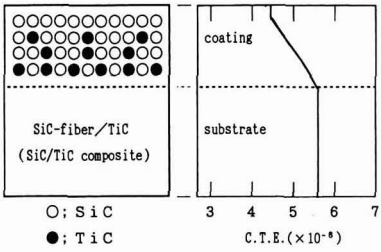

Fig. 1. Conceptual structure of TiC-SiC FGM.

Table 2. The CVD conditions for fabrication of TiC-SiC composites and the thermal expansion coefficients.

TiC volume%		0	15.0	24.1	38.1	62.5	100
Feed gas	$SiCl_4$ (l/min)	0.52	0.31	0.25	0.14	0.09	0
	$TiCl_4$ (l/min)	0	0.15	0.19	0.32	0.37	0.31
	CH_4 (l/min)	0.25	0.25	0.25	0.25	0.25	0.25
	H_2 (l/min)			4.75~5.04			
Thermal Expansion coefficient (10^6K^{-1})		4.55	4.61	5.19	5.45	6.67	7.42

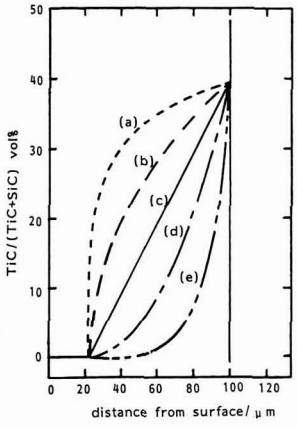

Fig. 2. Compositional distributions dependent on n numbers in Eq.(1). (a) n=0.2, (b) n=0.5, (c) n=1.0, (d) n≈2.0, (e) n=5.0.

3. Thermal Stress Analysis of Functionally Gradient TiC-SiC Materials

Table 4 shows the properties of the CVD-coated TiC/SiC composites used for the thermal stress analysis.[2] The thermal expansion coefficient and Young's modulus are the values in the directions parallel and perpendicular to the substrate surface, respectively. The Poisson ratio, bending strength, and compression strength are the literature values,[3-7] for the single TiC and SiC phases. They are estimated from the rule of mixture for the composites with the knowledge that these composites are of columnar structures.

The residual stress was analyzed for the cross-section, shown in **Fig.4**, by the Finite Element Method. The x and

Table 3. Stepwise changes of gas flow rate for coating compositionally gradient TiC-SiC layers.

Gradation pattern		1		
Time /min.		0 ~ 50	50 ~ 66	
Gas flow rate /l·min⁻¹	$SiCl_4$	0.14	0.52	
	$TiCl_4$	0.32	0	
	CH_4	0.25	0.25	
	H_2	4.75	4.75	
Prepared composition /TiC vol%		38.1	0	
Prepared thickness /μm		75	25	
Gradation pattern		2		
Time (min.)		0 ~ 22	22 ~ 44	44 ~ 66
Gas flow rate /l·min⁻¹	$SiCl_4$	0.14	0.31	0.52
	$TiCl_4$	0.32	0.15	0
	CH_4	0.25	0.25	0.25
	H_2	4.75	4.75	4.75
Prepared composition /TiC vol%		38.1	15.0	0
Prepared thickness /μm		33	33	33

Table 4. Properties of CVD-deposited TiC-SiC composites.

TiC volume%	0	15.0	24.1	38.1	62.5	100
Density (kg/m³)	3180	3580	3700	3740	4310	4840
Young's Modulus (GPa)	220	214	213	285	400	467
Thermal Expansion coefficient (10^6K^{-1})	4.55	4.61	5.19	5.45	6.67	7.42
Flexural strength (MPa)	500	530	550	590	640	750
Compressive strength (MPa)	1370	1500	1570	1740	1930	2254
Poison's ratio	0.24	0.23	0.22	0.22	0.21	0.19

z components of the principal stress and (x-z) component of the shear stress in a temerature range from 1623K to 300K as coating temperature were estimated using the one-dimensional and two-dimensional planar stress analysis.[8]

4. Results and Discussion

Figure 5 illustrates the optical microscopic structures of the cross-sections of the SiC-TiC composite materials coated with the gradient composition of TiC-SiC. Both Patterns 1 (n=0.2) and 2 (n=1.0) had a thickness as designed.

Figure 6 shows the stereomicroscopic photographs of the coating layers of these composites and the single SiC phase (thickness: approximately 100μm). For the specimen coated with SiC, the coating layer came off extensively, with the thermal cracks running in parallel to the edge in the inside fairly close to the edge. However, few cracks were observed on the surface. Similar cracks were observed in the composite coated with the gradient composition of Pattern 2, but the coating layer came off less extensively.

Figure 7 shows the SEM photographs of the delaminated coating layer. The damage of the substrate accompanied the delamination of the coating layer of the single SiC phase. On the other hand, the coating layer of the gradient composition caused no damage to the substrate, when it came off. However, cracks were found in the inside fairly close to the edge.

The coating layer of the gradient composition of Pattern 1 produced the good results; no cracking resulted, and no damage or delamination of the coating layer was observed.

Figure 8 shows the results of the one-dimensional thermal stress analysis for several n levels in the range n=0.2 to 0.5. The absolute level of stress ratio (ratio of the stress generated to bending or compressive strength) is low at 0.15 or less, irrespective of the n value examined. Based on this, it is judged that both the coating layer and substrate will not be damaged.

However, it should be noted that the results of the one-dimensional thermal stress analysis are only applicable to an infinite plane, and the two-dimensional analysis is necessary for the local phenomena around the edge, such as those observed in this study.

Figure 9 shows the results of the two-dimensional thermal stress analysis for several n values in the range n=0.2 to 0.5.

It is observed that the damage around the edge originates the cracks running in the direction parallel the coating layer thickness. Thus, it is considered that it is not caused by the stress in the z direction. The principal stress in the z direction, which is parallel the coating layer thickness, attains a maximum at the interface with the substrate, a position which is in the inside near the edge. It is no more than 20MPa, which is sufficiently lower than the tensile strength of the coating layer or substrate.

The principal stress in the x direction, which is perpendicular to the coating layer thickness, attains a maximum at almost the same postion as that in the z direction. The highest level at n=0.2 is 40MPa. It increases with n level, to as high as 100MPa at n=1.0. At n=5.0, a level which is close to that of the coating layer of single phase SiC, no tensile stress will be generated at the interface between the coating layer and the substrate. However, a tensile stress of no more than 140MPa is generated in the substrate. This tensile stress is close to the bending strength of the substrate.

A similar trend is observed with the shear stress in the x-z direction. It is fairly low, no more than 50MPa at n=0.2, but it increases with the n level to no more than 80MPa at n=1.0. At n=5.0, a shear stress of 100MPa or higher is generated at the peculiar point in the vicinity of the interface between the coating layer and the substrate. Ito et al. also observed the presence of the peculiar point with respect to tensile shear stress at the interface between the coating layer and the substrate, where the substrate of a Ni-base alloy (INCO X-750) is coated with stabilized ZrO_2.[9] This system

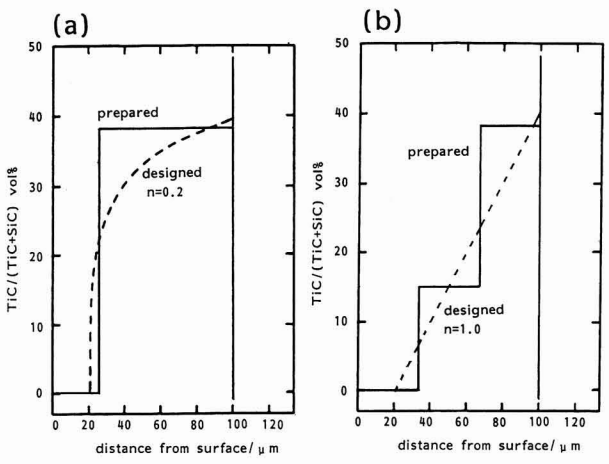

Fig. 3

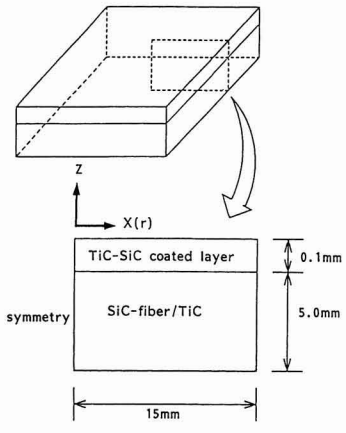

Fig. 4

Fig. 3. A comparison of designed and prepared compositional distributions. (a) n=0.2, (b) n=1.0.

Fig. 4. The parameters for calculation of thermal stress by F.E.M.

is similar to that investigated in this study in that the coating layer has a higher thermal expansion coefficient than the substrate.

These results indicate that the effects of reducing thermal stress vary greatly, depending on the n level for the gradient composition distribution function. No damage is observed in the substrate at n=1.0, although the coating layer comes off. The following prediction could be performed. The delaminations of the coating layer occurs at the interface because the generated tensile stress is higher than the bonding strength between the coating layer and the substrate. The coating layer itself is not damaged because the generated tensile stress is lower than the tensile strength of the coating layer or the substrate. In other words, the coating layer of the gradient composition comes off at a stress lower than the tensile strength of the coating layer. In contrast, destruction of the substrate itself, as observed with that coated with the single SiC phase, is caused by the principal tensile stress in the x direction and tensile shear stress in the x-z direction, as predicted from the results of calculation using n=5.0.

Thus, the experimental results and thermal stress analysis results are in good agreement with each other for the coating layer of gradient composition.

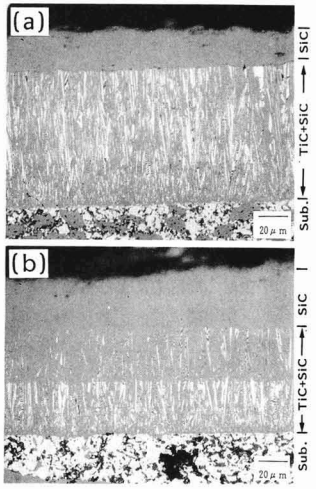

Fig. 5. The cross-sectional surfaces of TiC-SiC layers with gradient compositions. (a) Pattern 1, (b) Pattern 2.

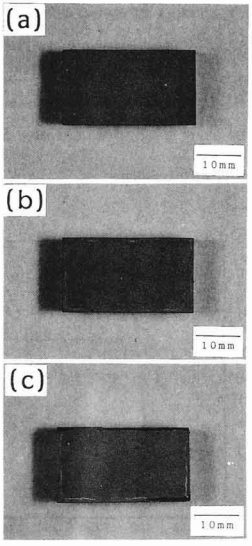

Fig. 6. The SiC/TiC composites coated with a variety of compositionally gradient TiC-SiC layers.
(a) Pattern 1, (b) Pattern 2, (c) SiC monolayer.

5. Conclusion

A continuous fiber reinforced ceramic matrix composite is coated with the gradient composition of TiC and SiC using the CVD technique developed to deposit oxidation-resistant SiC, where the substrate has a higher thermal expan-

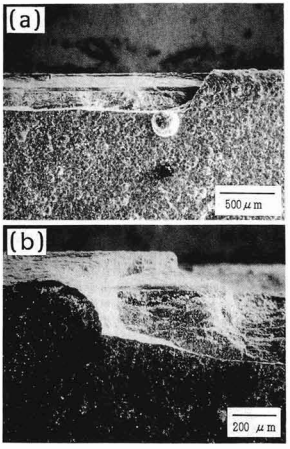

Fig. 7. Fracture along an edge of the coated SiC/TiC composites.
(a) Pattern 2, (b) SiC monolayer.

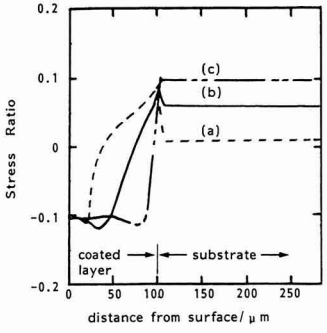

Fig. 8. Stress ratios calculated by 1-dimensional analysis for thermal stress. (a) n=0.2, (b) n=1.0, (c) n=5.0.

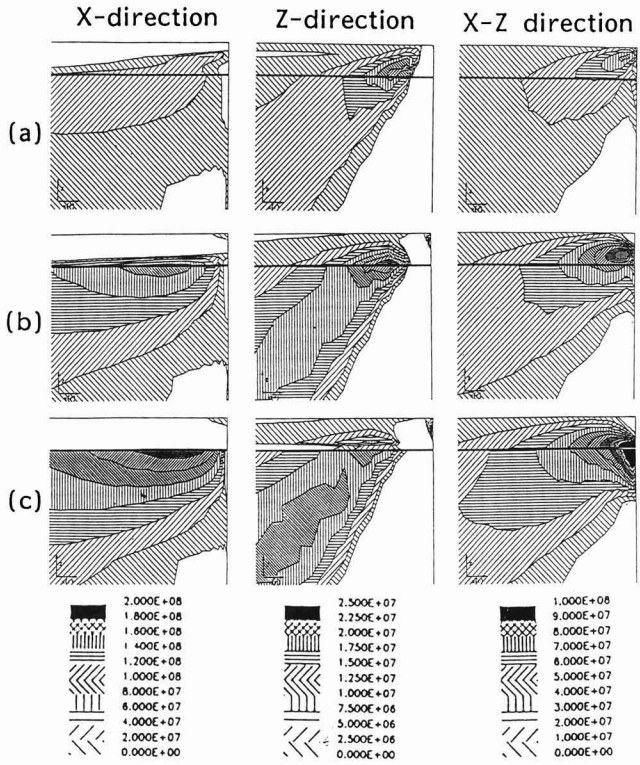

Fig. 9. Tensile stress in x, z (principal) and x-z direction (shear) calculated in 2-dimensional analysis. (a) n=0.2, (b) n=1.0, (c) n=5.0.

sion coefficient than SiC. The experimental results are compared with the thermal stress analysis results.

1) The substrate of TiC reinforced with continuous SiC fibers, having a thermal expansion coefficient α: $5.6\times10^{-6}K^{-1}$, is coated with various gradient compositions of TiC and SiC. The coating layer comes off or is damaged, depending on its composition. The coating layer of the single SiC phase comes off in the vicinity of the edges. This is accompanied by damage of the substrate. In contrast, the specimen coated with the gradient composition can be free of the coating layer delamination or damage of the substrate, when the gradient composition is carefully controlled.

2) The results of the two-dimensional thermal stress analysis, using the Finite Element Method, indicate that stress in the direction parallel to the coating layer (principal or shear stress) is tensile in the vicinity of the interface between the coating layer and the substrate. It attains a maximum in the vicinty of the edges of the substrate. These values can be reduced, when the gradient composition is used for the coating layer.

Acknowledgement

This study was performed through Special Coodination Funds of the Science and Technology Agency of the Japanese Government.

References:

1) M. Niino, Kino Zairyo, 10, 31-43 (1987).
2) C. Kawai and M. Miyake, Seramikkusu Ronbunshi, 99, 1088-1093 (1991).
3) E.A Almond, Powder Metallur., 25, 146 (1982).
4) S.G. Seshadri, M. Srinivasan and K.M. Keeler, Ceram. Eng. Sci. Proc., 8, 671-684 (1987).
5) M.S.S.J. (ed.), Kyokugen Jyotai to Zairyo, Shokabo (1987) 126.
6) T. Hirai and M. Sasaki, Tankakeiso Seramikkusu, Uchida Rokakuho (1988) 55.
7) G.V. Samonov, High-temperature Materials No.2, Properties Index, Plenum Press (1964) 177-178.
8) J. Teraki and T. Hirano, Proc. 4th Sympo. on Keisha Kinoo Zairyo (1991) 209-214.
9) Y. Ito, Proc. 28th Sympo. on X-ray Material Strength (1991) 10-16.

This article is a full translation of the article appearing in Journal of the Ceramic Society of Japan (Japanese version), Vol.100, No.9, pp.1117-1121, 1992.

Preparation and Properties of TiO_2 Films by Complexing Agent-Assisted Sol-Gel Method

Toshikazu Nishide and Fujio Mizukami*

Material Research Laboratory, Nissan Research Center, Nissan Motor Co., Ltd.
1, Natsushima-cho, Yokosuka-shi, 237 Japan
*National Chemical Laboratory for Industry
1-1, Higashi, Tsukuba-shi, 305 Japan

The TiO_2 films were prepared on glass or silicon wafer substrates by sol-gel method using glycols or their either derivatives as ligands, directed toward control of optical properties. The effect of ligands on the indices and crystal phases of TiO_2 films was investigated. On the glass substrates, the refractive indices of TiO_2 films depended on the ligands used, although all the films were fired under the same conditions. The 2-(2-methoxyethoxy) ethanol (MEE) ligand gave the most high refractive indices among the ligands used. On the other hand, the 2-methyl-2, 4-pentanediol (MPO) ligand gave the most low refractive indices when the films are fired bellow 510°C. The change in refractive indices is discussed in connection with crystal phase of TiO_2 films measured by X-ray diffraction analysis. In the TiO_2 film prepared using MEE as the ligand, the anatase crystal appeared at low temperature (400°C). It gave high refractive indices. In the TiO_2 film prepared using MPO as the ligand, amorphous TiO_2 appeared bellow 510°C and gave low refractive indices. The ligands influence the size of titanium oxide sols and TiO_2 crystal phases, and change the refractive indices of the films. In other words, the lignds can control the refractive indices of TiO_2 films on glass substrates. The crystal phase of TiO_2 films on silicon wafer also depended on the ligand used. The MPO and trimethylene glycol monomethyl ether (TME) ligand accelerated the transformation from anatase to rutile form. In contrast MEE ligand inhibited the change to rutile form even at 900°C. Thus, anatase or rutile in the TiO_2 film on the silicon wafer can be selectively formed by the selection of ligands used in sol-gel precess.

[Received February 3, 1992; Accepted May 21, 1992]

Key-word: TiO_2 films, Sol-gel, Ligand, Refractive index, Crystal phase

1. Introduction

A number of researchers have discussed powders and thin films of ceramic materials, such as metallic oxides prepared by the sol-gel process.[1] One of the new sol-gel processes proposed uses an organic ligand added to the metallic alkoxide solution for the preparation of metallic oxide. The oxide mixture thus prepared is then formed into metallic complexes to be hydrolyzed into sol and then gel, which is fired to produce the ceramic sinter.[2]

Maeda et al synthesized cordierite by the sol-gel process using an organic ligand and discussed that the ligand helps to reduce the temperature at which the coordierite phase is formed.[3] They added 2–(2–methoxyethoxy) ethanol (MEE) as the organic ligand to a mixed alkoxide solution of silicon, aluminum and magnesium, and hydrolyzed and fired the mixture to produce the cordierite powder. When MEE is added in a quantity of 4/5 equivalents or more relative to the total metallic ions, the cordierite phase directly results from the amorphous, complex oxide gel at 1000°C. This is compared to 1300°C at which cordierite is formed by the conventional process in which powdered oxides are mixed. These results indicate that MEE works to control the complex oxide structures. Therefore, it is expected that the structures and properties of metallic oxides are designed by the use of an adequate ligand to control their structures and properties.

Several researchers attemped to apply the sol-gel process to the production of TiO_2 thin films.[4-6] Yaldas added water to an alcohol solution of titanium alkoxide to synthesize titania sol. After being coated over a glass or silicon wafer, the titania sol is fired to prepare the TiO_2 thin film. The refractive index of the thin film is found to vary depending on substrate type and film thickness.[4] Yoko et al. hydrolyzed an ethanol solution of titanium isopropoxide with equimolar water to prepare the sol, fired it to produce the TiO_2 thin film over an glass substrate, and observed its electromotive force for light.[5] Takahashi et al. hydrolyzed an isopropanol solution of titanium isopropoxide with diethanol amine and water to prepare the titania sol, fired it to form the TiO_2 thin film over a glass or silicon wafer, and observed its refractive index.[6] They found that anatase is transformed into rutile at 550° to 600°C when the ligand is used.

These results indicate that properties of the TiO_2 thin films depend significantly on the conditions under which they are prepared. However, few researchers have extensively discussed the effects of the ligand on properties of the thin TiO_2 films.

Therefore, in this study, the authors have synthesized TiO_2 thin films by the sol-gel process, in which glycol or its ether-derivative is used as the organic ligand, and investigated its effects on refractive index and structures (crystalline phases) of these films, with the objective to control their optical properties by the ligand.

2. Experimental Procedure

2.1. Specimen Preparation

The commercial, special-grade reagents were used di-

rectly as the starting materials without purification.

Titanium tetraisopropoxide ($Ti(O\text{-}i\text{-}pr)_4$, 0.1mols) placed in 200ml of ethanol, to which 0.1mols of an organic ligand was added. The solution was heated under reflux at 80°C for 1.5h. The organic ligands used in this study were 2-(2-methoxyethoxy) ethanol (MEE), 2-methyl-2, 4-pentane diol (MPO), and trimethylene glycol monomethylether (TME). After having been cooled to 40°C, each ligand was mixed with 0.1mols of water and 0.02mols of 70% nitric acid, and the solution was heated under reflux at 80°C for 1.5h. The resulting sol solution was coated on a soda lime glass or silicon wafer (111) by a spinner. The spinner was controlled at a speed to have a thickness of 0.1μm after firing for the analysis of refractive index and 0.3μm for X-ray diffraction analysis. Each specimen was fired to 400° to 900°C by an electrical oven.

The ligand-free system was also investigated, where 0.1mols of titanium tetraisopropoxide ($Ti(O\text{-}i\text{-}pr)_4$) was dissolved in 200ml of ethanol, to which 0.1mols of water and 0.02mols of 70% nitric acid were added. After having been allowed to stand for more than 1h, the solution was coated on a substrate and fired in the similar manner.

2.2. Analytical Procedure

The thickness of the thin film was determined by a surface shape analyzer (DEKTAK 3030, Nippon Shinku), and the thermal analysis was conducted by thermogravimetric/differential thermogravimetric analyzer (TG-DTA2000, Mac Science). The crystalline phases in the TiO_2 thin film were identified by a X-ray diffractometer (RAD-B Model, Rigaku Denki), where the diffraction conditions, such as X-ray intensity, were set constant. Refractive index was determined by an Elipsometer (DHA-OLX, Mozojiri Kogaku Kogyo) at a wavelength of 632.8nm.

3. Results and Discussion

3.1. Thermal Analysis

The thermal analysis of the ligand-free titania gel shows exothermic peaks at 138° and 199°C, which are accompanied by weight loss. In general, an exothermic peak accompanied by weight loss is observed with a gel containing an organic compound, from which it is judged that the thin film contains no alkoxy-derived organic matter at 199°C or higher.

Figure 1 shows the representative thermal analysis results (DTA and TG curves) with the titania gel containing the organic ligand, shown in Fig.1(a), being with the gel containing MEE as the ligand. Weight loss continues until the temperature reaches 300°C. There are two peaks observed at around 159° and 280°C, which, being accompanied by notable weight loss, result from the combustion of alkoxy group and MEE, respectively. The weight loss is observed similarly with the gel containing TME as the ligand in a temperature range below 303°C. The exothermic peaks, accompanied by weight loss, are observed at around 153° and 303°C, which result from the combustion of alkoxy group and TME. Thus it is considered that the TiO_2 film will contain no organic residua at above 300°C when MEE or TME is used as the ligand.

Fig.1(b) shows the thermal analysis results with the titania gel containing MPO as the ligand. In this case, the specimen continuously loses weight until it is heated to 500°C or so. There are four exothermic peaks at 148°, 257°, 371°, and 484°C, each corresponding to a characteristic weight loss. These also result from the combustion of alkoxy group or MPO. Therefore, it is considered that organic matter is still present in the TiO_2 film until it is heated to around 500°C, but is no longer present at higher temperatures, when MPO is used as the organic ligand.

3.2. TiO_2 Film over Glass Substrate

Figure 2 shows the effects of firing temperature on the refractive index of the TiO_2 thin film formed over the glass substrate. As shown in the figure, the relationship between refractive index and firing temperature is affected by the organic ligand used. The refractive index of the ligand-free film increases almost linearly with firing temperature. That of the MEE-containing film increases with firing temperature at a lower rate beyond 500°C. However, its refractive index is higher than any other film prepared in this study at the same firing temperature. The refractive index of the film derived from the TME-containing sol is essentially constant up to 500°C, irrespective of firing temperature, but increases rapidly with temperature thereafter. That of the film derived from the MPO-containing sol increases with firing temperature moderately at up to 510°C but increases

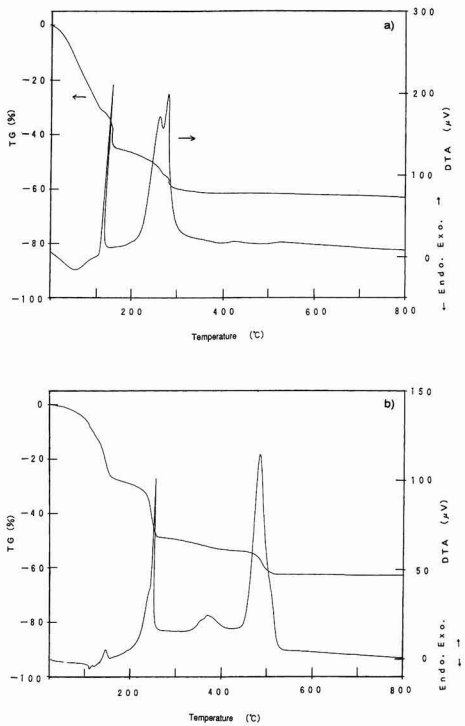

Fig. 1.(a) DTA and TG curves of titanium oxide gel prepared by the hydrolysis of $Ti(O\text{-}i\text{-}Pr)_4$ reacted with 2-(2-methoxyethoxy) ethanol (MEE) ligand.
(b) DTA and TG curves of titanium oxide gel prepared by the hydrolysis of $Ti(O\text{-}i\text{-}Pr)_4$ reacted with 2-methyl-2, 4-pentanediol (MPO) ligand.

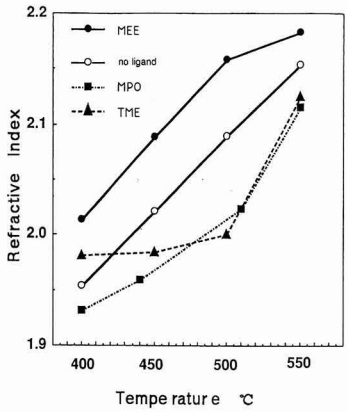

Fig. 2. Refractive indices of TiO_2 films fired at various temperatures prepared by the hydrolysis of Ti(O-*i*-Pr)$_4$ reacted with several ligands (MEE, MPO, trimethylene glycol monomethyl ether (TME)) and Ti(O-*i*-Pr)$_4$ only on the glass substrates.

rapidly with temperature thereafter. It has the lowest refractive index up to 440°C among the thin films prepared in this study.

In order to investigate the causes for the change in refractive index of the TiO_2 film according to organic ligand, X-ray diffraction analysis was conducted for the thin films prepared at various firing temperatures. **Figure 3** contains the X-ray diffraction patterns of the ligand-free thin films, and **Figs.4** through **6** contain those from the ligand-containing sols. The crystalline phase and peak intensity change depending on the type of ligand used. The large peaks at 2θ=25.3° and 27.4° are relevant to anatase (101) and rutile (110), respectively.[6] These peaks are discussed in detail below:

Figure 3 shows that the anatase peak increases in intensity as firing temperature increases, suggesting growth of the anatase phase. Fig.4 shows the X-ray diffraction patterns of the TiO_2 film derived from the MEE-containing sol as the organic ligand. The peak relevant to anatase is clearly found at as low as 400°C, increasing in intensity as firing temperature increases. Thus, it also shows growth of the anatase phase. On the other hand, the TiO_2 thin film containing TME or MPO as the organic ligand, behaves differently, as illustrated in Figs.5 and 6. For the thin film containing TME, the anatase phase changes little in intensity at 400° to 550°C, and no growth of the anatase phase is suggested by the X-ray diffraction analysis results. On the other hand, for the thin film derived from the MPO-containing sol, no anatase peak is found at 440°, and TiO_2 remains amorphous at this temperature level. The peak relevant to the anatase crystal starts to appear at around 510°C.

In any case, the thin film is thicker at 550°C by 10 to 15% than at 400°C and is densified as firing temperature increases.

The TiO_2 thin film derived from the MEE-containing sol has the highest refractive index among those prepared in this study. These results are in good agreement with the X-ray diffraction analysis results. The peak relevant to the anatase phase starts to appear at around 400°C and increases in intensity as firing temperature increases, suggesting growth of the crystalline phase with firing temperature. The derived from the MEE-containing sol film shows the highest refractive index compared to any other because the growth of the anatase phase starts at a lower temperature and is densified with firing temperature.

The film derived from the MPO-containing sol shows a lower refractive index than the others up to 440°C because the TiO_2 is amorphous. An increased refractive index at above 510°C corresponds to the peak of anatase appearing at such temperature. Thus, it is apparent that increased refractive index results from the crystallization of TiO_2.

The refractive index of the film derived from the TME-containing sol is kept low and is essentially constant up to around 500°C, in spite of the crystallization of TiO_2 into the anatase phase at as low as 400°C. These results are in

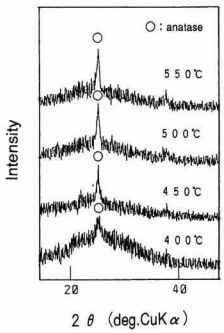

Fig. 3

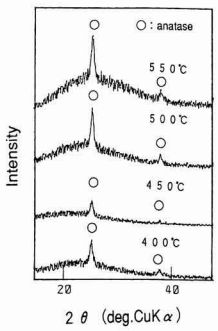

Fig. 4

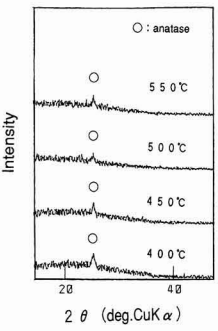

Fig. 5

Fig. 3. X-ray diffraction patterns of TiO_2 films fired at various temperatures prepared by the hydrolysis of Ti(O-*i*-Pr)$_4$ only on the glass substrates.

Fig. 4. X-ray diffraction patterns of TiO_2 films fired at various temperatures prepared by the hydrolysis of Ti(O-*i*-Pr)$_4$ reacted with MEE ligand on the glass substrates.

Fig. 5. X-ray diffraction patterns of TiO_2 films fired at various temperatures prepared by the hydrolysis of Ti(O-*i*-Pr)$_4$ reacted with TME ligand on the glass substrates.

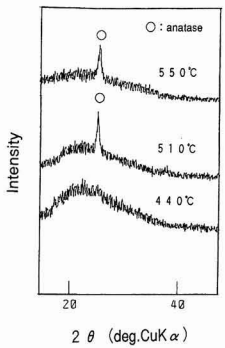

Fig. 6. X-ray diffraction patterns of TiO_2 films fired at various temperatures prepared by the hydrolysis of Ti(O-*i*-Pr)$_4$ reacted with MPO ligand on the glass substrates.

agreement with the X-ray diffraction analysis results because the intensity of the anatase peak is low and remains essentially unchanged in the temperature range from 400° to 500°C. There are a number of small pores, approximately 1μm in diameter, on the surface fired up to 500°C, as shown in **Fig.7**a. However, these pores disappear when firing temperature is increased to 550°C (Fig.7b). No such phenomenon is observed with the other films prepared in this study. The essentially constant refractive index of the films derived from the TME-containing sol fired up to 500°C will result from the presence of these small surface pores. It is observed that increasing the firing temperature to 550°C removes these pores from the surface to density the specimen, which is accompanied by an increased refractive index.

These results indicate that the ligand affects the structures of the titania sol and TiO_2, and changes refractive index of the thin film. In other words, the ligand can be used to control refractive index.

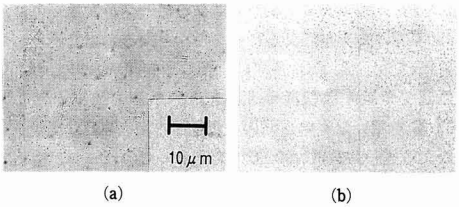

Fig. 7. Microscope photographs of TiO_2 film's surface derived from Ti(O-*i*-Pr)4 and TME ligand, (a) fired at 500°C, (b) fired at 550°C.

3.3. TiO_2 Thin Film on Silicon Wafer

There are two types of crystalline TiO_2, anatase and rutile. The phase transformation between these two types depends on starting materials, synthesis process, and conditions, which change the temperature at which the phase transformation starts.[7] In order to clarify the effects of the ligand on phase transformation temperature, the TiO_2 thin film is formed on a silicon wafer, which is much more resistant to heat than soda lime glass. The synthesized titania sol, coated on a silicon wafer, is fired at 700° to 900°C to form the TiO_2 thin film, and the expression of the anatase and rutile phases are followed by X-ray diffraction analysis.

Each specimen shows characteristic changes as firing temperature is increased from 700° to 900°C.

Figure 8 presents the X-ray diffraction patterns of the ligand-free film. The anatase peak dominates the rutile peak up to 800°C. However, this relationship is reversed at 900°C, and the peak of the rutile phase observed at this temperature is more intense than any anatase peak observed.

Figure 9 presents the patterns of the TiO_2 thin film derived from the MPO-containing sol as the ligand. The anatase to rutile phase transformation occurs in this system at

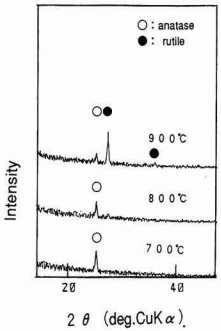

Fig. 8

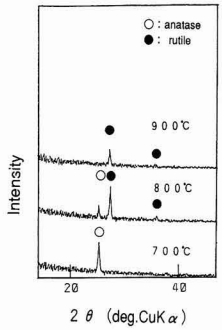

Fig. 9

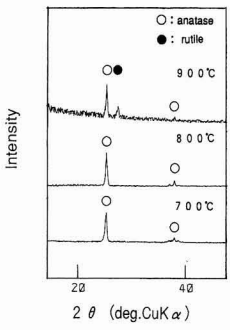

Fig. 10

Fig. 8. X-ray diffraction patterns of TiO_2 films fired at various temperatures prepared by the hydrolysis of Ti(O-*i*-Pr)$_4$ only on the silicon wafer substrates.

Fig. 9. X-ray diffraction patterns of TiO_2 films fired at various temperatures prepared by the hydrolysis of Ti(O-*i*-Pr)$_4$ reacted with MPO ligand on the silicon wafer substrates.

Fig. 10. X-ray diffraction patterns of TiO_2 films fired at various temperatures prepared by the hydrolysis of Ti(O-*i*-Pr)$_4$ reacted with MEE ligand on the silicon wafer substrates.

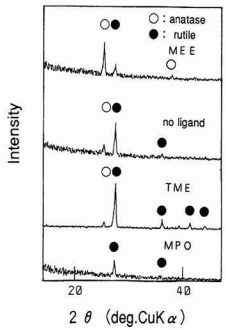

Fig. 11. X-ray diffraction patterns of TiO_2 films fired at 900°C prepared by the hydrolysis of Ti(O-*i*-Pr)$_4$ with several ligands (MEE, MPO, TME) and Ti(O-*i*-Pr)$_4$ only on the silicon wafer substrates.

a lower temperature than in the ligand-free film. A similar trend is observed with the thin film derived from the TME-containing sol; the rutuile peak starts to appear at 800°C and dominates the anatase peak clearly at 900°C. The effects of ligand to lower the temperature at which the rutile phase starts to appear are also observed in the other systems. For example, the thin TiO_2 film formed on a silicon wafer, derived the sol containing diethanol amine as the ligand, has only the anatase peak when fired at 500°C. However, it has both the anatase and rutile peaks when fired at 600°C, as revealed by X-ray diffraction analysis. Thus, phase transformation occurs at temperature somewhere between 550° and 600°C.[6] Each of the ligands used in this study causes the phase transformation to occur at a higher temperature than diethanol amine. MPO lowers the temperature at which the phase transformation starts more extensively than any other ligand used in this study, but only to 800°C. This may be attributable to the difference between diethanol amine and glycol in the chemical structure and property changes caused thereby, which affect the structures of the ligand-containing sol and gel.

The thin film derived from the MEE-containing sol as the ligand behaves differently (**Fig.10**). In this case, only the anatase peak is observed at up to 800°C, and the rutile peak is very weak even in the film fired at 900°C. Thus, the transformation to the rutile phase is controlled. **Figure 11** summarizes the X-ray diffraction patterns of the thin films fired at 900°C. The anatase phase is transformed into the rutle phase as firing temperature increases in the ligand-free film. The rutile phase accounts for most of the crystalline phases, with only small quantities of the anatase phase left in the film fired at 900°C. The anatase to rutile phase transformation is accelerated when TME is used as the ligand. The accelerated transformation is more apparent with MPO because essentially no anatase phase is left in the film.

On the other hand, MEE as the ligand works to decelerate the phase transformation because the anatase phase is still the major crystalline phase even at 900°C, which is a firing temperature level which causes the phase transformation extensively in the other systems, and there is only a trace quantity of the rutile phase observed.

These results indicate that the organic ligand can be used to control the crystalline phases of TiO_2. In other words, it is possible to selectively form the anatase and rutile phases in the thin TiO_2 film.

4. Conclusion

The TiO_2 thin films are prepared by the sol-gel process, using glycols and the ether derivative (MEE, MPO and TME) as the ligands, in order to investigate the effects of these ligands on refractive index and the crystalline phases of the thin films.

1) The TiO_2 thin film formed on a soda lime glass substrate varies in temperature-dependence of refractive index, depending on the ligand type used.

2) The thin film formed on a soda lime glass substrate also varies in anatase peak intensity, depending on the ligand. This change corresponds well to the change in refractive index.

3) The thin film formed on silicon wafer varies in anatase and rutile peak intensity, depending on the ligand.

4) It is possible to control the refractive index and the crystalline phases of the TiO_2 thin film by carefully selecting the ligand.

References:

1) C.J. Brinker and G.W. Scherer, Sol-Gel Science, Academic Press (1990); D. Segal, Chemical Synthesis of Advanced Ceramic Materials, Cambridge University Press (1989).
2) F. Mizukami, Kagaku to Kogyo, 42, 875-877 (1989); F. Mizukami, Petrotech, 12, 728-733 (1989); F. Mizukami, Proc. I.E.J., 14, 376-381 (1990).
3) K. Maeda, F. Mizukami, S. Miyashita, S. Niwa and M. Toba, J. Chem. Soc., Chem. Commum., 1990, 1268-1269 (1990).
4) B.E. Yoldas, App. Optics, 21, 2960-2964 (1982).
5) T. Yokoo, K. Kamiya and S. Sakka, Denkikagaku, 54, 284-285 (1986); T. Yoko, K. Kamiya and S. Sakka, Yogyo Kyokaishi, 95, 150-155 (1987).
6) Y. Takahashi and Y. Matsuoka, J. Mater. Sci., 23, 2259-2266 (1988).
7) Fain Seramikkusu Jiten, Gihodo Shuppam (1987) 309.

This article is a full translation of the article appearing in Journal of the Ceramic Society of Japan (Japanese version), Vol.100, No.9, pp.1122-1126, 1992.

Synthesis of Si-O-C Fibers from Rice Husk Carbide
–Explanation of Formation Condition–

Katsuyoshi Shimokawa, Itsuma Sekiguchi, Yoshikazu Suzuki and Yoshinobu Ueda

Government Industrial Development Laboratory, Hokkaido
2-17, Tsukisamu-Higashi, Toyohira-ku, Sapporo-shi, 062 Japan

In our previous studies, ceramic materials were synthesized by reactions of oxy-silicate minerals such as Siliconoxide (SiO_2), Talc ($3MgO{\cdot}4SiO_2{\cdot}H_2O$), Olivine ($2(Mg, Fe)O{\cdot}SiO_2$) and Chlorite ($H_4Mg_2Al_2SiO_9$) with carbon, or obtained from carbide of rice husk which is one on natural organic materials. In the previous report, a ceramic fiber with a two or three-layered structure was synthesized; each layer has different concentrations of constituents, Si, O, and C. The aspect ratio of the fiber was large. The yield of the ceramic fiber, however, was small. In this study, an attempt to find suitable experimental conditions for greater yield and homogeneous definite quality of the ceramic fibers was carried out. In addition, the reaction mechanism from rice husk carbide to the fiber was investigated. The obtained optimum conditions were as follows. (1)Reaction temperature was 1480°C; (2) the ratio of mixing N_2 and H_2 was 1:2 in volume; (3) the linear velocity of gas flow was about 0.7cm/sec. A gaseous reaction of SiO with CO was clearly shown to be responsible for the production of the ceramic fibers, in comparison with the experiments using standard samples and gases such as Si, SiO and SiO_2, and Ar, N_2, H_2, CO and CO_2.

[Received February 3, 1992; Accepted May 21, 1992]

Key-words: SiO_xC_y fiber, SiO+CO reaction, Vapor phase reaction, Rice husk, SiC fiber, SiO_x fiber, Mechanism of fiber production

1. Introduction

A number of researchers have been attempting the synthesis of various types of ceramic materials from silicon-containing, natural minerals and rice husk. On the other hand, ceramic fibers have been used as the reinforcing agents for various composite materials.

While attempting to synthesize ceramics from silicate-containing minerals and rice husk carbide, the authors have discovered the ceramic fibers consisting of three elements of silicon, oxygen, and carbide, which are prepared by the vapor-phase reactions.[1] These fibers are not mixtures of SiC and SiO_2; they are of Si-O-C compounds having chemical structures from SiC to SiO_2. Each fiber is a two- or three-layered cylinder with a high aspect ratio. The reactions involved, though they are anticipated to be similar to those for the synthesis of SiC and Si_3N_4, have not been fully investigated in order to understand the conditions under which they are formed because of insufficient quantities of the fibers produced so far. In this study, the authors have investigated several parameters, which are considered to enhance fiber yield, in order to clarify the relationships between synthesis conditions and fiber properties, and between the fiber formation and reactions.

2. Experimental Procedure

2.1. Synthesis of Si-O-C Fibers

The starting material was commercial rice husk carbide, which was baked at 350° to 400°C and crushed to 100 meshes or less. Rice husk carbide (abbreviated to RHC or (SiO_2 + C)) has an elementary composition of 56.63wt%carbon; 1.82wt%hydrogen; 7.47wt%oxygen; and 0.45wt%nitrogen. Its silica content is 32.61wt% on a dry basis, as determined by the industrial analysis (JIS M-8812). The standard specimens were prepared in order to investigate the reaction mechanisms; Si(99.99%), SiO (99.9%) and SiO_2 (Aerogil silica), all supplied by commercial reagent as the silicon sources, and commercial carbon black as the carbon source. Each reaction gas (Ar, N_2, H_2, CO and CO_2) was 99.9% up to pure and was passed directly into the reaction system.

Figure 1 illustrates the test apparatus, where the porcelain reactor tube, 28mm in diameter and 1m in length, is placed, horizontal type electrical oven and is completely separated from the atmosphere. The Si-O-C fibers are formed in rings on the reactor tube walls approximately 15cm apart from the reactor tube center. The temperature is 1500°C at the reactor center and 1200°C at the position where the fibers are formed. They are found to grow towards radial direction in the reactor tube. The temperature distributions within the reactor tube are predetermined to find, without using thermocouple, the temperature levels at the positions where the specimen is located and the fibers are deposited. Each reaction gas is controlled at a constant flow rate by a mass flow controller. Part of the effluent gas is recycled back to the reaction system via the sample inlet nozzle for the gas chromatograph. A trace quantity of gas is recirculated by a small-size dry vacuum pump in order to minimize differential pressure and turbulence, which may occur as a result of the effluent recycling. The effluent gas total volume and are periodically measured by a dry gas

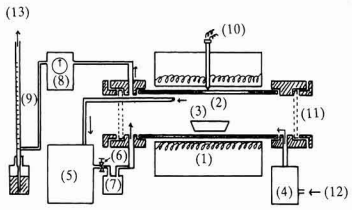

Fig. 1. Apparatus for synthesis of ceramic fiber. (1) Furnace, (2) Reactor, (3) Sample, (4) Gas flow meter, (5) Gas chromatograph, (6) Needle valve, (7) Dry vacuum pump, (8) Dry gas meter, (9) Lather flowmeter, (10) Thermocouple, (11) Window, (12) Gas inlet, (13) Gas outlet.

meter and a lather flow meter that determines flow rate by the movement of soap film.

Approximately 1g of the specimen, rice husk carbide or the standard specimen (Si, SiO or SiO_2), is put in a mullite boat and placed at the center of the reactor tube. The reactor system is sufficiently purged with the reaction gases (Ar, N_2, H_2, CO and CO_2), either alone or in mixture for example N_2:H_2=1:2 volume, and are then flown at a given rate (0 to 60ml/min). The zero gas flow rate means that the gases are contained in the reactor tube after the reactor is purged with these gases. They are heated at 30°C/min to 1200°C and at 10°C/min thereafter. The reaction temperature is 1440° to 1550°C, at which they are held for changable 30min to 4hrs for the reactions. The product is cooled from the reaction temperature to 800°C in 2h and then allowed to cool naturally. A given, trace quantity of gas is flown into the reactor system upon completion of the reaction step, until the reactor system is cooled to near room temperature in order to prevent inflow of air. After being cooled, the product is withdrawn from the reactor tube for analysis. The synthesized fibers are treated by a muffle furnace at 650°C for 2h in air when free carbon or hydrocarbon compounds are to be removed from the fibers.

2.2. Observation and Analysis of Si-O-C Fibers

The synthesized fibers are observed by scanning electron microscope (SEM) and transmission electron microscope (TEM, Hitachi, H-800NA Model, 200kV) for their shapes. The crystalline structures are identified by a powder X-ray diffractometer (XRD, Rigaku Denki) using CuKα. The thermal analysis is made using a differential thermal balance (DTA-TG, Rigaku Denki), where the specimen is heated at 10°C/min. The elementary analysis for carbon and oxygen present in the fibers is made by an O/N Analyzer EMGA-550 and C/S Analyzer EMIA-511 (Horiba). The effluent gas is analyzed by gas chromatography; adsorbent: molecular sieve 5A, activated charcoal, and Porapak-Q (column size: 3mm in diameter, 3m long, column temperature: 100°C, respectively), carrier gas: Ar flown at 50ml/min.

3. Results and Discussion

3.1. Optimal Conditions for Si-O-C Fiber Production

Figure 2 illustrates the effects of reaction temperature and reaction gases on the production of the fibers, where the amount of fiber is its percentage weight of the quantity of SiO_2 present in the starting material. In the cases of Ar and N_2 gases, each gas is contained in the reactor tube (referred to as STOP). In the case of N_2 + H_2 (1:2 by volume), the mixture is passed to the reactor tube at 30ml/min. The fiber amount increases with reaction temperature in all cases. It is also found that a trace quantity of H_2 gas provides more than twice the amount as Ar or N_2, and that the fiber amount changes with reaction temperature more moderately in the case of the N_2/H_2 mixture than in any other system. This indicates that the fiber is formed more stably over a wide reaction temperature range with the mixed gas. It is particularly noted that the N_2/H_2 mixture provides a high product yield, although N_2 gas alone gives only a small amount of the fiber. By this it is meant that H_2 plays a vital role for production of the fibers, for example by accelerating reduction of the SiO_2 component.

Figure 3(a) presents the macrograph, and Fig.3(b) presents the SEM image of the ceramic fibers thus prepared. The fibrous product is formed over the reactor tube walls kept at around 1150°C in any case, growing radially from the walls to the tube center in such a way to plug the tube. The SEM image given in Fig.3(b) indicates that the product fiber has a high aspect ratio. **Figs.4**(a) and (b) contain the representative X-ray diffraction patterns of the fibrous product, as-prepared and as-fired at 800°C in air, respectively. Each product has the similar patterns, irrespective of reaction gases used. Peak A is relevant to the Si-O-C fiber, as reported previously.[1] The peaks relevant to other crystals are also found, such as β-SiC and trace quantities of α-cristobalite at 2θ=22.8°C, which are mostly of microcrystalline fibers. They change little, when fired at 800°C for 1h in air.

Figure 5 shows the effects of reaction time on fiber amount, which increases linearly with reaction time in all cases of reaction gas used. It is approximately 85% of the amount of SiO_2 present in the starting material when it is reacted with H_2 gas flown at 20ml/min for 4h. The N_2/H_2 mixture also produces a high fiber yield.

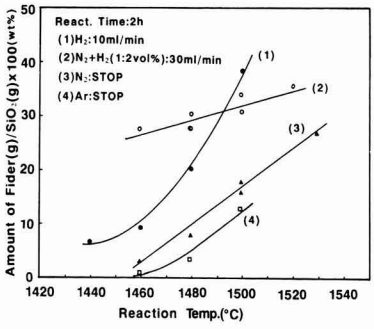

Fig. 2. Effects of reaction temperatures on producing amount of ceramic fiber.

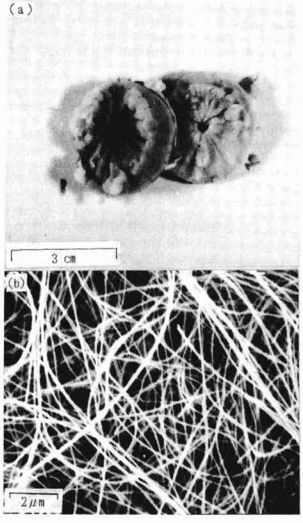

Fig. 3. Micrograph (a) and the SEM image (b) of ceramic fiber.

Figure 6(a) and (b) show the photographs of the fiber specimens prepared at 1480°C for 2h and 1520°C for 2h, respectively, **Figs.7**(a) and (b) show the SEM images of the specimens prepared at 1520°C for 2h and 1550°C for 2h, respectively. The product is soft, elastic, and sponge-like when prepared at 1480°C (Fig.6(a)), irrespective of gas atmosphere. On the other hand the product shown in Fig.6(b) is a hard, plate-shape fiber, which is low in elasticity. The SEM image presented in Fig.7(a) shows that part of the fiber becomes thin and fragile, and that in Fig.7(b) shows the fiber whose surface starts to melt, suggesting that the fiber will lose its inherent properties when exposed to high temperatures. However, no significant change is observed on the fiber surface which is exposed to high temperatures, as long as the retention time is sufficiently short. Thus, the properties of the fiber change with time when its surface is heated by radiation heat. In other words, it is necessary to allow the reactions to proceed slowly at relatively low temperatures, or to devise special installation, such as heat-shielding plate, in order to prevent the fibers from being exposed to high temperatures when high temperature should be used to produce elastic fibers.

Figure 8 shows the effects of gas flow rate on the amount of fibers produced. This figure shows the results under the conditions of 1500°C and 2h. With Ar or N_2 as the reaction gas, the fiber amount is less when gases are flown than when gases are closeted in the reactor tube. It corresponds to 5wt% or less that of SiO_2 present in the starting material when the gas flow rate exceeds 30ml/min. On the other hand, with the H_2 or N_2/H_2 mixture, the flow system gives at least the same amount as does the batch system. The fiber is formed in a narrow gas flow rate range, attaining a maximum at 30 to 40ml/min. With H_2 gas flowing at 40ml/min or more, a nearly grey, slag type fiber is produced, which contains trace quantities of α-cristobalite, silicon, and β-SiC. It is thus desirable to maintain the gas flow rate at around 40ml/min, or about 0.7cm/sec as linear velocity, to produce the fibrous product at a high yield.

3.2. Thermal Changes of the Fibers

The fibers synthesized are investigated whether they are affected by radiation heat or the reaction product gases, such as CO and CO_2, to change their physical properties, and whether they are amenable to oxidation. Their thermal behavior is analyzed by a differential thermal analyzer, where the specimen is heated either in air or in Ar gas atmosphere. The fiber possibly contains amorphous SiC or Si_3N_4 fibers,[1] and their thermal analysis results are compared to those for the β-SiC and α-Si_3N_4 whiskers produced from the same starting material of rice husk carbide. The results are given in **Fig.9**. The specimens for the analysis are those prepared at 1480°C for 2h with Ar, N_2, and N_2/H_2 mixture, which are untreated fibers selected from the portion containing minimum quantity of free carbon.

The specimen prepared with N_2 gas has an exothermic

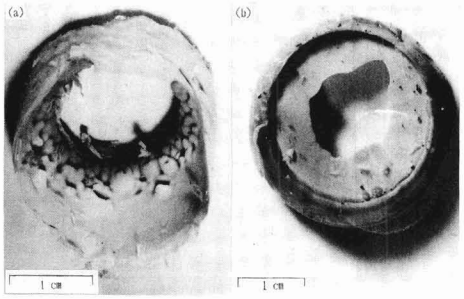

Fig. 6. Photographs of ceramic fiber synthesized; (a) at low temperature (1480°C), and (b) high temperature (1520°C).

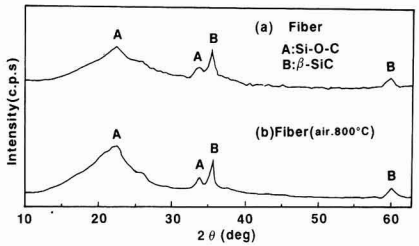

Fig. 4. XRD patterns of fiber (a), and calcinated (a) at 800°C in air (b).

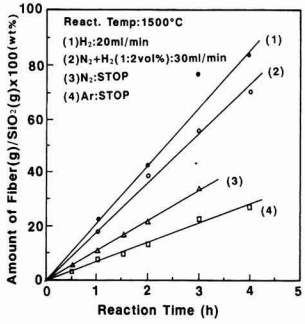

Fig. 5. Effects of reaction times on producing ceramic fiber.

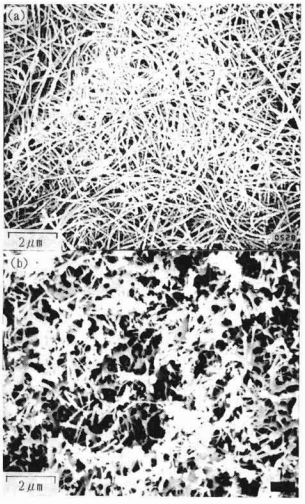

Fig. 7. SEM photographs of ceramic fiber synthesized; (a) at 1520°C for 3h in N_2, (b) at 1550°C for 2h in N_2.

peak at around 1083°C, resulting from oxidation, and it increases in weight by 9.46wt%. That one prepared with Ar has an exothermic peak at around 1075°C, showing a weight increase by 9.61wt%. Thus, they are close with respect to the temperature at which the fiber is formed and oxidation starts. Similar trends are observed for the fiber prepared with N_2/H_2 mixture.

Each of these fiber specimens contains cristobalite, judging from the temperature at which the exothermic peak develops, and is totally of cristobalite when heated to 1400°C.

The thermal analysis is also made for the fiber prepared in an inert gas atmosphere (Ar flowing at 20ml/min) to establish the DTA-TG curves. It has a small, broad, exothermic peak at 875°C which is not accompanied by weight change, and a small, broad peak at 1285°C which is accompanied by a weight increase (1.16wt%). The latter peak is conceivably a resulting from the exothermic reactions. However, these peaks are not fully understood at this stage of time. However, it is observed that the fiber changes little both in color and shape at up to 1350°C in the inert gas atmosphere and that no cristobalite is detected in the as-prepared fiber. On the other hand, at higher temperatures, reduction in volume and sintering of the fibers are observed, and cristobalite is found locally.

The β-SiC fiber increases in weight by 23.06wt% in an oxidative atmosphere as a result of the exothermic reactions represented by the peaks at 1225° and 1333°C. On the other hand, the Si_3N_4 specimen gradually increases in weight from about 1200°C or so, eventually increasing by 7.46wt%, accompanied by the exothermic reactions occurring at 1388°C. This suggests that it is oxidized. The fibrous product prepared in this study thus shows DTA-TG curves clearly different from those of the SiC or Si_3N_4 fiber; it is gradually oxidized from around 1000°C in air.

Based on the results previously discussed, it is considered that the fiber consists of silicon, oxygen, and carbon, which may be represented by the chemical formula SiO_xC_y (x: 0 to 2, y: 1 to 0). However, its molecular structure as a whole is indefinite because its chemical composition differs by each fiber.

Elementary analysis is conducted to determine the carbon and oxygen contents of the fibers product. They fluctuate fairly widely, 3.50 to 7.50wt%Carbon and 42.50 to 43.28wt%Oxygen, respectively. Based on this, its average molecular composition may be represented by the formula $Si_{1.0}O_{1.5}C_{0.25}$(or Si_4O_6C).

One may discuss the oxidation-induced weight increase presented earlier based on the above assumed chemical composition.

$$Si_4O_6C\,(s) + 2O_2\,(g) \rightarrow 4SiO_2\,(s) + CO_2\,(g) \quad . (1)$$

The oxidation-induced weight increase of 9.06wt% is derived from the above equation. It is observed that the synthesized fiber increases in weight by about 9.5wt% at up to 1400°C, as predicted from the TG curve. These values are in agreement with each other, and the weight increase is considered to be related to the assumed chemical composition.

3.3. Formation of Fiber and Product Gases

The reactions to produce the fibers are considered to be similar to those leading to the production of SiC or Si_3N_4, based on the starting material composition and gas atmosphere in which they are synthesized. One of the most important parameters in the synthesis of these is oxygen in SiO_2 as the starting material. Various cases in the synthesis of the fibers from rice husk carbide and standard specimen are discussed from the angle of the product gases.

Figure 10 shows the typical gas composition and its change with time, as analyzed at the outlet of the test apparatus. The results for the fatch system in which N_2 gas is contained at 1480°C are shown. The product gases in this case are H_2 and CO, of which H_2 is produced by the reactions as well as decomposition of the hydrogen-containing components present in the starting material. At a reaction temperature of 1300°C or higher, production of these gases is accelerated with temperature. However, production of H_2 has a maximum reaction time at a given temperature level, decreasing thereafter. On the other hand, the CO content increases at a given temperature, though slightly. However, when the reactions are completed, H_2 content decreases continuously, whereas CO content shows a rapid increase. In contrast, the N_2 content decreases as temperature increases, and is constant at a level in a reaction temperature range. The reactions to form Si_2ON_2, Si_3N_4, or SiC generally proceed in the system in which SiO_2 + C and N_2 are present at as high as 1480°C. Thus, the N_2 content is considered to decrease continuously in such a system. However, in the system of this study, it is constant while the reactions are retained. This should be considered relative

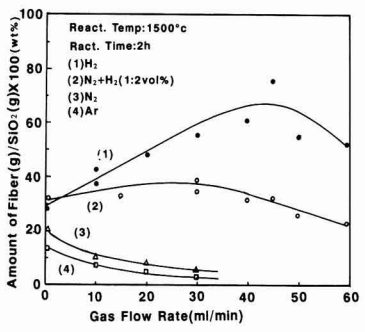

Fig. 8. Effects of gas flow rates on producing ceramic fiber.

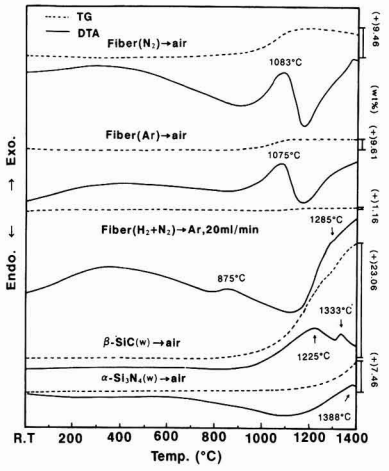

Fig. 9. Results of DTA-TGA of ceramic fiber.

to other compositions, in particular with that of CO. When the reaction system is being heated, it is also observed that a trace quantity of C_2H_2 is detected at below 500°C, and that the CO_2 content, attaining a maximum at 750°C, disappears above 1250°C. Furthermore, the CH_4 content attains a maximum at 1000°C, and it is detected, although in trace quantities still at 1480°C. No O_2 is detected at any temperature level.

Figure 11 shows the product gas composition and its change with time for the system in which the H_2 gas, which gives the fibrous product at a high yield, is contained in the reactor tube (STOP run). The CO content increases to a high level of 30% or more, which is approximately 2 times that of the N_2 (STOP) system and more than 4 times that of the Ar (STOP) system. A large quantity of fibers is formed in this H_2 (STOP) system, from which it is judged that CO plays a vital role in the formation of the fibers. In addition, a trace quantity of CH_4 is detected in this system. This results from decomposition of the starting material at low temperature and also from methanation by C and H_2 or by CO_2 and H_2 at high temperatures. CH_4 is also considered to play some positive role in the formation of the fibers.[2,3]

Figure 12 shows the typical X-ray diffraction patterns of the residue in sample boat. β-SiC is the only product in the (a) RHC + H_2 (STOP) system, where the quantity of fibers formed is 21.6wt%. In the (b) RHC + N_2 (STOP) system, the quantity of fibers formed is 14.0wt%, where Si_2ON_2, β-SiC and α-cristobalite are formed, as indicated by the X-ray diffraction analysis results. However, Si_3N_4 is not formed.

Next, the role of H_2 in the reaction process is investigated. SiO, the standard specimen, is used as the Si source and carbon from CO as the carbon source. The starting material is reacted with a mixture of H_2 and CO (70/30) at 1480°C, where the gas mixture is flown at 10ml/min. The quantity of fibers formed is approximately 25wt%. **Figure 13** shows the gas composition and flow rate changing with time. Increasing the reaction temperature from 1300°C decreases the CO gas composition and increases the H_2 gas composition.

Gas flow rate decreases to almost half while the reaction temperature is held at 1480°C, and then it becomes constant. This means that approximately 50% of the gases are consumed by the reactions with SiO, for the formation of SiC, SiO_2 and the SiO_xC_y fibers. The H_2 gas composition increases, relatively by quantity of CO consumed. However, its absolute quantity remains essentially unchanged. **Figure 14** shows the X-ray diffraction patterns of the residue. α-cristobalite and β-SiC are detected, suggesting that SiO is oxidized by flowing excessive quantity of CO. Production of the fibers is accelerated in the presence of H_2, suggesting some catalytic actions of H_2.

3.4. Formation of Si-O-C Fibers

Based on the effluent gas composition changing with time and the analysis results of the residue, it is considered that the conditions under which the fibers are massively formed are deeply related to the behavior of the gaseous species, such as SiO and CO.

Therefore, it is necessary to investigate formation of the gaseous species, in consideration of the interactions between the chemical species, such as SiO_2, C, CO, H_2, and N_2.

In order to substantiate the above concept, the fibers are produced with the standard specimens of Si, SiO and SiO_2 as the silicon sources, and solid carbon, CO and CO_2 as the

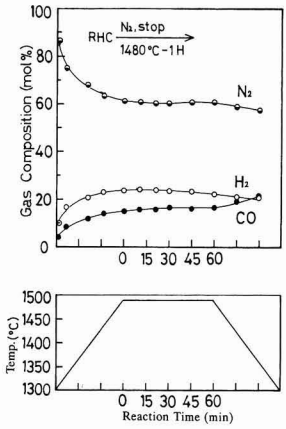

Fig. 10. Changes of gas composition with passage time at each of reaction temperature.

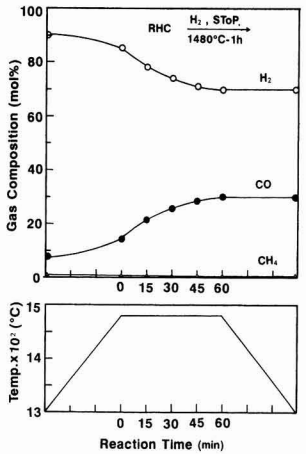

Fig. 11. Changes of gas composition with passage time at each of reaction temperature.

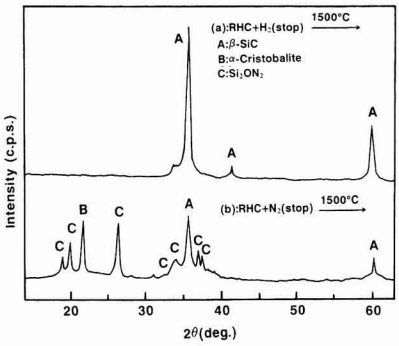

Fig. 12. XRD of residual sample; (a) after reaction in H_2 (stop), (b) after reaction N_2 (stop).

carbon sources. **Table 1** shows the relationships between the residue composition and the amount of fibrous product, which are the results of X-ray diffraction analysis of the residues, where Si-O-C fiber (wt%) means its amount relative to that of SiO_2 for any type of the starting material. The results shown in Fig.14 for Run 7, in which SiO as the starting material is treated with the H_2/CO mixture, are also shown in Table 1 for comparison.

When Si is used as the silicon source (Runs 1 to 3), no fibrous product results with any reaction gas.

The possible reactions with Si are listed below:

$$Si\,(s) + C\,(s) \rightarrow SiC\,(s) \quad \ldots\ldots\ldots\ldots (2)$$

$$Si\,(s) + CO\,(g) \rightarrow SiO\,(g) + C\,(s) \quad \ldots\ldots (3)$$

$$Si\,(s) + 2CO\,(g) \rightarrow SiC\,(s) + CO_2\,(g) \quad \ldots (4)$$

$$Si\,(s) + CO_2\,(g) \rightarrow SiO\,(g) + CO\,(g) \quad \ldots\ldots (5)$$

$$Si\,(s) + 2CO_2\,(g) \rightarrow SiO_2\,(s) + 2CO\,(g) \quad \ldots (6)$$

The reaction of Si with C (Run 1) produces β-SiC only by direct carbonization (Reaction (2)), as the sole product. In the case of CO (Run 2), the products are mostly β-SiC and a smaller quantity of α-cristobalite, for which Reactions (4) and (6) are responsible. However, the quantity of the product by the latter reaction should be minor because CO_2 is massively exhausted from the system. Reaction (3) will occur to only a negligible extent, if it occurs at all, because no fibrous product is observed. Similarly, Reaction (6) dominates Reaction (4) in the case of CO_2 (Run 3) because of forming SiO_2 much more than SiC.

When SiO is used as the silicon source (Runs 4 to 6), the fibrous product results, except for the case in which CO_2 is used as the carbon source.

The possible reactions, in addition to Reactions (3) and (5) described earlier, are listed below[2,4-6]:

$$SiO\,(s) + C\,(s) \rightarrow Si\,(s) + CO\,(g) \quad \ldots\ldots (7)$$

$$SiO\,(s) + 2C\,(s) \rightarrow SiC\,(s) + CO\,(g) \quad \ldots\ldots (8)$$

$$SiO\,(s) + CO\,(g) \rightarrow Si\,(s) + CO_2\,(g) \quad \ldots\ldots (9)$$

$$SiO\,(s) + 2CO\,(g) \rightarrow SiC\,(s) + CO_2\,(g) \quad \ldots (10)$$

$$SiO\,(s) + CO_2\,(g) \rightarrow SiO_2\,(s) + CO\,(g) \quad \ldots (11)$$

Reactions (7) and (8) occur in Run 4. Reaction (7) will help produce SiC and SiO_2 when Reactions (2) through (6) proceed. However, in this case, SiO_2 is formed to a smaller extent than SiC. Reactions (9) and (10) occur in Run 5, the resulting CO_2 being consumed by Reaction (11) and others to form SiO_2 and, to a smaller extent, SiC.

It is also considered that CO, which is either produced by the reactions of SiO(g) or added to the reaction system, will produce the SiO_xC_y compounds by the following reaction proceeding in a reducing atmosphere.

$$SiO\,(g) + CO\,(g) \rightarrow SiO_xC_y\,(g) \quad \ldots\ldots\ldots (12)$$

In the system for synthesizing SiC or Si_3N_4, a large quantity of Ar or N_2 is normally present, and the formed CO gas is immediately exhausted from the reaction system, with the result that SiC or Si_3N_4 is stably produced. On the other hand, the quantity of Ar or N_2 present in the system for Reaction (12) is relatively smaller, and a relatively larger quantity of CO gas formed is retained to support Reaction (12). In addition, SiO_xC_y as the vapor-phase product by Reaction (12) is precipitated when the temperature to around 1200°C. However, this compound is not of stoichiometric composition, consisting of silicon, oxygen and carbon

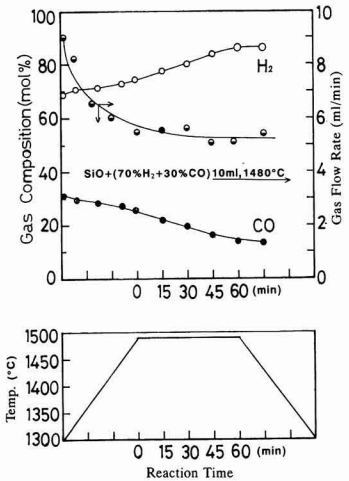

Fig. 13. Changes of gas composition and quantity with passage time at each temperature.

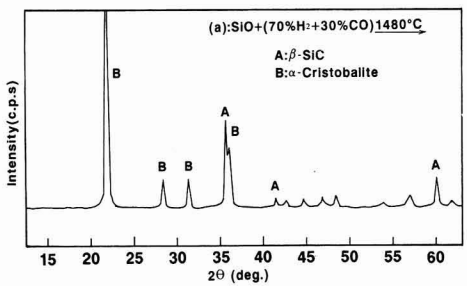

Fig. 14. XRD of residual sample after reaction of SiO + (70%H_2 + 30%CO) system at 1480°C.

Table 1. Relation between results of XRD of residual material in sample and amount of formed fiber in each of reaction systems.

	System	Gas Feed (ml/min)	Relative Intensity β-SiC (%)	α-Cri. (%)	α-Quartz (%)	Si (%)	* Si-O-C fiber (wt%)
1	Si + C	-	100	-	-	-	0
2	Si + CO	20	94	5	1	Tr	0
3	Si + CO_2	20	30	70	-	-	0
4	SiO + 2C	-	75	25	-	-	5.7
5	SiO + CO	20	20	80	-	-	20
6	SiO + CO_2	20	-	100	-	-	0
7	SiO+($H_2$70,CO30%)	10	30	70	-	-	25
8	SiO_2 + C	-	40	60	-	-	17
9	SiO_2 + CO	20	Tr	99	-	-	0
10	SiO_2 + CO_2	20	-	100	-	-	0

*Si-O-C fiber : amount of fiber(g)/SiO_2(g)×100(wt%)

whose contents vary depending on the atmosphere in which the compound is formed. For example, it will be oxygen-rich when formed in a CO_2-rich system.

SiO is formed in Run 4 by Reactions (3) and (5) to serve as the starting material for the fibrous product. However, it is consumed mostly for production of SiC and SiO_2 in a natural convection system, rarely for the fibers. On the other hand, in Run 5, it is supplied as the starting material and is also produced in a flow system to increase fiber yield.

In Run 6, in which CO_2 is used as the carbon source, cristobalite is formed by Reaction (11), and essentially no fibrous product results in an oxidative atmosphere.

With SiO_2 as the silicon source (Runs 8 to 10), no fibrous product is formed, except in the system in which solid carbon is used as the carbon source.

Run 8, in which solid carbon is used as the carbon source, produces SiC and SiO_2 by the following reactions, in addition to those already described:

$$SiO_2\,(s) + C\,(s) \rightarrow SiO\,(g) + CO\,(g) \quad \ldots\ (13)$$

$$SiO_2\,(s) + 2C\,(s) \rightarrow Si\,(s) + CO_2\,(g) \quad \ldots\ (14)$$

At the same time, a relatively large quantity of the fibrous product will be formed.

In Run 9, a small quantity of SiC is possibly formed by Reaction (15) which, however, will not proceed much, judging from quantity of SiC produced.

$$SiO_2\,(s) + CO\,(g) \rightarrow SiO\,(g) + CO_2\,(g) \quad \ldots\ (15)$$

Similarly, the above reaction rarely occurs in Run 10, where aerogil silica is crystallized. The product is transformed into α-cristobalite.

In Run 7, where hydrogen is used as one of the reactants, it seems that hydrogen works as the catalyst to accelerate production of the fibers. The rice husk carbide system will be represented by the above hydrogen-assisted system. In such a system, the following reactions will partly proceed:

$$C\,(s) + 2H_2\,(g) \rightarrow CH_4\,(g) \quad \ldots\ (16)$$

$$SiO_2\,(s) + CH_4\,(g) \rightarrow SiO\,(g) + CO\,(g) + 2H_2\,(g) \quad \ldots\ (17)$$

$$2C\,(s) + H_2\,(g) \rightarrow C_2H_2\,(g) \quad \ldots\ (18)$$

$$SiO_2\,(s) + C_2H_2\,(g) \rightarrow SiO\,(g) + 2CO\,(g) + H_2O\,(g) \quad \ldots\ (19)$$

$$C\,(s) + H_2O\,(g) \rightarrow CO\,(g) + H_2\,(g) \quad \ldots\ (20)$$

It is considered that hydrogen functions as the catalyst for these reactions to accelerate formation of the gaseous species, such as SiO and CO. This concept will support those shown in Fig.11 and will be one of the reasons for high reactivity of rice husk carbide.

The above reactions conceivably follows Reaction (13) and activates the following reaction in a flow of nitrogen:

$$2SiO\,(g) + N_2\,(g) + CO\,(g) \rightarrow Si_2ON_2\,(s) + CO_2\,(g) \quad \ldots\ (21)$$

At the same time, Reactions (2), (7), and (11) are activated to form the products such as Si_2ON_2, β-SiC and cristobalite. Furthermore, the fibrous product will be formed by Reaction (13). Reaction (21) will develop into Reaction (22), described below, at high temperature or in a reducing atmosphere, to produce Si_3N_4:

$$3SiO_2\,(s) + 6C\,(s) + 2N_2\,(g) \rightarrow Si_3N_4\,(s) + 6CO\,(g) \quad \ldots\ (22)$$

However, in the system investigated in this study, the reactions are not so developed to form silicon nitride but proceed to an extent of producing Si_2ON_2.

4. Conclusion

The authors have investigated the synthesis conditions under which fibrous SiO_xC_y compound is massively produced from rice husk carbide, as well as the mechanisms involved in the process, by analyzing the effluent gases and residue from the systems, where synthesized rice husk carbide and the standard specimens are used as the starting materials.

1) The yield of the fibrous product formed increases as operating temperature increases in the range tested (1440° to 1530°C). A small quantity of H_2, either alone or in combination with N_2, produces a higher yield (more than twice) than Ar or N_2 gas alone. At the same time, a N_2/H_2 mixture functions to stabilize the formation of the fibrous product over a wider temperature range.

2) The yield of the fibrous product increases linearly as reaction time increases in any reaction system tested. The presence of H_2, either alone or in combination with N_2, favors production of the fibrous product. Particularly noted is the greatly increased yield, to approximately 85wt%SiO_2, when the starting material is treated with H_2 alone for 4h.

3) The effects of gas flow rate are investigated in the range from 0 to 60ml/min. Ar or N_2 gas produces higher fiber yield when used in a batch system (gas flow rate: 0ml/min) than in a flow system. On the other hand, H_2 or N_2/H_2 mixture produces a higher yield in a flow system. The optimum gas flow rate range is fairly narrow, and the yield attains a maximum at 30 to 40ml/min.

4) The fibrous product is sponge-like and elastic when prepared at 1500°C or less, but it is dense and hard when prepared at 1520°C. Those prepared at higher temperatures have surfaces changed or sintered by radiated heat.

It is observed that the as-prepared product starts to deform gradually as a result of oxidation at around 1000°C in air. It maintains its inherent properties in an inert atmosphere, until it is heated to 1350°C.

5) Formation of the fibers is considered by the various systems using rice husk carbide and standard specimens as the starting materials, in which the effluent gases and residues are analyzed to postulate the possible reactions involved in the synthesis. As a result, it is concluded that the fibrous product SiO_xC_y is formed by the reactions between SiO and CO, and its composition varies depending on the gas atmosphere in which it is formed.

References:

1) K. Shimokawa, I. Sekiguchi, Y. Suzuki, K. Yabe and Y. Ueda, Seramikkusu Ronbunshi, 99,757-762 (1991).
2) E. Maeda, T. Funabashi and R. Uchimura, ibid., 97, 1505-1510 (1989).
3) K. Shimokawa, I. Sekiguchi, Y. suzuki and Y. Ueda, Hokkaido Oyo Chigaku Godo Kenkyukai Ronbunshu, 2, 26-36 (1991).
4) Y. Adachi, M. Sobue, S. Shinozaki, and J. Hangas, Seramikkusu Ronbunshi, 98 429-438 (1990).
5) H. Saito, T. Hayashi and K. Miura, J. chem. Soc. Jpn. 401, (1982).
6) H. Saito, T. Hayashi and K. Miura, ibid., 1371-1377 (1981).

This article is a full translation of the article appearing in Journal of the Ceramic Society of Japan (Japanese version), Vol.100, No.9, pp.1127-1134, 1992.

Preparation of Tazheranite Powders by Solid Phase Reaction and Conductivity of Sintered Bodies

Hideto Kuramochi, Hidehiko Kobayashi, Toshiyuki Mori,* Hiroshi Yamamura* and Takashi Mitamura

Department of Applied Chemistry, Faculty of Engineering, Saitama University
255, Shimo-Ohkubo, Urawa-shi, 338 Japan
*Tsukuba Research Laboratory, TOSOH Co.
43, Miyukigaoka, Tsukuba-shi, 305 Japan

$Ca_{0.20}Zr_{0.80-x}Ti_xO_y$ composition (x=0.04~ 0.25) powders, whose phases were the tazheranite (x=0.04~0.10) and the calzirtite (x=0.20) of single phases, were prepared at 1300°C for 10h by the solid phase reaction. The range of the tazheranite composition was broadened up to x=0.15 by firing them at 1500°C for 4~10h. The conductivity of the sintered bodies, fabricated at 1500°C for 4h in x=0.04~0.15 and 10h in x=0.20, was measured at 400°~900°C using the complex impedance method in the air. The activation energies of the conductivity were 120-130kJ/mol, thus it is presumed that the mechanism of the conductivity were 120-130kJ/mol, thus it is presumed that the mechanism of electric conduction was dominated by an oxygen ion conduction in the range of these temperatures. In the case of x=0.04~0.15 composition samples, the resistance of grain decreased with an increase of x, while that of grain boundary increased. With regard to the calzirtite (x=0.20) composition sintered body, it is made ascertained that the specific resistance took a figure up one place. The results have suggested that the elevation of conductivity is due to the increase of dissolved TiO_2 amount, the valence deviation of Ti, the change of grain size and the segregation of a trace amount of calzirtite phase at the grain boundaries of the tazheranite of single phase.

[Received February 5, 1992; Accepted May 21, 1992]

Key-words: Tazheranite, Calzirtite, Fluorite structure, Conductivity, Complex impedance method

1. Introduction

Much attention is being focused on the CaO-ZrO_2-TiO_2 system because it is useful for the treatment of high level radioactive waster[1] or solid electrolyte with anion vacancies.[2] Studies on the ZrO_2 rich region have been directed at the doping effect of TiO_2 on phase transformation and physical properties: i.e., instability of cubic ZrO_2 phase,[3,4] shrinking of cubic lattice,[4,5] enhancement of sintering due to the liquid phase,[5,6] and improvement of thermal shock resistance.[7]

Tetragonal calzirtite and cubic tazheranite belong to this ternary system mineral. The former is denoted as $CaZr_3TiO_9$[8] or $Ca_2Zr_5Ti_2O_{16}$,[9] and its CaO content is about 20mol%. Although the latter has almost the same composition as calzirtite, the valency of Ti contained changes from 4+ to 3+, thus its crystal structure is cubic fluorite type with oxygen ion vacancies.[10] As mentioned above, these two kinds of minerals are of interest from a structural point of view, but there have been few reports[11] in which their single phase has been synthesized. In addition, tazheranite has potential as an ionic conductor because its structure is cubic fluorite type with some defects.

In this study, single phase tazheranite powders, whose composition were $Ca_{0.20}Zr_{0.80-x}Ti_xO_y$ ($y<2$) in the CaO-ZrO_2-TiO_2 system, were synthesized by substituting a part of ZrO_2 of the calzirtite and the tazheranite with TiO_2. A possiblity for the conductive material of them were also investigated. In particular, synthesized various powders, whose part of ZrO_2 were substituted with TiO_2, were syntherized, and the tazheranite single phase region was determined from the relationship between formation phase and TiO_2 substitution amount. Finally, these powders were employed to make sintered bodies, and conductivities were measured by the complex impedance method. Various contribution factors of the grain or the grain boundary to conductivity was considered.

2. Experiment

2.1. Synthesis of Powder

Commercial $CaCO_3$ powder (Kanto Chemical, guaranteed reagent), ZrO_2 powder (TOSOH, TZ-0, purity=99.9%), and TiO_2 powder (Idemitsu-Kosan, IT-S) were used as starting materials. These powders were weighted to become compositions of $Ca_{0.2}Zr_{0.8-x}Ti_xO_y$:$x$=0.04-0.25, they were mixed for 24h by wet-ball milling using a zirconia ball and ethanol. After being substantially dried, they were annealed at 1000°C for 10h to decompose the carbonate. This process was determined from the result of TG-DTA (Rigaku Denki, TAS-200) analysis. Annealed powders were wet-ball milled again for 24h. After being dried, they were fired at 1200°-1300°C for 2-20h. The crystalline phase was identified by a powder X-ray diffractometer (Rigaku Denki, RAD-C, CuKα, 40kV, 30mA). Lattice constants were calculated from (111), (200), (220), (311), (222), and (400) peak positions of tazheranite. At that time, Si powder was used as the external standard, and/or NiO powder was used as the internal standard. The morphology, particle size, and dispersion of the synthesized powder were observed by SEM (JEOL, JSM-5400).

2.2. Fabrication of Sintered Body

The obtained powders were substantially mixed, crushed, and classified with #100 mesh. They were first uniaxially

compacted (49MPa) and then pressed by CIP (196MPa) to obtain green pellets (10mmϕ). They were sintered at 1400°-1600°C for 1-10h in order to obtain sintered bodies. The heating rate was 4°C/min, and the cooling rate was 4°C/min down to 900°C and then furnace cooling to the room temperature.

In order to determine the crystalline phase and the lattice parameters of the sintered bodies, the bodies were crushed and crushed into powders. The determination process was the same as that described in section 2.1. The surface of the sintered bodies were mirror finished; and the bulk density was determined according to the Archimedean method, where distilled water was used as the medium. After thermal etching, the microstructures were observed with SEM. The distribution of each element and valency of Ti were examined by EPMA (Shimadzu, EMX-SM) and XPS(Ulvac-Phi, ESCA/AES 558U-P), respectively.

2.3. Electrical Conductivity Measurement

The sintered bodies were sliced into 2mm thick disks. After Pt paste (Shoei Chemical, D-4001) was applied to both sides, the disks were annealed in air at 850°C. The specimens were set on a measurement cell, and the conductivity was measured by the complex impedance method in air using a frequency response analyzer (Schlunberger, Solartron 1250 FRA) and a potensiostat (Hokuto Denko, HA-501G). The measurement frequency was changed from 1Hz to 65kHz, and the measurement temperature was changed from 400°C to 900°C.

3. Results and Discussion

3.1. Single-Phase Region of Tazheranite Powder

The phase diagram of the CaO-ZrO_2-TiO_2 system[3] examined in this study is shown in **Fig.1**. According to the diagram, there is a large single phase area around the ZrO_2 rich region, and the right side of the *a-a'* line is a tetragonal region, and the left side is a cubic region. Then we focused on this cubic region, the relationship between the amount of TiO_2 substitution and the created phase was examined. For this purpose, powders with various ZrO_2-TiO_2 molar ratios were synthesized in order to produce compositions of $Ca_{0.20}Zr_{0.80-x}Ti_xO_y$ (x=0.04, 0.10, 0.15, 0.20, 0.25; y<2), while the CaO content remained constant as 20mol%. The resulting fluorite type cubic phase was recognized as tazheranite phase regardless of composition, and the tetragonal phase was recognized as calzirtite phase. The sintering temperature was determined to be less than 1300°C because intergranular melt occurs above 1460°C, which is ascribed to the liquid phase formation.[5,6,12]

First, in order to examine the calcination condition, the powder in x=0.15 was calcined at 1200°C-1300°C for 2-20h. There is no residue of the starting material, and only the CaO-ZrO_2-TiO_2 compound was detected in the powder heated at 1300°C for 10h. Then, the calcination condition of the powders with various compositions was determined to be 1300°C, 10h. The XRD patterns of the resulting powders are shown in **Fig.2**. Nearly single phase tazheranite with a trace amount of calzirtite, including $CaTiO_3$, was created in the composition of x=0.04 and 0.1. The powder with x=0.15 was a mixture of tazheranite and calzirtite, which was determined by the XRD peaks above 2θ=60°, while the XRD peaks of tazheranite and calzirtite overlap in Fig.2. When the amount of TiO_2 substitution was increased, nearly single phase calzirtite with a trace amount of tazheranite and monoclinic ZrO_2 was created in x=0.20. In the resulting powder in x=0.25, the residue to starting material and monoclinic ZrO_2 was detected beside the calzirtite.

It was revealed from these results that single phase tazheranite can be synthesized in the composition range of x=0.04-0.10 in the $Ca_{0.20}Zr_{0.80-x}Ti_xO_y$ composition by controlling the amount of TiO_2 substitution. SEM observation revealed that the powders with a composition of x=0.04-0.2 sintered at 1300°C for 10h has grain size of 1-2μm, and a part of them was agglomerated.

3.2. Microstructure and Electric Conductivity of Sintered Body

Figure 3 illustrates the XRD patterns of the sintered bodies with the composition of x=0.04-0.20 (sintering condition; 1500°C, 4h except for x=0.20, 10h for x=0.20). Although the produced phases of the sintered bodies in x=0.04 or 0.20 agreed with those for the powders, the calzirtite phases of powder in x=0.10 and 0.15 transformed to tazheranite phase in the sintered bodies. Then, the valency of Ti in the sintered bodies was examined in order to confirm the existence of tazheranite. **Figure 4** shows the XPS analysis of the sintered bodies. They were tazheranite single phase although the TiO_2 substitution amount was different, x=0.04 and x=0.15. In both sintered bodies with x=0.04 and 0.15, valency change was confirmed by the chemical shift of Ti $2p_{1/2}$ peak from 4+ to 3+. And the rate of 3+ for various Ti valencies was larger in the sintered bodies of x=0.15. It can be concluded that the range of the tazheranite composition was broadened up to x=0.15 by sintering at 1500°C. At that time, trace amounts of calzirtite and $CaTiO_3$ were present.

Figure 5 shows the SEM photographs of the thermally etched face of the sintered bodies (1500°C 4h). They were both tazheranite single-phase; however, TiO_2 substitution ratio was different as x=0.04 and x=0.15. In both cases, grain growth occurred aggressively, and then the grain size was about 30μm for x=0.04 and 15μm for x=0.15. Spherical pores of less than 0.4μm were observed in the grain of the sintered body in x=0.15. As densification occurred substantially around grain boundaries and pores at triple points, the pores were thought to be left behind within the grain due to the rapid grain growth. On the other hand, the sintered

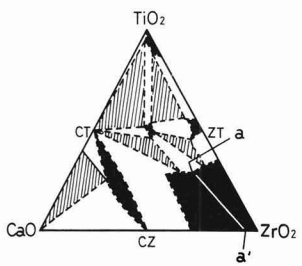

Fig. 1. Phase diagram of CaO-ZrO_2-TiO_2 system.[3]
■: One phase area, □: Two phases area, ▨: Three phases area.

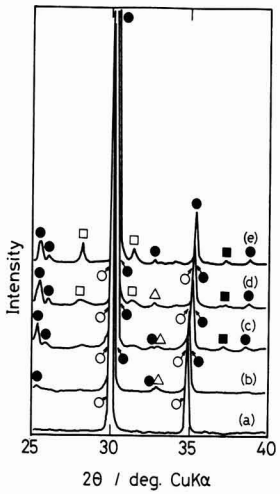

Fig. 2

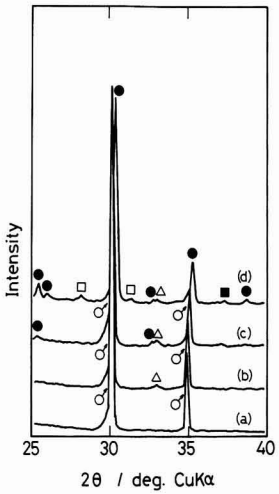

Fig. 3

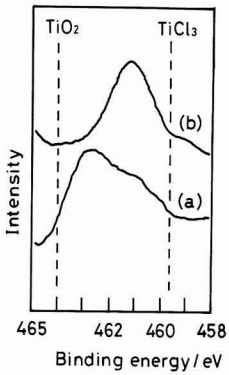

Fig. 4

Fig. 2. X-ray diffraction patterns of $Ca_{0.20}Zr_{0.80-x}Ti_xO_y$ powders prepared at 1300°C for 10h.
Composition x= (a) 0.04, (b) 0.10, (c) 0.15, (d) 0.20, (e) 0.25.
○Tazheranite, ●: Calzirtite, △: $CaTiO_3$, □: m-ZrO_2, ■: unknown.

Fig. 3. X-ray diffraction patterns of $Ca_{0.20}Zr_{0.80-x}Ti_xO_y$ sintered bodies fabricated at 1500°C.
Holding time; (a), (b), (c): 4h, (d) :10h Composition x= (a) 0.04, (b) 0.10, (c) 0.15, (d) 0.20.
○: Tazheranite, ●: Calzirtite, △: $CaTiO_3$, □: m-ZrO_2, ■: unknown.

Fig. 4. XPS analysis of $Ca_{0.20}Zr_{0.80-x}Ti_xO_y$.
Composition x=(a) 0.04, (b) 0.15.

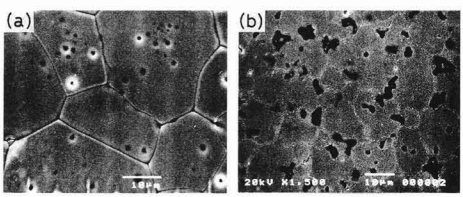

Fig. 5. SEM photograph of $Ca_{0.20}Zr_{0.80-x}Ti_xO_y$.
Composition x= (a) 0.04, (b) 0.15.

body in x=0.15 has smaller grain than that in x=0.04 and had few pores in the grains. This is because the trace amount of the second phase (calzirtite and $CaTiO_3$ from Fig.3) suppressed the grain growth. And segregation of the second phase was observed around the grain boundaries and the triple points. In order to confirm the second phase, distribution state of the elements in both sintered bodies was examined by EPMA. In the case of tazheranite single-phase in x=0.04, the elements of Ca, Zr, and Ti were distributed randomly in the grain and grain boundary, while the sample of x=0.15 with a trace amount of the second phase has a small amount of Zr and a large amount of Ca, Ti near the triple points.

Accordingly, the microstructure of the tazheranite sintered body was dependent on the amount of TiO_2 substitution, and the pores in the grain decreased with an increase in this amount. In the case of sintered body in x=0.15, Ca and Ti rich compound (=$CaTiO_3$), as a trace amount of the second phase, segregated around the triple points and the material (=calzirtite) with the same composition as the grain segregated around the grain boundaries.

The conductivities of the tazheranite sintered bodies with various degrees of TiO_2 substitution (x=0.04-0.15) and the calzirtite sintered body (x=0.20) were measured using the complex impedance method. The effects of the pores were estimated to be identical between the samples because the porosities of the samples were almost the same. This was confirmed by the SEM observation.

If it is assumed that a electric conduction is governed by the ionic conduction of which mechanism is a random transport of oxide vacancies, the slope of logσT-1/T plots provides the activation energy of the conductivity.[13] Here, σ is a conductivity and T is an absolute temperature. **Figure 6** shows the logσT-1/T plot of the bulk conductivity (bulk means the sum of grain and grain boundary) for each sintered body. The activation energy deduced from the slope of the conductivity was 120-130kJ/mol, which was not affected by the amount of TiO_2 and the produced phase. This value is almost identical to that for 15-16mol% CaO stabilized ZrO_2 (about 126kJ/mol[14]) and 5wt% CaO stabilized ZrO_2 doped of 5mol% TiO_2 (130kJ/mol[15]). Although electronic conduction often occurs in the compound containing TiO_2, the electronic conduction was not considered in this study, because it has already been reported that there is no electronic conduction in Y_2O_3-ZrO_2-TiO_2 system in air.[16,17] The measured DC conductivity simultaneously increased with time. Accordingly, oxide ion conduction is dominant in the electric conduction of tazheranite and

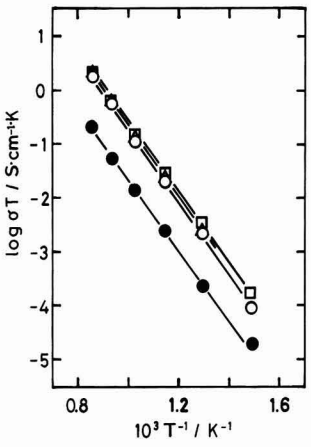

Fig. 6

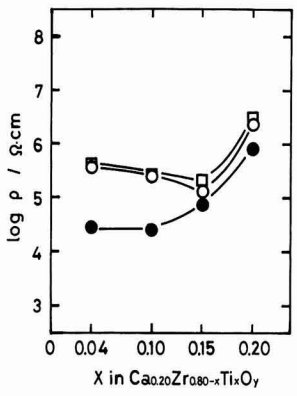

Fig. 7

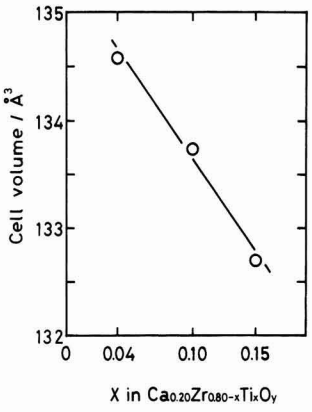

Fig. 8

Fig. 6. Arrhenius plots of conductivity of $Ca_{0.20}Zr_{0.80-x}Ti_xO_y$.
Composition x=○: 0.04, △: 0.10, □: 0.15, ●: 0.20.

Fig. 7. Dependence of Ti concentration on specific resistance of $Ca_{0.20}Zr_{0.80-x}Ti_xO_y$ at 500°C.
□: Total, ○: Grain, ●: Grain boundary.

Fig. 8. Dependence of Ti concentration on cell volume of $Ca_{0.20}Zr_{0.80-x}Ti_xO_y$.

calzirtite sintered bodies, which is also the case with CaO stabilized ZrO_2.

Compared with the cubic tazheranite (x=0.04-0.15), the conductivity of tetragonal calzirtite (x=0.20) was one order lower in all temperature range measured.

3.3. Factors Affecting the Grain and Grain Boundary Resistances

In the previous Section 3.2. the bulk conductivities for each sintered body was discussed. In this Section, the conductivities inside of grain and also at grain boundry are considered.

Figure 7 shows the relationship between the resistances for bulk, grain and grain boundary at 500°C and the TiO_2 substitution amount. As the grain resistance is almost identical to that of bulk in the composition range of x=0.04-0.20, the grain resistance is dominant in the resistance of the sintered body. In the tazheranite single phase sintered body at the composition range of x=0.04-0.15, the grain resistance decreased with an increase in the amount of TiO_2 substitution, and that for calzirtite in x=0.20 increased considerably. On the other hand, the grain boundary resistance remained constant up to x=0.10, but it increased with an increase in the amount of TiO_2 substitution above x=0.15. This tendency was also the case with the results measured at 400°-600°C, where the resistances of grain and grain boundary can be separated qualitatvely.

The factors governing the resistance of the tazheranite sintered body (x=0.04-0.15), which showed decrease in grain resistance with an increase in TiO_2 substitution amount, were then examined qualitatively.

The decrease in grain resistance with an amount of TiO_2 substitution up to x=0.15 could be ascribed to the increase in the amount TiO_2 solution into the grain and the increase in vacancy accompanied by the Ti valency change in the grain. The cubic fluorite phase is believed to govern the

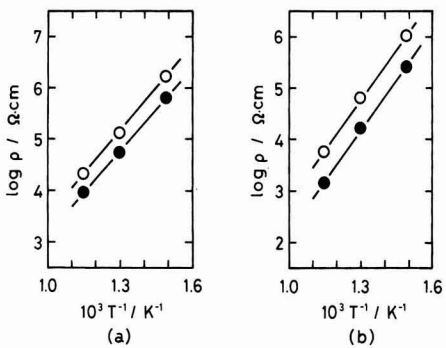

Fig. 9. Dependence of temperature on specific resistance of $Ca_{0.20}Zr_{0.80-x}Ti_xO_y$.
(a) Grain conductivity, (b) Grain boundary conductivity.
Cooling rate; ○: 4°C/min, ●: 25°C/min.

grain resistance of the tazheranite single phase. The relationship between the cell volume of cubic fluorite phase and amount of TiO_2 substitution was then examined in order to confirm the TiO_2 amount dissolved into the grain. The results are shown in **Fig.8**. The cell volume decreased with an increase in amount of TiO_2 substitution. This is because the Zr^{4+} ion in the cubic fluorite structure was replaced by small ion, Ti^{3+} or Ti^{4+}. [5] As shown in Fig.4, a variation of Ti valency in tazheranite occurred. Then, the sintered body of x=0.15 with a large amount of TiO_2 substitution is believed to have a larger fraction of Ti^{3+} ion and large amount of vacancy. Accordingly, the decrease in grain resistance in a tazheranite single phase was thought to be attributed to the increase in TiO_2 solution into the fluorite lattice and the

increase of vacancy due to the variation of Ti valency.

On the other hand, the variation of the grain boundary resistance can be ascribed to the existence of pores, the segregation of the second phase, and the change in grain size. From the SEM observation and EPMA results, a segregation phase tended to exist around the grain boundaries, and the triple points and the grain size decreased from 40μm to 15μm when the amount of TiO_2 substitution was increased. Figure 3 shows that when the amount of TiO_2 substitution was increased, segregation of $CaTiO_3$ occurred around x=0.10 and that of a trace amount of calzirtite occurred around x=0.15. It can be said that the increase in resistance of the grain boundary above the composition of x=0.15 is ascribed to the segregation of the trace amount of calzirtite near the grain boundaries, which was detected by XRD. In order to examine the effect of such a trace amount of calzirtite, a complex impedance measurement was conducted on the sintered body in x=0.15. This sample was made with a cooling rate of 25°C/min. The result of X-ray diffraction showed that the created phase was tazheranite single phase in which a trace amount of $CaTiO_3$ was contained, but the calzirtite phase was not detected even in a trace amount.

Figure 9 shows the temperature dependence of (a) grain and (b) grain boundary specific resistances. The sintered body made with the cooling rate of 25°C/min showed smaller grain and grain boundary specific resistances than those with 4°C/min. This can be ascribed to the transformation of the trace amount of calzirtite to tazheranite. This tendency was also the case with the result measured at 400°-600°C, where the specific resistances of grain and grain boundary can be separated.

In conclusion, tazheranite single phase with large amount of TiO_2 substitution was produced while the cubic fluorite structure was maintained. It was clarified that the grain resistance, being dominant of the bulk resistance, decreased in that sample.

4. Conclusion

$Ca_{0.20}Zr_{0.80-x}Ti_xO_y$ composition (x=0.04, 0.10, 0.15, 0.20) powders and sintered bodies were prepared by solid state reaction, and the single phase region of the tazheranite was examined. The conductivities of the resultant tazheranite and calzirtite were then measured using the complex impedance method. The results are as follows:

1) In the CaO-ZrO_2-TiO_2 system, the tazheranite single phase in the range of x=0.04-0.10 was synthesized by changing the $Ca_{0.20}Zr_{0.80-x}Ti_xO_y$ composition with the amount of TiO_2 substitution. The range of tazheranite composition was apparently broadened up to x=0.15 by firing at 1500°C.

2) The activation energies of the conductivities of sintered bodies of tazheranite (x=0.04-0.15) and calzirtite (x=0.20) were 120-130kJ/mol. It is presumed that the mechanism of electric conduction was dominated by an oxygen ion conduction in the temperature range of 400°-900°C in the air. This mechanism was not affected by the amount of TiO_2 substitution and the created phase.

3) In the case of tazheranite single phase with the composition of x=0.04-0.15, the resistance of grain decreased with an increase in the amount of TiO_2 substitution, and that of grain boundary increased. This suggests that the decrease in grain resistance is ascribed to the increase of dissolved TiO_2 amount and the increase of vacancy due to the deviation of Ti valence. In addition, the increase in grain boundary resistance was thought to be affected by the change of grain size and the segregation of a trace amount of calzirtite phase.

Acknowledgement

The authors sincerely thank Prof. H. Kaneko and Associate Prof. H. Toimatsu at Mining College, Akita Univ. for suggesting the measurement of complex impedance method.

References:

1) For example, A.E. Ringwood, S.E. Kesson, N.G. Ware, W. Hibberson and A. Major, Nature, 278, 219-223 (1979). W.J. Buykx, D.J. Cassidy, C.E. Webb and J.L. Woodlfrey, Am. Ceram. Soc. Bull., 60, 1284-1288 (1981).
2) J.M. Reau, J. Portier, A. Levasseur, G. Villeneuve and M. Pouchard, Mater. Res. Bull., 13, 1415-1423 (1978).
3) L.W. Coughanour, R.S. Roth, S. Marzullo and F.E. Sennett, J. Res. Natl. Bur. Stand. (U.S.), 54, 191-199 (1955).
4) D.C. Agrawal, R. Gopalakrishnan and D. Chakravorty, J. Am. Ceram. Soc., 72, 912-915 (1989).
5) Y. Hon and P. Shen, Mater. Sci. Eng., A131, 273-280 (1991).
6) K.C. Radford and R.J. Bratton, J. Mater. Sci., 14, 59-65 (1979).
7) N.C. Biswas and D.Chakravorty, J. Mater. Sci. Lett., 1, 119-120 (1982).
8) For example, T.B. Zdorik, G.A. Sidorenko and A.V. Bykova, Dokl. Akad. SSSR, 137, 681-684 (1961).
9) For example, Y.A. Pyatenko and Z.V. Pudovkina, Kristallografiya, 6, 196-199 (1961).
10) A.A. Konev, Z.F. Ushchapovskaya, A.A. Kashaev and V.S. Lebedeva, Dokl. Akad. Nauk SSSR, 186, 917-920 (1969).
11) M.O. Figueiredo and A.C.D. Santos, Zirconia '88: Advances in Zirconia Science and Technology, Elsevier Applied Science (1989), 81-87.
12) A. Jongejan and A.L. Wilkins, J. Less-Common Met., 20, 273-279 (1970).
13) Chem. Soc. Jpn. (ed.), Kinoosei Seramikkusu no Sekkei, Gakkai Shuppan Ctr (1982) 65.
14) T.H. Etsell and S.N. Flengas, Chem. Rev., 70, 339-376 (1970).
15) K.C. Radford and R.J. Bratton, J. Mater. Sci., 14, 66-69 (1979).
16) S.S. Liou and W.L. Worrell, Appl. Phys., A49, 25-31 (1989).
17) H. Naito and H. Arashi, 7th Sympo. Solid State Ionics in Jpn. Ext. Abst., A-108 (1991).

This article is a full translation of the article appearing in Journal of the Ceramic Society of Japan (Japanese version), Vol.100, No.9, pp.1135-1139, 1992.

Effect of Stabilizing Agents on Synthesis of Monodispersed Al_2O_3 Powders by Hydrolysis of Aluminium Sec-Butoxide

Seok-Keun Lee, Kazuo Shinozaki and Nobuyasu Mizutani

Department of Inorganic Materials, Faculty of Engineering, Tokyo Institute of Technology
2-12-1, O-okayama, Meguro-ku, Tokyo, 152 Japan

Effects of hydrolysis-rate-control-additives (carbonyl compounds such as ethylacetoacetate and acetylacetone) on the hydrolysis behavior of aluminum secondary butoxide and condition for the formation of monodispersed alumina particles were investigated. The reactive enol form of the carbonyl compounds substituted butoxyl group of aluminum secondary butoxide and chelated the aluminum atom. The chelating ligand would not be easily removed upon hydrolysis reaction because the aluminum-ligand bond was sufficiently strong. As a consequence, the rate of hydrolysis and polycondensation of modified precursor decreased. By hydrolyzing this modified stable precursor, the monodispersed alumina particles were prepared in the wide range of water concentration; about 8 times that of non-modified precursor when 0.006mol/l ethylacetoacetate was added and about 4 times when 0.006mol/l acetylacetone was added. The average particle size of obtained monodispersed particles and the geometrical standard deviation were 0.2μm and 1.18, respectively. The morphology of particles changed with increasing water concentration as follows; agglomerates of coarse texture → monodispersed particles → agglomerates of fine texture.

[Received February 14, 1992; Accepted May 21, 1992]

Key-words: Alumina, Synthesis, Hydrolysis, Alkoxide, Additive, Carbonyl compound, Chelate, Monodispersed particle

1. Introduction

Metal alkoxide is widely used as a precursor to synthesize glass or ceramic fine particles by the sol-gel method. The reactivity of metal alkoxide is sensitive to nucleophilic reagents such as water. Such a high reactivity is due to the alkoxyl group which has a high electron affinity.[1] Therefore, almost all alkoxides, except Si alkoxide, must be kept away from water.

Recently, many researchers have tried to modify some alkoxide precursors in order to control their hydrolysis and polycondensation. The practical methods are alcohol exchange reaction,[2,3] catalyst addition method,[4] using a chloride alkoxide,[5,6] and chelating.[7,8] The alcohol exchange reaction increases with a decrease in the stearic hindrance of alkoxyl group in the alcohol solvent.[9] Acetic acid is mainly used in the catalyst addition method. It improves the hydrolysis rate of Si alkoxide.[10] Because it depresses the gelation rate of transition metal alkoxides, it is useful for synthesing a homogeneous and transparent gel.[11] Chloride alkoxide is given by a reaction between metal chloride and alcohol. It is very stable, and the hydrolysis rate is very small. However, the gelation rate increases with an increase in the chain length of the alcohol.[12] β-diketon is mainly used to form a chelate. Acetyl acetone is used as a stabilizer for various alkoxides such as $W(OEt)_6$,[13] $Zr(OPr^i)_4$,[14] and $Ti(OBu^n)_4$.[15] The above-mentioned modification of the alkoxide presursors has been utilized in the synthesis of transparent gels or fine oxide particles. However, a monodispersed particle has not been synthesized by this method.

Monodispersed alumina fine particle can be synthesized only when a mixed solvent of n-octanol and acetonitrile is used in the alkoxide method.[16] This is because the Al alkoxide is particularly easy to hydrolysis, which is different from the alkoxide presursors for TiO_2[17] and ZrO_2.[18] In this case, the range of water concentration to form monodispersed particles is very narrow.

In this study, a method controlling the rate of hydrolysis and polycondensation of aluminum alkoxide, which will facilitate the synthesis of alumina monodispersed particle, was investigated. For this purpose, an attempt to modify an aluminum secondary butoxide was conducted by adding some carbonyl compounds, and the effects of the modification on the synthesis condition and the process of monodispersed Al_2O_3 fine particles were investigated.

2. Experiment

2.1. Sample Preparation

Alminium secondary butoxide (Soekawa Rikagaku) was dissolved in *n*-acetonitrile (Wako Jyunyaku, guaranteed grade)(0.05mol/l). Hydoxypropyl cellulose (0.2g/l) was added as a surface active agent. Ethylacetoacetate (denoted as EAcH) or acetylacetone (denoted as AcAcH) was then added as a stabilizer into the solution. Distilled water dissolved in acetoanilil was added to the solution, and the mixture was stirred for 45sec to hydrolyze. *n*-octanohol and acetonitrile were dehydrated using molecular sieves. (3A, Wako Junyaku). The resulting water content was less than 100ppm. After being aged for 1h, solids in the hydrolysis product were isolated by a centrifuge. This precipitate was rinsed in alcohol. After isolation, the resulting particle was dried at 60°C for 24h.

2.2. Evaluation of Sample

The morphology and the degree of agglomeration of the

particles were observed by a scanning electron microscope (SEM, JERO: JSMT200). In order to obtain the average particle size and the geometrical standard deviation, 400 particles were selected at random. The structural change of aluminum secondary butoxide accompanied by the addition of the stabilizer was analyzed by infrared spectrometer (Nihonbunkou; FT-IR8100). The water content of the solution and the consumption of water during hydrolysis were quantitatively analyzed by a Curl-fisher titration apparatus (Mitsubishi Kasei: VA-05).

3. Result and Discussion

3.1. Modification of the Precursor

Figure 1 shows the FT-IR spectra of an aluminum secondary butoxide dissolved in n-octanohol with no additive. The spectra of the same solutions with EAcH(b), with AcAcH(c) and with ethyl acetate (denoted as SAe) (d) are also shown in the figure. New bands around 1530cm^{-1} and 1600cm^{-1} can be seen in the spectra of solution (b), (c). These bands correspond to ν(C–C) and ν(C–O) vibration mode;[7] these modes represent chemical bonds of Al atom with EAc or AcAc group.[19] From these results, by adding EAcH or AcAcH, the Al atom of the aluminum secondary butoxide is considered to be chelated as follows.

$$Al(OB^s)_3 + XEAcH \rightarrow Al(OBu^s)_{3-X}(EAc)_X + XBu^sOH \quad .....(1)$$

$$Al(OBu^s)_3 + YAcAcH \rightarrow Al(OBu^s)_{3-Y}(AcAc)_Y + YBu^sOH \quad .....(2)$$

On the other hand, no band indicating a modification of the aluminum secondary butoxide appeares in the spectrum of the solution (d). The band around 1750cm^{-1} is attributed to the starting material.

Among the carbonyl compounds, EAcH and AcAcH chelated to Al, but SAe did not chelate. This is because the former contains a hydroxyl group. In other words, in a β-diketone compound, such as EAcH or AcAcH, the keto and enol forms coexisted as follows;

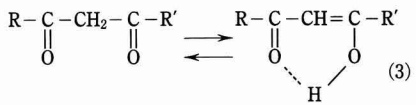

(3)

(keto form) (enol form)

Here, R, R' are alkyl groups. The reactive enol form substituted a part of butoxyl group of aluminum secondary butoxide. It chelated the Al atom, and the anion became stable. The enol content in each carbonyl compound is listed in **Table 1**.

As mentioned above, the chelated aluminum secondary butoxide changed its reactivity. Thus, the reactivity in hy-

Table 1. The enol content of some carbonyl compounds.

Compound	Enol Content (%)
CH_3COOEt (SAe)	No enol found*
CH_3COCH_2COOEt (EAcH)	8.0
$CH_3COCH_2COCH_3$ (AcAcH)	76.4

*Less than 1 part in 10 million.

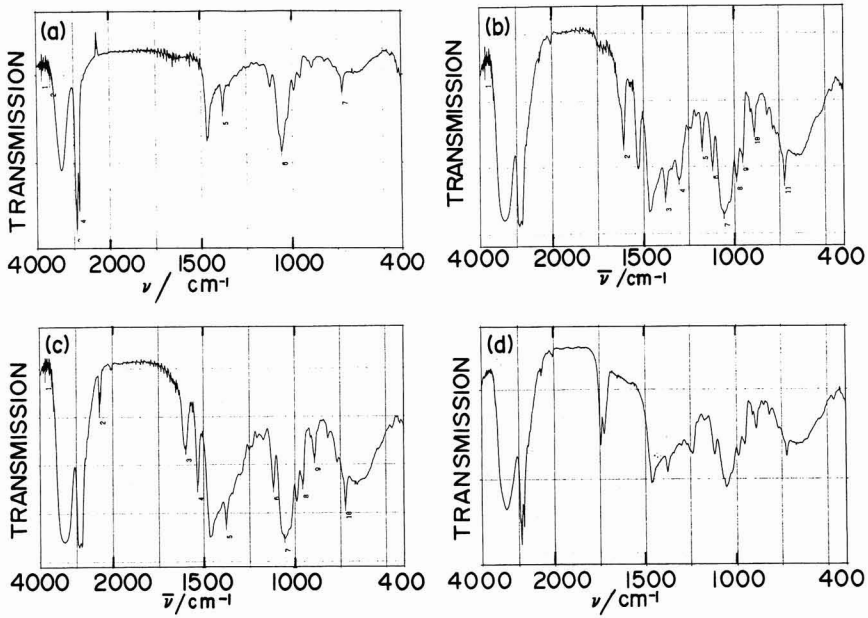

Fig. 1. Infrared spectra of modified aluminum secondary butoxide with various carbonyl compounds in octanol: (a) No Additive, (b) ethylacetoacetate, (c) acetylacetone and (d) ethylacetate.

drolysis and polycondensation is thought to be different from the intrinsic one.

3.2. Water Concentration Range of Monodispersed Particle Formation

Figure 2 shows the relationship of water concentration and the amount of added ethylacetoacetate for preparing monodispersed particles. The water concentration to form monodispersed particles was broaden by adding a small amount of EAcH. The monodispersed particles were formed only in a narrow range of water concentration, 0.02-0.08mol/l. By adding EAcH with 0.006mol/l, the monodispersed particles were formed in a wide range of water concentration, 0.15-0.65mol/l (which was 8 times as large as that of the nondoped one). However, the water concentration range decrease with and increase in EAcH concentration over 0.06mol/l. As a result, only agglomerate or gel was formed when EAcH was added over 0.03mol/l.

The relationship between the water concentration and morphology of the formed particles remained constant below the water concentration of 0.027mol/l, although the range in which each product formed was different among the samples with various EAcH. In detail, when the water concentration was extremely high or low, gel was formed. For a moderate water concentration, the morphology of particles changed with an increasing water concentration as follows; (a) agglomerates of coarse texture → (b) monodispersed particle → (c) agglomerates of fine texture. This is illustrated in **Fig.3**. On the other hand, the particles prepared without additive changed morphology from monodispersed particle to agglomerate with an increase in water concentration. In extremely higher water concentrations, the gel phase was formed.[16] The difference between the two cases (especially the creation mechanism of the agglomerate of coarse texture) can not be substantially explained by the experimental results. However, it was suggested to be caused by the modification of aluminum secondary butoxide by the EAcH group. This will be discussed in detail in Section 3.3.

Concerning the monodispersed Al_2O_3 synthesized with EAcH, the average particle size and the geometrical standard deviation were determined to be 0.2μm and 1.18, respectively. These values were the same as those of the particle synthesized without EAcH.[16] Hence, the addition of EAcH broadened the water concentration range in which monodispersed particles were created, but it has no effect on particle size and geometrical standard deviation.

Figure 4 shows the relationship of water concentration and the amount of AcAcH for preparing monodispersed Al_2O_3 particles. In this case, the water concentration range in which monodispersed particles were created was also broaden, but the effect on broadening was not as large as that of EAcH. For example, monodispersed particles were prepared in a water concentration of 0.15–0.65mol/l when 0.006mol/l of EAcH was added. The concentration changed to 0.25-0.50mol/l when the same amount of AcAcH was used. This can be attributed to the difference in the amount of the enol form in EAcH and AcAcH (Table 1). When over 0.01mol/l of AcAcH was added, the created phase was first

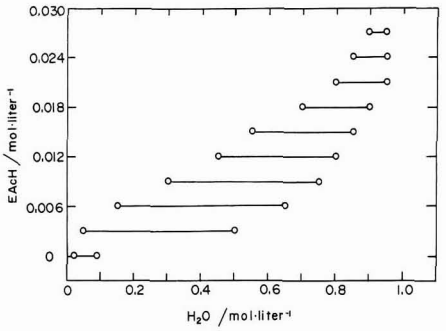

Fig. 2. The relation of water concentration and amount of ethylacetoacetate addition for preparing monodispersed Al_2O_3 particles.

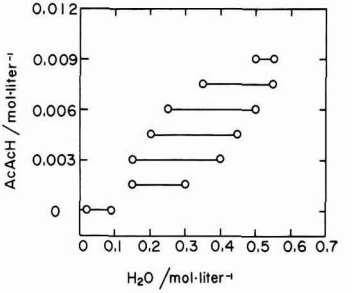

Fig. 4. The relation of water concentration and amount of acetylacetone addition for preparing monodispersed Al_2O_3 particles.

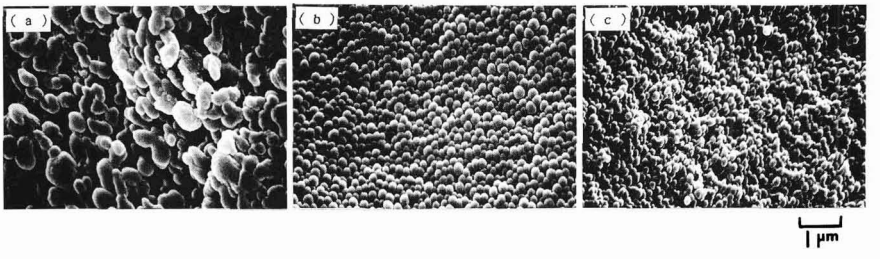

Fig. 3. SEM photographs of Al_2O_3 particles prepared by hydrolyzing the modified aluminum secondary butoxide with 0.006mol/l ethylacetoacetate in various water concentration (a) 0.1mol/l, (b) 0.6mol/l and (c) 1.2mol/l.

agglomerate and then changed to the gel phase with an increase in AcAcH. However, the relationship between water concentration and created phase was similar to that for EAcH.

3.3. Hydrolysis and Polycondensation

Figure 5 shows the changes of water concentration with hydrolysis time. Here, the concentration of aluminum secondary butoxide is 0.95mol/l. Quantitative analysis of the water in solvent is not sufficient to analyze the amount of hydrolysis product, but direct analysis is difficult. Hence, the amount of the hydrolysis product was estimated by the water content of solvent. About 0.045mol/l of water was consumed during the hydrolysis and plycondensation without additive. In order to substitute the alkoxyl group of 0.05mol/l of aluminum secondary butoxide by hydroxyl group, 0.075mol/l of water is theoretically needed. Accordingly, the water consumed during hydrolysis and polycondensation was two-thirds that of the theoretical value. From these results, the hydrolysis reaction of aluminum secondary butoxide is thought to follow.

$$Al(OBu^s)_3 + 2H_2O \rightarrow Al(OBu^s)(OH)_2 + 2Bu^sOH \quad \ldots\ldots\ldots (4)$$

Two of the three butoxyl groups bonded to an aluminum were believed to react with water. In this case, the rate of plycondensation was smaller than that when all the butoxyl groups reacted. This is because the steric hindrance was enhanced by the butoxyl group having a longer chain than hydroxyl group. In addition, the hydroxyl and the butoxyl group must are brought close together for polycondensation, but the low probability of such an proximity of ions would lessen the polycondensation rate. Thus, the chain-like oligomers creat during polycondensation and is thought to become a presursor by intertwining with each other. On the other hand, the pH of the solution can assumed to be constant because the composition of solvent was about the same, while the hydrolysis depends on pH of the solution.[22]

The reaction according to Eq.(4) occurred in a water concentration of 0.02-0.08mol/l, in which monodispersed Al_2O_3 particle were created. When the water concentration increased and the concentration of the hydroxyl group became larger than the butoxyl group, the hydrolysis according to the following equation occurred.

$$Al(OBu^s)_3 + 3H_2O \rightarrow Al(OH)_3 + 3Bu^sOH \quad \ldots\ldots\ldots\ldots (5)$$

In this condition, three-dimensionally polycondensed oligomers were formed by dehydration and condensation between the hydroxyl groups. In this case, the plycondensation rate was so high that an agglomerate consisting of fine particle or gel phase was created.

On the other hand, Fig.5 shows that the amount of water consumed during hydrolysis or polycondensation is smaller with additive than that without additive. This is because the aluminum secondary butoxide was modified by the stabilizer and the necleophoric attack become decreasing; this has already been described in Section 3.1. When the presursor was chelated as Eq.(1) or (2), the steric hindrance became too large to be affected by hydrolysis. This was caused by a difference in length between the OBu^s group and EAc or AcAc group. Therefore, as shown in Fig.2 or 4, the range in which monodispersed particles were created was thought to shift to the right side.

Furthermore, the EAc or AcAc group, which substituted the OBu^s group and chelated the Al atom, was substantially stable. Then, the chelating ligand would not be removed upon hydrolysis reaction. This assumption was confirmed by **Fig.6**, in which changes of water concentration in the solution with the amount of added carbonyl compound is illustrated. The water consumption decreases with an increase in both EAcH and AcAcH addition. No water was consumed when EAcH was added over 0.08mol/l or when AcAcH was added over 0.03mol/l. This can be explained as follows. Almost all the butoxyl groups in aluminum secondary butoxide were substituted by EAc group when 0.08mol/l of EAcH was added. Then, the following addition of water would not lead to hydrolysis. In such a case, particles did not appear. When an adequate amount of stabilizer (less than 0.027mol/l, in the case of EAcH) was added, not only the rate of hydrolysis but also that of polycondensation was depressed by the EAc or AcAc group bonding Al atom. In this way, monodispersed particles can be synthesized in a wide range of water concentration. Here, these EAc or AcAc groups remained in the particle synthesized, but the amount was quite small. In the case of maximum water concentration range when the EAcH was added by 0.006mol/l, for example, 0.96mol% of residue was contained.

Accordingly, when EAcH is added as a stabilizer, hydrolysis and polycondensation are thought to occur as follows. First, when a stabilizer was added, part of the butoxyl groups were substituted by the EAc groups, and the Al atoms were chlated. Second, adding water to the formed

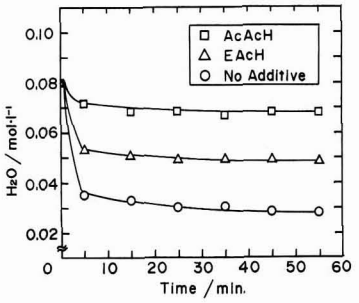

Fig. 5. Changes of water concentration in solution with hydrolysis time. $Al(OBu^s)_3$ concentration: 0.05mol/l.

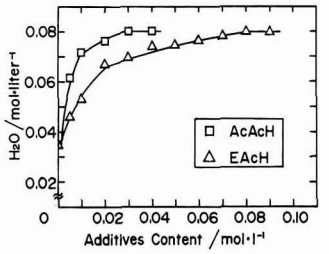

Fig. 6. Changes of water concentration in solution with amount of carbonyl compounds addition. $Al(OBu^s)_3$ concentration: 0.05mol/l, hydrolysis time: 5min, initial water concentration: 0.08mol/l.

precursor, the residual butoxyl group slowly hydrolyzed, while the chelating one remained unchanged. In this case, monodispersed Al_2O_3 particles were thought to be synthesized in the same polycondensation shown in Eq.(4).

4. Conclusion

In order to control the hydrolysis rate and polycondensation of aluminum, the modification of an aluminum secondary butoxide alkoxide was attempted, and a formation of monodispersed particle was investigated. The results are as follows.

1) The aluminum secondary butoxide was chelated by the enol form of the hydroxyl group existing in EAcH or AcAcH which were added as stabilizers. Precursors, of which the reactivity had been modified, were obtained.

2) The substituted EAc or AcAc group was very stable, and such a group was not easily removed upon hydrolysis reaction. As a result, the rate of hydrolysis and polycondensation was controlled to form a monodispersed particle in a wide range of water content.

3) The monodispersed Al_2O_3 particles were prepared only in a narrow range of water concentration, 0.02-0.08mol/l. The water concentration in which monodispersed particles were synthesized was broadened up to 0.15-0.65mol/l (about 8 times) and up to 0.25-0.50 (about 4 times) by adding EAcH or AcAcH with 0.006mol/l, respectively. The average grain size of the resultant monodispersed particles was about 0.2μm.

4) The morphology of particles changed with an increase in water concentration was as follows; agglomerates of coarse texture → monodispersed particle → agglomerates of fine texture. These changes were irrespective of the additive, EAcH or AcAcH.

References:

1) D.C. Bradley, R.C. Mehrotra and D.P. Gaur, Metal Alkoxides, Academic Press, London (1978) 149-167.
2) I. Artaki, S. Sinha, A.D. Irwin and J. Jonas, J. Non-Cryst. Solids, 72, 391-402 (1985).
3) L.W. Kelts, N.J. Effinger and S.M. Melpolder, ibid., 83, 353-374 (1986).
4) S. Doeuff, M. Henry, C. Sanchez and J. Livage, ibid., 89, 206-216 (1987).
5) D.C. Bradley, F.M. Abd-El Halim and W. Wardlaw, J. Chem. Soc., 3450-3454 (1950).
6) K. Watenpaugh and C.N Caughlan, Inorg. Chem., 5, 1782-1786 (1966).
7) C. Sanchez, F. Babonneau, S. Doeuff and A. Leaustic, Ultrastructure Processing of Advanced Ceramics, ed. by J.D. Mackenzie and D.R. Ulrich, Wiley, New York (1988) 77-87.
8) J.C. Debsikdar, J. Mater. Sci., 20, 4454-4458 (1985).
9) I.D. Varma and R.C. Mehrotra, J. Chem. Soc., 2966-2969 (1960).
10) E.J.A. Pope and J.D. Mackenzie, J. Non-Cryst. Solids, 87, 185-198 (1986).
11) M. Henry, A. Vioux and J. Livage, French Patent 8512019 (1985).
12) C. Alquier, M.T. Vandenborre and M. Henry, J. Non-Cryst. Solids, 79, 383-395 (1986).
13) H. Unuma, T. Tonooka, Y. Suzuki, T. Furusaki, K. Kodaira and T. Matsushita, J. Mater. Sci. Lett., 5, 1248-1250 (1986).
14) J.C. Debsikdar, J. Non-Cryst. Solids, 86, 231-240 (1986).
15) M. Emili, L. Incoccia, S. Mobilio, G. Fagherazzi and M. Guglielmi, ibid., 74, 129-146 (1985).
16) N. Mizutani, M. Ideda, S.K. Lee, K. Shinozaki and M. Kato, Seramikkusu Ronbunshi 99, 183-186 (1991).
17) T. Ikemoto, K. Uematsu, N. Mizutani and M. Kato, Yogyo Kyokaishi 93, 261-266 (1985).
18) B. Fegley, Jr., P. White and H.K. Bowen, Am. Ceram. Soc. Bull., 64, 1115-1120 (1985).
19) Charles J. Pouchert, The Aldrich Library of FTIR Spectra, 1st Ed. (1985) 1278A.
20) J. March, Advanced Organic Chemistry, 3rd Ed. John Wiley&Sons, New York (1985) 66-68.
21) A. Gero, J. Org. Chem., 19, 1960-1970 (1954).
22) J. Livage, M. Henry and C. Sanchez, in Progress in Solid State Chemistry (1988) 259-342.

This article is a full translation of the article appearing in Journal of the Ceramic Society of Japan (Japanese version), Vol.100, No.9, pp.1140-1144, 1992.

Control of Crystal Shape and Modification of Calcium Carbonate Prepared by Precipitation from Calcium Hydrogencarbonate Solution

Yoshiyuki Kojima, Akiko Sadotomo, Tamotsu Yasue and Yasuo Arai

Department of Industrial Chemistry, Faculty of Science and Engineering, Nihon University
1-8, Kanda-Surugadai, Chiyoda-ku, Tokyo, 101 Japan

The control of three modifications and crystal shape of calcium carbonate which precipitated by outgassing dissolved CO_2 in calcium hydrogencarbonate solution was studied. The starting saturated solution (10.3×10^{-3}mol $CaCO_3 \cdot dm^{-3}$) of calcium hydrogencarbonate was prepared by passing a stream of CO_2 through the suspension of fine limestone powder at 2°C and then diluted with pure water to concentrations of $2.8\sim8.5\times10^{-3}$mol $CaCO_3 \cdot dm^{-3}$ (initial supersaturation degree: 20~60). Characteristics of the precipitated calcium carbonate were determined by means of X-ray diffraction, infrared spectroscopy, scanning electron microscopy and chemical analysis. The formation region of three modifications was affected remarkably by synthetic conditions such as stirring, pH (6.2~8.0), heating temperature (20°~100°C) and concentration (initial supersaturation degree: 20~60) of calcium hydrogencarbonate solution. When calcium carbonate was precipitated by outgassing dissolved CO_2 in calcium hydrogencarbonate solution under stirring with 240rpm, rhombohedral-like calcite about 10μm in size and prismoidal-like aragonite with 2×50μm in size and 99.7% in purity were independently formed at temperatures below 30°C and above 50°C respectively, while no vaterite was observed. However, vaterite was found as an independent phase by adding an alkaline solution of NaOH or NH_4OH into calcium hydrogencarbonate solution without stirring. Especially, NH_4OH solution was excellent as additive to form hexagonal plate-like crystals of vaterite as compared with NaOH solution. For example, hexagonal plate-like vaterite crystals 20μm in size and 99.7% in purity formed from calcium hydrogencarbonate solution with a supersaturation degree of 20 at pH7.5~7.8 without stirring. These vaterite-crystals were unstable and transformed to the stable phase of hexagonal plate-like calcite by heating at 600°C. The uniform hexagonal plate-like crystals of calcium carbonate can be expected as a new functional inorganic filler for paper, plastics and rubber.
[Received February 27, 1992; Accepted June 16, 1992]

Key-words: Calcium carbonate, Calcium hydrogencarbonate, Hexagonal plate-like vaterite, Inorganic filler, Polymorphism of calcium carbonate

1. Introduction

Commonly called lime stone, calcium carbonate is abundant in Japan and is amply supplied to industries such as steel making and cement manufacturing. Its precipitated products for semifine applications are used as inorganic fillers for paper, plastics, rubber, and other materials.

For such inorganic fillers today, kaolinite-clay minerals are used in large quantities. They are composed of fine flat hexagonal crystals. When applied as a paper manufacturing filler to base paper, crystals lie parallel and close to the paper surface, enabling improvement of the gloss, smoothness and printability of the paper. With plastics and rubber, they give a favorable effect on tensile strength, tensile elasticity, and rigidity. Thus, as inorganic fillers, they are essential materials. However, they are rather scarce, expensive and under unstable demand in Japan, making it urgent to develop alternatives. In particular, precipitated calcium carbonate is at high level in terms of whiteness and chargeability and is expected to be a potential alternative. However, there has been no successful attempt to turn rhombohedral calcite into flat hexagonal crystals.

The authors have already reported on the transformation of calcium hydroxide of hexagonal laminations into hexagonal plates[1,2] and on the synthesis of calcium carbonate composed of hexagonal plates by carbonating the calcium hydroxide composed of hexagonal plates just mentioned.[3] However, this method requires a 2-step process, which was so complicated that the problem of uniform carbonation of calcium hydroxide crystals must be solved. It is generally recognized that hexagonal systems, such as calcium hydroxide, tend to show flat crystal contours due to the development of the (001) plane. There are three modifications of calcium carbonate as alternatives to kaolinite-clay minerals including calcite, aragonite, and vaterite. The authors were interested in transforming vaterite, one of the hexagonal systems, into hexagonal plates.

Ordinarily, precipitated calcium carbonate is industrially manufactured by heterogeneous solid-liquid phase system reactions, having CO_2 gas blown into milk of lime and the product precipitated on the alkali side. This method yields fine calcite particles of several μm in diameter. In order to synthesize fine particles of calcium carbonate in the laboratory, studies have been made on the reactions of $CaCl_2$-Na_2CO_3, $CaCl_2$-$(NH_4)_2CO_3$, and $CaCl_2$-K_2CO_3 systems.[4-12] Also, there have been reports on the production zones of 3 modifications of calcium carbonate precipitated on the acid side by decarbonating a calcium hydrogencarbonate ($Ca(HCO_3)_2$) solution by heating.[13-17]

In such conventional reports, spindle-shaped, spheric, and flat hexagonal crystals are shown for vaterite shapes.[9,18-20] However, there have been few reports on the details of the production of homogeneous flat hexagonal vaterite. Again, because only a slight difference in synthesizing conditions will result in a large difference, opinions are divided on production conditions for the three modifications.

Precipitated calcium carbonate modifications were ob-

tained under a homogeneous sedimentation method which precipitates calcium carbonate on the acid side in liquid phase reactions, or in detail, a method which dissolves powdered lime stone with CO_2 gas blown into calcium hydrogencarbonate solutions differing in concentration and in pH and which decarbonates them by heating. Investigating their production zones and control of their crystal shapes, a pure flat hexagonal vaterite phase was synthesized. This paper reports on this theme.

2. Samples and Test Method

2.1. Samples

The original calcium carbonate was powdered lime stone produced at Kuzuu, Tochigi Prefecture. It was manually pulverized in an agate mortar and sifted with a JIS standard sieve (200 mesh). The pulverized product having a specific surface area of $1.3m^2g^{-1}$ piled under the 200-mesh sieve was used. The results of X-ray diffraction analysis showed that the powdered lime stone was a highly crystallized calcite. The results of chemical analysis showed that it had a purity of 97.5%, containing impurities such as 1.14%MgO, 0.73%SiO_2, 0.26%Al_2O_3, 0.19%P_2O_5, 0.14%Fe_2O_3, and 0.03%SrO, etc.

For CO_2 gas blown into the lime stone powder suspended solution, a product by Suzuki Shookan (purity: 99.9%) was used. In order to adjust the pH level of calcium hydrogencarbonate solutions, sodium hydroxide guaranteed, and aqueous ammonia, extrapure (ammonia 28%), both made by Kanto Kagaku Co., Ltd were used.

2.2. Test Method

The solubility of calcium carbonate has a negative coefficient, causing the production of its solution to increase at lower temperatures. In order to prepare a calcium hydrogencarbonate, 0.045mol (4.5g) of the powdered lime stone was weighed out and was held together with $3dm^3$ of pure water at 2°C in a thermostatoven. In other words, CO_2 gas was blown into a line stone powder suspended solution at 2°C for 1h at a rate of $2dm^3\ min^{-1}$. The suspended solution was then filtered through a glass filter (G5) to obtain a saturated calcium hydrogencarbonate solution. The calcium hydrogencarbonate solution had a pH level of 6.2 and a concentration of about 10.3×10^{-3}mol $CaCO_3\cdot dm^{-3}$.

In order to investigate the synthesis and morphological control of calcium carbonate solutions, the pH(6.2 to 8.0) of the calcium hydrogencarbonate solution in this specified concentration (2.8 to 8.5×10^{-3}mol $CaCO_3\cdot dm^{-3}$) was adjusted, except pH6.2, by using sodium hydroxide and aqueous ammonia. The solution was heated with a mantle heater at the specified rate (1° to 40°C min^{-1}) up to the specified temperature (20° to 100°C) to precipitate modifications of calcium carbonate; a 240rpm agitation was applied to the solution when necessary. In addition, several methods for indicating the supersaturation level of calcium carbonate are known.[21] In the present study, the initial supersaturation level (α) of calcium carbonate was defined as $(C_i\text{-}C_s)/C_s$ for the sake of convenience. Here, $(C_i\text{-}C_s)$ is the initial supersaturation concentration of calcium carbonate, C_i is the concentration of the calcium hydrogencarbonate solution used, and C_s is the solubility of calcium carbonate (calcite): 1.4×10^{-4}mol $CaCO_3\cdot dm^{-3}$(20°C).[22,23]

The modifications of the calcium carbonate obtained and their crystal shapes were examined by X-ray diffraction analysis and SEM observation. Although there have been reports on how to determine the ratio of two existing modifications, it is difficult to determine the quantities of three modifications at a time.[24] Thus, in the present study, the ratio of the existing modifications was determined using their infrared absorption spectra, microscopy, and the ratio of the strongest X-ray diffraction peaks together.[25] In order to determine impurities in the powdered limestone, a chelatometric titration and induction coupling plasma (ICP) analysis were used together.

To adjust initial supersaturation level, a method, which obtains Ca^{2+} content by a chelatometric titration employing an EDTA solution, was used. Furthermore, an NN diluted powder was used for the reagent. To transform by heating flat hexagonal vaterite into calcite, the vaterite was held at the specified temperature (100° to 800°C) for 10min in an electric furnace.

3. Test Results and Discussion

3.1. Synthesis of Calcium Carbonate Modifications and their Morphological Control

Calcium carbonate has three crystal shapes: calcite (rhombohedral), aragonite (rhombic), and vaterite (hexagonal). Their production zones vary widely with synthesizing conditions, and these crystals have peculiar shapes. Thus, these features are often used in morphological control of calcium carbonate.

Calcium carbonate is insoluble in water (1.3×10^{-4}mol $CaCO_3\cdot dm^{-3}$, 25°C), but it is soluble in an acid solution having CO_2 gas dissolved. The present study began with preparing a calcium hydrogencarbonate solution by dissolving calcium carbonate in a carbonate solution. Conditions such as CO_2 gas blowing time, gas feed, and temperature have an effect on this preparation.

Figure 1 shows the effect of temperature on the quantity of dissolved calcium carbonate when CO_2 gas is blown into a lime stone powder suspended solution for 1h. At 2°C, the quantity of dissolved calcium carbonate was maximum 10.3×10^{-3}mol $CaCO_3\cdot dm^{-3}$, which was about 73 times that at 20°C (supersaturation level 72). At higher temperatures, carbonic acid (H_2CO_3) in the solution is thermally dissociated, emitting CO_2 gas. This causes the quantity of dissolved calcium carbonate to decrease. At 95°C, it is 2.4×10^{-3}mol $CaCO_3\cdot dm^{-3}$, about 1/4 of that at 2°C. When the solution is held at 100°C, the quantity of dissolved calcium carbonate further decreases. It is 1.4×10^{-3}mol $CaCO_3\cdot dm^{-3}$ when an equilibrium is reached after 5min of boiling.

Thus, in order to precipitate calcium carbonate, ① a method in which calcium hydrogencarbonate is prepared at 2°C, and ② a temperature at which calcium carbonate can be dissolved in large quantities and can then be decarbonated by heating is employed.

If CO_2 gas is blown for 1h into a calcium carbonate suspended solution at 2°C, the pH of the saturated calcium hydrogencarbonate solution obtained by filtering is 6.2. Near this pH level, impurities (Fe^{3+} Al^{3+} and P^{5+}) in the limestone powder do not dissolve. Thus this method is also effective to synthesize high-purity calcium carbonate. ICP analysis of impurities in this calcium carbonate solution did not detect Al^{3+}, Fe^{3+}, Sr^{2+} and P^{5+}. However, Si^{4+} by about 0.2% in terms of SiO_2 was detected. Again, MgO, the im-

purity which had shown the highest content in the raw materials, decreased to 0.4%.

When synthesizing calcium carbonate from a calcium hydrogencarbonate solution, the modifications and the particle size and shape obtained vary with conditions such as concentration, heating rates, hold time, and agitation speed. When calcium hydrogencarbonate solutions differing in initial supersaturation level are heated, calcite, aragonite, and vaterite crystals precipitate. Controlling synthesizing conditions, the production zones of single phases of these crystals and the control of crystal shapes were investigated.

First, a calcium hydrogencarbonate solution (8.5×10^{-3}mol $CaCO_3\cdot dm^{-3}$) at a supersaturation level of 60 was heated without agitation to investigate variations in the quantity of dissolution. With a heating rate of 5°Cmin^{-1}, precipitation started at around 60°C, and the quantity of dissolution plummeted at around 70°C. With a higher heating rate of 10°Cmin^{-1}, the precipitation temperature shifted toward the high temperature side. In addition, at temperatures having no immediate precipitation, calcium carbonate precipitated when the solution was held for a long time.

Figure 2 shows the production zones of precipitated calcium carbonate modifications obtained by holding calcium hydrogencarbonate solutions at various supersaturation levels at the specified temperatures, (a) without agitation and (b) with a 240rpm agitation. At a supersaturation level of around 40 to 60, with agitation, only a calcite phase was produced at heating temperatures below 30°C and only an aragonite phase at temperatures above 50°C. At temperatures between 30° and 50°C, calcite and aragonite coexisted. At lower supersaturation levels, the production zones of the calcite only phase and the aragonite only phase shifted toward the high temperature side. Without agitation, crystals precipitated within 2h at temperatures above 50°C with a supersaturation level of 60, and at temperatures above 95°C with a supersaturation level of 20. The precipitated calcium carbonate modifications were a mixture of vaterite and aragonite with supersaturation levels above 50, a mixture of the three modifications with supersaturation levels between 40 and 50, and a calcite-only phase with supersaturation levels below 40. This proved that agitation has a great effect on the production zones of the three modifications. However, such trends are not in equilibrium, they depend on hold time, heating rates, and other conditons. For example, if the hold time is extended, then the zone of crystal precipitation shifts toward the low temperature side, causing a transformation into calcite to be promoted.[26,27]

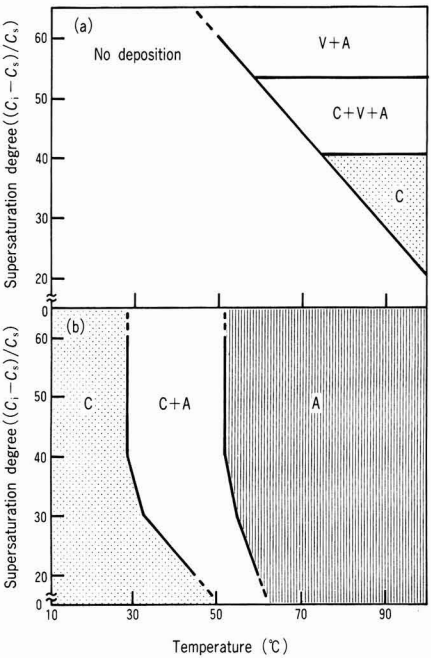

Fig. 2. Effect of heating temperature and supersaturation degree of calcium hydrogencarbonate solution on formation region of modification of calcium carbonate.
(a): No stirring; Holding time: 2h, Rising rate: 5°C min^{-1}.
(b): Stirring; Stirring speed: 240rpm, Holding time: 30min, rising rate: 5°C min^{-1}.
C: Calcite, A: Aragonite, V: Vaterite.

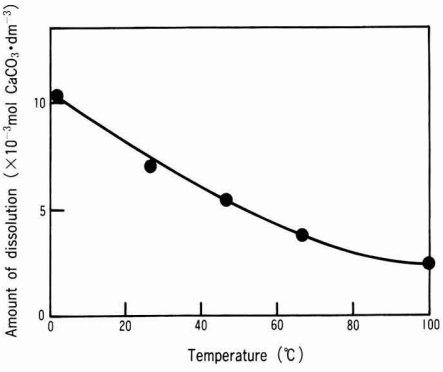

Fig. 1. Dissolution of calcium carbonate in the solution dissolved carbon dioxide at different temperatures.
Flow rate of CO_2: 2dm^{3}min^{-1}, 1h.

Figure 3 shows SEM photographs of calcium carbonate products obtained from heating at a rate of 5°C min^{-1} up to the specified temperature with a supersaturation level of 60. (a) through (c) are with agitation. At 30°C, a rhombohedral calcite-only phase having a grain size of about 10μm occurs. At 40°C, a mixture of columnar aragonite and rhombohedral calcite occurs, and at 60°C, a columnar aragonite-only phase having a grain size of about 45μm occurs, (d) is without agitation. At 60°C, a mixture of irregular vaterite and columnar aragonite having a grain size of about 100μm occurs.

The shape of columnar aragonite varies widely with temperature. This trend is shown in **Fig.4**. At 50°C, the major side is about 40μm. As temperature rises, it increases, and at 100°C, the mean major side is about 90μm. The aspect ratio also increases with temperature, ultimately over 20. Variations in the major side of columnar aragonite crystals were investigated with respect to heating rates, revealing that the higher the heating rate, the slower the growth of the major side. With heating rates below 5°C min^{-1}, the major side of crystals grows rapidly. For heating at a rate of 1°C min^{-1}, aragonite grows having a mean major side of 160μm at 100°C. The effect of agitation speed was also investigated, proving that the lower the agitation speed, the larger

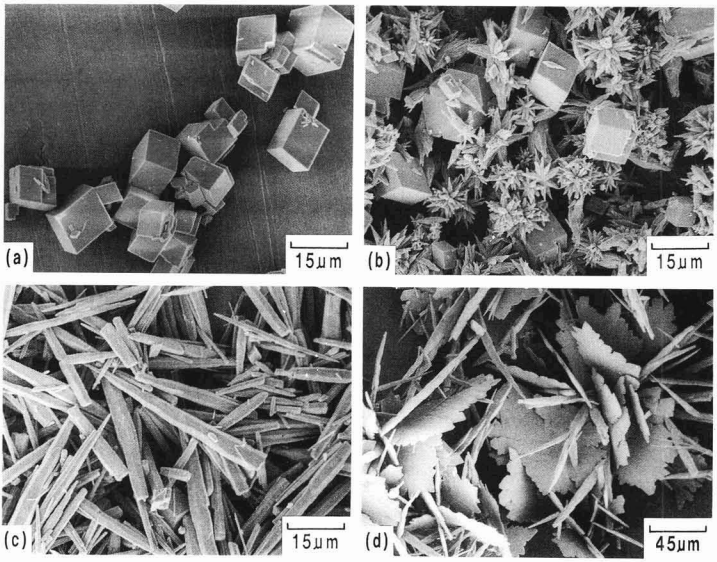

Fig. 3. Effect of heating temperature on crystal shape and modification of calcium carbonate.
Supersaturation degree: 60, pH: 6.2, Rising rate: 5°C min^{-1}, Heating temperature (°C), (a): 30, (b): 40, (c): 60, (d): 60.
(a)-(c): Stirring; Stirring speed: 240rpm, (d): No stirring.

the aspect ratio.

The above results proved that single phases of calcite and aragonite could be obtained by heating with an agitation while controlling the temperature for precipitation from a calcium hydrogencarbonate solution and that the major side of aragonite crystals could be controlled by temperature, hold temperature, and agitating speed. In addition, in order to obtain a vaterite only phase, it seems effective to heat the calcium hydrogencarbonate without agitation.

3.2. Synthesis of Flat Hexagonal Vaterite Crystals and their Shape Control

In order to obtain flat hexagonal calcium carbonate crystals, it seems reasonable to synthesize hexagonal vaterite. It is reported that a vaterite-only phase is produced when alcohol, acetone, or any other organic substance is added to the reactions of a high- or low-concentration $CaCl_2$-$(NH_4)_2CO_3$ solution.[28-33]

Vaterite is ordinarily unstable and is readily produced when the rate of calcium carbonate production is increased. In order to accelerate vaterite production, a test in which an alkaline substance was added to the calcium hydrogencarbonate solution while heating the solution at a higher rate was conducted. The addition of an alkaline substance decreased the concentration of the calcium hdrogencarbonate solution in order to permit vaterite to precipitate in temperature ranges above 40°C favorable for vaterite production.[13] For such alkaline substances, sodium hydroxide and aqueous ammonia were chosen.

Using either of these two alkaline substances, the pH of the calcium hydrogencarbonate solution was adjusted from 6.8 to 8.0, heat it to 100°C at a rate of 10°C min^{-1}, and held there for 5min. **Figure 5** shows the zone of vaterite production for calcium hydrogencarbonate solutions at various supersaturation levels with their pH adjusted with 1-N sodium hydroxide. The hatched portion represents the production zone of the vaterite only phase. With supersaturation levels of at around 60, the pH is around 6.9 to 7.0. With lower supersaturation levels, the pH must be adjusted upward. With a supersaturation level of 20, pH is around 7.3 to 7.5. If the pH is lower than the hatched portion, then vaterite with a trace of calcite is produced, and if the pH is higher, the calcite with a trace of vaterite is produced.

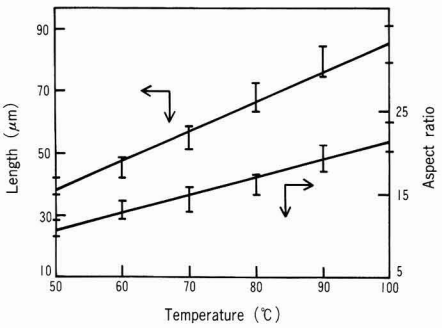

Fig. 4. Effect of heating temperature on particle size of aragonite.
Supersaturation degree: 60, pH: 6.2, Rising rate: 5°C min^{-1}.

Aragonite that is stable in high temperature ranges is not produced. This is because if there are cations having a larger ion radius than that of Ca^{2+} ions, then calcite and vaterite stable at 6-coordination are more readily produced.[14] In addition, if the pH is adjusted to higher than 8.0, then crystallized calcite is produced immediately.

Figure 6 shows the SEM photographs of vaterite products obtained, (a) with a supersaturation level of 20 and a pH level of 7.3, it shows thick flat hexagonal crystals of

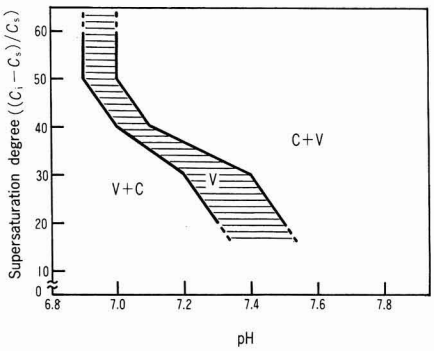

Fig. 5. Formation region of vaterite ($Ca(HCO_3)_2$-NaOH system). Heating temperature: 100°C, Holding time: 5min, Rising rate: 10°C min^{-1}, Control of pH: 1N NaOH solution. C: Calcite, V: Vaterite.

about 10μm, and (b) with a supersaturation level of 50 and a pH level of 7.0, it exhibits flower-like crystals, of about 25μm each, composed of petals and a central core. These results show that the pH has little effect on grain size of vaterite which varies with the level of supersaturation. In fact, when the pH was adjusted to 7.5 with a supersaturation level of 20, flat hexagonal crystals were about 10μm.

Figure 7 shows the zone of vaterite production using ammonia solution for pH adjustments. Although at a supersaturation level of 60, a vaterite-only phase can be obtained only with pH7.0, there exists a production zone sandwiched between two straight lines with supersaturation levels up to 30. In the pH range of above 7.8, there was no supersaturation level at which a vaterite-only phase could be obtained. A comparison between Figs.5 and 7 shows that a larger vaterite production zone can be obtained with aqueous ammonia than with sodium hydroxide.

Figure 8 shows SEM photographs of vaterite products obtained; (a) with pH 7.5 and supersaturation level 20, flat hexagonal crystals 1μm thick and about 20μm in diameter are shown. With a supersaturation level of 20, flat hexagonal crystals can be obtained irrespective of pH level, (b) with pH7.1 and supersaturation level 50, *ume* blossom-like crystals about 20μm with both core and edges grown are shown, (c) with pH7.5 and supersaturation level 40 shows precipitates showing the same trends are observed.

Figure 9 shows a variety of vaterite crystal shapes appearing in crystal growth; (a) through (d) show vaterite crystal shapes obtained with $Ca(HCO_3)_2$-NaOH systems, and (e) through (h) show ones obtained with the $Ca(HCO_3)_2$-NH_4OH systems. If sodium hydroxide is added, then thick flat hexagonal crystals of about 10μm are produced (a). As supersaturation level rises, crystals grow spreading their edges like flower petals (b) and grain size grows (c). Furthermore, via snow-like crystals, the crystals turn into flat ones peculiar to hexagonal crystals (d). On the other hand, if aqueous ammonia is added, then flat hexagonal crystals of about 20μm are produced with a low level of supersaturation, as shown in Fig.9(e). As the level of supersaturation rises, the crystals grow at their center and edges (f). Then, via *ume* blossom-like crystals (g), the crystals settle down into roundish disks (h). Again, as crystal shapes gradually change from (a) to (d) and from (e) to (h), the precipitation temperature and pH decrease. Thus, the optimal conditions for obtaining flat hexagonal crystals are to allow, by raising the precipitation temperature, crystals to be precipitated rapidly from the calcium hydrogencarbonate solution with a low level of supersaturation and a high level of pH. In addition, adding sodium hydroxide is effective to obtain small flat hexagonal vaterite crystals and adding aqueous ammonia is effective to obtain large vaterite crystals.

It was shown earlier, that adding an alkaline substance permitted vaterite to be produced more readily. **Figure 10** shows pH variations during the heating of a calcium hydrogencarbonate solution with a supersaturation level of 40 and with aqueous ammonia added. With the sample containing no aqueous ammonia, pH does not vary in a temperature range up to 60°C but stays at around 6.3. Thereafter, it rises because molecular carbonic acid (H_2CO_3) and hydrogencarbonate ions (HCO_3^-) dissolved in the solution are thermally dissociated, causing the concentration of carbonic acid ions (CO_3^{2-}) to increase. At around 85°C, calcium carbonate crystals start precipitating and at 100°C, pH is about 7.4. In other words, the nearer the pH of the calcium hydrogencarbonate solution to the alkali side, the higher the ratios of existing HCO_3^- and CO_3.[34] If aqueous ammonia is added, then HCO_3^- increases drastically. For example, at 18°C with pH6.3, $[H_2CO_3]/[HCO_3^-]$= 0.55/0.44. If the pH is adjusted to 7.4 with aqueous ammonia, then $[H_2CO_3]/[HCO_3^-]$=0.09/0.91. A rise in the HCO_3^- concentration accelerates dissociation into CO_3^{2-}, causing crystals to be precipitated at low temperatures.

With solutions adjusted to pH7.1 and pH7.4, crystals precipitate at around 50° and 40°C, respectively. In addition, adding aqueous ammonia causes pH to fall. This is because

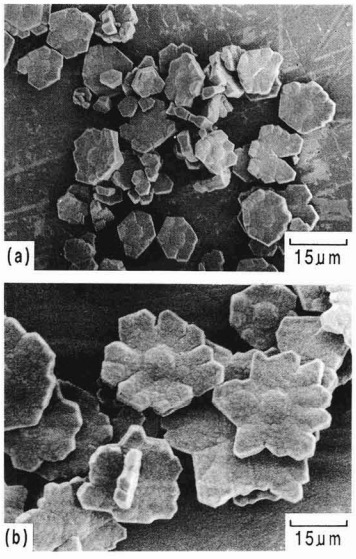

Fig. 6. Crystal shape of vaterite ($Ca(HCO_3)_2$-NaOH system). Heating temperature: 100°C, Holding time: 5min, Rising rate: 10°C min^{-1}.
(a) Supersaturation degree: 20, pH:7.3,
(b) Supersaturation degree: 50, pH: 6.9.

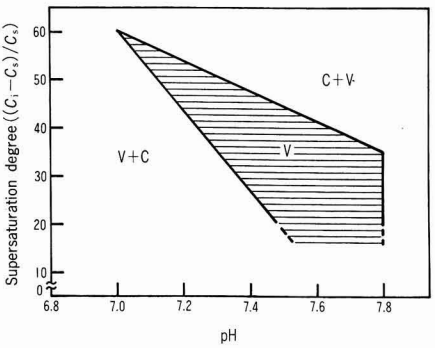

Fig. 7. Formation region of vaterite ($Ca(HCO_3)_2$-NH_4OH system). Heating temperature: 100°C, Holding time: 5min, Rising rate: 10°C min^{-1}, Control of pH: 1N NH_4OH solution.
C: Calcite, V: Vaterite.

HCO_3^- dissociates into CO_3^{2-}, which reacts with Ca^{2+} ions, producing calcium carbonate. In a temperature range above 85°C, the dissociation of HCO_3^- into CO_3^{2-} is accelerated, causing CO_2 to be emitted and ultimately resulting in a rise in pH once again. In other words, modifications of calcium carbonate are assumed to vary with CO_3^{2-} ion production rates. Again, the difference in crystal shape between sodium hydroxide and aqueous ammonia additives can partly be ascribed to free Na^+ and NH_4^+ ions being adsorbed onto respectively different crystal planes.

When using calcium carbonate as an inorganic filler, it is important to control grain size as well as grain shape. The control of vaterite grain size was also investigated. Particularly important here are heating rates for the calcium hydrogencarbonate solution. **Figure 11** shows the effect of supersaturation level and heating rates on vaterite grain shape. With a supersaturation level of 20 and a heating rate of 10°C min^{-1}, flat hexagonal crystals of about 20μm are

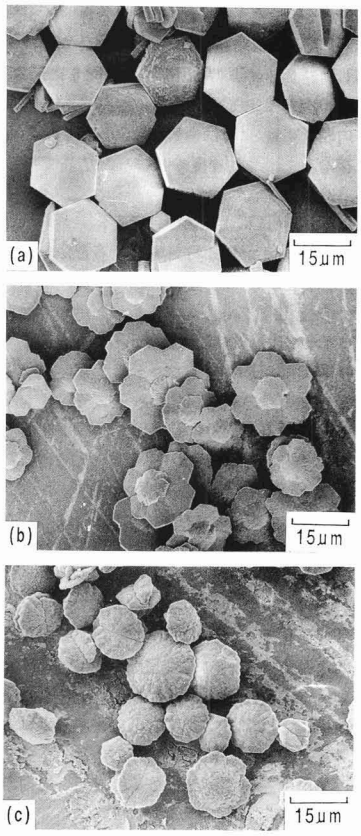

Fig. 8. Crystal shape of vaterite ($Ca(HCO_3)_2$-NH_4OH system). Heating temperature: 100°C, Holding time: 5min, Rising rate: 10°C min^{-1}. (a) Supersaturation degree: 20, pH: 7.5, (b) Supersaturation degree: 50, pH:7.1, (c) Supersaturation degree: 40, pH:7.6.

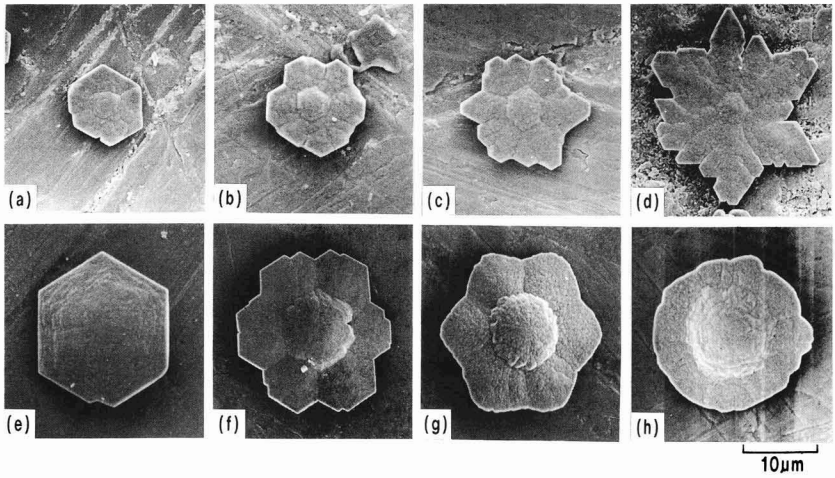

Fig. 9. Change in crystal shape of vaterite. Heating temperature: 100°C, Holding time: 5min, Rising rate: 10°C min^{-1}. Supersaturation degree, (pH): (a): 20, (7.3), (b): 30, (7.2), (c): 40, (7.0), (d): 50, (6.9), (e): 20, (7.5), (f): 40, (7.2), (g): 50, (7.1), (h): 60, (7.0). (a)-(d): $Ca(HCO_3)_2$-NaOH system, (e)-(h): $Ca(HCO_3)_2$-NH_4OH system.

produced, as shown in Fig.9(a). As the heating rate increases, the grain size gradually decreases, and it is about 7.0μm when the heating rate is 40°C min^{-1}. This trend is prominent at higher levels of supersaturation. With a supersaturation level of 50, vaterite crystals about 4.5μm, which is about 1/4 of the product with a heating rate of 10°C min^{-1} were obtained. However, raising the level of supersaturation, makes produced vaterite crystals roundish, as shown in Fig.9(g). The figure shows that a supersaturation level of about 30 is suitable for obtaining favorable small flat hexagonal crystals.

It was discovered that varying the level of supersaturation or heating rates was effective for the control of vaterite grain size and could in practice control it to a range around 4.5 to 20μm.

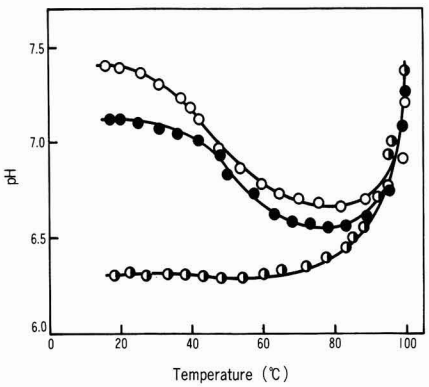

Fig. 10. Change in pH value by heating calcium hydrogencarbonate solution ($Ca(HCO_3)_2$–NH_4OH system).
Supersaturation degree: 40, Rising rate: 10°C min^{-1}.
○, ●: $Ca(HCO_3)_2$-NH_4OH system, ◑: No addition (pH 6.2), ●: pH 7.1, ○: pH 7.4.

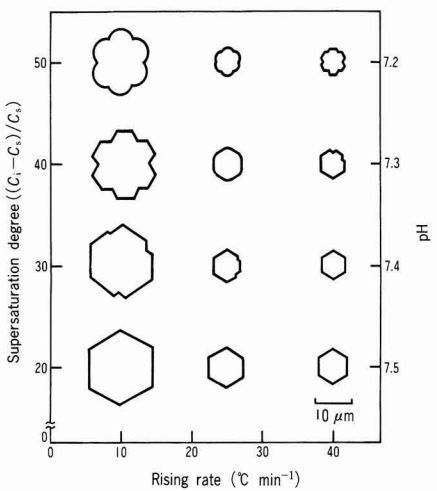

Fig. 11. Schematic illustration for shape and size controls of vaterite ($Ca(HCO_3)_2$-NH_4OH system).
Heating temperature: 100°C, Holding time: 5min.

3.3. Stabilization of Flat Hexagonal Vaterite Crystals

Among the three modifications of calcium carbonate, vaterite has the highest solubility of 2.3×10^{-4}mol $CaCO_3 \cdot dm^{-1}$ and is ready to transform into aragonite or calcite. The other two modifications have a lower solubility. It is also known that when heated, vaterite turns into calcite at around 400°C.[35] Thus, in order to use vaterite as an inorganic filler, it must be transformed into calcite, a stable phase.

The stabilization of flat hexagonal vaterite crystals was then investigated by heating. **Figure 12** shows the results of X-ray diffraction analysis of variations in heated vaterite. In the temperature range up to around 400°C, vaterite re-

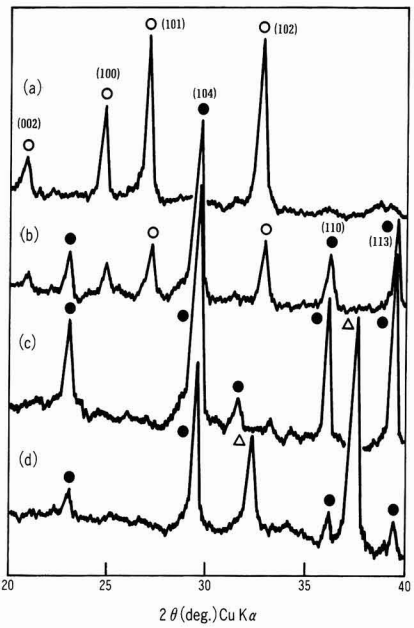

Fig. 12. Thermal behavior of hexagonal plate-like vaterite.
Heating temperature (°C), (a): 400°, (b): 500°, (c): 600°, (d): 800°.
○: Vaterite, ●: Calcite, △: Calcium oxide.

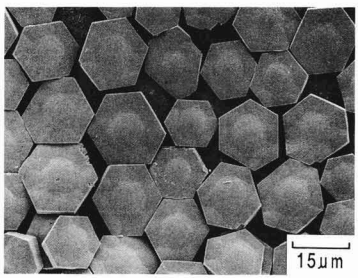

Fig. 13. Crystal shape of calcite obtained by heating hexagonal plate-like vaterite at 600°C.

mains by itself. Its flat hexagonal crystals are oriented having the (002) plane more developed than well-known burred vaterite crystals. Samples heated to 500°C show calcite peaks, and samples heated to 600°C are turned completely into calcite. This calcite has peak intensity for the (113) plane grown as compared to conventional rhombohedral crystals. Samples heated to 800°C have calcite pyrolyzed and showed calcium oxide intermingled.

Figure 13 contains the SEM photograph of a 600°C heated sample of flat hexagonal vaterite. While retaining the flat hexagonal shape of vaterite, the crystals have turned into calcite. Their surfaces are smooth, showing no cracks. In addition, it was verified that the flat hexagonal calcite immersed in water retained its flat hexagonal crystal shape despite more than three months of agitation.

In the present study, a calcium hydrogencarbonate solution with a pH level of about 6.2 is prepared by blowing CO_2 gas into a limestone powder suspended solution. At this pH level, there is no dissolution of Fe^{3+}, Al^{3+}, and P^{5+}, and these can be removed as sediments. Thus the purity of the calcium carbonate obtained by heating the calcium hydrogencarbonate solution was 99.7%. The purity of the vaterite obtained with an alkaline substance added was also nearly the same.

4. Conclusion

Preparing modifications (calcite, aragonite and vaterite) of calcium carbonate by decarbonating in heating a slightly acid calcium hydrogencarbonate solution obtained by dissolving limestone powder (purity: 97.5%) in a CO_2 gas fed solution, the synthesis of their single phases in stable zone and control of their crystal shapes were investigated. Holding a calcium hydrogencarbonate solution with an initial supersaturation level of around 40° to 60° at around 20° to 30°C while agitating it yields a rhombohedral calcite only phase, or in temperature ranges above 50°C it yields a columnar aragonite only phase. Again, aragonite crystals can be modified into columnar ones having a major side of about 40 to 160μm by varying factors such as heating temperature, heating rates, and agitation speed.

The production of a vaterite only phase was investigated by varying the pH level of the calcium hydrogencarbonate solutions at various levels of supersaturation by adding sodium hydroxide or aqueous ammonia. When sodium hydroxide was added, a vaterite only phase was obtained in a pH range of 6.9 to 7.0 with a supersaturation level of 60 and in a pH range of 7.3 to 7.5 with a supersaturation level of 20. When aqueous ammonia was added, a vaterite only phase was produced only at pH 7.0 with a supersaturation level of 60 and in a pH range of 7.5 to 7.8 with a supersaturation level of 20.

In addition, under adjusted conditions of pH 7.5 and supersaturation level 20 by using aqueous ammonia, flat hexagonal vaterite crystals of about 20μm were obtained. The purity of the vaterite was 99.7%, which proved the performance of the method in achieving a high purity of calcium carbonate products. Furthermore, vaterite grain size can be controlled over a wide range from 4.5 to 20μm by varying the level of supersaturation or heating rates. The flat hexagonal vaterite crystals thus obtained can be transformed by heating into calcite, a stable phase, without losing their flat hexagonal shape. It was verified that even when immersed in water for 3 months, the calcite crystals retained their flat hexagonal shape.

Acknowledgement

The authors would like to thank K. Matsuda and K. Sasaki, students at the Science and Engineering Dept., of Nihon University, who helped us with experiments, as well as S. Matsumura, Managing Director of Yoshizawa Sekkai Industries Co., Ltd. who supplied us with limestone samples.

References:

1) Y. Tanaka and M. Setoguchi, Sekko to Sekkai, No.183, 5-11 (1983).
2) T. Yasue, Y. Kojima and Y. Arai, ibid., 206, 3-9 (1987).
3) T. Yasue, Y. Tsuchida, K. Tanaka and Y. Arai, ibid., 196, 3-12 (1985).
4) D. Kralj, L. Brecevic and A.E. Nielsen, J. Cryst. Growth, 104, 793-800 (1990).
5) T. Yamaguchi, K. Murakawa, Zairyo, 30, 856-860 (1981).
6) G. Lucas, Bull. Soc. Fr. Mineral. Crystallogr., 70, 185-191 (1947).
7) Y. Inoue. Y. Kanazi, G. Hashizume and T. Miwa, Zairyo, 14, 719-724 (1965).
8) T. Noda, Kogyo Kagaku, 37, 733-736 (1934).
9) T. Noda, ibid., 37, 736-738 (1934).
10) J. Stolkowski, C.R. Acad. Sci., 225, 312-314 (1947).
11) J.D.C. McConnell, Miner. Mag., 32, 535-544 (1960).
12) S.R. Kamhi, Acta Cryst., 16, 770-772 (1963).
13) Y. Kitano, Bull. Chem. Soc. Jpn., 35, 1973-1980 (1962).
14) Y. Kilano, Gendai Kagaku, 6, 12-19 (1974).
15) Y. Kilano, Kogyo Kagaku, 59, 1346-1350 (1956).
16) Y. Kitano and D.W. Hood, Geochim. Cosmochim. Acta, 29, 29-41 (1965).
17) A. Tokuyama, H. Shimabukuro and E. Hika, Sekko to Sekkai, 155, 7-13 (1978).
18) Kokai Tokkyo 63-50316.
19) H. Vater, Zeit. Kristal., 27, 477-504 (1897).
20) B.R. Heywood, S.R. Rajam, J.D. Birchall and S. Mann, Biochem. Soc. Tran., 16, 284-285 (1988).
21) Y. Arai and T. Yasue, Funtai to Kogyo, 21, 3, 68-76 (1989).
22) Y. Arai and T. Yasue, Sekko to Sekkai, 228, 41-52 (1990).
23) J.M. Garcia-Ruiz and J.L. Amoros, Estud. Geol., 36, 193-200 (1980).
24) M.S. Rao, Bull. Chem. Soc. Jpn., 46, 1414-1417 (1973).
25) A.G. Xyla and P.G. Koutsoukos, J. Chem. Soc. Faraday Trans. 1, 85, 3165-3172 (1989).
26) H.R. Langelin, A. Delannoy, J. Nicole and J. Hennion, Inform. Chim., 252/253, 135-138 (1984).
27) T. Ogino, T. suzuki and K. Sawada, J. Cryst. Growth, 100, 159-167 (1990).
28) K. Nakamae, S. Nishiyama, S. Tauara, Y. Fujimura, J. Yamashiro, A. Urano and T. Matsumoto, J. Adhesion Soc. Jpn., 22, 573-579 (1986).
29) A.G. Turnbull, Geochim. Cosmochim. Acta, 37, 1593-1601 (1973).
30) O. Yamaguchi, N. Takashita and K. Shimizu, Bull. Chem. Soc. Jpn., 52, 1217-1218 (1977).
31) I. Kayama, Sekko to Sekkai, 146, 19-24 (1977).
32) A.J. Easton and D. Clauger, Mineral. Mag., 50, 332-336 (1986).
33) E. Pompe and H.A. Lehmann, Z. Chem., 20, 383 (1980).
34) L.N. Plummer and E. Busenberg, Geochim. Cosmochim. Acta, 46, 1011-1040 (1982).
35) Y. Arai and T. Yasue, Zairyo Gijutsu, 2, 296-304 (1984).

This article is a full translation of the article appearing in Journal of the Ceramic Society of Japan (Japanese version), Vol.100, No.9, pp.1145-1153, 1992.

Thermal Stress Characteristics of Graphite Coated with Y_2O_3

Yoshiyasu Itoh, Yutaka Ishiwata, Matsuo Miyazaki and Hideo Kashiwaya

Heavy Apparatus Engineering Labo., Toshiba Corporation
2-4, Suehiro-cho, Tsurumi-ku, Yokohama-shi, 230 Japan

The thermal stress of a graphite body coated with Y_2O_3 by plasma spraying was analyzed using a finite element method program. Especially, the effect of the intermediate layer Nb on the thermal stresses of the Y_2O_3 surface was studied by considering the stress relaxation. The analytical results indicated that the thermal stresses, σ_r, σ_t at the Y_2O_3 surface decreased with increasing thickness of Y_2O_3 and Nb layers. It was confirmed by experiments that the failure mode of the Y_2O_3/Nb/graphite composite was surface cracking by the thermal stresses, σ_r, σ_t induced during cooling. The critical heating temperature of the Y_2O_3/Nb/graphite composites was estimated by the finite element analysis. On the other hand, it was also confirmed that the strength and ductility of as-sprayed films of Y_2O_3 and Nb were improved by the recrystallization and sintering during the heating test.
[Received March 2, 1992; Accepted June 16, 1992]

Key-words: Y_2O_3, Nb, Graphite, Thermal stress, Residual stress, Plasma spray, Finite element method analysis

1. Introduction

Because of its excellent high-temperature characteristics and unique physical and chemical properties, graphite is widely used in industrial areas including rocket nozzles, moderators and reflectors for nuclear reactors, electrodes, and heat generators. In particular, in a nonoxidizing atmosphere, it is thermally and chemically so excellent up to high temperature ranges that it is an essential material for crucibles and boats used to dissolve, refine, and reduce metals and oxides. However, if it is used to dissolve very active materials such aluminum and titanium, then it reacts with such materials at high temperatures. In order to prevent this, graphite crucibles and boats are ordinarily coated with ceramics.[1)]

In particular, yttrium oxide coating has been proven to be effective. However, it involves problems such as cracking and separation because of the difference in coefficients of thermal expansion between the coating and base material.[2)] In this study, various types of ceramics for coating the surfaces of metallic bases have been attmepted, and it has been shown that thermal stresses generated in coatings have a great effect on coating cracking and adhesion. In addition, quantitative studies on the thermal stress (residual stress) characteristics of ceramic coating materials have been conducted.[3,4)] The conclusion providing an intermediate layer between coating and base is effective in releaving residual stresses.

In this paper, the thermal stress (residual stress) characteristics due to heating and cooling of yttrium coatings on graphite bases are discussed. In particular, analytical studies under a FEM and experimental studies using heating tests on the residual stress releaving effect of niobium used for the intermediate layer are addressed.

2. Analytical Method

Each sample for analysis consisted of a graphite base disk, 20mm thick and 25mm in radius, coated on one side with an intermediate niobium Nb layer t_{bond} thick. In addition, each was further coated with yttrium oxide Y_2O_3 t_{top} thick, as shown in **Fig.1**. For analysis, a thermal elasticity FEM program (square elements) was used. Because the samples were axially symmetrical, the hatched portion in Fig.1 was divided into finite elements for analysis. Damage to the Y_2O_3 coating was mainly caused by thermal stresses generated during cooling as described later, therefore, the thermal stresses generated during even cooling from a high temperature to room temperature (temperature difference ΔT), or residual stresses, were to be evaluated. In order to discover the effect of the intermediate Nb layer on residual stresses in analysis, samples with various thicknesses of intermediate and top coatings were used; t_{bond}: 0, 0.1, 0.25, 0.5mm and t_{top}: 0.05, 0.1, 0.25, 0.5mm.

2.2. Material Constants

Table 1 shows the chemical compositions of Y_2O_3 and Nb powders for plasma spray and graphite. The grain size of both powders was 10 to 44μm. The powders were applied in plasma spray in air under the conditions shown in **Table 2** to the isotropic graphite base having the surface roughed by blasting. For isotropic graphite, a type (ISO88 made by Toyo Tanso Co., Ltd.) comparable to Y_2O_3 and Nb in terms of coefficients of thermal expansion was selected.

In order to measure the material constants necessary for

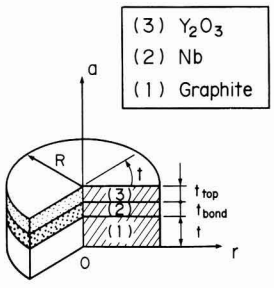

Fig. 1. Analysis model of ceramic coated graphite.

Table 1. Impurities of materials used.

Materials	Chemical compositions (ppm)									
Y_2O_3	Dy_2O_3	Ho_2O_3	Fe_2O_3	SiO_2	Al_2O_3	ZrO_2	MgO	CaO	Na_2O	–
	<100	<100	4	49	1	<2	0.8	4	65	–
Nb	Ta	Si	Sb	Ca	Fe	Cu	Ni	Ti	Mg	W
	365	15	10	10	75	20	10	10	80	<100
Graphite	Al	B	Ca	Fe	Mg	Ni	Si	Ti	–	–
	14	3	6	26	0.2	4	2	33	–	–

thermal stress analysis, samples were cut out of the coatings sprayed thicker on the graphite base. **Figure 2** shows some of the results of 4-point bending tests at room temperature with sprayed Y_2O_3 and Nb coatings and the graphite base. The load-strain relationship of Y_2O_3 coating shows a non-linear behavior beginning from the low level of bending loads. This may result from pores generated in the coating during spraying and local deformations caused by microcracks. The sprayed Nb coating showed a linear load-strain relationship resulting in a bending fracture. Despite being a well known ductile material, this may be because Nb was embrittled by oxides and by O_2 and N_2 gases contained in the coating.

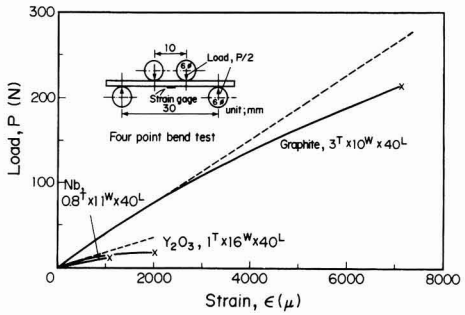

Fig. 2. Load-strain relationships for plasma-sprayed films and graphite.

Table 2. Conditions of plasma spraying.

Powders	Nb	Y_2O_3
Plasma gun	PLASMA TECHNIK AG, F-4	
Nozzle	Standard ø6mm	
Current (A)	600	550
Voltage (V)	63	67
Spray distance (mm)	110	110
Traverse speed (cm/min.)	400	400
Powder feed (g/min.)	13	9
Primary gas, Ar	0.49MPa, 55L/min.	0.49MPa, 42L/min.
Secondary gas, H_2	0.49MPa, 7L/min.	0.49MPa, 12L/min.

Figure 3 shows the thermal expansion-contraction curves for sprayed Y_2O_3 and Nb coatings and graphite measured in Ar atmosphere with a thermal expansion measuring instrument DL-1500 made by Shinku Riko. They show prominent hysteresis. This suggests that, as shown by their forming processes, sprayed coatings are not thermally stable but are contracted by sintering and recrystallized during heating at a rate of 5K/min. Because the test results showed that the thermal expansion-contraction curves settled after the second cycle, the coefficients of linear thermal expansion were determined accordingly. **Table 3** shows Young's modulus, Poisson's ratios, and the results of 4-point bending tests (each: mean for 5 test pieces) obtained at room temperature.

Table 3. Material constants obtained by experiments.

Materials	Graphite	Nb	Y_2O_3
Young's modulus (GPa)	12.1	49.2	31.8
Poison's ratio	0.15	0.4	0.27
Thermal expansion (1/K)	7.4	7.7	8.5
Bending strength (MPa)	74.0	53.9	37.3

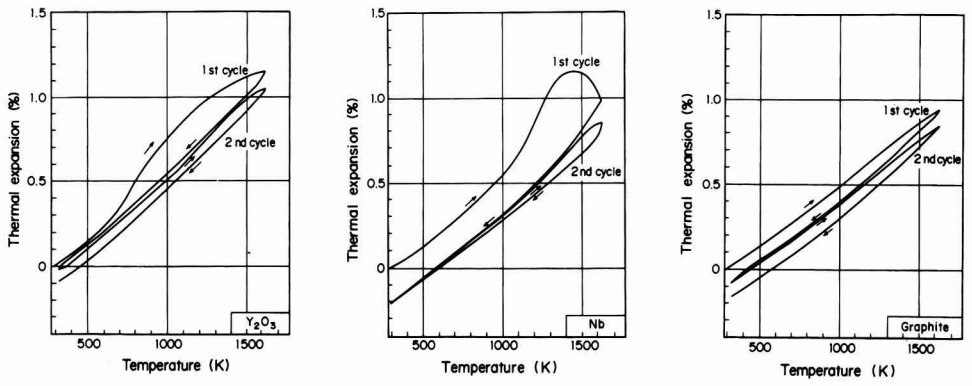

Fig. 3. Thermal expansion curves for plasma-sprayed films and graphite. (a) Y_2O_3 film, (b) Nb film, (c) Graphite.

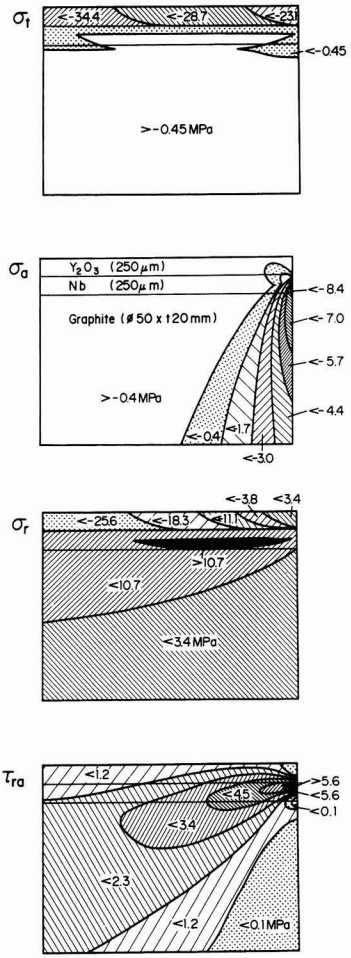

Fig. 4. Stress distributions on the cross-section of ceramic coated graphite.

3. Thermal Stress Distribution

Figure 4 shows the results of FEM analysis of thermal stresses generated near the boundary edge of a ceramic coating during even heating with a temperature difference of 1000K from room temperature to a high temperature. Because the coefficients of linear thermal expansion of Y_2O_3 and Nb are larger than that of the graphite base, the sprayed coatings are subject to a radial stress (σ_r) and a tangential stress (σ_t), both compressive. In even cooling with a temperature difference of 1000K from high to room temperature, the distribution characteristics are just the same as in Fig.4, except for the sign. Thus, the coatings are subjected to tensile stresses (σ_r, σ_t) during cooling.

On the other hand, at the edge of the interface between different materials, it is known that the axial stress (σ_a) vertical to the interface and shearing stress (τ_{ra}) show stress singularities.[5,6] In the present analysis, stress components σ_a and τ_{ra} showed prominent stress concentrations at the edges of the two interfaces between Y_2O_3 and Nb and between Nb and graphite. In particular, stress component σ_a became a tensile stress in the Y_2O_3 coating during heating and a compressive stress during cooling.

Thus, possible types of damage to the coatings of the Y_2O_3-Nb-graphite system under study may be ① separation-like cracking due to stress components σ_a and τ_{ra} at the edge of the interfaces during heating and ② vertical cracking due to stress components σ_r and σ_t at the center of the coatings during cooling.

3.2. Effect of Coating Thickness on Thermal Stresses

Because separation-like coating cracking due to stress components σ_a and τ_{ra} in the edge of the interfaces during heating are confined to the vicinity of the edge of the interfaces, they seldom have a great effect on the operating performance of the coatings. Vertical coating cracking due to stress components σ_r and σ_t at the center of the coatings during cooling take place over relatively wide areas and are expected to have a great effect on the working performance of the coatings. Focusing on stress components σ_r and σ_t at the center of the coatings, this paragraph will address the effect of the thicknesses of the Y_2O_3 and Nb coatings formed by plasma spraying. **Figure 5**(a) shows the data obtained on thermal stresses generated in Y_2O_3 coatings. The stress values here are divided by the temperature difference ΔT. The thinner the Y_2O_3 coating, the higher the values of ther-

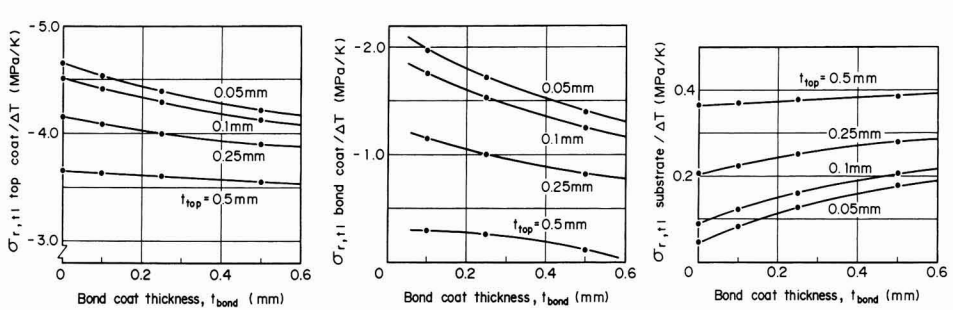

Fig. 5. Effects of Y_2O_3 and Nb coating thickness on thermal stress. (a) Stress at top coat, (b) Stress at bond coat, (c) Stress at substrate.

mal stresses σ_r and σ_t generated in the Y_2O_3 coating. The thicker the intermediate Nb layer, the lower the values of thermal stresses σ_r and σ_t generated in the Y_2O_3 coating. In other words, the thicker the surface and the intermediate layers, the more thermal stresses in the surfacial Y_2O_3 layer are released. Again, the thinner the surface Y_2O_3 layer, the fewer thermal stresses are released by the intermediate layer. Fig.5(b) shows the effect of coating thickness on thermal stresses generated in the intermediate Nb layer. Evidently, the thicker the Y_2O_3 and Nb coatings, the lower the thermal stresses σ_r and σ_t generated in the intermediate Nb layer.

Figure 5(c) shows the effect of coating thickness on thermal stresses σ_r and σ_t generated in the surface of graphite base. Here, the thermal stresses differ from those in the coatings. The thicker the Y_2O_3 and Nb coatings, the higher the thermal stresses σ_r and σ_t generated in the surface of the graphite base.

In summary, in the surface of the graphite base during heating, tensile thermal stresses σ_r and σ_t, occur which are much lower than those σ_r and σ_t generated in the Y_2O_3 coating during cooling. Thus, in even-heating tests, the primary type of damage is vertical cracks in the Y_2O_3 coating during cooling, and damage to coating can be controlled by increasing the thicknesses of the Y_2O_3 and Nb coatings.

4. Damage to Coating by Heating

4.1. Test Method

Y_2O_3-Nb-graphite samples made by coating the graphite base with intermediate Nb and surface Y_2O_3 layers by plasma spraying in air under the conditions shown in Table 2 were used. Applying the increasing thermal load shown in **Fig.6**, their heat resistance characteristics were investigated. The heat cycle consisted of even heating of the samples at a rate of 10K/min up to the specified temperature, holding the samples for 1h, and cooling them at a rate of 10K/min. While rising the holding temperature by 50K increments from 1623K, the surface of the coating in 50 magnifications was observed at each temperature level. Damage was searched for, and the critical heating temperature was detected. In the test, an electric furnace, was used, and the samples were loaded with the heat cycle mentioned above in a vacuum of 4×10^{-5} Torr.

4.2. Results of Heating Test

After the heating test, no coating separations were found on the Y_2O_3-Nb-graphite samples made by coating graphite disks, 25mm in radius and 20mm thick with an intermediate layer 250μm thick and a Y_2O_3 surface layer 250μm thick. However, vertical cracks at the center of the Y_2O_3 surface layers were found. This agrees well with the results derived from the FEM analysis. In addition, the critical heating temperature which caused vertical cracks in the Y_2O_3 surface layers was 1923K. **Figure 7** shows the results of the SEM observation of an as sprayed coating before the heating test. No macrocracks are found in the Y_2O_3 surface layers, but microcracks are found in the as-sprayed coating, as conventionally reported on testing for the zirconia coatings.[7] They were, probably generated when melted particles deposited on the base surface during plasma spraying were rapidly cooled and condensed. They must be discriminated from macrocracks in coatings by heating tests. **Figure 8** shows the results of SEM observation of a Y_2O_3 surface coating after a 1923K heating test. Evidently, microcracks in the as sprayed phase of the coating are found along with macrocracks. It is also noticeable that the Y_2O_3 coating formed by plasma spraying is turned by 1923K heating into a clear crystal grain structure. During the heating test, recrystallization and sintering progressed in the coating, and some of the microcracks observed in the as-sprayed phase were lost in sintering. **Figure 9** shows the results of observation of the cross-section structure of a sample after a 1923K heating test. The macrocracks found in the Y_2O_3 surface coating in the heating test still remain there. This may be because in addition to the low level of thermal stresses acting on the intermediate Nb layer, the Nb coating embrittled in the as sprayed phase, like the Y_2O_3 surface layer, recovered ductility as it was recrystallized and sintered by intense heating. Figure 9 also shows that the

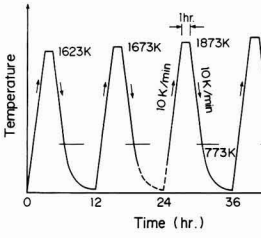

Fig. 6. Pattern of thermal cycle testing.

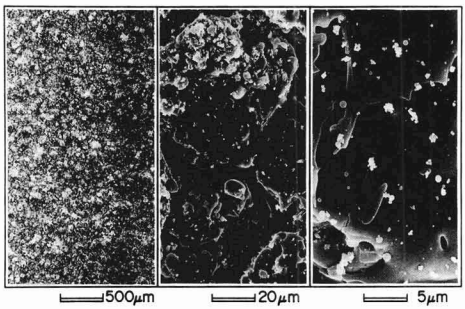

Fig. 7. SEM photographs of as sprayed Y_2O_3 surface.

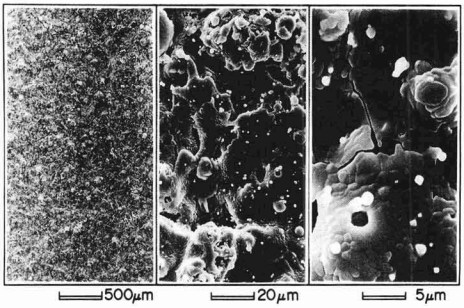

Fig. 8. SEM photographs of Y_2O_3 surface after heating at 1923K.

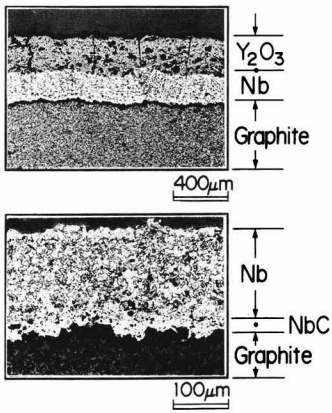

Fig. 9. Microphotographs of plasma sprayed coatings and interface after heating at 1923K.

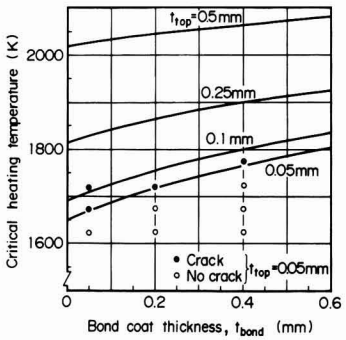

Fig. 10. Comparison of critical heating temperature between experiments and estimated results.

Nb layer has a clear crystal grain structure. It was also discovered that a slight NbC diffusion layer was formed at the interface between Nb and graphite.

From the results of FEM analysis in Fig.5(a), the coating strength, with the critical heating temperature causing cracks in the coating assumed as 1923K, can calculated as 65MPa. This is much higher than the 4-point bending strength 37.3MPa of the as sprayed Y_2O_3 coating shown in Table 3. Although the loading method was different, this may be because of the recrystallization and sintering promoted in the sprayed coating during the heating test. The calculated strength seems a reasonable value as compared to the 4-point bending strength 62.3MPa of the sintered Y_2O_3 obtained by 1923K for 1h under atmospheric pressure.[3] **Figure 10** shows critical heating temperatures of the coatings of Y_2O_3-Nb-graphite samples estimated from the results of FEM analysis in Fig.5(a), with the strength of the Y_2O_3 surface layer assumed as 65MPa. Here, the results are also shown for a heating test with various thicknesses of the intermediate layer: 50, 200 and 400μm again a constant thickness 50μm of the Y_2O_3 surface layer. Within the scope of the present test, there seems to be a good agreement between the estimated and measured values. Fig.10 shows that the critical heating temperature of the coating of the Y_2O_3-Nb-graphite system can be raised by increasing the thicknesses of the Y_2O_3 surface layer and the intermediate Nb layer. In addition, the thinner the Y_2O_3 surface layer, the more effective is the intermediate layer.

5. Conclusion

1) Thermoelastic FEM analysis proved the following: In the coated Y_2O_3-Nb-graphite system subjected to even heating, compressive thermal stresses σ_r and σ_t act during heating on the Y_2O_3 surface layer, which has a larger coefficient of linear thermal expansion than the graphite base, and tensile residual stresses act during cooling. The thicker the surface Y_2O_3 and intermediate Nb layer, the lower the thermal stresses σ_r and σ_t acting on the surface Y_2O_3 layer.

2) Coated Y_2O_3-Nb-graphite samples prepared by plasma spraying were subjected to an increasing heat cycle test in order to reveal critical heating temperatures. As the thickness of the intermediate Nb layer increased, the critical heating temperature rose, which agreed well with the estimated values from the thermoelastic FEM analysis.

3) In a heating test with coated Y_2O_3-Nb-graphite samples, the Y_2O_3 and Nb layers formed by plasma spraying were recrystallized and sintered, resulting in improving strength and ductility over their as-sprayed phase. In addition, NbC diffusion layer was formed at the interface between Nb and graphite.

References:

1) T. Ishii and M. Nagaoki, Shin Tansozairyo, Kindai Henshusha, (1986) 260-268.
2) J.W. Koger, C.E. Holcombe and J.G. Banker, Thin Solid Films, 39, 297-303 (1976).
3) Y. Ito, Y. Ishiwata and H. Kashiwaya, Seramikkusu Ronbunsh, 97, 747-752 (1989).
4) Y. Ito and H. Kashiwaya, ibid., 98, 1238-1244 (1990).
5) D.B. Bogy, Int. J. Solids Structure, 6, 1287-1313 (1970).
6) V.L. Hein and F. Erdogan, Int. J. Fracture Mechanics, 7, 317-330 (1971).
7) Y. Ito, Y. Ishiwata and H. Kashiwaya, Seramikkusu Ronbunshi, 98, 561-566 (1990).

This article is a full translation of the article appearing in Journal of the Ceramic Society of Japan (Japanese version), Vol.100, No.9, pp.1154-1158, 1992.

Effects of Y_2O_3 Addition on the Sinterability and Microstructure of Mullite(Part I)
— Phase Transformation and Sinterability —

Chii-Shyang Hwang and Der-Yang Fang

Department of Materials Engineering, National Cheng-Kung University
Tainan, Taiwan, R.O.C.

The effect addition of Y_2O_3 on the sinterability and microstructure of mullite was studied by differential thermal analysis, X-ray powder diffraction, scanning and transmission electron microscopy, and dilatometry. The mullite powder compacts containing 2~10wt%Y_2O_3 were sintered at 1500°C in air. The solid state reaction of Y_2O_3 and mullite during the sintering process produced some crystalline phases of yttrium silicates and α-Al_2O_3. The product phases were dependent on the amount of Y_2O_3 addition. The yttrium silicate and α-Al_2O_3 melted into a liquid phase at higher sintering temperature, which enhanced the sinterability of mullite powders. During the furnace cooling process, the liquid phase crystallized, and different crystalline phase were obtained depending on the amount of Y_2O_3.

[Received March 2, 1992; Accepted May 21, 1992]

Key-words: Y_2O_3, Mullite, Liquid phase sintering, Microstructure, Crystallization

1. Introduction

Mullite is the only stable compound at atmospheric pressure in an Al_2O_3–SiO_2 binary system. It is useful as a high temperature structural material because its high temperature strength and creep resistance are superior to alumina.[1] In addition, its dielectric constant is relatively low. Because mullite is difficult to sinter, dense sintered bodies can only be obtained by sintering over 1650°C for 2-4h when high purity powders prepared by hydrolysis of metal alkoxide or by the sol-gel method.[3-7] Therefore, many studies have been concerned about additives to improve its sinterability.[8]

It has already been reported that the addition of Y_2O_3 to mullite or Al_2O_3–SiO_2 binary system drastically lowers the sintering temperature.[9] In this case, rod like grains were created, and such gains improved the fracture toughness of the sintered body at high temperatures.[10] It has also been reported that strength degradation did not occur until 1200°C.[11,12] It is widely known that Y_2O_3 is also effective on Si_3N_4 to improve the sinterability and mechanical properties at high temperatures.[13-15] The properties of Y_2O_3–Al_2O_3–SiO_2 glass have been studied as a grain boundary model of Si_3N_4 sintered body.[16,17]

In this study, mullite powders added with Y_2O_3 were prepared, and the phase relation, sinterability, and microstructure were examined in order to improve the sinterability of mullite ceramics.

2. Experimental

2.1. Preparation and Sintering of Samples

The mullite powder (Chichibu Cement Co. Ltd., MP20) used in this experiment had a Al_2O_3/SiO_2 molar ratio of 1.51, a purity of 99.85%, and an average grain size of 1.46μm. The purity of Y_2O_3 (Wako Junyaku Co. Ltd.) was 99.9%, and the average grain size was 15μm. Additive powders less than 1μm were classified by sedimentation after being milled in an alumina pot. Mullite and Y_2O_3 powders were weighed to make a prescribed composition. After being wet milled in alumina pot for 12h using ethanol, they were evaporated to dryness on a 90°C water bath. A powder mixture was obtained by drying a 100°C oven overnight. The powder was pressed into a 5×5×45mm^3 rectangular bar by isostatic pressing two times, first at 25MPa, and then at 98MPa. The die used was coated by bakelite.

2.2. Sintering

In order to investigate the temperature dependence of powder phase, differential thermal analysis (DTA) was conducted by SETARAM TAG–24 up to 1500°C at a rate of 6°C/min. The temperature of the compact bodies was raised in the SiC furnace up to 1500°C at a rate of 6°C/min. They were maintained at that temperature for 2h and were then furnace cooled. Some of the powders and compact bodies were placed in a Pt foil, heated at that prescribed temperature, and quenched in air. Crystalline phases were identified, and microstructures were observed on both furnace cooled and quenched samples.

2.3. Measurement and Observation

Crystalline phases were identified by Powder X-ray diffraction method (XRD). XRD measurements were conducted by Rigaku Denki D/Maz111, in which a CuKα ray was generated by 30kV, 20mA, and a scanning rate of 4°/min. Shrinkage of the rod sample during the heating was measured by a differential dilatometer (SETARAM, DHT2050KN) at a rate of 6°C/min. The bulk density of the compact body was calculated from the volume and weight, and that for the sintered body was estimated by the Archimedes method in which water was used as a medium. The microstructure of the sintered body was observed by scanning electron microscopy (SEM, HITACHI, S-2500) and transmission electron microscopy (TEM, JOEL400-EX). Specimens are denoted as MY*X*. Here, *X* is the weight % of Y_2O_3 amount. In this study *X*=2, 3, 5, and 10.

3. Results and Discussion

3.1. DTA Profile of the Powders

Figure 1 shows the DTA curves of the sample with various amounts of Y_2O_3 added. There is an endothermic peak between 1310-1319°C in samples MY5 and MY10. In samples MY2 and MY3, a weak endothermic peak can be seen in this temperature range. Only sample MY10 exhibits a relatively sharp endothermic peak between 1390-1420°C. Accordingly, the reaction during the rising temperature is different among samples with various amounts of Y_2O_3.

3.2. Phase Relationship During the Sintering

Figure 2 shows the XRD patterns of the samples MY5 and MY10 quenched at various temperatures. In accordance with this result, the reaction and phase relationship of both samples during the elevating temperature can be expressed as follows:

$$2Y_2O_3 + 3Al_2O_3{\cdot}2SiO_2 \xrightarrow{\text{until } 1300^\circ C} 2Y_2SiO_5\,(X) + 3Al_2O_3 \quad \ldots\ldots\ldots\ldots (1)$$

$$2Y_2SiO_5\,(X_1) + 3Al_2O_3{\cdot}2SiO_2 \xrightarrow{\text{from } 1300^\circ \text{ to } 1390^\circ C} 2Y_2Si_2O_7\,(\alpha) + 3Al_2O_3 \quad \ldots\ldots\ldots\ldots (2)$$

$$Y_2Si_2O_7\,(\alpha) \xrightarrow{\text{from } 1385^\circ \text{ to } 1405^\circ C} Y_2Si_2O_7\,(\beta) \quad \ldots\ldots\ldots\ldots\ldots\ldots\ldots\ldots (3)$$

$$Y_2Si_2O_7\,(\alpha \text{ or } \beta) + Al_2O_3 + (3Al_2O_3{\cdot}2SiO_2) \longrightarrow \text{Liquid} \quad \ldots\ldots\ldots\ldots\ldots (4)$$

In short, the reaction of Y_2O_3 and mullite produced $Y_2SiO_5(X_1)$ and α-Al_2O_3 at 1200°C. The reaction of $Y_2SiO_5(X_1)$ and mullite produced α-$Y_2Si_2O_7$ and α-Al_2O_3 at around 1300-1390°C. In sample MY10, α-$Y_2Si_2O_7$ transformed into β-$Y_2Si_2O_7$ at around 1385-1405°C. In sample MY5, the β-$Y_2Si_2O_7$ phase was not created even at higher temperatures. At 1500°C, the $Y_2Si_2O_7$ phase disappeared, and mullite and a small amount of α-Al_2O_3 were detected in both samples. Accordingly, the reaction was different between samples with various amounts of added Y_2O_3. These results correspond to Fig.1, the endothermic peak at around 1310°-1390°C was due to the creation of X_1-Y_2SiO_5 and α-Al_2O_3. The endothermic peak at around 1390-1420°C was due to the transformation from α-$Y_2Si_2O_7$ to β-Y_2SiO_7.

Ito et al. reported that the transformation temperatures amoung polymorphic $Y_2Si_2O_7$ as follows;[18]

$$\alpha \xrightarrow{1225^\circ C} \beta \xrightarrow{1445^\circ C} \gamma \xrightarrow{1535^\circ C} \delta$$

The formation temperature of β-$Y_2Si_2O_7$ obtained in this study is slightly different from that reported by Ito et al. The increase in added Y_2O_3 was thought to enhance the creation of high temperature phase and β-$Y_2Si_2O_7$. On the other hand, no α-Al_2O_3 was detected even though a considerable amount should have been created according to Eqs.(1) and (2). This point can be explained in the following because the intensity of XRD pattern of compounds containing Y is larger than those of mullite and Al_2O_3, the XRD pattern of Al_2O_3 becomes relatively small. Furthermore, if 100g of MY10 powder (containing 10g or 0.044mol Y_2O_3) is used, then 6.77g (0.066mol) Al_2O_3 should have

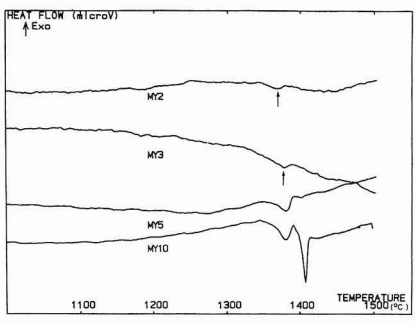

Fig. 1. DTA curves of the samples with various amount of Y_2O_3 addition.

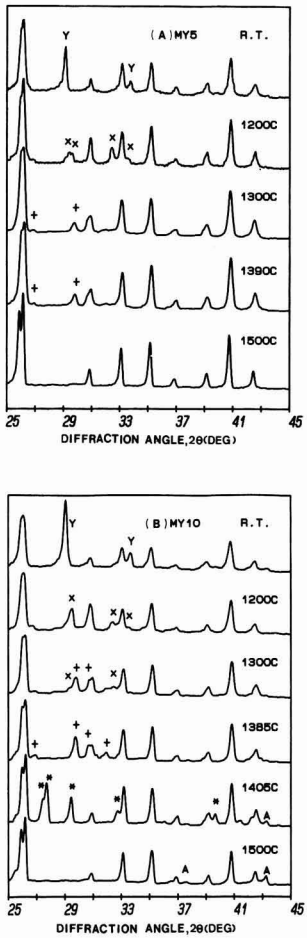

Fig. 2. XRD patterns of the samples quenched at various temperatures.
(A) 5wt%Y_2O_3, (B) 10wt% Y_2O_3 addition. (Y:Y_2O_3, X:$Y_2SiO_5(X_1)$, A:α-Al_2O_3, +:α-$Y_2Si_2O_7$, ✱:β-$Y_2Si_2O_7$, unmarked:mullite.)

been created according to Eq.(1). However, the particle size of Al_2O_3 grown below 1300°C was so small that its XRD pattern was hardly detected. Above 1300°C, 0.066mol of Al_2O_3 should have been created according to Eq.(2). Because the eutectic temperature of Al_2O_3–SiO_2–Y_2O_3 ternary system is 1350°C,[19] part of Al_2O_3 become eutectic mixture with $Y_2Si_2O_7$. Therefore, the XRD pattern of Al_2O_3 (2θ=43.4°) became small. In the case of the MY5 sample doped with 5wt%Y_2O_3, the amount of Al_2O_3 produced was relatively small, and the Al_2O_3 and $Y_2Si_2O_7$ made eutectic mixture. Therefore, the XRD pattern of Al_2O_3 was thought to be barely recognized.

Figure 3 shows the XRD patterns of the samples with various amounts of Y_2O_3 fired at 1500°C for 2h and then furnace cooled. The other crystalline phases can be seen. These phases were different among samples with various amounts of additive. α-$Y_2Si_2O_7$ and a small amount of α-Al_2O_3 were formed in sample MY5, and α-$Y_2Si_2O_7$ and small amount of α-Al_2O_3 were detected in sample MY10. On the other hand, in specimens MY2 and MY3, crystalline phases other than mullite have not been detected. Compared to the quenched sample shown in Fig.2, the furnace cooled sample showed a different reaction during cooling process from 1500°C accompanied by changing the amount of added Y_2O_3. In other words, α/β $Y_2Si_2O_7$ and α-Al_2O_3 were deposited from the liquid phase (reverse reaction of Eq.(4)) in samples MY5 and MY10. The liquid phase turned into the glass phase in samples MY2 and MY3. In accordance with these results, the liquid phase formed during the sintering crystallized at the cooling process, and the crystallization rate increased with increasing the Y_2O_3 addition.

3.3. Temperature Programed Shrinkage Profile and Bulk Density of the Sintered Bodies

In order to investigate effects of Y_2O_3 addition on shrinkage of mullite, the shrinkage profile up to 1600°C was measured. The results are shown in **Fig.4**. The initial temperature of the shrinkage shifted from 1400°C to 1200°-1300°C when Y_2O_3 was added. The shrinkage rate of that for no additive was relatively small, and the total shrinkage was 5% when heated 1600°C. In contrast, the shrinkage rate of sample with added Y_2O_3 increased with the amount of additon. The total shrinkage of those for 5 and 10wt% additive was 18%. In short, the sinterability of mullite was drastically enhanced by Y_2O_3 addition.

Because the eutectic temperature of Al_2O_3–SiO_2–Y_2O_3 ternary system is about 1350°C,[19] the enhancement of sinterability was ascribed to the liquid phase. According to Eq.(1)-(4), the liquid phase was thought to be created not from a simultaneous reaction between three component (Al_2O_3, SiO_2, Y_2O_3) but from the reaction between $Y_2Si_2O_7$ and Al_2O_3.

Compared to the other profiles, the shrinkage of the sample MY10 showed relatively large shrinkage at around 1200°-1310°C and a remarkable expansion at around 1380°-1410°C. According to the reports by Ito[18] and Lee[20] about lattice constant and volume change accompanied by phase transformation of the yttrium silicate and to the results in the previous section, the shrinkage is thought to be ascribed to a solid reaction as follows;

$$2Y_2O_3 + 3Al_2O_3{\cdot}2SiO_2 \longrightarrow 2Y_2SiO_5\,(X_1) + 3Al_2O_3$$
$$\Delta V = -12.5\%$$

Otherwise the shrinkage did not appear significantly because the reaction temperature was low and the density was also low. On the other hand, the expansion was ascribed to the 6% of volume expansion accompanied by the transformation from α-$Y_2Si_2O_7$ to β-$Y_2Si_2O_7$.

According to the analysis of the above crystalline phase, the theoretical density of the furnace cooled MY*X* sintered body was estimated as follows.

(a) Products in samples MY*X* formed by the reaction between Y_2O_3 and mullite.

MY10: $Y_2O_3 + 3Al_2O_3{\cdot}2SiO_2 \longrightarrow \beta$-$Y_2Si_2O_7 + 3Al_2O_3$

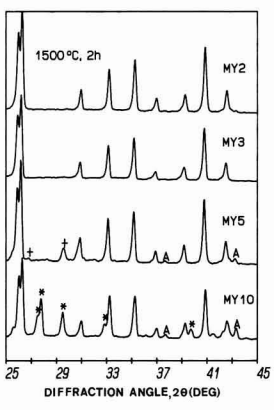

Fig. 3. XRD patterns of the samples with various amount of Y_2O_3 addition fired at 1500°C for 2h and cooling in furnace. (A:α-Al_2O_3, +:α-$Y_2Si_2O_7$, ✱:β-$Y_2Si_2O_7$, unmarked:mullite.)

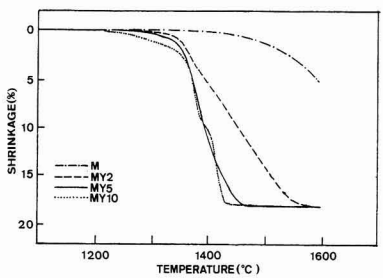

Fig. 4. Shrinkage curves of the green samples with various amount of Y_2O_3 addition.

Table 1. Theoretical density, bulk density, and relative density of sintered body.

specimens	Theoretical density (g/cm³)	Bulk density (g/cm³)	Relative density (%)
1700°C,1h (MY0)	3.17	3.13	98.74
1500°C,2h (MY2)	3.20	3.16	98.75
1500°C,2h (MY3)	3.22	3.15	97.83
1500°C,2h (MY5)	3.28	3.18	97.00
1500°C,2h (MY10)	3.37	3.24	96.14

MY5: $Y_2O_3 + 3Al_2O_3{\cdot}2SiO_2 \longrightarrow \alpha\text{-}Y_2Si_2O_7 + 3Al_2O_3$

MY2, MY3: $Y_2O_3 + 3Al_2O_3{\cdot}2SiO_2 \longrightarrow$ glass

(b) Theoretical density (g/cm^3) of the formed phase.

$3Al_2O_3{\cdot}2SiO_2$: 3.17, $\alpha\text{-}Y_2Si_2O_7$: 4.30, $\alpha\text{-}Al_2O_3$: 3.99, $\beta\text{-}Y_2Si_2O_7$: 4.03, Y_2O_3 : 5.03, glass : 3.77*

(* The theoretical density of glass was estimated from the density measured on a model glass by the Archimedes method. The composition of model glass was the same as that in the MY2 sintered body). The theoretical density calculated based on (a) and (b), bulk density, and relative density of sintered body are listed in **Table 1**. According to Table 1, the relative density decreased with an increase in the addition of Y_2O_3. Then, it changed from 98.7% in specimen MY2 to 96.1% in specimen MY10. The relative density of specimen MY2 sintered at 1500°C for 2h was about the same as that of no-additive sintered at 1700°C for 1h. Therefore, the effect of the addition of Y_2O_3 on the sinterability of mullite has been illustrated.

3.4. Microstructure Observation

Figure 5 shows SEM photographs of the samples sintered at 1500°C for 2h furnace cooled. There is a tendency for the pore size and pore amount to increase with an increase in the amount of added Y_2O_3. Pores of less than 1μm were distributed randomly in specimen MY2, and pores of about 3-5μm existed in specimen MY10. In general, the microstructure of the sintered bodies was uniform, even if the Y_2O_3 addition amount was relatively small such as 2 or 3wt%. Accordingly, the wettability of mullite particle by the liquid phase formed in the sintered body was quite good. **Figure 6** shows the SEM photographs of sample MY10 sintered at various temperatures. The pore size of the sintered body was small and uniform at around 1450°-1500°C when heated. The pores increased in size and decreased in number when the specimen was kept at 1500°C. This is because the small pores existing in the liquid phase joined to form a large pore. The decrease in relative density was ascribed to the volume expansion accompanied by the formation of such a large pore.

Figures 7, **8**, and **9** show the TEM microanalysis of samples MY2, MY5, and MY10 sintered at 1500°C for 2h and furnace cooled. The grain boundary phase in sample MY2 was recognized to be amorphous because the brightness of the grain boundary layer was dark gray, which was indispensable with inclination of the sample. Electron diffraction patterns in Fig.7(B) exhibit a crystalline phase. This is because the electron beam as large as 0.5μm irradiated not only amorphous grain boundary phase but also the vicinal crystalline phase. The grain boundary of sample MY5 was amorphous, or $\alpha\text{-}Y_2Si_2O_7$ crystalline phase. The grain boundary of sample MY10 was $Y_2Si_2O_7$ crystalline phase. The grain boundary of sample MY10 was $Y_2Si_2O_7$ crystalline phase (most of them were β form, but a small amount of $\alpha\text{-}Y_2Si_2O_7$ was detected), and no amorphous phase was detected. These results correspond to the X-ray diffraction shown in Section 3.2. In short, the amorphous grain boundary phase remained in the sintered body with a small amount of added Y_2O_3 during the cooling process while it turned to crystalline phase in that with a large amount of additive. The Y_2O_3–Al_2O_3–SiO_2 ternary glass created during the sintering process tended to crystallize when the Y_2O_3 amount was increased.

Murakami[8] pointed out that the Y_2O_3–Al_2O_3–SiO_2 ternary glass is difficult to crystallize due to the high activation energy if the composition comes to the eutectic composition. The composition of glass existing in the MY2 and MY10 specimens, sintered at 1500°C for 2h and quenched out of the furnace, is listed in **Table 2**. The composition was measured by EDS, and the result was converted to oxide composition. The average values of the measurements at two points are listed, but the measured values were almost identical within the specimen. Accordingly, the analytical value can be utilized in order to compare the compositions between specimens. The SiO_2/Y_2O_3 ratio of the specimen MY2 was larger than that of MY10, but the content of Al_2O_3 was almost the same. The composition of MY2 glass was

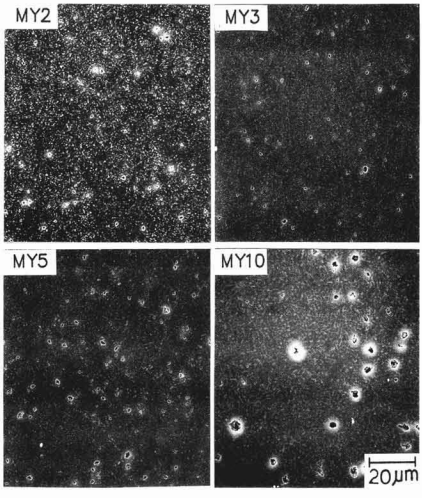

Fig. 5. SEM photographs of the samples with various amount of Y_2O_3 addition sintered at 1500°C for 2h.

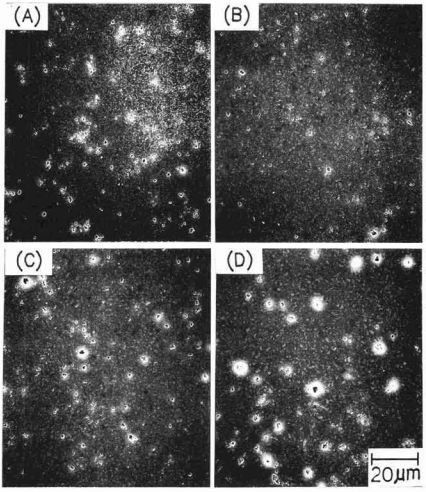

Fig. 6. SEM photographs of the 10wt%Y_2O_3-mullite sample sintered at (A) 1450°C, 3min, (B) 1475°C, 3min, (C) 1500°C, 3min, (D) 1500°C, 1h.

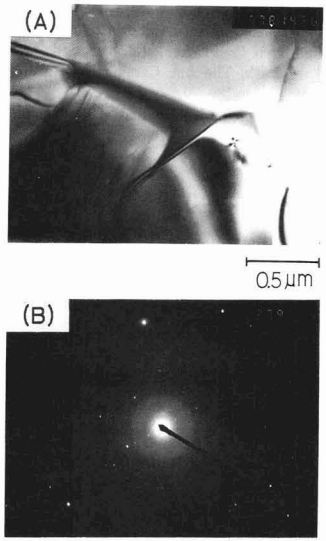

Fig. 7. TEM microanalysis of 2wt%Y_2O_3-mullite sample sintered at 1500°C for 2h and cooling in furnace. (A) bright field image, (B) electron diffraction pattern.

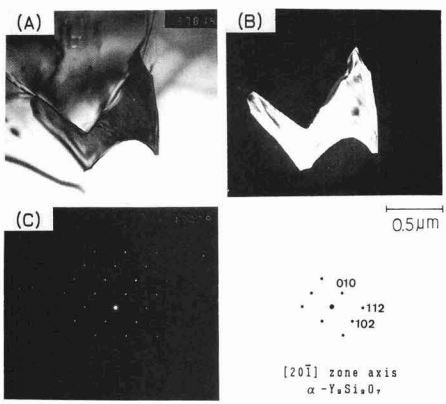

Fig. 8. TEM microanalysis of 5wt%Y_2O_3-mullite sample sintered at 1500°C for 2h and cooling in furnace. (A) bright field image, (B) dark field image, (C) electron diffraction pattern showing α-$Y_2Si_2O_7$ phase.

closer to the eutectic composition of the Y_2O_3–Al_2O_3–SiO_2 ternary system than MY10. These results correspond to those of Murakami. Accordingly, the glass phase existing in MY2 and MY3 was due to their higher activation energy than those in MY5 and MY10.

On the other hand, Michel et al.[21-23] reported that the Al_2O_3 content of liquid sintering mullite was between $3Al_2O_3{\cdot}2SiO_2$ (sintered-mullite) and $2Al_2O_3{\cdot}SiO_2$ (fused-mullite). In this study, becuase the starting material, mullite, has a composition close to $3Al_2O_3{\cdot}2SiO_2$, the amount of SiO_2 (free silica) dissolved into the liquid phase from mullite might increase with an increase in the amount of Al_2O_3

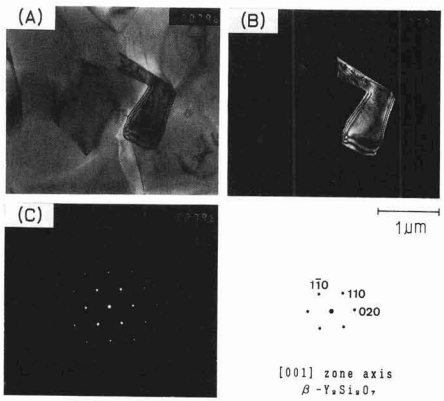

Fig. 9. TEM microanalysis of 10wt%Y_2O_3-mullite sample sintered at 1500°C for 2h and cooling in furnace. (A) bright field image, (B) dark field image, (C) electron diffraction pattern showing β-$Y_2Si_2O_7$ phase.

Table 2. Compositions of glass existing in MY2 and MY10 specimens sintered at 1500°C for 2h and quenched out of furnace (wt%).

Specimens	Al_2O_3	SiO_2	Y_2O_3
MY2	20.67	43.14	36.19
MY10	20.29	38.75	40.96

dissolved into mullite during the sintering. For this reason, the SiO_2 content relatively increased in samples with small Y_2O_3 addition (i.e., 2wt% added sample). Then, the composition came close to the eutectic composition of the Y_2O_3–Al_2O_3–SiO_2 ternary system. The crystallization of the liquid phase depended not only on the composition but also on the morphology. Because the liquid phase formed in MY2 and MY3 was smaller than those in MY5' and MY10, the amount of liquid phase in the grain boundary was relatively small. Accordingly the grain boundary layer was relatively thin, and it was hard to crystallize. The crystallization of the liquid phase during the furnace cooling will be reported in the next paper.

4. Conclusion

1) The addition of Y_2O_3 improved the sinterability of mullite, and a dense sintered body was obtained by sintering the mixed powder at 1500°C.

2) The solid reaction of Y_2O_3 and mullite during the sintering process produced some crystalline phases. First, X_1-Y_2SiO_5 and α-Al_2O_3 were formed. Second, the former reacted with mullite for producing α/β $Y_2Si_2O_7$ phase and α-Al_2O_3. At last $Y_2Si_2O_7$ and α-Al_2O_3 melted into the liquid phase at higher temperatures.

3) During the cooling process, the liquid phase crystallized, and the crystalline rate increased with an increase in the

amount of added Y_2O_3. The phase created also varied with the amount of Y_2O_3, α and β-$Y_2Si_2O_7$ were mainly crystallized in the 5 and 10wt% added samples, respectively.

(Part of this work has been reported at the 30th Symposium on Basic Ceramic Science, the Ceramic Society of Japan, Osaka, January 1992.)

Acknowledgement
This work was supported by Research Fund of National Science Committee, Republic of China (NSC80–0405–E006–14). The authors would like to thank Dr. K. Hamano for his helpful discussions.

References:

1) P.A. Lessing, R.S. Gordon and K.S. Mazdiyasni, J. Am. Ceram. Soc., 58, 149-150 (1975).
2) S. Kanzaki, M. Ohashi, H. Tabata, T. Kurihara, S. Iwai and S. Wakabayashi, Ceramics Transaction vol.6, Mullite and Mullite Matrix Composites, ed. by S. Somiya, R.F. Davis and J.A. Pask, Am. Ceram. Soc. Westerville, Ohio, (1990) 389-399.
3) M.G.M.U. Ismail, Z. Nakai and S. Somiya, ibid. 231-241.
4) S. Prochazka and F.J. Klug, J. Am. Ceram. Soc., 66, 874-880 (1983).
5) K.S. Mazdiyasni and L.M. Brown, ibid., 55, 548-552 (1972).
6) B.E. Yoldas, Am. Ceram. Soc. Bull., 59, 479-483 (1980).
7) S. Kanzaki, H. tabata, T. Kumazawa and S. Ohta, J. Am. Ceram. Soc., 68, C6-7 (1985).
8) Y.M. Agamawi and J. White, Trans. Brit. Ceram. Soc., 61, 293-323 (1962).
9) Y. Murakami and H. Yamamoto, Seramikkusu Ronbunshi, 99, 215-221 (1991).
10) T. Mori, N. Kosugi, Y. Ishikawa and Y. Kubota, Seramikkusu Ronbunshi, 98, 1307-1312 (1990).
11) N. Ushifusa and S. Ogihara, J. Ceram. Soc. Japan. Inter, Ed.97, 678-684 (1989).
12) T. Milamura, H. Kobayashi, N. Ishibashi and T. Akiba, Seramikkusu Ronbunshi, 99, 351-356 (1991).
13) W.E. Lee and G.E. Hilmas, J. Am. Ceram. Soc., 72, 1931-1937 (1989).
14) M.K. Cinibulk and G. Thomas, ibid., 73, 1606-1612 (1990).
15) J.C. Almeida, A.T. Fonseca, R.N. Correia and J.L. Baptista, Mater. Sci. and Engineer., A109, 395-400 (1989).
16) K. Oda and T. Yoshio, Seramikkusu Ronbunshi, 97, 1493-1497 (1989).
17) K. Oda and T. Yoshio, Seramikkusu Ronbunshi, 99, 1150-1152 (1991).
18) Jun Ito and Harold Johnson, Am. Miner., 53, 1940-1952 (1968).
19) Phase Diagram for Ceramist, Vol.2, Am. Ceram. Soc. Columbus, Ohio, (1969) 165.
20) W.E. Lee, C.H. DrummondIII, G.E. Hilmas and S. Kumar, J. Am. Ceram. Soc., 73, 3575-3579 (1990).
21) D. Michel, L. Mazerolles, R. Portier, Ceramic Transactions vol.6, Mullite and Mullite Matrix Composites Ed. by S. Somiya, R.F. Davis and J.A. Pask, Am. Ceram. Soc. Westerville, Ohio, (1990) 435-447.
22) H. Schneider, ibid. 135-157.
23) J.A. Pask, Ceramics Int. 9,4, 107-113 (1983).

This article is a full translation of the article appearing in Journal of the Ceramic Society of Japan (Japanese version), Vol.100, No.9, pp.1159-1164, 1992.

Correlation between Gas Sensing Properties and Preferential Orientations of Sputtered Tin Oxide Films

Jae-Sang Ryu, Yuichi Watanabe and Masasuke Takata

Department of Electrical Engineering, Nagaoka University of Technology
1603-1, Kami Tomioka-cho, Nagaoka-shi, 940-21 Japan

Investigations on preferential orientation of tin oxide films were carried out under various conditions of film fabrication from the view point of the effect on sensing mechanism. The preferential orientation of (110) crystallographic plane resulted in the increase of sensitivity for H_2 gas. The observed relationship between the sensitivity and preferential orientation has been understood by considering the maximum atomic density on the (110) plane, which ensures the large numbers of adsorption sites for atmospheric gas as well as of direct reaction sites for H_2 gas.

[Received April 10, 1992; Accepted May 21, 1992]

Key-words: Thin film, Sputtering, SnO_2, Preferential orientation, Gas sensing mechanism

1. Introduction

Tin oxide is an n-type semiconductor which is widely used for gas sensors and as transparent electrode in such forms as sintered bodies and both thick and thin films. Many studies concerning the gas sensors have been conducted with the purpose of improving its sensitivity by optimizing the process[1-4] and doping with other oxides.[5-7] Understanding the sensing mechanism is crucial in order to improve the sensing properties. A gas sensing mechanism has been proposed as follows:[8]

(1) Gate action model: Electrical conduction through a space charge layer at the vicinity of grain boundaries is controlled by a chemisorbed gas which changes the potential barrier.
(2) Surface conduction: Carrier density contributing to surface conduction is changed by a charge exchange between the adsorbed gas, and the sensor.
(3) Oxidation and reduction: The intrinsic conduction of the material is changed by a redox reaction with the adsorbed gas.
(4) Self-heating effect: Electrical conductivity is changed by elevating the surface temperature accompanied by gas adsorption.

Model (1) is thought to be a predominant gas sensing mechanism in bulk sintered body and model (2) is in thin film. One of the carrier-supplying reactions in surface conduction is a direct transfer from the adsorbed gas to the semiconductor oxide, and another is a charge exchange between the chemisorbed surface oxygen and outer adsorbed gas.

It is usually not sufficient to explain such a gas detection with a single mechanism. In particular, gas detection of a thin film is thought to consist of complex processes such as adsorption.[9] on electrical conduction. In our previous paper,[10] we reported that the hydrogen gas sensing of sputtered tin oxide depended heavily on the sputtering condition, such as oxygen content in sputtering gas and sputtering gas pressure. This is because the a sputtering condition influences crystallinity, orientation, and thickness of the sputtered film. As a result, it changes the sensing properties.

Among the factors influencing the detection properties, we investigated the crystal structure, in particular, the preferential orientation depending on the preparation process. In addition, we discussed these effects on gas sensing properties and sensing mechanism.

2. Experimental

2.1. Preparation of Thin Film

Tin oxide thin film was prepared by r.f. magnetron sputtering method (instrument: SPK-301, Tokki). Tin oxide powder (purity 99.99%, Furuuchi Chem.) was used as a target, and thin films were deposited on non-alkaline glass (corning #7059, 7mmW×17mmL) substrate in a mixed gas (argon<99.999%> + oxygen<99.9%%>) atmosphere. The substrate temperature was raised when sputtered, though not intentionally. The crystal structure and orientation of tin oxide was changed by controlling the atmospheric gas composition, sputtering gas pressure, and sputtering time. Sputtering conditions are listed in **Table 1**.

The crystal structure of the film was examined by the X-ray diffraction method (Rint 1500 with Hitachi Workstation 2050, Rigaku Denki). The scanning speed was 2θ=4°/min, and the sampling width was 2θ=0.020°. The film thickness was deduced from the step between film surface and substrate measured by a surface profiler (Surfcom 200B, Tokyo Seimitsu).

2.2. Measurement of Resistivity and Gas Sensitivity

All the films obtained were annealed at 500°C for 18h in air to eliminate the residual strain. Gold electrodes were sputtered on the annealed samples (electrode width=1mm) using a simple sputtering instrument (SC-701, Sanyu

Table 1. Sputtering conditions.

Target	SnO_2 powder (purity: 99.99%)
Substrate	alkali-free glass (Corning #7059)
T/S spacing	40 mm
Sputtering gas	$Ar+O_2$
(O_2 content	0 ~ 30 %)
Sputtering gas pres.	$8x10^{-4}$ ~ $3x10^{-2}$ Torr
Presputtering time	1 hr
Sputtering time	1 ~ 5 hr
RF input power	200 W (3.96 W/cm^2)

denshi). Silver paste was used to connect the electrodes with wires, and these specimens were subjected to gas sensing measurement. Dry air containing 50ppm hydrogen gas was used as the detection gas. Electrical measurement was conducted by digital electrometer (TR8652, Advantest), programmable voltage constant power supply (TR6142, Advantest), and digital multimeter (TR51 and TR6846, Advantest) using the four electrodes method.

The sensing property was obtained as a change in resistance when the detection gas was introduced at a rate of 20ml/min at 300°C. Here, the sensitivity was defined as the ratio of the resistance in dry air (R_a) to the resistance in detective gas (R_g), which was expressed as

$$\text{Sensitivity} = \frac{R_a}{R_g} \quad \cdots\cdots\cdots\cdots\cdots (1)$$

2.3. Estimation of Crystal Orientation

The crystal orientation of the tin oxide films depended heavily on the sputtering conditions. Many methods have been proposed to estimate the crystal orientation from X-ray diffraction pattern (i.e., Lotgering method[11]). In this study, an orientation (F) was determined according to the following equation;

$$F(hkl) = \frac{I(hkl)}{I(110) + I(101) + I(211)} \quad \cdots\cdots (2)$$

Here, $I(hkl)$ is the integrated intensity of the X-ray diffraction from the (110), (101), or (211) plane. In the equation, only the diffraction intensities from (110), (101), and (211) are taken into account for two reasons. One is that the sum of these intensities was as large as 52.1% of the sum of all intensities in the XRD pattern of tin oxide powder, which can be estimated as non oriented sample. Another is that these peaks can easily be detected in the film specimen. According to Eq.(2), $F_p(hkl)$ for the powder sample can be calculated to be $F_p(110)$=0.409, $F_p(101)$=0.320, and $F_p(211)$=0.272, respectively. If the $F(hkl)$ for a film specimen exceeded these value, then the crystal plane was taken to be oriented.

3. Result

3.1. Sputtering Condition and Crystal Structure of Tin Oxide Films

The thickness of the fabricated thin films was 0.3-1.5μm, which depended heavily on sputtering condition. In accordance with XRD analysis, the intensity and half width of a specific crystalline peak was different among the samples prepared under different conditions. In short, crystalline orientation and size changed with processing.

Figure 1 shows the XRD profiles of the film prepared in Ar + O_2 atmosphere. Here, sputtering pressure, time, and RF powder were fixed at 8mTorr, 2h, and 200W, respectively. From Fig.1, it is apparent that the relative intensity for each peak is different from that of powder, while the main phase of the films is SnO_2 irrespective of oxygen content in sputtering gas. In particular, the relative intensity of the (110) plane increased with an increase in the oxygen partial pressure of sputtering gas. The crystalline orientation of the (110) plane depended heavily on the total sputtering pressure in addition to oxygen content. The relationship between the sputtering condition and (110) plane orientation is listed in **Table 2**.

3.2. Gas Sensing Properties in Tin Oxide Thin Films

Figure 2 shows the hydrogen gas sensitivities and (110) orientations as a function of oxygen content in the sputtering gas.

The sensitivity of the film prepared in sputtering gas without oxygen was unity. That is, such a film showed no resistivity change in a hydrogen atmosphere of 50ppm. The sensitivity increased to 13 as the oxygen content in sputtering gas increased.

On the other hand, the dependence of the orientation of (110) plane on oxygen content was similar to that of sensitivity. In other words, the orientation increased with an increase in the oxygen content. Accordingly, it suggested a close relationship between sensitivity and orientation.

Table 3 shows the (110) plane orientations (110) and resistivities both in air and 50ppm H_2 gas containing air at 300°C for films prepared at various sputtering condition. The sensitivity increased with an increase in the (110) plane orientation. **Figures 3** and **4** show the correlation between resistivities and (110) or (101) orientations of the films prepared under various sputtering conditions. Sensitivity was shown to depend on the (110) plane orientation and to inversely depend on the (101) plane orientation.

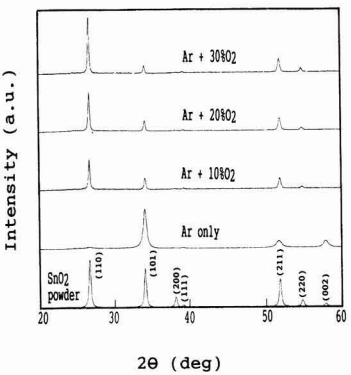

Fig. 1. XRD profiles of the films prepared by sputtering in Ar+O_2 atmosphere of 8×10^{-3}torr, in which the O_2 content was changed from 0 to 30%. Powder XRD profile for SnO_2 is also presented.

Table 2. The relationship between the sputtering conditions and (110) plane orientations, $F(110)$, of films prepared by sputtering in Ar+O_2 atmosphere at the input power of 200W.

total gas pressure (Torr)	oxygen content (%)	F(110)*
8×10^{-3}	0	0.019
	10	0.452
	20	0.465
	30	0.605
3×10^{-3}	20	0.754
8×10^{-3}	20	0.465
3×10^{-2}	20	0.511

*F(110) = 0.409 for random orientation

4. Discussion

The results suggested a correlation between gas sensitivity of the tin oxide thin film and crystalline structure, especially orientation. This correlation can be ascribed to various factors, but one of the main factors is the sensing mechanism.

Gas sensing mechanisms can be classified into two groups, as far as sensitivity was expressed on the basis of conductivity change. The trapping of conduction electrons in tin oxide by the adsorption of oxygen gas onto its surface or grain boundary is a prerequisite for the first mechanism. If a reactive gas desorbs adsorbed oxygen, the trapped electrons are released and increase the conductivity. In this model, the total conduction electrons, including the trapped ones by adsorped oxygen, remains constant. Thus, the sensitivity depends on the number of trapped electrons which is equal to that of adsorbed oxygen.

In contrast, in the redox mechanism conductivity, the jump is ascribed to a newly formed electron derived from direct reaction between tin oxide and reactive gas. In this model, the sensitivity is improved when the site number to react with reactive gas is increased.

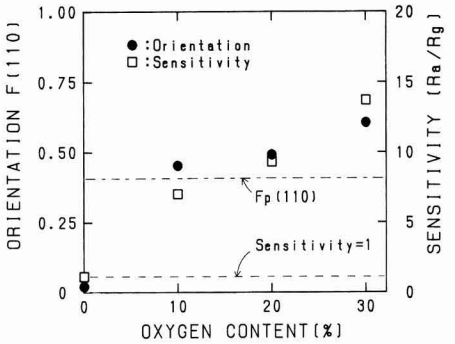

Fig. 2. The H_2 gas sensitivities (□) and (110) orientations (●) as a functions of O_2 content in the sputtering gas (sputtering gas pressure; 8×10^{-3}torr, radio-frequency power; 200W).

Table 3. The (110) plane orientations, $F(110)$, with relation to the sensitivities obtained from electrical resistivities in air and 50ppm H_2 gas at 300°C for films prepared at various sputtering conditions.

sputtering condition		resistivity at 300°C(Ω·cm) in air	resistivity at 300°C(Ω·cm) in 50 ppm H_2	sensitivity	F(110)
sputtering pressure (mTorr)	3	3.3×10^{1}	3.3×10^{0}	10.0	0.754
	8	6.8×10^{-1}	2.3×10^{-1}	3.0	0.430
	30	5.0×10^{-2}	4.5×10^{-2}	1.1	0.511
oxygen content (%)	0	1.9×10^{-1}	1.7×10^{-1}	1.1	0.019
	10	6.9×10^{0}	9.9×10^{-1}	7.0	0.452
	20	5.2×10^{0}	5.6×10^{-1}	9.3	0.491
	30	6.1×10^{0}	4.5×10^{-1}	13.7	0.605
sputtering time (h)	1	5.0×10^{1}	3.3×10^{0}	15.0	0.678
	2	5.2×10^{0}	5.6×10^{-1}	6.0	0.475
	3	5.0×10^{-1}	1.3×10^{-1}	4.0	0.375
	5	5.0×10^{-2}	5.0×10^{-2}	1.0	0.279

*RF power = 200W

In both mechanisms, the sensitivity depends on the atomic density of the tin oxide surface. **Figure 5** shows the schematic illustration of SnO_2 crystal structure. Tin oxide belongs to space group D $4h14[P42/mnm]$ and tetragonal rutile structure. Its unit cell is composed of six atoms, and each tin atom is located at the center of the regular octahedron formed by six oxygen atoms. On the other hand, each oxygen atom is in a trigonal site made by tin atoms.

Shaded parts (a) and (b) in Fig.5 represent the (110) and (101) plane, respectively. Two oxygen atoms (●) and two tin atoms (○) are contained in the shaded part of the (110) plane. On the other hand, no oxygen atom and two tin atoms are contained in the shaded part of (101) plane. The surface atomic densities of tin and oxygen atoms at typical lattice planes of tin oxide are listed in **Table 4**. According to this table, the (110) plane has the maximum atomic den-

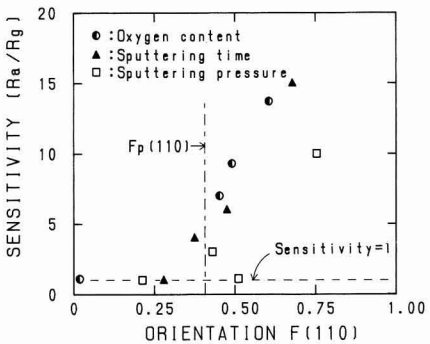

Fig. 3. The correlation between sensitivities and (110) orientations of films prepared at various sputtering conditions: ◐: oxygen content from 0 to 30% under fixed sputtering time of 2h and total pressure of 8×10^{-3}Torr, ▲: sputtering time from 1 to 5h in Ar+20%O_2 atmosphere of 8×10^{-3} Torr, □: total gas pressure from 8×10^{-4} to 3×10^{-2} Torr for 2h in Ar+20%O_2 atmosphere. The radio-frequency power for sputtering was 200W in all cases.

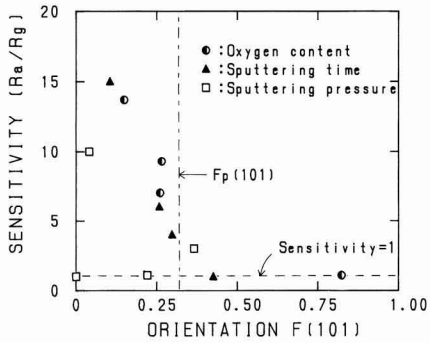

Fig. 4. The correlation between sensitivities and (101) orientations of films prepared at various sputtering conditions: ◐: oxygen content from 0 to 30% under fixed sputtering time of 2h and total pressure of 8×10^{-3} Torr, ▲: sputtering time from 1 to 5h in Ar+20%O_2 atmosphere of 8×10^{-3} Torr, □: total gas pressure from 8×10^{-4} to 3×10^{-2} Torr for 2h in Ar+20%O_2 atmosphere. The radio-frequency power for sputtering was 200W in all cases.

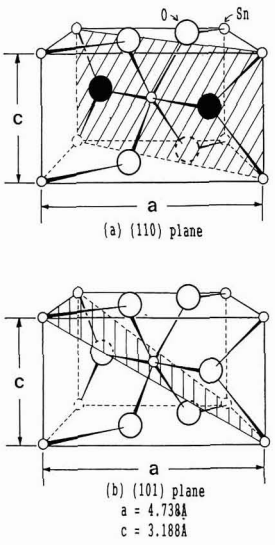

Fig. 5. Schematic presentations of (110) and (101) crystal plane of unit cell of SnO_2 (Large circles: oxygen atoms, small circles: tin atoms).

Table 4. The surface atomic densities of tin and oxygen atoms at typical lattice plane of tin oxide.

crystal plane	surface atomic density of tin(A^{-2})	surface atomic density of oxygen(A^{-2})
(110)	0.0936	0.0936
(101)	0.0739	0
(211)	0.0493	0.0493
(200)	0.0662	0
(002)	0.0445	0.0891

sity. The observed relationship between the sensitivity and preferential orientation has been understood by considering the atomic density, which correlates the adsorption sites for atmospheric gas as well as the direct reaction site for H_2 gas.

5. Summary

Tin oxide thin films were fabricated by r.f. magnetron sputtering. Investigations of the relationship between hydrogen gas sensing property and preferential orientation were carried out from the perspective of the sensing mechanism. The dependency of gas sensitivity on preferential orientation was confirmed by tin oxide film fabricated under various conditions. The observed relationship has been understood by considering the maximum atomic density on the (110) plane.

References:

1) T. Suzuki, T. Yamazaki, H. Yoshioka and K. Hikichi J. Mater. Sci., 23, 1106-1111 (1988).
2) A. Mansingh and C.V.R. Vasant Kumar, J. Mater. Sci. Lett., 7, 1104-1106 (1988).
3) M. Nitta, S. Kanefusa and M. Haradome, J. Electro chem. Soc., 125, 1676-1679 (1978).
4) P. Tischer, H. Pink and L. Treitinger, Jpn. J. Appl. Phys., Suppl. 1, 19, 513-517 (1980).
5) T. Suzuki, T. Yamazaki, K. Takahashi and T. Yokoi, J. Mater. Sci., 24, 2127-2131 (1989).
6) T. Seiyama, A. Kato, K. Fujiishi and M. Nagatani, Anal. Chem., 34, 1502 (1962).
7) T. Suzuki, T. Yamazaki, H. Yoshioka and K. Hikichi, J. Mater. Sci., 23, 145-149 (1988).
8) K. Hara, Proc. 1st Sensor Sympo., Fukuoka Japan (1981) 109-112.
9) M. Takada and H. Yanagida, Yokyokyokaishi, 87, 13-21 (1979).
10) J.S. Ryu and M. Takata, Proc. Sec. Cong. Particle Technol., Kyoto Japan, Sept. 19-22 (1990) 518-525.
11) F.K. Lotgering, J. Inorg. Nucl. Chem., 9, 113-123 (1959).

This article is a full translation of the article appearing in Journal of the Ceramic Society of Japan (Japanese version), Vol.100, No.9, pp.1165-1168, 1992.

Effect of Intergranular Phase on Mechanical Properties of Si_3N_4-Si_2N_2O Composites

Kazuo Nakamura, Yasuharu Okashiro*, Masayoshi Ohashi, Kiyoshi Hirao, Takaaki Nagaoka, Koji Watari, Masaki Yasuoka and Shuzo Kanzaki

Government Industrial Research Institute, Nagoya
Hirate-cho 1-1, Kita-ku, Nagoya-shi, 462 Japan
*Kitagawa Ironworks Co., Ltd.
77-1, Moto-machi, Fuchu-shi, 726 Japan

Ce/Si ratio increased with the formation of Si_2N_2O in Ce-doped Si_3N_4 based ceramics with SiO_2 addition. The intergranular liquid remained as a glass on cooling until the ratio exceeded a certain level when the intergranular liquid crystallized as cerium nitrogen apatite ($Ce_5(SiO_4)_3N$-$Ce_{4.67}(SiO_4)_3O$) during cooling. There were large differences in flexural strength, fracture toughness between the specimens with the intergranular glassy phase and the ones with the intergranular crystalline phase. Mechanical properties of the bulk bodies depended on those of the intergranular phases.
[Received April 10, 1991; Accepted June 16, 1991]

Key-words: Si_3N_4, Si_2N_2O, Intergranular phase, Fracture toughness, Flexural strength

1. Introduction

High strength, high fracture toughness and resistance to thermal shock, silicon nitride (Si_3N_4) ceramics are expected to find wide applications as high-temperature structure materials because of its strong covalent bond, silicon nitride can hardly be sintered by utilizing of solid-phase diffusion. It is usually manufactured by liquid-phase sintering by adding metallic oxides and nitrides such as Y_2O_3, Al_2O_3, and AlN. Although the volume fraction of the liquid phase decreases as sialon (solid solution of silicon nitride) and silicon oxynitride (Si_2N_2O) are produced or it evaporates, it will not completely disappear and remains as an intergranular phase.[1-5] Such intergranular phases have a great effect on the thermal and mechanical properties of silicon nitride ceramics. This suggests that such properties can be controlled by controlling the chemical composition of intergranular phases.

The role of the intergranular phase influential on the mechanical properties of Si_3N_4-Si_2N_2O composites was investigated by varying the Ce-Si ratio of the intergranular phase by controlling the ratio between SiO_2 and CeO_2 (the additives to silicon nitride) and the sintering conditions.

2. Experimental Procedure

The Si_3N_4 powder (made by Denki Kagaku Kogyo; α percentage: 92%) used in the present study was a high-purity fine powder synthesized by directly nitriding silicon, of impurity oxygen: 1.7wt%, total metal impurities: 268ppm, and specific surface area (BET): 21.7m^2/g. The SiO_2 powder (made by Hokko Kagaku) and the CeO_2 powder (made by Mitsuwa Kagaku) were high-purity powders of purity: both 99.9% or up and specific surface area: 140 and 17m^2/g, respectively.

These powdered raw materials were mixed in a ratio of Si_3N_4:SiO_2:CeO_2=100:20:1~4 by weight with methanol in a vibrational mill made of silicon nitride. The mixed product was then dried (150°C, 12h), sifted (60-mesh), and hot-pressed at 1700°C and 1750°C for 1, 2 and 4h under a pressure of 49MPa.

Tree-point flexural strength was measured at room temperature to 1300°C on bars 4×3×40mm, ground with a #400 diamond wheel, and chambered the edges with a #600 diamond disk. A span length of 30mm was used with a cross-head speed of 0.5mm/min. Fracture toughness (K_{IC}) was measured using an indentation microfracture method. The Vickers indentor was driven in under a load of 10kgf, and K_{IC} was calculated using Marshall and Evans' equation.[6] Bulk densities were obtained by an Archimedian method. To identify the phases in the sintered bodies a powder X-ray difractometer (CuKα, 40kV-100mA) was used. The ratio of component phases was obtained from the integrated intensity ratios of Si_2N_2O (110) + (200), α-Si_3N_4 (101) and β-Si_3N_4 (200) diffraction lines to Si (200) by an internal standard method (internal standard: silicon).

3. Results and Discussion

Figure 1 shows the variations in crystalline phase composition with hot pressing time for the samples with a weight ratio of Si_3N_4:SiO_2:CeO_2=100:20:1 hot-pressed at 1750°C. As the ratio of α-Si_3N_4 decreases, the ratios of β-Si_3N_4 and Si_2N_2O increase. The production of β-Si_3N_4 and Si_2N_2O proceeds, through a process in which the raw material α-Si_3N_4 (low-temperature type) particles melt in the liquid phase, precipitating as β-Si_3N_4 (high-temperature type), or react with SiO_2 in the liquid phase, precipitating as Si_2N_2O.[1,7] In the present study, when α-Si_3N_4 was used up, 58vol%Si_2N_2O and 42vol%β-Si_3N_4, except the intergranular phase, were produced.

Figure 2 shows the ratios of Si_2N_2O in the samples hot-pressed under different conditions. It was assumed that Si_2N_2O production reactions were nearly completed in the sample with Si_3N_4:SiO_2:CeO_2=100:20:4 hot-pressed at 1750°C for 4h (Si_2N_2O volume percentage: 58%). The Si_2N_2O contents of the other samples are shown on the basis

Si_2N_2O quantity rated as 100, of the sample mentioned above. The ratios of Si_2N_2O increased with time, and Si_2N_2O production was promoted as CeO_2 content and sintering temperature increased. It is assumed that as sintering (reaction) proceeded, the component phases in the specimens widely changed, causing the chemical composition of the liquid phase in the grain boundaries, to change accordingly.

When only CeO_2 is used as the sintering aid, Ce^{3+} ions can not dissolve in β-Si_3N_4 lattices, and thus the composition of the liquid phase can not change during the α-β transformation of Si_3N_4. However, in Si_2N_2O production, SiO_2 in the liquid phase is gradually consumed, probably causing the Ce-Si ratio in the liquid phase to increase. The Ce_2O_3-SiO_2 ratio of the intergranular phase increases in CeO_2-doped Si_2N_2O ceramics during Si_2N_2O production due to the mechanisms similar to the above.[2,3] When the Ce_2O_3-SiO_2 ratio in the Si_2N_2O ceramics exceeded a certain critical level, the intergranular phase crystallized as a $Ce_5(SiO_4)_3N$-$Ce_{4.67}(SiO_4)_3O$ solid solution (Ce-N-apatite) during cooling. In the present study, the intergranular phases of those samples with a high Si_2N_2O production (black marks in Fig.2a to d, Si_2N_2O production: 85% or up (dotted line)) also crystallized as Ce-N-apatite. The black-mark samples Si_2N_2O (>85%) and the white-mark samples Si_2N_2O (<85%) in Fig.2 and figures thereafter correspond to group C and group A, respectively, which will be described later.

Table 1 shows the bulk and relative densities of the hot-pressed samples. In any case, with relative densities of above 95%, all samples were densified well.

Figure 3 shows variations in fracture toughness (K_{IC}) of the hot-pressed samples. The samples can be classified into groups A and C in terms of K_{IC}, group A for low K_{IC} values below $4MNm^{-3/2}$ and group C for high K_{IC} values above $5MNm^{-3/2}$. With samples of these two groups, the crystallization of intergranular phases was investigated by XRD. While the intergranular phases of group A were scarcely crystallized, those of group C were all crystallized as Ce-N-apatite. The coefficient of thermal expansion of the apatite phase ($10\times10^{-6}°C^{-1}$) is much larger than those of Si_2N_2O (a: 1.26×10^{-6}, *b*: 3.89×10^{-6}, *c*: $3.99\times10^{-6}°C^{-1}$) and Si_3N_4 (*a*: 3.23×10^{-6}, *c*: $3.72\times10^{-6}°C^{-1}$).[3,8] On the other hand, the coefficients of thermal expansion of Ce-O-N glass are 4 to $5\times10^{-6}°C^{-1}$, which are much the same as those of Si_2N_2 and Si_3N_4. In the samples of group C, having the intergranular phases crystallized, large residual stresses compared to those of group A were probably generated at the interfaces between intergranular phase (apatite phase) and Si_2N_2O and Si_3N_4 grains, causing the interfacial bond to be reduced. Furthermore, because the intergranular phase at the interface on columnar Si_2N_2O and Si_3N_4 grains were probably subjected to tangential tensile residual stresses and radial compressive residual stresses, cracks tended to propagate along the columnar grains (crack deflection) and crack bridging occurred, causing K_{IC} to rise. Also, with the samples of group C, K_{IC} rose as the content of additive (CeO_2) and hot-pressing increased. This may be because crack bridging was effectively occurred as Si_2N_2O and Si_3N_4 particles grew larger. On the other hand, the toughness of group A was not improved. This may be because residual stresses were rather small and that intergranular bonding is strong, not resulting in crack deflection. The low level of toughness of group A can also be ascribed to a relatively high intergranular phase content.

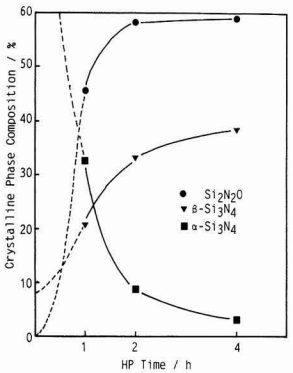

Fig. 1. Variation in crystalline phase composition of the sample (Si_3N_4:SiO_2:CeO_2=100:20:1 by weight) by hot-pressing at 1750°C.

Figure 4 shows the temperature dependence of bending strengths of representative samples of groups A and C. A large difference was found between the two groups. With group A, although the strength gradually deceased as the temperature rose, a high strength above 500MPa was maintained even at 1300°C, suggesting that the intergranular vitreous phase has a considerably high softening point. On the other hand, the samples of group C, were expected to show a high percentage of Si_2N_2O production and a lower ratio of the intergranular phase, and decreases in strength degradation at high temperatures due to slow crack growth were expected to be controlled as in the crystallization of the intergranular phase of Si_3N_4 ceramics.[9] However, the strength fall sharply at 1200°C. Two reasons can be assumed. ① The Ce-N-apatite existing as an intergranular phase is decomposed into an amorphous phase and $Ce_2Si_2O_7$ by heat treatment at above 700°C. On the surface of the samples, Ce^{3+} is oxidized into Ce^{4+}, producing CeO_2. These decomposing and oxidizing reactions gave rise to crack sources. ② The intergranular phase of the samples of group C was crystallized as an apatite as mentioned above. However, because complete crystallization was difficult, some vitreous phase probably remained, and metallic impurities in considerable quantities were likely to be concentrated in the vitreous phase, causing the glass softening point to be low.

4. Conclusion

1) As Si_2N_2O formation proceeded, the Ce/Si ratios of the intergranular phases (liquid) of CeO_2-doped Si_3N_4-Si_2N_2O composite increased.

2) The intergranular phase remained as a vitreous (amorphous) phase during cooling, but as the Si_2N_2O was formed, causing its Ce/Si ratio to exceed a certain critical level, it crystallized as $Ce_5(SiO_4)_3N$-$Ce_{4.67}(SiO_4)_2O$ solid solution (Ce-N-apatite).

3) There were large differences in thermal and mechanical properties, such as fracture toughness and high-temperature strength, between the specimens having an amorphous intergranular phase and the specimens having a crystalline (Ce-N-apatite) intergranular phase. This indicated that the prop-

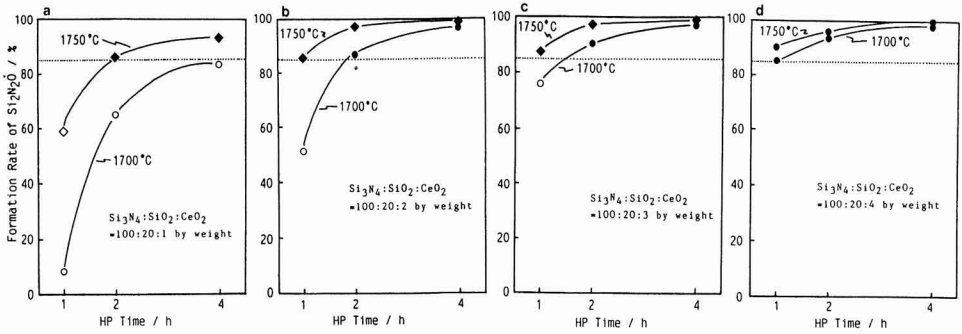

Fig. 2. Formation rate of Si_2N_2O in the samples (Si_3N_4:SiO_2:CeO_2=100:20:1-4 by weight) after hot-pressing.

Table 1. Bulk and relative density of Si_3N_4-Si_2N_2O composites.

HP Time(h)	1				2				4			
CeO_2 add.	1	2	3	4	1	2	3	4	1	2	3	4
1700°C Bulk Density(g/cc)	2.98	2.98	2.99	3.00	2.97	2.97	2.99	3.00	2.94	2.96	2.98	2.99
Relative Den.(%)	95	98	100	100	99	100	100	100	99	99	100	100
1750°C Bulk Density(g/cc)	2.95	2.97	2.98	2.99	2.95	2.97	2.98	2.99	2.95	2.97	2.98	2.99
Relative Den.(%)	98	100	100	100	99	100	100	100	99	100	100	100

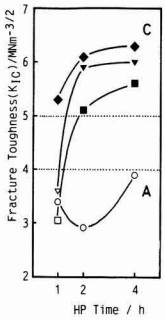

Fig. 3. Variation in fracture toughness K_{IC}) of Si_3N_4-Si_2N_2O composites hot-pressed at 1700°C.
○: Si_3N_4:SiO_2:CeO_2=100:20:1 by weight, □■: 100:20:2, ▽▼: 100:20:3, ◆: 100:20:4.

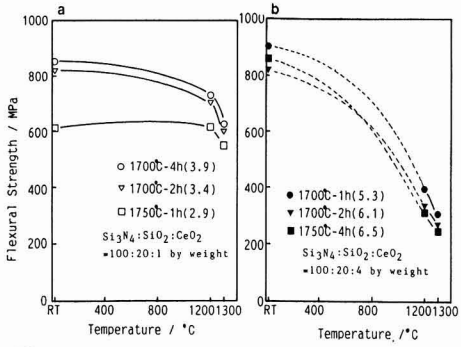

Fig. 4. Flexural strength of the Si_3N_4-Si_2N_2O composites at elevated temperatures, K_{IC}(MNm$^{-3/2}$) shown in parentheses.

erties of the intergranular phase governed the properties of silicon nitride bulk bodies.

References:

1) G.K. Layden, Rep. R75-912072-4, United Technical Research Center (1976).
2) M. Ohashi, S. Kanzaki and H. Tabata, Seramikkusu Ronbunshi, 96, 1073-1080 (1988).
3) M. Ohashi, S. Kanzaki and H. Tabata, J. Am. Ceram. Soc., 74, 109-114 (1991).
4) A. Tsuge, H. Inoue and K. Komeya, ibid., 72, 2014-2016 (1989).
5) D.R. Messier and E.J. Deguire, ibid., 67, 602-605 (1984).
6) D.B. Marshall and A.G. Evans, ibid., 64, C182-183 (1981).
7) K.H. Jack, Non-Oxide Technical and Engineering Ceramics, ed. by S. Hampshire, Elsevier-Appled Science (1986) 1-30.
8) M.B. Henderson and D. Taylor, Trans. Brit. Ceram. Soc., 74, 49-53 (1975).
9) A. Tsuge, K. Nishida and M. Komatsu, J. Am. ceram. Soc., 58, 323-326 (1975).

This article is a full translation of the article appearing in Journal of the Ceramic Society of Japan (Japanese version), Vol.100, No.9, pp.1169-1171, 1992.

Grain Size Dependence of High-Temperature Dielectric Properties of (Pb, La)TiO_3 Ceramics

Kenji Ohshima, Seiji Takahashi and Makoto Kuwabara

Department of Applied Chemistry, Faculty of Engineering, Kyushu Institute of Technology
1-1, Sensui-cho, Tobata-ku, Kitakyushu-shi, 804 Japan

An investigation has been made on the grain size dependence of the dielectric properties in $0.99Pb_{0.7}La_{0.2}TiO_3$+$0.01MnO_2$ ceramics exhibiting two anomalous peaks of dielectric constant; One is a sharp peak at the Curie point (~160°C), and the other a broad one above the Curie point. The sharp dielectric constant peak showed no significant change with grain size, while the broad dielectric constant peak significantly increased as the grain size increased. Complex impedance analysis revealed that the dielectric properties of the present materials can well be described using an equivalent circuit with two sets of *R-C* parallel circuits being connected in series. Evidently, these two *R-C* parallel circuits give the dielectric properties of the bulk of the grains which provide the sharp dielectric peak and those of the grain boundary region, which yield the broad one, respectively. The origin of the broad dielectric peak is most likely interpreted to be interfacial polarization at the grain boundaries.

[Received March 9, 1992; Accepted May 21, 1992]

Key-words: Lead titanate, (Pb, La)TiO_3, Ferroelectrics, Dielectric constant, Complex impedance analysis, Interfacial polarization, Grain size

1. Introduction

In the temperature characteristics of the dielectric constant of an MnO_2 contained (Pb, La)TiO_3 ceramic system (hereinafter PLT ceramics), a broad peak showing a relaxed dispersion was observed on the high temperature side and at the same time an ordinary sharp peak was observed at the Curie point. The peaks are a result of the phase transformation from tetragonal to cubic.[1] From detailed analysis of the complex impedance characteristics of this material, the dielectric constant peak showing a relaxed dispersion was ascribed with high probability to the interfacial polarization caused by a high-resistance, high-capacitance phase generated at grain boundaries in the ceramics, however, its detailed mechanisms remained unknown.[2] In order to fully understand these mechanisms, the authors investigated the dependency on grain size of the broad dielectric constant peak on the high temperature side in the dielectric constant-temperature characteristics of PLT ceramics.

2. Experiment

The composition of the experimental samples was $0.99Pb_{0.7}La_{0.2}TiO_3$+$0.01MnO_2$. The starting materials were $PbTiO(_2O_4)_2$-$4H_2O$ (Central Glass), La_2O_3(Mitsuwa Kagaku), TiO_2 (Kojundo Kagaku) and MnO_2(Kojundo Kagaku). All had a purity 99.9% or higher. These materials, together with ethanol as dispersant, were submitted for 48h to wet ball-mill mixing and milling using zirconia balls. The product was then calcined at 700°C for 3h, pulverized for 48h in a wet ball-mill, dried, and graded. The resulting powder was rubber pressed under a pressure of 2000kg/cm^2 and molded into pellets, which were then sintered in air. Both sides of the sintered pellets were polished and coated with silver paste as electrodes in order to make samples for measurement. The dielectric constant, dielectric loss and complex impedance of the samples were measured using a vector impedance meter (YHP-4192A) in a temperature range from room temperature to 600°C (heating/cooling rate: 3°C/min). The average grain size of the samples was obtained under an intercept method from SEM photographs of the samples polished and thermally etched.

3. Results and Discussion

Table 1 shows the firing conditions used for preparing the samples as well as the densities and mean grain size. **Figure 1** shows the dielectric constant-temperature characteristics of the samples measured at 1kHz. The Curie temperature of $PbTiO_3$ is around 490°C. That of the experimental samples is lower due to solid dissolution of La. Corresponding to this, a sharp dielectric constant peak (peak 1) is observed in the range of 140° to 180°C, and another broad dielectric constant peak (peak 2) is found on the high temperature side. In conventional studies, peak 2 was also detected in samples having a composition of $0.99Pb_{1-x}La_{2x/3}$-TiO_3+$0.01MnO_2$ (x=0.01, 0.10, 0.15, 0.20). In addition, it was discovered that peak 1, with its temperature independent of frequency, slightly diminishes as the frequency increases but peak 2 shows a prominent relaxed dispersion.[1,2] As grain size increased, as shown in Fig.1, peaks 1 and 2 shifted toward the high temperature side. The frequency dependency was the same as that with samples having a different La content. Conventional studies have revealed

Table 1. Specifications of the samples with different grain sizes used in this study.

Sample	Sintering Temp. (℃)	Time (h)	Density (g/cm^3)	Grain size (μm)
1	1125	3	7.09	1.1
2	1200	10	7.03	3.2
3	1230	16	6.75	6.3

that from the complex impedance characteristics in the high temperature range in which peak 2 appears, the equivalent electric circuit of these samples can be represented as shown in **Fig.2**. This suggests that if τ_1 ($=R_1C_1$) < τ_2 ($=R_2C_2$), then the R_1C_1 parallel circuit portion provides the transgranular electrical properties of the samples and the R_2C_2 parallel circuit portion provides the intergranular electrical properties which give rise to peak 2 showing a relaxed dispersion. **Figures 3** through **6** show the temperature dependency of R_1, R_2, C_1, and C_2 obtained by a simulation using the equivalent electrical circuit in Fig.2 on the basis of the Cole-Cole plot of complex impedance of the samples at various temperatures. Here, R and C are shown in Ω·cm (resistance × cross section of sample/thickness of sample) and in F/cm (capacitance × thickness of sample/cross section of sample), respectively. As shown in Figs.3 and 4, the temperature dependency of R_1 and R_2 is given by exactly linear relations in log$R$-1/T plotting as observed with ordinary semiconductors or insulators. While $1/C_1$ shown in Fig.5 stands is linearly related to temperature, proving to fall under the Curie-Weiss law, C_2 in Fig.6 slightly decreases as temperature rises, deviating from the Curie-Weiss law. **Figures 7** and **8** show the grain size dependence of R_1, R_2, C_1, and C_2 at 502°C obtained from the plottings in Figs.3 through 6. As grain size increases, R_1 slightly, while R_2 decreases prominently and almost linearly. C_1 remains nearly constant irrespective of grain size, however, C_2 increases almost linearly as grain size increases. Considering that R_2 and C_2 are closely related to grain size, grain size increase corresponding to the decrease in the number of grain boundaries per unit length, it can be understood that they represent the electrical properties of grain boundaries. If for example, the resistance and capacity of grain boundaries are nearly constant, then a decrease in the number of grain boundaries causes the total resistance of the grain boundaries to decrease while causing the total capacitance to increase. This can explain the dependent behavior of R_2 and C_2 with respect to grain size. These results lead to the conclusion that peak 2 in the dielectric constant-temperature characteristics appears due to the resistance and capacitance (R_2, C_2) of the grain boundaries.

4. Conclusion

Investigating the dielectric constant-temperature characteristics and complex impedance properties of a ceramic system having a composition of $0.99Pb_{0.7}La_{0.2}TiO_3$+ $0.01MnO_2$, the following results were obtained:

1) Peaks 1 and 2 in the dielectric constant-temperature characteristics shifted toward the high temperature side as grain size increased.

2) The value of peak 2 in the dielectric constant-temperature

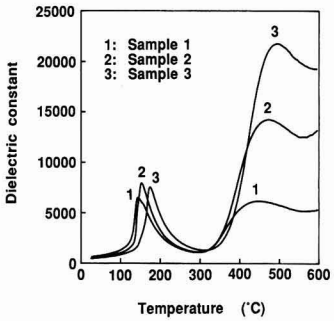

Fig. 1. Temperature dependence of dielectric constant for the present samples, measured at 1kHz.

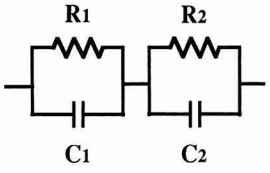

Fig. 2. An equivalent circuit used for the complex impedance analysis.

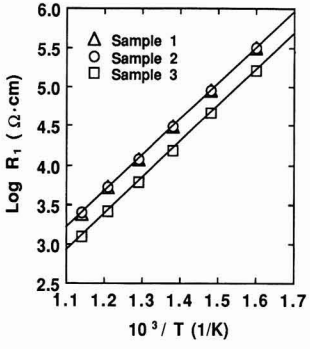

Fig. 3

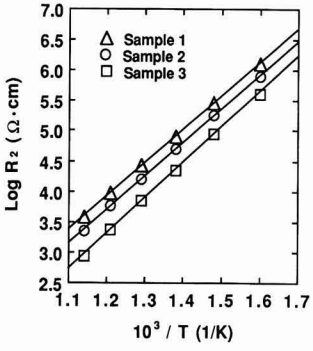

Fig. 4

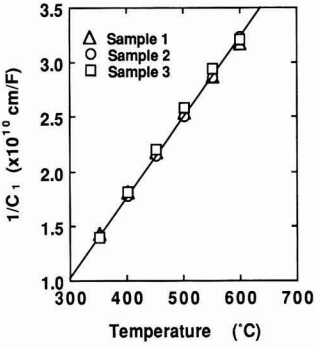

Fig. 5

Fig. 3. Temperature dependence of the equivalent resistance R_1 for the present samples.

Fig. 4. Temperature dependence of the equivalent resistance R_2 for the present samples.

Fig. 5. Temperature dependence of the equivalent capacitance C_1 for the present samples.

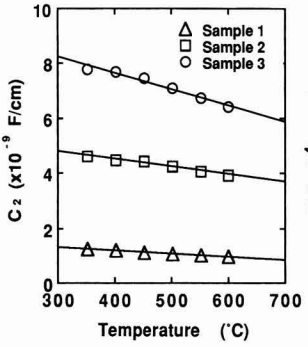

Fig. 6

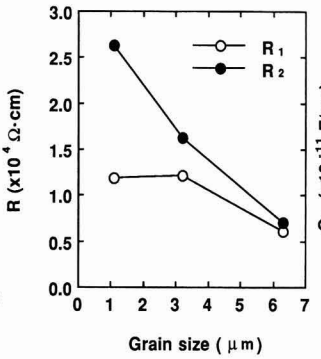

Fig. 7

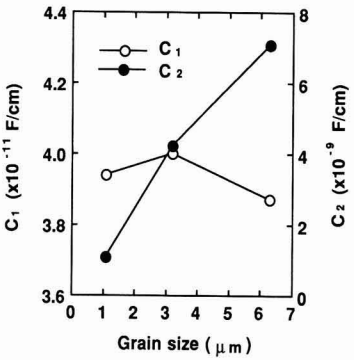

Fig. 8

Fig. 6. Temperature dependence of the equivalent capacitance C_2 for the present samples.

Fig. 7. Grain size dependence of the equivalent resistances R_1 and R_2.

Fig. 8. Grain size dependence of the equivalent capacitances C_1 and C_2.

characteristics increased as grain size increased.

3) Both R_1 and R_2 linearly decreased as grain size increased. R_2 was more dependent on grain size than R_1.

4) C_1 remained nearly constant irrespective of grain size, and C_2 increased nearly linearly as grain size increased.

5) The dependency on grain size of R_2 and C_2 can be attributed to variations in the number of grain boundaries per unit length, and peak 2 in the high temperature range can be ascribed to interfacial polarization at the grain boundaries.

References:

1) K. Goda and M. Kuwabara, Seramikkusu Ronbunshi, 99, 163-167 (1991).

2) K. Goda and M. Kuwabara, Ceramic Transactions, Vol.22, Ceramic Powder Science, Am. Ceram. Soc., (1991) 503-508.

This article is a full translation of the article appearing in Journal of the Ceramic Society of Japan (Japanese version), Vol.100, No.9, pp.1172-1174, 1992.

Sintering of Hydroxyapatite Powders with SiC Platelets Dispersion

Tatsuo Noma, Noriyuki Shoji, Satoshi Wada and Takeyuki Suzuki

Department of Applied Chemistry, Tokyo University of Agriculture and Technology
2-24-16, Nakamachi, Koganei-shi, 184 Japan

Hydroxyapatite (HAp) powders with SiC platelets dispersion were synthesized by a wet process (at 98°C for 24h) and hydrothermal process (at 150°C, 0.5MPa for 4h). The transmission electron microscopy showed that SiC platelets were homogeneously surrounded by fine HAp crystals. The SiC-HAp composites were sintered at various temperatures. SiC loading obstructed the densification but improved the Vickers hardness up to 1.3 times that of pure HAp ceramics.
[Received April 13, 1992; Accepted May 21, 1992]

Key-words: Hydroxyapatite, Silicon carbide, Platelet, Composite ceramics, Hydrothermal, Composite particle

1. Introduction

Hydroxyapatite (HAp) is the main component of hard body tissue. It is highly histocompatible and is ready to combine directly and firmly with bones and teeth, therefore, it has potential for implants such as artificial dental roots and tooth fillers.[1] The compressive strength of dense HAp ceramics is sufficient for artificial teeth materials, and there have been reports on achieving a sufficiently high density to provide transparency.[2,3] However, HAp ceramic is a typical type of ceramic with low toughness, and its breaking energy is about 1/100 of that of dense teeth (390 to 560J/m^2).[4] This makes it difficult to use HAp ceramic alone at locations under heavy load, limiting the application of HAp sinter. Therefore, for wider application of HAp ceramics, it is necessary to improve its mechanical properties, especially its fracture toughness.

It is well known that combining different components into composites is effective in improving mechanical properties of fracture toughness of ceramics.[5] In order to effectively improve toughness without losing bioaffinity, an inherent property of HAp, it is preferable to use a starting material of a composite powder with second-phase particles coated with HAp so that second-phase particles are homogeneously dispersed in the HAp phase.

There have been several reports on manufacturing HAp composites. Ioku et al. have manufactured ceramic composites having excellent mechanical properties by dispersing metastable zirconia particles or Si_3N_4 whiskers.[6,7] However, if zirconia dispersion is used, then it involves the trouble of allowing zirconia to be stabilized in reactions during firing. On the other hand, whiskers are suspected to be carcinogenic in the body because of artixenic affinity caused by their shape, making it hazardous to apply whisker dispersed ceramics to biomaterials.[8]

The present study is intended to examine whether or not dispersing platelets is effective in improving the mechanical properties of those ceramic materials which have a very low breaking strength, such as HAp. Composite powders containing SiC plate crystals as the second phase were synthesized by wet method and hydrothermal synthetic method and sintered. SiC-HAp ceramic composites having the second phase dispersed honogeneously were prepared, and crystal phase variations were investigated with respect to, heating temperature, dispersion of particles, sintering behavior, and hardness of ceramic.

2. Experimental

SiC-HAp composite powders were synthesized by two methods: wet and hydrothermal. SiC plate crystals (AME, 22μm mean dia. and 10μm thick) were added by 5-15vol% to a 0.167M $Ca(NO_3)_2$-$4H_2O$ (guaranteed, made by Kokusan Kagaku) with pH adjusted to about 10 with NH_3 water. A 0.1μm$(NH_4)_2HPO_4$ (guaranteed, made by Kokusan Kagaku) with pH adjusted with NH_3 water was then added to about 10, and the solution was then dripped at room temperature to obtain gel sediments. During agitation, the sediments were submitted to (1) wet treatment of 98°C for 2h under normal pressure (wet method) or (2) hydrothermal treatment at 150°C for 4h under 0.5MPa (hydrothermal method) to obtain SiC-HAp composite powders. The composite powders were suction filtered, rinsed, and dried completely in air at 90°C. They were then calcined at 600°C for 1h in an electric furnace, pulverized in an alumina mortar, and sieved. The lots through the 120μm mesh were used for sintering. They were pressed under a uniaxial pressure of 200MPa into pellets 10mm in dia. and 5mm thick. The pellets were sintered for 4h in air at 800-1200°C without any additional pressure. The heating rate was 20°C/min.

A powder X-ray diffractometer (Rigaku RAD-2B, 30KV-20mA, Cukα) was used to identify phases, and a transmission electron microscope (TEM) (Hitachi H-700H, 200kV) was used to observe the shapes and mixtures of particles. The powders were treated with nitric acid and filtered to remove SiC particles. Ca and P contents were then determined by chemical analysis: an ammonium oxalate weight method for Ca and a phosphomolybdate method for P. The bulk density of ceramic was measured under an Archimedian method using mercury, and relative densities were obtained for the values calculated from the theoretical densities of α-SiC and HAp (3.21 and 3.16g/cm^3 respectively) and their volume percentages. SiC dispersion was checked under an optical microscope by observing the surfaces which were mirror polished with a diamond polishing machine (ML-150 by Maruto). The Vickers hardness of surfaces was measured using a micro-hardness tester (MVK-E

by Akashi, 50gf, 15s).

3. Results and Discussion

Figure 1 shows the SEM photograph of SiC plate crystals used as the starting material. The starting material was sedimentally classified to remove fine spherical SiC particles. The mean diameter and mean thickness after classification were 22μm and 10μm, respectively. SiC was identified as α-type by powder X-ray diffraction (XRD).[9] From the SiC-HAp composite powdered prepared by wet or hydrothermal treatments, no compounds were detected other than XRD peaks for SiC and HAp. The results of TEM observation showed that SiC platelets were surrounded by HAp microcrystals and were not in direct contact with each other (**Fig.2**). In general, entanglement and mutual contact of dispersed phases make the material inhonogeneous. If ceramic materials are prepared from such raw powders, then the size of fracture origin is larger, often degrading the mechanical properties of ceramics. In the composite powders prepared in the present way, no inhonogeneity causing such defects will be detected.

Figure 3 shows the relationship between SiC content and Ca/P ratio of composite powder at synthesis. With composite powders prepared by wet treatments, a Ca/P ratio of about 1.6 was obtained as in other studies.[10] As SiC content increased, the Ca/P ratio of such composite powders remained nearly constant, while that of the composite powders prepared by hydrothermal treatments decreased. SiC is so chemically stable that when it is hydrothermally oxidized at above 500°C, it produces amorphous SiO_2.[11] Thus, under the hydrothermal treatment conditions in the present test, SiC cannot be oxidized. The SiC-HAp composite powder, which was hydrothermally treated under the same conditions with a 15vol% SiC additive, etched for 30min previously in an agitated $HF\text{-}HNO_3$ acid, was submitted to chemical analysis. It was found that the Ca/P ratio was 1.668, which was nearly a stoichiometric ratio. Again, from XRD of synthesized composite powders, only diffraction lines for HAp and SiC were detected. This suggests that large decreases in Ca/P ratio can be attributed to Ca in HAp being taken into the amorphous SiO_2 contained as an impurity in SiC or the amorphous SiO_2 produced by oxidation of slight metallic Si contained in SiC.

It is generally known that when heated above approximately 1300°C, pure HAp decomposes into tricalcium phosphate (TCP) and CaO as follows:

$$Ca_{10}(PO_4)_6(OH)_2 \rightarrow 3Ca_3(PO_4)_2 + CaO + H_2O\uparrow$$

The results of XRD showed that ① in temperature ranges above 800°C, with all SiC-HAp composite powders synthesized under the wet and hydrothermal methods, a metastable

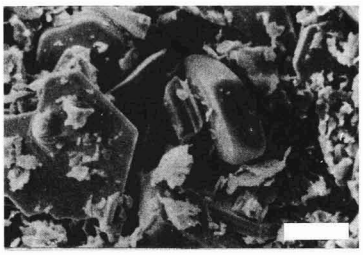

Fig. 1. Scanning electron micrograph of SiC platelets. (bar=20μm)

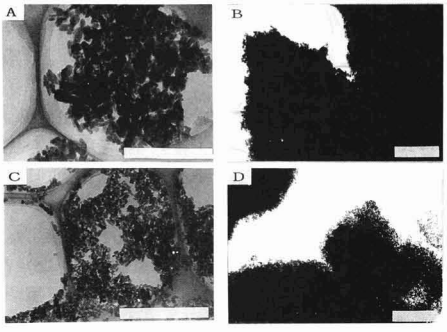

Fig. 2. Transmission electron micrographs of Sic-HAp composite particles. (A) wet process, pure HAp, (B) wet process, SiC 5vol%, (C) hydrothermal process, pure HAp, (D) Hydrothermal process, SiC 5vol%. (bar=1μm).

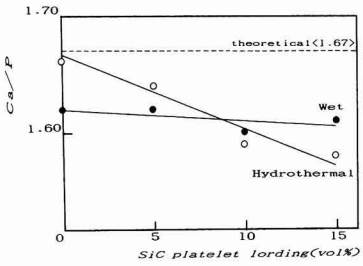

Fig. 3. Ca/P ratio of SiC-HAp composite particles as a function of platelet loading.

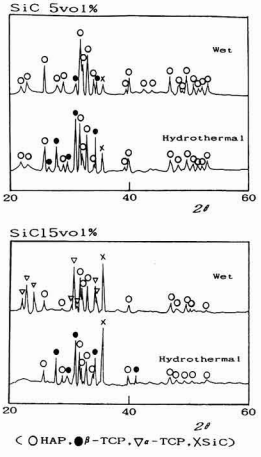

Fig. 4. X-ray diffraction profiles of SiC-HAp composite ceramics.

phase α-TCP and a stable phase β-TCP were produced and ② decomposition from HAp into TCP increased as the SiC content increased.

Figure 4 shows the XRD profiles for the composite powder samples synthesized under the wet and hydrothermal methods and sintered at 1000°C. Under either synthesis method, decomposition into TCP occurred. However, with an SiC content of 5vol%, decomposition was faster with composite powders synthesized under the wet method than under the hydrothermal method. Furthermore, with an SiC content of 15vol%, decomposition into TCP was faster with composite powders synthesized under the hydrothermal method. It is known that the decomposition temperature of HAp depends greatly on Ca/P ratio. For a Ca/P ratio close to the stoichiometrical ratio (1.67), the decomposition temperature of HAp is relatively high, and for Ca-P ratios below 1.67, the decomposition temperatures of HAp are low.[10] As shown in Fig.3, with an SiC content of 5vol%, the Ca/P ratio is higher with the composite powders synthesized under the hydrothermal method. With an SiC content of 15vol%, the ratio is smaller with the same composite powders. Thus, decomposition rates compared between wet and hydrothermal synthesis methods depend on the value of Ca/P ratio.

Figure 5 shows the relationship between sintering temperature and relative density for the wet and hydrothermally synthesized SiC-HAp composite powders. For the hydrothermally synthesized SiC-HAp composite powders, the density continuously rose in temperature ranges up to 1200°C. For the wet synthesized composite powders, densification was completed at around 1100°C, about 100°C lower than that of the hydrothermally synthesized powders. It is generally known that wet synthesized powders consist of fine, irregularly shaped particles.[14] Densification proceeded faster because of a higher free surface energy than that of hydrothermally synthesized powders. With both wet and hydrothermal treatments and with a sintering temperature of 1200°C, the relative density was about 93.5% for the HAp only samples but decreased as SiC content increased. The decreases in the distances between HAp particles were

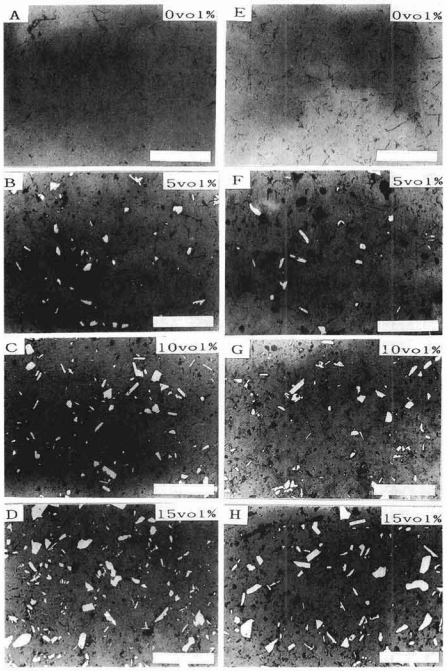

Fig. 6. Optical micrographs of SiC-HAp composite, (A)-(D): wet process, (E)-(F): Hydrothermal process, platelet loading is also shown in each figures (bar=200μm).

① prevented because SiC is hard to sinter and ② hindered two-dimensionally by the plate-shape of the particles. In practice, because part of the HAp in the composite samples decomposed into β-TCP (3.07g/cm^3) or α-TCP (2.86g/cm^3) with a lower theoretical density, the relative density of the ceramic is estimated to be a little higher.

Figure 6 shows the optical micrographs of the polished surfaces of the sintered products which achieved the highest densities with various values of SiC content (Fig.5). In the sintered products, it was also discovered that SiC platelets were evenly distributed in the matrix, with none of them being in direct contact with each other.

Figure 7 shows the Vickers hardness of the samples in Fig.6. For each sample, the value was the mean of 50

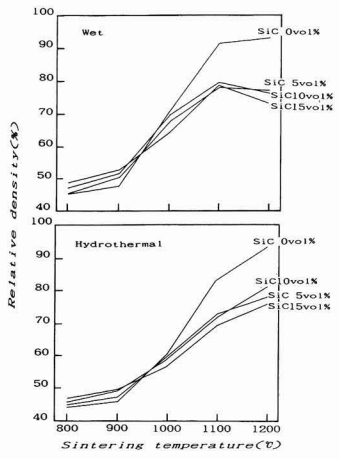

Fig. 5. Relative density of SiC-HAp composite ceramics as a function of sintering temperature.

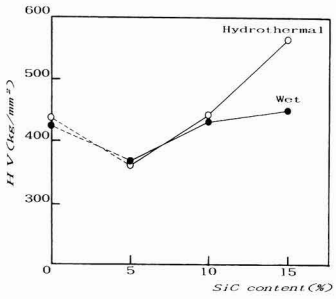

Fig. 7. Micro Vickers hardness of SiC-HAp composite ceramics as a function of platelet loading.

random measurements. The SiC distribution prevented the densification of the ceramic, causing decomposition from HAp into TCP to be accelerated due to decreases in Ca/P ratio. However, it was effective in improving hardness, which rose as SiC content increased. The relative densities of the sintered composites with 10vol% SiC were rather low, 79.5% for the wet method and 81.1% for the hydrothermal method, but their hardnesses were comparable to that of the HAp only samples having a relative density of 93.5%. Among the composites with 15vol% SiC, the samples synthesized under the wet method (relative density: 78.53%) showed a hardness of 449kgf/mm^2, and the samples synthesized under the hydrothermal method (relative density: 75.7%) showed a hardness of 564kgf/mm,^{2} about 1.3 times as large as that of the hydrothermally synthesized HAp-only samples.

Although the maximum relative density of the composite samples prepared in the present study was 81.1%, so low that no measurement of fracture toughness was possible, fracture toughness can be improved by promoting densification. This allows platelets to be distributed, resulting in the development of crack deflection or pull-out mechanisms.[5] The coefficients of thermal expansion of HAp and SiC are 11×10^{-6} and $4.4\text{-}4.9\times10^{-6}°C^{-1}$, respectively.[15,16] Since the coefficient of SiC is smaller than that of the matrix, compressive stresses normal to the interfaces act during cooling from sintering temperature to room temperature. This causes SiC to be compressed on the matrix, allowing energy consumption to be increased when SiC platelets are pulled out. This, in turn, results in a contribution to improved fracture toughness. Thus, it is still necessary to increase the density of sinter by treatments such as HIP and to investigate how SiC platelets are related to mechanical properties such as fracture toughness and strength.

4. Conclusion

SiC-HAp ceramic composites were obtained by wet and hydrothermally synthesizing the composite powders prepared by homogeneously dispersing and mixing hydroxyapatite and SiC platelet crystals.

The results obtained in the present study are as follows:
1) For both wet and hydrothermally treated samples, dispersed SiC platelets were surrounded with HAp microcrystals, none of them being in direct contact with each other.
2) For the composite powders synthesized hydrothermally, as the SiC content increased, the Ca/P ratio decreased. This caused the promotion of HAp decomposition. Furthermore, decreases in Ca/P ratio could be controlled by etching the SiC.
3) For the wet synthesized composite powders, densification was completed at a temperature of about 100°C lower than that for the densification of the hydrothermally synthesized composite powders.
4) Although SiC plate crystals hindered the densification of ceramic, the hardness of the sinter improved as the SiC content increased. The hydrothermally treated samples with 15vol% SiC showed a hardness of 564kgf/mm,^{2} about 1.3times higher than that of the HAp only samples.
5) SiC platelets were homogeneously dispersed in the HAp matrix, showing no direct contact between them.

(Reported in part at the 4th Fall Symposium of the Ceramic Society of Japan in October, 1991)

Acknowledgement
We would like to thank Dr. K. Ioku at Dept. Science, Kochi University, who has provided useful discussions concerning the nonstoichiometry of apatite. A part of the present study was funded by a subsidy from the Izumi Science and Technology Promotion Foundation.

References:

1) H. Aoki and S. Niwa, Baioseramikkusu no Kaikatsu to Rinsho, Quintessence shuppan (1987) 26-48.
2) K. Uematsu, M. Takagi, T. Honda, N. Uchida and K. Saito, J. Am. Ceram. Soc., 72, 1476-1478 (1989).
3) Y. Hirayama, H. Igata, H. Akiyama, K. Naganuma, S. Ojima and M. Kawakami, Proc. Sintering'87, Tokyo, (1987) 382-383.
4) M. Akao, Seramikkusu, 20, 1096-1103 (1985).
5) K. Niihara, ibid., 26, 457-463 (1991).
6) K. Ioku, M. Yoshimura and S. Somiya, bioceramics, 1, 62, (1989).
7) K. Ioku, T. Noma, N. Ishizawa and M. Yoshimura, Seramikkusu Ronbunshi, 98, 1334-1342 (1990).
8) J.D. Birchall, D.R. Stanley and M.J. Mockford, J. Mater. Sci. Lett., 7, 350-352 (1988).
9) JCPDS #29-1131.
10) H. Monma and T. Kanazawa, Yogyo Kyokaishi, 86, 72-76 (1978).
11) M. Yoshimura, J. Kato and S. Somiya, Silicon Carbide Ceramics, ed. by S. Somiya, M. Yoshimura and M. Mitomo, Uchida Rokakuho (1987) 121-134.
12) Y. Haneda, Handotai Gijutsu no Saikin no shinpo, Maki shoteu (1974) 109-119.
13) A. Makishima and H. Aoki, Baio Seramikkusu, Gihodo Shuppan (1984).
14) T. Kanazawa, T. Umegaki and H. Monma, Seramikkusu, 10, 461-468 (1975).
15) M. Jarcho, C.H. Bolen, M.B. Thomas, J. Bobick, J.F. Kay and R.H. Doremus, J. Mater. Sci., 11, 2027-2035 (1976).
16) K. Inomata, Silicon Carbide Ceramics, ed. by S. Somiya and K. Inomata, Uchida Rokakuho (1988) 1-8.

This article is a full translation of the article appearing in Journal of the Ceramic Society of Japan (Japanese version), Vol.100, No.9, pp.1175-1178, 1992.

Information & Communications News

Development of Multi-Layered, Thin-Film SOI

The Japan Fine Ceramics Center (JFCC) has developed the first multi-layered, thin-film SOI, in which the single-crystalline silicon layer is formed on an insulating substrate, which is the promising LSI substrate of the next generation. The thin-film SOI structure, which is covered with single silicon crystals forming a surface layer of several tens of nm thick, will be more densely integrated and will make the device faster than the conventional silicone substrate. It has been attracting much attention as the substrate for LSI's of the next generation, such as 1GB memory. The SOI structure in which multi-layered insulating layers are embedded will be applicable to the three-dimensional circuit elements. The new SOI is the world's first multi-layered, thin-film structure. The MBE apparatus, capable of ion injection, is used to produce the new structure. The apparatus is jointly developed by JFCC and Nippon Shinku. Ion injection and thin-film silicon growth, which have been operated separately in conventional systems, is effected in the same chamber. This combination has led to the development of the multi-layered structure of the silicon and silicon oxide layers. The MBE apparatus will be sold by Nippon Shinku.

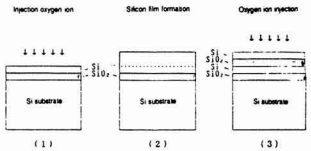

Fig. 1. Multi-layer SOI manifacturing process.

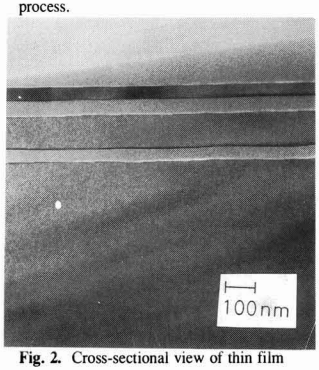

Fig. 2. Cross-sectional view of thin film SOI structure (TEM microgram).

Composite with Glass Matrix

The Agnecy of Industrial Science and Technology's Government Industrial Research Institute, Hokkaido, has developed a composite by the sol-gel process, in which silica glass as the matrix is reinforced with silicon carbide whiskers. Tetramethylorthosilicate (TMOS) is hydrolyzed with water to form the gel, which is fired after being evenly dispersed with the whiskers. Highly densified sinter can be produced, as long as the whisker content is 15% or lower. The secrets are the TMOS concentration, at which the mixture is gelled without causing reagglomeration or precipitation, and the prevention of cracks during the drying process to remove the solvent. The whiskers are evenly dispersed by the aid of supersonic waves. The other features are the addition of fine silica particles to facilitate evaporation of the solvent, which prevents cracks during the drying process, and the curing of the gel at room temperature to strengthen its structure. The composite is still not sufficiently strong for use as a structural material, but it is attracting attention because of the glass matrix. The new technique will be applicable to the production of medical materials.

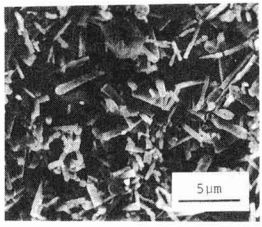

Fig. 1. A SEM picture of the etched surface of the specimen containing 15vol% SiCw.

Nb_3Al Superconducting Filamentary Wire which Withstand High Current Density and High Field

The Japan Atomic Energy Research Institute (JAERI), in cooperation with Sumitomo Electric Industry Co., Ltd., has developed a Nb_3Al filamentary wire which withstands a high magnetic field of 12T and a high current density of 40000A/cm^2. Superconducting magnets are necessary for confining high temperature plasma of 200,000,000°C, and the cost of this superconducting magnets comprises one-third the of total construction cost. R&D on the nuclear fusion reactor has advanced in the construction of Industrial Thermonuclear Experimental Reactor (ITER)). ITER is 17m high and operates under a magnetic field of 12T; therefore, the force imposed on the magnet is estimated to be 40000t. As a result, deformation caused by the magnetic force is unavoidable, and a stress-strain of 0.4% is generated. This stress-strain causes deterioration in superconductivity so that superconducting material can withstand such a high stress-strain because the Nb_3S_M filamentary wire withstands a high magnetic field of over 10T. However, it is seriously affected by stress-strain. Nb_3Al has been known as a material which withstands a high magnetic field; however, it was difficult to obtain high current density. JAERI has succeeded in the fabrication of Nb_3Al filamentary wire which withstands high current density.

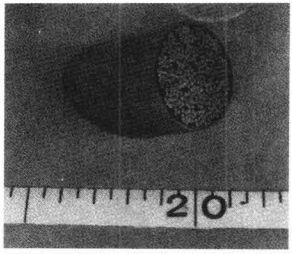

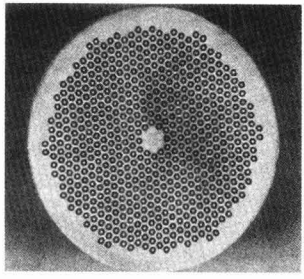

Superconducting Ultra-High Frequency Filter

The Central Research Laboratory of Matsushita Electric Industrial Co., Ltd. has succeeded in the development of a superconducting filter. The filter applied Bi system superconductor and a special design

technique. As a result, the size of the filter has become very compact. The high frequency filter is an indispensable part for electronic equipment which handle high frequency waves. The research subject of the filter is how to reduce the size and how to achieve low loss. The superconducting filter can respond the problem. The new filter is available for 4.8GHz band, and it is 5mm×5mm in size.

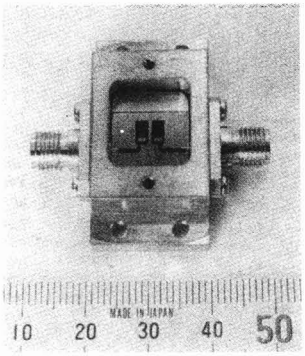

High Temperature Superconducting Current Lead

Fuji Electric Co., Ltd., in cooperation with Furukawa Electric Industry Co., Ltd. developed Japan's first high temperature superconducting urrent lead device. There are some high temperature superconducting current lead elements developed by other companies, but they were only elements and not a finished device such as a current lead. The urrent lead is composed of six Bi system superconducting current lead elements which are cooled with helium gas of 65K. It can transmit maximum of 1300A.

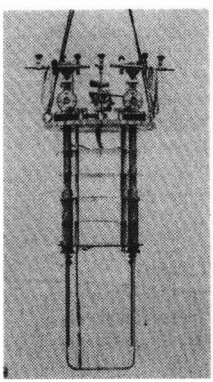

New Ceramic Cutting System

The Agency of Industrial Science and Technology's Government Industrial Research Institute in Kyushu has developed a system that accurately and efficiently cuts hard, dense ceramic materials, such as alumina. The conventional grindstone rotates at a high speed or is fabricated to have rough surface, in order to cut ceramic materials. The new system is characterized by the boring device, which rotates at 3000rpm while vibrating the object at a high frequency of 40kHz and an amplitude of 6 to 7μm. The high frequency vibration enables hard ceramic materials to be cut at lower power because of the greatly reduced resistance received by the boring device during operation (approximately one-fifth the resistance that the conventional grindstone would receive). This increases the efficiency and rotational speed. The bore surfaces are smoother, have less swelling and are less deformed than those made by the conventional grindstone. The institute is now planning to realize higher-frequency vibrations.

High-Speed Grindstone

Noritake Co., Ltd. has developed a grindstone made of cubic boron nitride, which rotates at the world's highest speed, in order to meet the demands for high-speed, precision cutting machines. Its rotational speed is 200m/sec (720km/hr) at the outer periphery, that of the conventional grindstone is 60 to 80m/sec. High-speed cutting machines are under increasing demanded by the precision cutting industry in order to increase service life and functions of materials that are difficult to cut. Recently, many companies have been increasing rotational speed. Some of the noteworthy machines presented at the International Machining Tools Exhibition held in Osaka in 1991 are the Mitsubishi Heavy Industries grinder, rotating at 100m/sec, and that of Toyota Koki, rotating at 100m/sec. The cBN grindstone consists of an iron core coated with the grindstone. Noritake has achieved the high speed by replacing the iron core with a carbon fiber core, for which the bonding techniques have been improved. The company has already started selling the grindstone to some makers.

Thin Film of Diamond

Goei Seisakusho has developed a technique to make thin film of diamond. A thin film, 100mm square at the most, is deposited over substrates of various shapes. Starting materials of hydrogen and methanol gas are chemically activated under a vacuum and then reacted to deposit the high energy carbon atoms. The new technique is characterized by its applicability to substrates of various shapes: a plane, spherical or rod-shape substrate or the edge thereof can be evenly coated with the thin diamond film. The film is 2 to 300μm thick and has a maximum area of 100mm square. The first product sent to the prospective users as a sampie is for the mechanical part which passes fibers at a high speed of 400 to 500m/sec. It is 100 times more durable than the conventional ceramic part. The company is now establishing a mass production system.

Ceramic Composite Material

The Science and Technology Agency's National Aerospace Laboratory has developed a ceramic composite material which maintains high strength even at high temperatures or in a highly oxidative atmosphere. It consists of a three-dimensional (3D) fabric of ceramic fibers filled with silicon carbide. The 3D fabric itself is made of a silicon carbide and titanium composite. Chemical vapor deposition is used to fill the fabric with silicon carbide, producing the strong plate of the ceramic composite. The product manufactured on a trail basis is 20cm long and 2.4cm wide, having the world's highest tensile strength of approximately 2.4tons/cm^2 at 1200°C. The Institute has developed the composite material in cooporation with Ube Industries and Shikibo. The product made for trial is still imperfect in that it is porous, and its strength will be further enhanced by improving the manufacturing process. The new composite is characterized by a monolithic structure of the fabric filled with the ceramic material in order to provide high resistance to oxidation and heat.

Carbon-Carbon Composite

Ishikawajima-Harima Heavy Industries (IHI) has developed a highly heat-resistant material, which can tolerate 2100°C, for space plans. It is a carbon-carbon (CC) composite, in which a carbon plate is reinforced with carbon fibers and coated with a ceramic material. It took 3 years for IHI to develop the technique to coat the CC composite with two layers of the ceramic films of silicon carbide and zirconia in this order. In the new process, a silicon carbide film is formed to a thickness of 100μm over the CC composite by chemical vapor deposition. A zirconia-base ceramic is then sprayed to a thickness of 40μm. The composite is finally heat-treated to form a highly heat-resistant films. The product, which is 20cm square at the largest, is available by the current production system. The new material can be used for engines, as well as the bodies, of supersonic planes.

Light Amplification Effect of Silica Glass

A research group at the Shonan Institute of Technology's Faculty of Engineering, headed by Prof. Y. Nagasawa, has discovered that silica glass has a light amplification effect. It has been confirmed that silica glass emits visible light when irradiated with light. The discovery may lead to the

development of silica glass as a material for solid-state laser. The material investigated is called UV28. It consists of silica glass to which sodium, calcium, potassium, or barium is added. It is normally used for optical filters, but it is known to emit light of wide wavelength range (350 to 700nm) when irradiated with the beams from a krypton fluoride eximalaser. The research group has found that the silica glass activated by the laser beams amplifies light by more than 3 times. This was confirmed by irradiating it with the beams from an argon laser. Silica glass shows the light emitting phenomenon by the mechanism known as Auger-free luminescence. The research group discovered this phenomenon 2 years ago, which led to discovery of the amplification effect by the same mechanism, and which may lead to realization of a solid-state laser.

Growth of Y System Superconductor by Czockralski Process

The Superconductive Technology Laboratory has prepared a single crystal Y system superconductor through the Czockralski process, which is used for manufacturing single crystal silicon. The laboratory succeeded in the preparation of a 5mm square single crystal Y system superconductor . The starting materials were a solution in which Yttrium (5%), Ba (30%), and copper (65%) contained a samarium seed crystal was doped in the solution to be lifted up. Lifting up at a velocity of 0.2 to 0.5mm per hour under 970 to 1000°C with rotation of 10 to 120rpm resulted in a 5mm square × 4mm long single crystal in 25 hours. It critical temperature was 92K. The laboratory is tying to let the seed crystal grow in the lateral direction in order to obtain a 1 or 2 inch long single crystal. This achievement demonstrated possibility of continuous growth of superconductors and opened the way the fabrication of electronic devices.

Thick YBCO Film

Kobe Steel Co., Ltd. has prepared a YBCO system thick film having a critical current density of 12,000A/cm^2. This was the first time in the world that the JC was over 10,000A/cm^2 for a thick film. Thick films of superconductors are expected to be used in applications such as magnetic shielding materials and tape-type wire of superconductor. However, JC has been increased only up to 7500A/cm^2 until now, and such a low JC is not sufficient for operational use. JC of 10,000A/cm^2 suggests the possibility of an operational use superconductor. The sol-gel process was applied in the preparation of the tin film, in addition to the application of the decomposition melting process and the peritectic reaction process. The company had established a process which integrated calcination partial melting, sintering, and annealing into one continuous process under a gas atmosphere. The new process incorporated the sol-gel process and the peritectic reaction process, realizing partial melting of a 123 phase superconductor upon the silver substrate under a low oxygen concentration atmosphere. Under a high oxygen concentration atmosphere, it is difficult to maintain the shape of the specimen because the melting point of silver and superconductor become close.

Heat Shielding Supporter Reducing Thermal Invasion to 1/5

Prof. T. Okada of Osaka University has developed a zirconia ceramic heat-shielding device supporting material which thermally insulates the superconducting helical coil from the vacuum vessel of a nuclear fusion experimental facility. The helical nuclear fusion experimental facility has a structure in which a helical coil winds up a donut-shaped plasma vacuum vessel. Through this structure, plasma is contained in a vacuum vessel without contacting the vessel wall thanks to the magnetic field generated by helical coils. The exterior temperature of the vacuum vessel is approximately 400K, and the helical coil must be kept below 4.2K. In order to thermally insulate coils from the vacuum vessel, a thermal shielding device and a multilayer thermal insulator are being used. When a stainless steel shielding device is used as a shielding device supporter, 16,000W invades the shielding device. When the new zirconia supporter is used, the invasion of heat is reduced to 1/5 that level.

Superconducting Sensor (SQUID) Development Continued by Self-Defense Agency

The Self-Defense Agency has begun full scale R&D on a submarine detection system in which SQUID is applied. The R&D has been commissioned to Mitsubishi Electric Corp., without any significant results. However, the Agency decided to continue R&D on the SQUID applied submarine detection system even after 1993. Mitsubishi Electric Corp. is now manufacturing the sensor system on trial basis. Because the system is expected to be mounted on aircraft, the system must be sufficiently compact. In addition, countermeasures against improvements in the ability of the detection system adopted by submarines, such as deep sea navigation and improvement in wiping technology, have intensified demands for increased accuracy of detection capacity. The Agency is trying to replace the conventional magneto-optic resonance sensor with SQUID in order to improve the detection capacity. Although the current performance of SQUID does not satisfy such requirements, the Agency has decided to continue R&D.

New Type of Cupurate Superconductor which Contains Much CO_3

Nippon Telegram and Telephone Co., Ltd.(NTT) has discovered a new superconductor which contains many CO_3 radicals. The CO_3 radical have been regarded as a substance which degrades superconductivity, and researchers have been trying to reduce CO_3. The discovery of the new superconductor will increase the possibility of R&D in a new area which has not received much attention.

Manufacture of Rotor for 70,000kW Superconducting Generator

Mitsubishi Electric Corp. has begun manufacturing the rotor which will be used for the demonstration generator of the superconducting power generation. The diameter of the rotor is the same as that of the 200,000kW generator and is only short in the length of the shaft direction. Thus, the mechanical strength and cooling characteristics of the rotor are equivalent to that of the operational 200,000kW generator. The materials used for the rotor have been tested. They are iron based super alloy, aluminum alloy, and titanium alloy. The rotor coil model, field winding coil, and dumper shielding model have already been tested on following points:

(1) Rotational coil model

High centrifugal force functions on rotational coil to provide mechanical effects on the coil during rotation.

Cooling characteristics are also different from the static condition during rotation.

(2) Field winding coil model

The coil has the same diameter as the operational 70,000kW generator.

(3) Damper shield model

To test magnetic field shielding, the damper shielding model was manufactured. Specifications of the 70,000kW superconducting generator are as follows:

Capacity (MVA) 83, Output (MW) 75, Voltage (kV) 10, Current (A) 4,792, Power factor 0.9, Number of poles 2, Frequency (Hz) 60, Rotation (r/min) 3,600

Superconducting Electro-Magnetic Propulsion Boat Does Not Navigate at High Speed by Quenching

Yamato, the Japanese first electromagnetic propulsion boat, was able to navigate at 5.5kt but could not navigate at higher speeds as expected. The test was inter-

rupted two times during experimental navigation. The cause of interrupted experimental navigation was quenching. For the first time, the testing team said that the interruption was caused by noise.

High-Resolution Optical Acoustic Microscope Using Interference Laser Beam

The Faculty of Engineering at the University of Tokyo has developed and made on an experimental basis an optical acoustic microscope which is capable of detecting a submicron-order flaw or crystal defect on the surface of a material, such as ceramics, in non-contact mode. The material is irradiated with an interference laser beam, and the propagation of ultrasonic waves and heat caused by heat generation are observed by utilizing the laser scattering phenomenon. The elastic modulus and heat conductivity of a material are found from the propagation of ultrasonic waves and heat conduction, respectively. This results in a high-resolution image. The prototype microscope used a YAG laser added with neodymium to make measuring experiments on a silicon single crystal wafer. The surface of the material implanted with 100 billion pieces of argon/cm^2 could be clearly confirmed up to a depth of 0.5μm.

The new optical acoustic method differs in the use of an irradiation beam that utilizes the interference of divided laser beams to repeat its strength and weakness in a shorter period than that of the conventional method. Repetition of radio heating and cooling causes the irradiate part of the material to generate ultrasonic waves with a GHz level of frequency. These ultrasonic waves are diffused around the irradiated part, and heat is also diffused periodically. The surface of the material has its form changed delicately during transfer of ultrasonic waves or heat. If it is irradiated with the third divided laser beam, then a change occurs in the scattered beam. The elastic modulus and heat conductivity can be found by this change. The interference laser beam that changes equivalent to the wavelength of the laser beam can find a local macro change because its high frequency limits the diffusion of ultrasonic waves to the irradiated part. Images can be displayed by continuously scanning the surface of the material and processing data.

Abstracts of Articles on Ceramics and Superconductivity from the Selected Journals of the Academic Societies

Jpn. J. Appl. Phys.
Vol.31 Part 1 No.4 April 1992
p.1020-1025

Preparation and Superconducting Properties of Bi-Pb-Sr-Ca-Cu-O Films (T_c=106 K) by the Dipping-Pyrolysis Process

Takaaki MANABE, Tatsuo TSUNODA, Wakichi KONDO, Yuji SHINDO, Susumu MIZUTA and Toshiya KUMAGAI

National Chemical Laboratory for Industry, Tsukuba, Ibaraki 305

Superconducting Bi-Pb-Sr-Ca-Cu-O (2223 as the major phase) films were prepared by the dipping-pyrolysis process on MgO(100) substrates using a metal naphthenate solution. From the XRD and SEM-EDX analyses, the formation of the 2223 phase with well-developed platelike grains was facilitated in the films by placing a Pb-containing BSCCO pellet on the surface of the prefired films during the heat treatment (850°C in air) and by the use of a nominal composition of Bi:Pb:Sr:Ca:Cu=1.8:0.4:2.0:2.4:3.6 in molar ratio, i.e., a Ca-and-Cu-rich composition compared to the 2223 phase. The values of $T_{c,zero}$ and J_c(77 K) were 106 K and 2×10^3 A/cm^2, respectively. The dependence of critical current densities on temperature showed that J_c was approximately proportional to $(1-T/T_c)^{3/2}$, which corresponds to the results of the promixity junction tunneling (SNIS) model.

KEYWORDS: Bi-Pb-Sr-Ca-Cu-O, high-T_c superconductor film, critical current density, dipping-pyrolysis process, metal naphthenates

Jpn. J. Appl. Phys.
Vol.31 Part 1 No.4 April 1992
p.1026-1032

Magnetic Shielding by Superconducting Y-Ba-Cu-O Prepared by the Modified Quench and Melt Growth (QMG) Process

Tsutomu SASAKI, Masamoto TANAKA, Mitsuru MORITA, Katsuyoshi MIYAMOTO and Misao HASHIMOTO

Advanced Materials & Technology Research Laboratories, Nippon Steel Corporation, 1618 Ida, Nakahara-ku, Kawasaki 211

Magnetic shielding capability has been investigated on Y-Ba-Cu-O crystals prepared by the modified quench and melt growth (QMG) process at 77 K and 4.2 K. Overall critical current densities in *large single-grained* specimens were estimated to be about 10^4 A/cm^2 based on the Bean model in order to predict shield effect. At 77 K, a single grain cylinder shields the inside up to about 0.2 T of the external field, and this value is the highest among all the values reported so far for tubes fabricated of oxide superconductors. A comparison between shielding characteristics of a *single grain* and those of a *polygrain* demonstrated that weaklinking high-angle grain boundaries should be eliminated for high field shielding. Lorentz force, flux creep, and flux jump are discussed.

KEYWORDS: Y-Ba-Cu-O superconductor, melt process, critical current density, magnetic shielding

Jpn. J. Appl. Phys.
Vol.31 Part 1 No.4 April 1992
p.1033-1038

Enlargement of Kinetic Inductance of NbN Superconducting Thin Films for Device Applications

Mohammad Sajjad HOSSAIN, Keiji YOSHIDA, Keisuke KUDO, Keiji ENPUKU and Kaoru YAMAFUJI

Department of Electronics, Kyushu University 36, Fukuoka 812

Experimental studies to enlarge kinetic inductance of NbN thin films using the effects of quality and thickness of the film are made by measuring Fiske current steps in the current-voltage (I-V) characteristics of NbN/Pb-In Josephson junctions. Experiments demonstrate that the specific kinetic inductance L_K can be enlarged over a wide range by changing stoichiometry of the film, as well as by making the film thickness thin, and that this enlargement becomes larger by both effects when the film thickness is in an ultra thin regime. This inductance is shown to be well fitted to $L_K=\mu_0\lambda^2/d$, where μ_0 is the vacuum permeability, d is the thickness, and λ is the magnetic penetration depth in the dirty limit. In the present experiment we attained the inductance as high as L_K=130 pH by the combined effects of impurity and thickness for a film with d=30 nm.

KEYWORDS: kinetic inductance, magnetic penetration depth, NbN thin film, dirty superconductor, Fiske mode

Jpn. J. Appl. Phys.
Vol.31 Part 2 No.4A April 1992
p.L392-L395

Electrical and Magnetic Properties of the High-T_c Superconductors $(Y_{1-x}M_x)Ba_2Cu_3O_y$ and $Y(Ba_{1-x}M_x)_2Cu_3O_y$ (M=Mg, Ca, Sr, Ba)

Yukichi TATSUMI, Takeji KEBUKAWA, Yutaka MISAWA and Katsuyuki FUJIWARA[1]

The superconducting state of $YBa_2Cu_3O_y$ substituted at the II a group was investigated by X-ray powder diffraction, iodometric titration, electrical resistivity and magnetization measurements. The T_c is shifted to low temperature by the substitution of Y or Ba from a heavy atom to light atom at $x=0.1$, and depends on the ionic radius. In the results obtained from the magnetic hysteresis loop, it is interesting that in the case of the substitution of Ca for $x=0.1$, the magnetization for Y is larger than that for Ba with decreasing temperature, and the magnetization in the case of Ba for Y is rapidly lowered at $x=0.1$.

KEYWORDS: high-T_c superconductor, resistivity, magnetic hysteresis loop, substitution of II a group, $(Y_{1-x}M_x)Ba_2Cu_3O_y$, $Y(Ba_{1-x}M_x)_2Cu_3O_y$, ionic radius

Jpn. J. Appl. Phys.
Vol.31 Part 2 No.4A April 1992
p.L396-L398

A New Superconductor with $T_c=47$ K in the Bi-Sr-Cu-O System (Nominal Composition $=Bi_4Sr_{8+x}Cu_{5-x}O_y$)

Tohru DEN and Toshiaki AIBA

Canon Research Center, Morinosato-Wakamiya, Atsugi-shi, Kanagawa 243-01

A new superconductive bismuth cuprate, with a nominal composition of $Bi_4Sr_{8+x}Cu_{5-x}O_y$, was discovered using resistivity and magnetization measurements. The onset transition temperatures of as-synthesized and He-annealed samples are 42 K and 47 K, respectively. This superconductive phase is very unstable at the synthesis temperature, and thus, changes into $Bi_4Sr_8Cu_5O_{19+\delta}$ and $Bi_2Sr_1Cu_2O_y$ with prolonged calcination. Because of this instability, a single phase cannot be obtained. X-ray diffraction measurements indicate the existence of a new phase with a large-value peak of $d=19.8$ Å.

KEYWORDS: high-T_c superconductivity, bismuth cuprate, annealing effect, $Bi_4Sr_8Cu_5O_{19+\delta}$

Jpn. J. Appl. Phys.
Vol.31 Part 2 No.4A April 1992
p.L399-L401

RHEED Intensity Monitored Growth of Bi-Sr-Ca-Cu-O Superconductors

Shigeki SAKAI, Yuji KASAI and Peter BODIN

Electrotechnical Laboratory, 1-1-4 Umezono, Tsukuba-shi, Ibaraki 305

In order to fabricate Bi-Sr-Ca-Cu-O superconducting thin films, the molecular beam epitaxy (MBE) technique with *in situ* monitoring by reflection high-energy electron diffraction (RHEED) is used. By coevaporated growth of $Bi_2Sr_2CaCu_2O_8$ on $LaAlO_3$ (100) substrates, RHEED intensity oscillation with a period corresponding to the growth of half a unit cell is observed. Out-of-phase oscillations are observed outside the specular spot. After the end of growth, a 10-minute RHEED intensity recovery at the specular spot is found. Possible mechanisms during and after growth are discussed.

KEYWORDS: RHEED intensity oscillation, MBE, BiSrCaCuO superconductor, thin film

Jpn. J. Appl. Phys.
Vol.31 Part 2 No.4A April 1992
p.L410-L412

Submicrometer-Scale Patterning of Superconducting Nb Films Using Focused Ion Beam

Hiroyuki AKAIKE, Akira FUJIMAKI, Yoshiaki TAKAI and Hisao HAYAKAWA

Department of Electronics, Faculty of Engineering, Nagoya University, Furo-cho, Chikusa-ku, Nagoya 464-01

We have developed a novel patterning technique for superconducting Nb films with submicrometer scales, using a focused ion beam (FIB). The technique makes use of a phenomenon wherein the plasma etching rate of Nb films exposed to a Ga^+ focused ion beam is much lower than that of unexposed Nb films, when they are etched by reactive ion etching (RIE) in CF_4 plasma. The etching rate of films exposed to 100 keV Ga^+ FIB at a dose $>2\times10^{16}/cm^2$ was less than one-quarter of that of unexposed films. Using this technique, we have fabricated 0.1-μm-wide Nb strips with the critical current density of 1×10^7 A/cm^2 at 4.2 K. This value is almost equal to that of bare films.

KEYWORDS: submicrometer patterning, Nb, focused ion beam, reactive ion etching, Ga ion, CF_4 plasma

Jpn. J. Appl. Phys.
Vol.31 Part 2 No.4B April 1992
p.L464-L466

Magnetic Shielding Property of Bi(Pb)-Sr-Ca-Cu-O Superconducting Tube

Keizou TSUKAMOTO, Mamoru ISHII, Hiromasa SHIMOJIMA, Chitake YAMAGISHI, Masasuke TAKATA[1] and Tsutomu YAMASHITA[2]

Central Research Laboratory, Nihon Cement Co., Ltd., Koutou-ku, Tokyo 135
[1]Department of Electrical Engineering, Nagaoka University of Technology, Nagaoka, Niigata 940-21
[2]Research Institute of Electrical Communication, Tohoku University, Sendai, Miyagi 980

The magnetic shielding property of a Bi(Pb)-Sr-Ca-Cu-O superconducting tube was examined. The measured internal magnetic flux density of the tube, as a function of the applied magnetic field, agreed with the critical state model calculated with the consideration of the hysteresis of the critical current density on the magnetic field.

KEYWORDS: magnetic shielding property, superconducting tube, critical state model, hysteresis of critical current density

Jpn. J. Appl. Phys.
Vol.31 Part 2 No.4B April 1992
p.L467-L470

Site Occupancy and Anharmonic Thermal Vibration in Superconductor $Tl_2CaBa_2Cu_2O_8$

Satoshi SASAKI, Kenichi KAWAGUCHI[1] and Masao NAKAO[1]

Research Laboratory of Engineering Materials, Tokyo Institute of Technology, Nagatsuta 4259, Midori-ku, Yokohama 227
[1]Sanyo Tsukuba Research Center, Koyadai 2-1, Tsukuba 305

Crystal structure analysis of $Tl_2Ca_{n-1}Ba_2Cu_nO_{2n+4}$ ($n=2$; $I4/mmm$) was performed using single-crystal X-ray intensity data up to $\sin\theta/\lambda=1.37$ Å^{-1}. The cell dimensions are $a=3.8471(6)$ and $c=29.397(5)$ Å. The chemical formula determined by X-ray diffraction is $(Tl_{0.864}Cu_{0.136})_2(Ca_{0.910}Tl_{0.090})Ba_2Cu_2O_8$. The O(3) atoms occupy the 4*e* sites at (1/2, 1/2, *z*). Difference-Fourier syntheses showed the existence of anharmonic thermal vibration for Tl and Ba atoms, which was described by the Gram-Charlier series expansion of the Gaussian density function. The *R* value was 0.015 ($R_w=0.014$) for 637 reflections averaged from 43188.

KEYWORDS: high-T_c superconductor, superconductivity, Tl-Ca-Ba-Cu-O, $Tl_2CaBa_2Cu_2O_8$, X-ray diffraction, single-crystal study, site occupancy, anharmonic thermal vibration

Jpn. J. Appl. Phys.
Vol.31 Part 2 No.4B April 1992
p.L471-L473

Low-Temperature ^{119}Sn-Mössbauer Study of Superconducting $Bi_4Sr_{3.5}Ca_{2.5}Cu_4Sn_{0.015}O_{16-y}$ Ceramic (2212 Phase)

Tetsuaki NISHIDA, Motomi KATADA[1], Norio MIURA[2], Yuichi DESHIMARU[2], Noboru YAMAZOE[2], Yasukuni MATSUMOTO[3] and Yoshimasa TAKASHIMA

Department of Chemistry, Faculty of Science, Kyushu University, Hakozaki, Higashiku, Fukuoka 812
[1]RI Research Center, Tokyo Metropolitan University, Minamiosawa, Hachioji 192-03
[2]Department of Materials Science and Technology, Graduate School of Engineering Sciences, Kyushu University, Kasuga-shi, Fukuoka 816
[3]Department of Electrical Engineering, Faculty of Engineering, Fukuoka University, Nanakuma, Fukuoka 814-01

The ^{119}Sn-Mössbauer spectra of superconducting $Bi_4Sr_{3.5}Ca_{2.5}Cu_4Sn_{0.015}O_{16-y}$ ceramic (2212 phase, T_c: 77 K), measured between 298 K and 7 K, consist of singlet peaks of Sn^{4+} with the δ's and Γ's of -0.01–0.07 and 1.05–1.27 mm·s^{-1}, respectively. The ln *A* (absorption area)-vs-*T* plot shows that the recoil-free fraction *f* increases with decreasing temperature, and that the Debye and Einstein temperatures are 340 and 185 K, respectively. The Θ_D of 340 K suggests that the Sn^{4+} is in the BiO_5 pyramids. The ln *A* shows a "normal" lattice vibration probably because of the long Cu-O(3) distance and the displacement of O(3).

KEYWORDS: superconductor, Bi(Sn)-Sr-Ca-Cu-O, low-T_c 2212 phase, ^{119}Sn-Mössbauer, lattice dynamics, "normal" vibration, Debye temperature, Einstein temperature, displacement

Jpn. J. Appl. Phys.
Vol.31 Part 2 No.4B April 1992
p.L477-L480

Forces Acting on a Magnet Placed over a Superconducting Plane

Zhongjin YANG

Department of Physics, University of Oslo, P.O.Box 1048,0316 Oslo 3, Norway

Based on the London theory, we have calculated the forces acting on a magnet placed above a superconductor. The results have been used to calculate (i) the forces acting on a spherical magnet over a superconducting plane; (ii) the forces acting on a ring-shape magnet above a superconducting plane; and (iii) the force between the tip of a magnetic force microscope (MFM) and a superconducting plane due to the diamagnetic response of the superconductor to the stray field of the tip.

KEYWORDS: high T_c superconductor, Meissner effect, London model, magnetic force microscope

J. Soc. Mat. Sci., Japan
Vol.41 No.464 May 1992
p.561-566

Thermal Fatigue Behavior of Alumina Ceramics by Water Quenching Method

Tadahiro NISHIKAWA*, Tie GAO*, Mamoru KOSAKAI**
Toru NISHIBE* and Manabu TAKATSU***

Thermal fatigue behavior of four kinds of alumina ceramics, having different fracture toughness/bending strength ratio, was investigated. After the testpieces pre-cracked by Knoop indentation were heated in a constant temperature, they were quenched in water, and their propagated crack lengths were measured. Since the heat transmission condition varied from natural convection to nucleant boiling in the range of this experimental temperature, the heat transfer coefficient was corrected before illustrating the $(K_{I\,max}/K_{IC})$-V curve. The thermal fatigue behavior of each alumina ceramics was discussed quantitatively based on the fatigue parameters n and A, which were derived from the crack propagation rate equation $V=A(K_I/K_{IC})^n$. For the alumina ceramics in which transgranular fracture was mainly observed, the n values were hardly different but $\log A$ values decreased with increasing particle size. This indicated that the crack propagation rate became low. For those in which more larger particles or pores were observed, the $\log A$ values and the crack propagation rate were quite different. Those different behaviors on thermal fatigue may be explained by different propagation mechanisms at crack tips. The control of microstructure is important for thermally used ceramics, because the microstructure determines the crack propagation pass.

Key words : Thermal fatigue, Water quenching method, Alumina ceramics, Heat transfer coefficient, Microstructure, R-curve behavior

* 名古屋工業大学材料工学科 〒466 名古屋市昭和区御器所町, Dept. of Mat. Sci. & Eng., Nagoya Inst. of Tech., Showa-ku, Nagoya, 466
** 住友セメント(株) 〒274 船橋市豊富町, Sumitomo Cement Co. Ltd., Toyotomi-cho, Funabashi, 274
*** 正会員 名古屋工業大学材料工学科 〒466 名古屋市昭和区御器所町, Dept. of Mat. Sci. & Eng., Nagoya Inst. of Tech., Showa-ku, Nagoya, 466

J. Soc. Mat. Sci., Japan
Vol.41 No.464 May 1992
p.588-592

Reactivity of a Y-Ba-Cu-O Superconductor with Electrooptic Crystals

Shoichi HASHIGUCHI*, Eungi MIN*, Shinichi KIKKAWA**
Fumikazu KANAMARU*** and Takeshi KOBAYASHI****

The YBCO thin films were deposited on LN and BNN substrates through an RF magnetron sputtering method. The YBCO thin films on BNN were c-axes oriented with T_c (zero)=72.5K and c =11.70 Å. The thickness of the reaction layer for BNN was one order of magnitude thinner than that for LN. From these results, the BNN single crystal was concluded to be suitable for an electrooptic substrate for YBCO thin film fabrication.

Key words : Reactivity, $YBa_2Cu_3O_y$, Electrooptic crystals, RF magnetron sputtering method

We investigated the reactivity of $YBa_2Cu_3O_y$ (YBCO) with electrooptic crystals, such as $LiNbO_3$ (LN), $LiTaO_3$ (LT), $Sr_{0.75}Ba_{0.25}Nb_2O_6$ (SBN), $KTa_{0.65}Nb_{0.35}O_3$ (KTN), $Ba_2NaNb_5O_{15}$ (BNN). The YBCO powder mixed with 5 wt% electrooptic crystal was heated at 700°C for 8 hr, 16 hr or at 900°C for 8 hr in air. The reactivity of LT, LN, KTN with YBCO was considerably high, and that of BNN was relativly low.

* 住友セメント(株) 〒101 東京都千代田区美土代町, Sumitomo Cement Ltd., Chiyoda-ku, Tokyo, 101
** 大阪大学産業科学研究所 〒567 茨木市美穂ヶ丘, The Inst. of Sci. & Ind. Res., Osaka Univ., Mihogaoka, Ibaraki, 567
*** 正会員 大阪大学産業科学研究所 〒567 茨木市美穂ヶ丘, The Inst. of Sci. & Ind. Res., Osaka Univ., Mihogaoka, Ibaraki, 567
**** 大阪大学基礎工学部電気工学科 〒560 豊中市待兼山町, Faculty of Eng. Sci., Osaka Univ., Machikaneyama-cho, Toyonaka, 560

J. Soc. Mat. Sci., Japan
Vol.41 No.464 May 1992
p.593-599

X-Ray Measurement of Triaxial Residual Phase Stress in Zirconia-Alumina Composite Ceramics

Keisuke TANAKA*, Motoyasu MATSUI**, Ryoichi SHIKATA***
and Tomozo NISHIKAWA****

The X-ray diffraction method was used to measure the residual stress in composite ceramics of zirconia mixed with various volume fractions of alumina. The triaxial state of the residual stress in each phase was determined from the X-ray diffractions of Al_2O_3 (146) by Cu-Kα radiation and of ZrO_2 (133) by Cr-Kα radiation. In as-sintered materials, the residual stress in the alumina phase was compression, and decreased linearly with the alumina volume fraction V_f. On the other hand, the tensile residual stress was observed in the zirconia phase, and increased linearly with V_f. Those residual stresses were due to the mismatch of the coefficient of thermal expansion. The theoretical prediction based on Eshelby's inclusion mechanics agreed well with the experimental results.

Key words : Residual stress, X-ray stress measurement, Composite ceramics, Zirconia, Alumina, Phase stress

* 正会員 名古屋大学工学部機械工学科 〒464-01 名古屋市千種区不老町, Dept. of Mech. Eng., Nagoya Univ., Chikusa-ku, Nagoya, 464-01
** 学生会員 京都大学大学院 〒606-01 京都市左京区吉田本町, Graduate Student, Kyoto Univ., Sakyo-ku, Kyoto, 606-01
*** 大阪セメント(株) 〒597 貝塚市二色中町, Osaka Cement, Nisikinaka-machi, Kaizuka, 597
**** 正会員 京都工芸繊維大学工芸学部物質工学科 〒606 京都市左京区松ヶ崎御所海道町, Dept. of Chem. & Mat. Tech., Kyoto Inst. of Tech., Sakyo-ku, Kyoto, 606